

Surface Interactions of Proteinogenic
Biomolecules and Gold Nanostructures on
 $\text{Si}(111)7\times 7$

by

Seyedeh Fatemeh Rahnemaye Rahsepar

A thesis
presented to the University of Waterloo
in fulfillment of the
thesis requirement for the degree of
Doctor of Philosophy
in
Chemistry

Waterloo, Ontario, Canada, 2015

© Seyedeh Fatemeh Rahnemaye Rahsepar 2015

AUTHOR'S DECLARATION

This thesis consists of material all of which I authored or co-authored: see Statement of Contributions included in the thesis. This is a true copy of the thesis, including any required final revisions, as accepted by my examiners.

I understand that my thesis may be made electronically available to the public.

Statement of Contributions

Seyedeh Fatemeh Rahnemaye Rahsepar contributed to the concept and design of the study. S. F. R. R. performed the experiments, analysed and interpreted the data, and the large-scale DFT-D2 calculations. S. F. R. R. wrote the papers (parts of which are used in Chapters 3 & 4). Tong Leung, Lei Zhang and Hanieh Farkhondeh discussed the results and commented on the manuscripts.

Abstract

The site-specific surface interactions and film growth mechanisms of adsorption of gold and of proteinogenic sulfur-containing amino acids, i.e., L-cysteine and L-methionine, on Si(111)7×7 are studied for the first time by X-ray photoelectron spectroscopy (XPS) and Scanning Tunneling Microscopy (STM) at room temperature under ultrahigh vacuum condition. The results are supported with large-scale density functional theory (DFT) calculations with dispersion correction for biomolecule adsorbates, to provide precise modeling of the equilibrium adsorption geometries of adsorbates on a Si₂₀₀H₄₉ slab used as the model Si(111)7×7 surface. Growth evolution of gold on the 7×7 surface is found to follow the Stranski-Krastanov mode, starting with completion of two distinct gold silicide layers to individual gold nanoisland formation. Of special interest is the formation of two-dimensional self-assembled gold silicide honeycomb nanonetwork at 0.76 monolayer coverage at room temperature. Observed for the first time, this honeycomb nanonetwork is made up of six triangular gold clusters (surrounding each corner hole) interconnected to one another at the dimer rows of the Si(111)7×7 substrate. With the corner holes of the 7×7 surface exposed, this novel gold silicide template offers a unique honeycomb network (4 nm in grids size) for surface functionalization and a nanopore pattern (~1 nm in pore size) for molecular trapping application.

In analogy to common simple aliphatic amino acids, such as glycine and alanine, sulfur-containing aliphatic amino acids, cysteine and methionine, exhibit an “universal” three-stage growth sequence on Si(111)7×7 surface at room temperature under ultra-high vacuum condition. In particular, the biomolecule first anchors to specific dangling bond sites on the 7×7 reconstruction via strong short-range covalent bonds (through Si–N and/or Si–S linkages in unidentate and/or bidentate arrangement of cysteine adsorption, and through Si–N linkage in unidentate arrangement of methionine adsorption), forming the interfacial layer (the first adlayer). This is then followed by the formation of a transitional layer (the second adlayer) and finally of a zwitterionic film (multilayer), both of which are driven by intralayer and interlayer hydrogen bonding. XPS study of thermal stabilities of these adlayers indicates that these proteinogenic biomolecules can be used to transform a highly reactive Si(111)7×7 surface to not just a permanent bio-organic surface but also a semi-permanent (or renewable) and a temporary bio-organic surfaces by manipulating the exposure and the post-annealing temperature. Our results on all the adsorbed proteinogenic biomolecules on Si(111)7×7 surface studied to date enable us to construct a reference XPS data table to guide future studies of biofilm growth on reconstructed Si(111) surface.

The STM study of adsorbed cysteine on Si(111)7×7 provides strong evidence for coverage-dependent adsorption structures of cysteine, from bidentate to unidentate attachments to self-assembled multimers, which involves formation of intralayer horizontal N···H–O hydrogen-bond as reported in our XPS study. In contrast to cysteine adsorption, high-resolution STM imaging demonstrates self-organization of methionine into a novel, stable Y-shaped trimer within a half unit cell on the 7×7 surface at room temperature, which is driven by hydrogen bonding among the unattached carboxylic acid groups in a ring configuration. The near-perfect match of the Y-shaped trimer with three-fold symmetry within the half-unit cell represents the first supported “magic-number” molecular cluster reported to date.

Our XPS experiments provide the primary experimental evidence for the formation of covalent bond between substrate and adsorbates and the feasibility of the intralayer and interlayer hydrogen bonding mediated dimers. They are also supported by our large-scale ab-initio DFT-D2 calculations. Using ab-initio DFT-D2 calculations, we also establish a common trend in the H-bond length among different types of hydrogen bonding ($O-H\cdots N < O-H\cdots O < N-H\cdots N < N-H\cdots O$) for di-molecular structures in the gas phase. Except for the N–H···N H-bond due to covalent bonding of the amino group with the surface, this trend can also be applied to biomolecular H-bonding surface interaction. These calculated results and the observed trends can be used to predict the adsorption behavior of larger biochemical materials, such as peptides and proteins.

The ultimate goal of the present study is to examine the molecular interaction of these aliphatic amino acids with gold clusters and other metallic nanostructures supported on the 7×7 surface. We have performed preliminary XPS and STM studies on the molecular interactions of cysteine with three distinct gold nanoassemblies on Si(111)7×7, including Au monomers and dimers, Au silicide honeycomb nanonetwork, and Au nanocrystallite film. These studies show unidentate and/or bidentate bonding arrangement of adsorbed cysteine with rather minor perturbation due to the presence of the supported Au monomers and dimers. On the Au silicide honeycomb nanonetwork, we observe the coexistence of two chemisorption states, involving unidentate adspecies through the thiol group interaction with Au atoms and of the amino group with Si atoms. Cysteine is found to chemisorb via the sulfur in neutral form on the supported Au nanocrystallite film to form the interfacial layer. These STM/XPS studies are reinforcing our hypothesis that the novel gold silicide honeycomb nanonetwork offers a number of interesting potential applications for molecular trapping and biofunctionalization.

Acknowledgements

First and foremost I would like to give my deepest gratitude to my supervisor Prof. Kam Tong Leung, who gave me the opportunity to be a part of the Waterloo Advanced Technology Laboratory (WATLab) family and opened the door that led to the fascinating world of science and technology. It has been an honor to be his student and I appreciate all his contributions of time, ideas, patience, and motivation from the very early stage of this thesis. I am indebted to him more than he knows. Beside my supervisor, I would also like to thank my advisory committee members, Dr. Marcel Nooijen, Dr. Qing-Bin Lu, and Dr. Dan Thomas for their insightful comments, suggestions and valuable feedback on the work, and to Dr. Zbig Wasilewski for serving on the examination committee.

I am also grateful to Dr. Lei Zhang for his help and advice in the use of the molecular beam epitaxy systems, scanning tunneling microscopy, and X-ray photoelectron spectroscopy equipment.

It is a pleasure to thank our staff at the Science Machining and Electronics Shops: Harmen Vander Heide, Peter Kessel, Jacek Szubra, Zhenwen Wang and Krunomir Dvorski for helping me every time I faced any technical problem. Their brilliance has always enabled me to return to my experiments by resolving the problems that I encountered.

I am truly thankful to my colleagues and group members, Lei Zhang, Nafiseh Moghimi, Marwa Abdellah, Avishek Chatterjee, Samad Bazargan, Hanieh Farkhondeh, Nina Heinig, Joseph Palathinkal, Md Anisur Rahman, Saurabh Srivastava, Donald McGillivray, Mahdi Beedel, Jung-Soo Kang, Shantinarayan Rout, Yan Wang-Duffort for their tremendous support and enthusiasm.

I would like to thank my family for all their love and encouragement; my parents Farkhonde and Hassan who raised me with love of education and supported me in my whole life; my lovely sister Azi for always being supportive and caring sibling; and most of all, my loving, supportive, encouraging, and patient husband Farzad for his faithful support during all this way.

I recognize that this research would not have been possible without the financial assistance of Natural Sciences and Engineering Research Council of Canada, University of Waterloo Office of Graduate Studies, and the Department of Chemistry at the University of Waterloo.

Finally, I would like to thank everybody who has been important to the successful realization of the thesis, and to express my apology that I could not mention them personally one by one.

Dedication

I dedicate this thesis to my lovely husband Farzad who has been a great source of motivation and inspiration, and to my wonderful parents Farkhondeh and Hassan, and my sister Azi who have supported me all the way since the beginning of my studies.

“The bond that links your true family is not one of blood, but of respect and joy in each other’s life.”

– Richard Bach

Table of Contents

| | |
|---|-------|
| AUTHOR'S DECLARATION..... | ii |
| Statement of Contributions | iii |
| Abstract..... | iv |
| Acknowledgements..... | vi |
| Dedication..... | vii |
| Table of Contents..... | viii |
| List of Figures..... | xi |
| List of Appendix Figures | xviii |
| List of Tables | xxiii |
| List of Appendix Tables..... | xxiv |
| List of Schemes..... | xxv |
| Chapter 1 Introduction..... | 1 |
| 1.1 Surface Science..... | 1 |
| 1.1.1 Surface Chemistry of Silicon | 2 |
| 1.1.2 Si(111)7×7 Surface | 3 |
| 1.2 Adsorption of Metals on Si(111)7×7 | 7 |
| 1.3 Adsorption of Organic/Bio Molecules on Si(111)7×7..... | 7 |
| 1.4 Molecular Interactions of Biomolecules with Metal Clusters Supported on Si(111)7×7..... | 10 |
| 1.5 Methodologies of Surface Sensitive Techniques..... | 10 |
| 1.5.1 X-ray Photoelectron Spectroscopy..... | 11 |
| 1.5.2 Scanning Tunneling Microscopy | 13 |
| 1.6 Scope of Thesis | 18 |
| Chapter 2 Experimental and Computational Details..... | 20 |
| 2.1 Generation of 7×7 Reconstructed Surface of Si(111)..... | 20 |
| 2.2 Molecular Beam Epitaxy of Metal and Organic Materials | 22 |
| 2.3 Analysis Chamber..... | 24 |
| 2.3.1 X-ray Photoelectron Spectroscopy for Chemical-State Composition Analysis..... | 24 |
| 2.3.2 Scanning Tunneling Microscopy for Atomic Resolution Imaging | 26 |
| 2.4 Computational Details | 28 |
| 2.4.1 Slab Model..... | 31 |
| Chapter 3 Two-dimensional Self-assembled Gold Silicide Honeycomb Nanonetwork on Si(111)7×7..... | 34 |

| | |
|---|-----|
| 3.1 Introduction..... | 34 |
| 3.2 Experimental Details..... | 35 |
| 3.3 Results and Discussion | 36 |
| 3.4 Summary | 42 |
| Chapter 4 Biofunctionalization of Si(111)7×7 by L-Cysteine..... | 44 |
| 4.1 Introduction..... | 44 |
| 4.2 Experimental Details..... | 46 |
| 4.3 Results and Discussion | 47 |
| 4.4 Summary | 63 |
| Chapter 5 Biofunctionalization of Si(111)7×7 by L-Methionine | 64 |
| 5.1 “Universal” Three-Stage Growth of α -Amino Acids on Si(111)7×7 as Mediated by Surface Hydrogen Bonding..... | 64 |
| 5.1.1 Introduction..... | 64 |
| 5.1.2 Experimental Details and DFT Calculations | 67 |
| 5.1.3 Results and Discussion | 69 |
| 5.1.4 Summary | 88 |
| 5.2 Novel Self-Organized Y-shaped Trimer of L-methionine: A Magic-Number Cluster Supported on Si(111)7×7 | 90 |
| 5.2.1 Introduction..... | 90 |
| 5.2.2 Experimental Details..... | 92 |
| 5.2.3 Results and Discussion | 93 |
| 5.2.4 Summary | 102 |
| Chapter 6 Molecular Interaction of Cysteine on Gold Templates Supported on Si(111)7×7..... | 104 |
| 6.1 Introduction..... | 104 |
| 6.2 Experimental Details..... | 105 |
| 6.3 Results and Discussion | 106 |
| 6.3.1 Interaction of Cysteine with Supported Gold Monomers and Dimers (0.004 ML) | 107 |
| 6.3.2 Interaction of Cysteine with Supported Gold Silicide Honeycomb Nanonetworks (0.76 ML)..... | 110 |
| 6.3.3 Interaction of Cysteine with Au Nanocrystallite Film (3.97 ML)..... | 113 |
| 6.4 Summary | 116 |
| Chapter 7 Conclusion and Future Work | 117 |

| | |
|--|-----|
| Appendix A Two-dimensional Self-assembled Gold Silicide Honeycomb Nano-network on Si(111)7×7 | 125 |
| Appendix B Biofunctionalization of Si(111)7×7 by L-Cysteine | 128 |
| Appendix C Biofunctionalization of Si(111)7×7 by L-Methionine..... | 139 |
| Appendix D Permissions..... | 159 |
| Bibliography | 161 |

List of Figures

- Figure 1.1 (a) Filled-state and (b) corresponding empty-state STM images ($10 \times 10 \text{ nm}^2$) of a clean Si(111) 7×7 surface obtained at a sample bias of -2 and $+2$ V, respectively, and a tunneling current of 200 pA. The faulted and unfaulted half unit cells are marked by F and U, respectively, in (a). (c) Filled-state STM image ($10 \times 10 \text{ nm}^2$) obtained at a less negative sample bias of -1.5 V shows discernible contrast between restatoms and adatoms. (d) Top view and (e) side view of the equilibrium dimer-adatom-stacking fault (DAS) model of a $\text{Si}_{200}\text{H}_{49}$ cluster (consisting of a top adatom layer, a restatom layer, a dimer bilayer, a base Si layer, and a layer of H atoms used for terminating the base Si layer) obtained by large-scale DFT calculations used as the model surface for Si(111) 7×7 . The sizes of the spheres used to represent the Si atoms are smaller with increasing distance from the surface (the top adatom layer). The adatoms, both corner adatoms (AAs) and center adatoms (CAs), and the restatoms (RAs) are highlighted by larger yellow and green circles for clarity, respectively. A prime symbol is used to denote a substrate atom in the adjacent half unit cell. The dangling bonds on the top of adatoms, restatoms, and corner hole are identified in (e). All STM images are collected by using a variable-temperature scanning probe microscope, manufactured by Omicron Nanotechnology, at WATLab and the model surface is generated by large-scale ab-initio quantum mechanical calculations using a Xeon computer cluster at WATLab..... 6
- Figure 1.2 Left panel shows a photograph of a typical XPS system, consisting of an X-ray cathode, an X-ray anode, and a quartz-crystal X-ray monochromator, sampling position of the illuminating X-ray (approximate), an electrostatic lens system, a hemispherical analyzer, and a seven-channeltron electron detector. Right panel shows the corresponding control electronics of the XPS instrument. 13
- Figure 1.3 (a) An infinitely thick potential barrier where the potential is V for $x > 0$ and 0 for $x < 0$. (b) Electron wavefunctions for two metal electrodes 1 and 2 with work function Φ_1 and Φ_2 separated by a large distance. (c) As the separation between the electrodes becomes sufficiently small, the electron wavefunctions from both electrodes become connected. With the electron wavefunction overlapping each other, tunneling through the barrier may now proceed especially when assisted by the application of a bias potential difference. 15
- Figure 1.4 Principle of operation of a STM, where V_t is the sample bias voltage between the tip and the sample and V_z is the voltage applied to the z piezo. In the constant current imaging mode, this z -piezo voltage is used to adjust the tip-to-sample separation so as to maintain a constant tunneling current. The control unit (CU) is used for the feedback loop. 15
- Figure 1.5 Schematic diagram of different scanning modes for STM imaging. (a) Constant current mode where the z -piezo voltage (corresponding to the height z) is adjusted to maintain a constant tunneling

| | |
|--|----|
| current I_t , and (b) constant height mode, where the z position (i.e., the z-piezo voltage) is kept fixed and the tunneling current is measured. | 16 |
| Figure 1.6 (a) By applying a positive bias to the sample (with respect to the tip), tunneling occurs from the occupied states of the tip to the empty-states of the sample (empty-state imaging). (b) By applying a negative bias to the sample, tunneling is reversed from the occupied states of the sample to the empty states of the tip. | 18 |
| Figure 2.1 (a) and (b) Photographs of the Omicron multi-technique UHV system taken from two different angles. This five-chamber UHV system consists of two molecular beam epitaxy chambers: MBE1 for low-temperature organic material deposition and MBE2, equipped with a RHEED system, for high-temperature metal and inorganic material deposition; and an analysis chamber equipped with a X-ray photoelectron spectrometer (XPS), a variable-temperature scanning probe microscope (SPM), and a low energy electron diffractometer (LEED); as well as a fast entry lock (FEL) chamber (out of view) and a center transfer chamber (CTC). (c) and (d) The machine drawings showing the top and side view, respectively. | 21 |
| Figure 2.2 (a) The schematic diagram of the sample holder assembly (Omicron User Manual), and (b) photograph of a Si(111) chip ($11 \times 2 \text{ mm}^2$, 0.3 mm thick, from Virginia Semiconductor Inc., USA) mounted on the assembled sample holder. | 22 |
| Figure 2.3 (a) Photograph of MBE1 chamber for deposition of bio/organic materials, which was equipped with four low-temperature precision effusion cells (two OME and two NTEZ cells), a quadrupole mass spectrometer, and a cooling water recirculator. The inset in (a) shows a magnified inside view of the MBE1 chamber, in which the sample stage was attached on a magnetic transfer rod. Photographs of (b) an OME effusion cell, and (c) a NTEZ effusion cell, along with a quartz and a polytetrafluoroethylene crucibles. Schematic diagrams of (d) the OME cell and (e) NTEZ cell, depicting the crucible, heating system, evaporant (powder), thermocouple and water-cooling mechanism. | 23 |
| Figure 2.4 Photographs of (a) MBE2 chamber for deposition of metals and inorganic materials equipped with two medium temperature (WEZ) and two high-temperature (EFM) effusion cells and a RHEED system, (b) WEZ effusion cell and (c) EFM effusion cell. | 24 |
| Figure 2.5 (a) Photograph of the X-ray photoelectron spectrometer, consisting of an X-ray source with a monochromator, and a hemispherical electron energy analyser with an entrance lens and an exit detector systems. (b) Schematic diagram of the X-ray monochromator with individual components: X-ray source and manipulator, and a quartz crystal mirror monochromator. The X-ray anode, monochromator and the sample position are appropriately aligned on the Rowland circle. (c) Schematic diagram of the relative | |

orientation of the photon emission direction of the monochromator with respect to the entrance lens direction of the analyser (i.e. the photoelectron emission direction). (d) Photograph of an X-ray source (XM 1000MKII) with the short and long filament cathodes, and the aluminum-coated anode surface.....26

Figure 2.6 Photographs of the Omicron VT-SPM system: (a) SPM chamber with a wobble stick, the laser electronics for AFM operation, and a camera; (b) VT-SPM microscope outside the chamber; (c) STM scanner stage with a STM tip; and (d) data acquisition computer with control electronics. 27

Figure 3.1 STM filled-state images of (a) 0.004, (b) 0.05, (c) 0.20, (d) 0.76, (e) 1.14, (f) 1.53, (g) 1.80, (h) 2.40, and (i) 3.97 ML of Au on Si(111)7×7 at room temperature, all collected with a sample bias of – 2.0 V and a tunneling current of 0.2 nA. The field of views for (a-c) and (d-i) are 50×50 nm² and 100×100 nm², respectively. The faulted and unfaulted half unit cells are marked by F and U, respectively, in (a). Insets in (a) and (d) show the Fourier transforms of the respective images, in which the 1/7th fractional spots corresponding to the periodic (7×7) reconstruction are clearly evident. 38

Figure 3.2 (a) XPS spectra of the Au 4f region for different Au coverages on Si(111)7×7 at room temperature. Solid and dashed lines mark the Au 4f peak positions for the gold silicide (Au_xSi) and metallic Au components, respectively. (b) Corresponding peak areas of the Au 4f_{7/2} peaks for Au_xSi and metallic Au components (along with their sum, marked as total), and of the Si 2p_{3/2} state at 99.3 eV. 40

Figure 3.3 Schematic model of the growth evolution of Au on Si(111)7×7 at room temperature. Left column shows optimized structures based on DFT calculations for the early growth stage up to the formation of the first gold silicide layer. Right column shows the evolution to the second Au silicide layer and the formation of metallic Au islands..... 42

Figure 4.1 Evolution of (a) O 1s, (b) N 1s, (c) C 1s, and (d) S 2s XPS spectra of cysteine deposited on Si(111)7×7 as a function of exposure time (5 s to 5400 s); and of the as-deposited 5400 s cysteine film upon annealing to 85°C, 175°C and 285°C. 49

Figure 4.2 Peak areas of various O 1s, N 1s, C 1s, and S 2s features (a) for different cysteine exposure times; and for a multilayer cysteine film (obtained with 5400 s exposure, solid lines) and a transitional layer (obtained by annealing the multilayer film at 85°C for 20 min, dashed lines) as functions of (b) annealing temperature, and (c) storage time in ultrahigh vacuum condition. (d) Schematic bonding model of available surface functional groups, and intra- and interlayer interactions for the interfacial layer, transitional layer and the multilayer film of cysteine on Si(111)7×7. 51

Figure 4.3 (a) Filled-state and (b) corresponding empty-state STM images (45×45 nm²) for a 3 s exposure of cysteine on Si(111)7×7 obtained with a sample bias of –2 and +2 V, respectively, and a tunneling current of 200 pA, with magnified views (7.2×7.2 nm²) shown in insets; and corresponding LDOS

profiles along long-diagonals [from corner atom (AA) to restatom (RA) and to center atom (CA)] (c) L1 and L2; and (e) L3 and L4; and (d) perspective view of the equilibrium geometry of a cysteine molecule adsorbed through N–H and S–H dissociation on adjacent center adatoms across a dimer wall on a $\text{Si}_{200}\text{H}_{49}$ slab as obtained by DFT calculation (Appendix B). Cysteine molecules in the faulted (FHUC) and unfaulted half unit cells (UHUC) are marked by up triangles and down triangles, respectively. The separation between two adjacent center adatoms across a dimer wall is 0.7 nm. 55

Figure 4.4 (Color online) (a) Empty-state STM image ($30 \times 30 \text{ nm}^2$) of a 25 s exposure of cysteine on $\text{Si}(111)7 \times 7$ recorded with a sample bias of +2 V and a tunneling current of 200 pA; magnified images of a bidentate cysteine molecule at (b) (AA, AA') and (c) (CA, CA') sites; H-bond mediated dimers formed from different unidentate cysteine molecules in (d) CA-CA in faulted half unit cell and (e) in unfaulted half unit cell, (f) AA-CA, (g) CA-CA' (across the dimer wall), and (h) AA-AA'; self-assembled cysteine trimers in (i) CA-AA-CA and (j) CA-CA-CA' sites on $\text{Si}(111)7 \times 7$ surface. LDOS profiles along the long-diagonals (m) L2 for monomer in (c), (l) L3 for dimer in (g), and (k) L4 for trimer in (j), all compared with the LDOS profile L1 of the unreacted unit cell in (a). 58

Figure 4.5 (a, b) Top views and (c, d) perspective views of equilibrium structures of cysteine dimer on (a, c) CA-CA and (b, d) CA-AA sites on a $\text{Si}_{200}\text{H}_{49}$ slab (used as a model $\text{Si}(111)7 \times 7$ surface), as obtained from the DFT calculations, superimposed onto corresponding magnified empty-state STM images in (a, b). Si adatoms are highlighted by larger yellow circles for clarity. 60

Figure 4.6 STM empty-state images collected at a sample bias +2 V and a tunneling current of 200 pA for cysteine exposures of (a) 5 s, (b) 10 s, (c) 20 s, and (d) 60 s on $\text{Si}(111)7 \times 7$ surface; and (e) lower panel: the corresponding total coverage (Cov.) and the relative surface concentrations for monomer (M), dimer (D) and trimer (T) configurations, middle and upper panels: various type of respective M and D configurations on $\text{Si}(111)7 \times 7$ sites. 62

Figure 5.1 Evolution of (a) O 1s, (b) N 1s, (c) C 1s, and (d) S 2s XPS spectra of L-methionine deposited on $\text{Si}(111)7 \times 7$ as a function of exposure time and of the as-deposited 2400-s film upon annealing to 85°C, 175°C and 285°C. XPS data are fitted with individual components (solid line) corrected with a Shirley background (dotted line). 73

Figure 5.2 Three-stage growth model of L-methionine on $\text{Si}(111)7 \times 7$ surface: Perspective views (left column) and magnified side views (right column) of (a) an interfacial layer, (b) transitional layer, and (c) zwitterionic layer. All of equilibrium configurations are obtained by DFT-D2 calculations using a supercell of three 7×7 unit cells, each of which is represented by a $\text{Si}_{200}\text{H}_{49}$ slab, to model the 7×7 surface. Magnified side-views show (a) a methionine molecule adsorbed on a Si center adatom, (b) an interlayer

N···H–O H-bond between molecules in the interfacial and transitional layers, and (c) an additional interlayer O···H–N and O···H–O H-bonds between the transitional layer and zwitterionic layer, and intralayer zwitterionic hydrogen bonding (O···H–N H-bond). For clarity, only the topmost layers of Si adatoms and the first bilayers of the three unit cells are shown. Si adatoms and restatoms are highlighted by larger yellow and green circles, respectively. The molecules in the transitional layer are slightly whitened for easier identification..... 79

Figure 5.3 Di-molecular structures resulting from formation of various types of H-bonds (marked by dashed lines) between different functional groups of isolated biomolecules. These models are generated by DFT-D2 calculations. The calculated bond length (Å) is depicted along with the corresponding bond energy (kJ/mol) shown in square parentheses. The molecule in the gray oval is shown with the >C–COOH group in plane in order to provide a reference orientation for the H-bond. The last row shows additional –SH donor or acceptor H-bonds in di-molecular configurations of cysteine..... 82

Figure 5.4 Top and side views of the most stable adsorption configurations for two proteinogenic biomolecules connected by (a1-a4) flat configurations with intralayer H-bond in the interfacial layer, (b1-b4) lateral configurations with interlayer H-bond, and (c1-c5) near-vertical configurations with interlayer H-bond in the transitional layer on a Si₂₀₀H₄₉ model 7×7 surface, as obtained by DFT-D2 calculations. The lengths (in Å) of the respective H-bonds are indicated, along with the corresponding bond energies (in eV) shown in parentheses. The biomolecules are (a1/b1/c1) glycine, (a2/b2/c2) alanine, (a3/b3/c3) cysteine, (a4/b4/c4) methionine, and (c5) glycyglycine. For clarity, the Si adatoms [corner adatom (AA) and center adatom (CA)] and restatoms (RA) are highlighted by larger yellow and green circles, respectively. The Si unit cell used in the calculation is partially truncated in order to provide a higher magnification of the adsorption region. We use a prime symbol to denote a substrate atom in the adjacent half unit cell. Each panel heading denotes the orientation of the >C–COOH backbone in the admolecules with respect to Si surface (as flat, tilt, or twist) at specific Si adatom sites, with the double bar (||) and semicolon (;) indicating the second molecule H-bonded, respectively, across the dimer wall or within the same half unit cell. 87

Figure 5.5 (a) Filled-state and (b) empty-state STM images (35×35 nm²) for 0.01 ML coverage of L-methionine on Si(111)7×7 obtained with a sample bias of –1.7 and +1.7 V, respectively, and a tunneling current of 0.2 nA; and magnified views (6×5 nm²) of filled-state images for (c) monomer “delta” dark depression features, (d) dimer “oval” dark depression feature, and (e) trimer “Y” dark depression feature, along with their corresponding empty-state images shown in (f), (g) and (h), respectively. The locations of the dissociated H atoms are marked by crosses in (c) and (d). In (a) and (b), the unit cells containing

methionine monomers and dimers are marked by light cyan and green diamonds, respectively, while the faulted and unfaulted half unit cells containing the trimers are marked by light magenta up and down triangles, respectively. 96

Figure 5.6 High-magnification STM filled-state images ($7.8 \times 7.8 \text{ nm}^2$) of (a1) “delta”, (b1) “oval” and (c1) “Y-shaped” dark depression features for L-methionine adspecies on Si(111) 7×7 surface at room temperature. LDOS profiles for the delta feature (a2) along the long-diagonal L11, and short-diagonals of the reacted (a3) unfaulted half unit cell (L12) and (a4) faulted half unit cell (L13), all compared with the corresponding profiles for the unreacted complete unit cell and half unit cell (a2) L01, (a3) L02, and (a4) L03, respectively. LDOS profiles for the oval features (b2) along the long-diagonal L24, and short-diagonals of the reacted (b3) unfaulted half unit cell (L25) and (b4) faulted half unit cell (L26), all compared with the corresponding profiles for the unreacted complete unit cell and half unit cell (b2) L04, (b3) L05, and (b4) L06, respectively. LDOS profiles for the Y features (c2) along the long-diagonal L37, and short-diagonals of the reacted (c3) unfaulted half unit cell (L38) and (c4) faulted half unit cell (L39), all compared with the corresponding profiles for the unreacted complete unit cell and half unit cell (c2) L07, (c3) L08, and (c4) L09, respectively. The silicon corner atom (AA) to restatom (RA) to center adatom (CA) on the faulted (F) half unit cell and the corresponding AA’, RA’ and CA’ on the unfaulted (U) half unit cell are used as reference points for the linescans of the LDOS profiles. The separation between two adjacent center adatom across the dimer wall (i.e. the CA-to-CA’ separation) is 0.68 nm and that between adjacent center adatom and corner adatom (i.e. the CA-to-AA separation) is 2.34 nm. The STM images are obtained with a sample bias of -1.7 V and a tunneling current of 0.2 nA . (a5)-(c5) depict the corresponding schematic diagrams of delta, oval and Y STM features, with the large and small black solid circles indicating the anchored locations of the dehydrogenated methionine and the dissociated hydrogen atom, respectively. 100

Figure 5.7 Overlays of the most stable equilibrium configurations of methionine adspecies on (a) M1 and (b) M2 “delta”, (c) “oval”, and (d) “Y-shaped” dark depression features of the STM filled-state images. The adsorption configurations have been obtained for methionine monomers, dimer and trimer on a supercell consisting of four $\text{Si}_{200}\text{H}_{49}$ slabs (used as a model of the Si(111) 7×7 surface) by DFT-D2 calculations. Only the top most Si layer is shown for clarity. The locations of the dissociated H atoms are marked by crosses. 101

Figure 6.1 Filled-state STM images of (a) 0.004, (b) 0.76, and (c) 3.97 ML coverages of Au on Si(111) 7×7 surface at room temperature, all collected with a sample bias of -2.0 V and a tunneling

| | |
|---|-----|
| current of 0.2 nA. The fields of view for (a), (b), and (c) are $25 \times 25 \text{ nm}^2$, $75 \times 75 \text{ nm}^2$ and $150 \times 150 \text{ nm}^2$, respectively. | 107 |
| Figure 6.2 XPS spectra of the Au 4f region for three Au nanoassemblies obtained with coverages of 0.004, 0.76 and 3.97 ML on Si(111) 7×7 at room temperature, (a) without and (b) with 20 min post-exposure of cysteine..... | 107 |
| Figure 6.3 XPS spectra of (a) O 1s, (b) N 1s, (c) C 1s, and (d) S 2s regions of L-cysteine deposited on Au(0.004 ML)/Si(111) 7×7 as a function of cysteine exposure time. | 109 |
| Figure 6.4 XPS spectra of (a) O 1s, (b) N 1s, (c) C 1s, and (d) S 2s regions of L-cysteine deposited on Au(0.76 ML)/Si(111) 7×7 as a function of cysteine exposure time. | 112 |
| Figure 6.5. Filled-state STM images ($75 \times 75 \text{ nm}^2$), obtained with a sample bias of -2.0 V , for (a) 5 s, (b) 20 s, and (c) 65 s exposure of cysteine on Au honeycomb nanonetwork supported on Si(111) 7×7 surface. Inset in (b) shows a magnified view ($\times 8$) of a cysteine adspecies on the nanopore/corner hole. | 113 |
| Figure 6.6 XPS spectra of (a) O 1s, (b) N 1s, (c) C 1s, and (d) S 2s regions of L-cysteine deposited on Au(3.97 ML)/Si(111) 7×7 as a function of cysteine exposure time. | 115 |

List of Appendix Figures

| | |
|--|-----|
| Figure A1 The magnified STM filled-state images of 0.004 ML of Au on Si(111)7×7 at room temperature, collected with a sample bias of −2.0 V and a tunneling current of 0.2 nA. The field of view is 30×30 nm ² . The faulted and unfaulted half unit cells are marked by F and U, respectively. The sextet (circle), triad (square), and scribble (upright triangle) features are located on the faulted, unfaulted, and faulted half unit cells, respectively. | 125 |
| Figure A2 STM (a) filled-state and (b) corresponding empty-state images of 0.20 ML of Au coverage on Si(111)7×7 at room temperature, collected with a sample bias of −2.0 V and +2.0 V, respectively, and a tunneling current of 0.2 nA. The field of view is 50×50 nm ² | 125 |
| Figure A3 Top views (upper) and perspective side views (lower) of equilibrium structures obtained by large-scale DFT calculations for (a) a pristine Si(111)7×7 surface, and (b) a Au ₉ Si ₃ cluster as a possible nucleation center, (c) a Au ₂₅ Si ₆ cluster, with the center adatom sites exposed, for coverage below one monolayer, and (d) a Au ₃₀ Si ₉ cluster for coverage between one and two monolayers, all for one half unit cell as one of the six segments of the honeycomb nano-network. The adatom and restatom sites are marked by black and blue circles while the Au atoms are marked in red. | 126 |
| Figure B1 XPS spectra of (a) O 1s, (b) N 1s, and (c) C 1s regions for a multilayer film (with 5400 s exposure) on Si(111)7×7 and for cysteine powder. XPS data points are fitted with individual components (solid line) and a Shirley background (dotted line). | 128 |
| Figure B2 S 2p XPS spectra of cysteine deposited on Si(111)7×7 for 5 s, 270 s and 5400 s, and of cysteine powder, and the as-grown cysteine multilayer film (obtained with 5400 s) upon annealing at 85, 175, and 285 °C for 10 min. XPS data points are fitted with individual components (solid lines) on a Shirley background (dotted line). It should be noted that the S 2p spectrum partially overlaps with one of the plasmon peaks of Si (~ 168.0 eV). ²¹² The S 2p _{3/2} peak is located at 164.1 eV binding energy for a thick cysteine film. ¹²⁰ | 131 |
| Figure B3 XPS spectra of the Si 2p region for cysteine deposited on Si(111)7×7 as a function of exposure time (5 s to 5400 s); and of the as-deposited 5400 s cysteine film upon annealing to 85°C, 175°C and 285°C. XPS data points are fitted with individual Si 2p _{3/2} and Si 2p _{1/2} components (solid lines) on a Shirley background (dotted line). | 132 |
| Figure B4 XPS spectra of the (a) O 1s, (b) N 1s, (c) C 1s, and (d) S 2s regions of a cysteine zwitterionic multilayer film (obtained with 5400 s exposure) on Si(111)7×7, and as a function of storage time in ultrahigh vacuum condition. XPS data points are fitted with individual components (solid lines) on a Shirley background (dotted line). | 133 |

Figure B5 (a) and (b) Top view and side view of the equilibrium dimer-atom-stacking fault (DAS) model of a $\text{Si}_{200}\text{H}_{49}$ cluster (included top adatoms layer, two Si bilayers, and terminated by H atoms) obtained by large-scale DFT-D2 calculations used as the model surface for $\text{Si}(111)7\times 7$. With increasing the distance from the surface, the sizes of the spheres used to represent the Si atoms were decreased. Si corner adatoms (AA), center adatoms (CA), and restatoms (RA) are highlighted by larger yellow, green, and blue circles for clarity, respectively. The dangling bonds represent on the top of adatoms, rest atoms, and corner hole. (c) Stick-and-ball models of an isolated cysteine molecule in neutral form. 136

Figure B6 Top and perspective views of the most stable equilibrium adsorption geometries of an unidentate cysteine molecule bonded through (a) S, (b) O, and (c) N atoms to the model $\text{Si}(111)7\times 7$ surface, a $\text{Si}_{200}\text{H}_{49}$ cluster, obtained by large-scale DFT-D2 calculations. Si corner adatoms (AA), center adatoms (CA), and restatoms (RA) are highlighted by larger yellow, green, and blue circles, respectively. For clarity, only part of the unit cell with the relevant adatoms for bonding with cysteine is shown. 137

Figure B7 Top and perspective views of the most stable equilibrium adsorption geometries of a bidentate cysteine molecule bonded through the N and S atoms to the model $\text{Si}(111)7\times 7$ surface at an adatom-adatom pair across the dimer wall: (a) AA-AA', and (b) CA-CA'. Si corner adatoms (AA), center adatoms (CA), and restatoms (RA) are highlighted by larger yellow, green, and blue circles, respectively. For clarity, only part of the unit cell with the relevant adatoms for bonding with cysteine is shown. 138

Figure C1 XPS spectra of (a) O 1s, (b) N 1s, and (c) C 1s regions for a methionine multilayer film (obtained with a 2400-s exposure) on $\text{Si}(111)7\times 7$ and for L-methionine powder. XPS data points are fitted with individual components (solid line) and a Shirley background (dotted line)..... 139

Figure C2 (a) Top and (b) side views of the equilibrium dimer-atom-stacking fault (DAS) model of a $\text{Si}_{200}\text{H}_{49}$ cluster (consisting of a top Si adatom layer, two Si bilayers, and a bottom layer of terminating H atoms) obtained by large-scale DFT-D2 calculations used as the model surface for $\text{Si}(111)7\times 7$. Spheres with decreasing sizes are used to represent the Si atoms with increasing distance from the surface. Dangling bonds are identified on the top of the adatoms, restatoms, and corner holes. Silicon adatoms and restatoms are highlighted, respectively, by larger yellow and green circles for clarity. 140

Figure C3 Peak areas of various O 1s and N 1s features (a) for different methionine exposure times and (b) for a multilayer methionine film (obtained with a 2400-s exposure) with increasing annealing temperature. 142

Figure C4 (a1-a3) Top and side views of the three most stable equilibrium adsorption geometries of an unidentate methionine molecule bonded through the N atom in accordance with our XPS results, with various orientations of the thiol ether group over the dimer wall on the model $\text{Si}(111)7\times 7$ surface, as

represented by a $\text{Si}_{200}\text{H}_{49}$ cluster, obtained by large-scale DFT-D2 calculations. (b1-b5) Top and side views of the most stable equilibrium adsorption geometries of an unidentate methionine molecule bonded through N atom within a half unit cell with various thiol ether orientations at different Si CA and AA sites. For clarity, only part of the unit cell is shown, along with the Si adatoms and restatoms highlighted by yellow and green circles, respectively. The adsorption energies of the respective geometries are given in square parentheses while the S-to-Si separations are indicated in round parentheses. A straight (–) and a curly horizontal bars (~) are used to indicate covalent bonding between N and a Si surface atom and long-ranged interaction between S and a Si surface atom, respectively. The structures supported by STM results (only for early growth stage) are marked by asterisk. 147

Figure C5 Top and side views of equilibrium di-molecular configurations of methionine molecules for various (a1-a2) “flat” and (b1-b12) “lateral” and “near-vertical” H-bonding on the $\text{Si}_{200}\text{H}_{49}$ model 7×7 surface, obtained by DFT-D2 calculations. The lengths of the respective H-bonds are indicated, along with the corresponding adsorption energies shown in square parentheses. Si adatoms and restatoms are highlighted, respectively, by larger yellow and green circles for clarity. Each heading panel describes the orientation of the $>\text{C}-\text{COOH}$ backbone in the admolecules with respect to Si surface (flat, tilt, or twist) at specific Si adatom sites, with the double bar (||) and semicolon (;) indicating the second admolecule H-bonded across the dimer wall or within the same half unit cell. The structures not supported by XPS results are greyed out, while plausible configuration (for early growth stage) supported by STM results is marked by an asterisk..... 148

Figure C6 Top and side views of equilibrium di-molecular configurations of cysteine molecules for various (a1-a6) “flat” and (b1-b14) “lateral” and “near-vertical” H-bonding on the $\text{Si}_{200}\text{H}_{49}$ model 7×7 surface, obtained by DFT-D2 calculations. The lengths of the respective H-bonds are indicated, along with the corresponding adsorption energies shown in square parentheses. Si adatoms and restatoms are highlighted, respectively, by larger yellow and green circles for clarity. Each heading panel describes the orientation of the $>\text{C}-\text{COOH}$ backbone in the admolecules with respect to Si surface (flat, tilt, or twist) at specific Si adatom sites, with the double bar (||) and semicolon (;) indicating the second admolecule H-bonded across the dimer wall or within the same half unit cell. The structures not supported by XPS results are greyed out, while plausible configurations (for early growth stage) supported by STM results are marked by asterisks..... 150

Figure C7 Top and side views of equilibrium di-molecular configurations of glycine molecules for various (a1-a4) “flat” and (b1-b11) “lateral” and “near-vertical” H-bonding on the $\text{Si}_{200}\text{H}_{49}$ model 7×7 surface, obtained by DFT-D2 calculations. The lengths of the respective H-bonds are indicated, along

with the corresponding adsorption energies shown in square parentheses. Si adatoms and restatoms are highlighted, respectively, by larger yellow and green circles for clarity. Each heading panel describes the orientation of the >C–COOH backbone in the admolecules with respect to Si surface (flat, tilt, or twist) at specific Si adatom sites, with the double bar (||) and semicolon (;) indicating the second admolecule H-bonded across the dimer wall or within the same half unit cell. The structures not supported by XPS results are greyed out, while plausible configurations (for the early growth stage) supported by STM results are marked by asterisks..... 152

Figure C8 Top and side views of equilibrium di-molecular configurations of alanine molecules for various (a1-a4) “flat” and (b1-b20) “lateral” and “near-vertical” H-bonding on the Si₂₀₀H₄₉ model 7×7 surface, obtained by DFT-D2 calculations. The lengths of the respective H-bonds are indicated, along with the corresponding adsorption energies shown in square parentheses. Si adatoms and restatoms are highlighted, respectively, by larger yellow and green circles for clarity. Each heading panel describes the orientation of the >C–COOH backbone in the admolecules with respect to Si surface (flat, tilt, or twist) at specific Si adatom sites, with the double bar (||) and semicolon (;) indicating the second admolecule H-bonded across the dimer wall or within the same half unit cell. The structures not supported by XPS results are greyed out, while plausible configurations (for early growth stage) supported by STM results are marked by asterisks. 155

Figure C9 Top and side views of equilibrium di-molecular configurations of glycylglycine molecules for various (b1-b10) “lateral” and “near-vertical” H-bonding on the Si₂₀₀H₄₉ model 7×7 surface, obtained by DFT-D2 calculations. The lengths of the respective H-bonds are indicated, along with the corresponding adsorption energies shown in square parentheses. Si adatoms and restatoms are highlighted, respectively, by larger yellow and green circles for clarity. Each heading panel describes the orientation of the >C–COOH backbone in the admolecules with respect to Si surface (tilt, or twist) at specific Si adatom sites, with the double bar (||) and semicolon (;) indicating the second admolecule H-bonded across the dimer wall or within the same half unit cell..... 156

Figure C10 Top and side views of equilibrium di-molecular configurations of methionine adspecies involving (a) two and (b) one H-bond on the 7×7 Si₂₀₀H₄₉ model surface, obtained by DFT-D2 calculations. The lengths of the respective H-bonds are shown, along with the corresponding adsorption energies shown in square parentheses. Si adatoms and restatoms are highlighted, respectively, by larger yellow and green circles for clarity. Each heading panel describes the orientation of the >C–COOH backbone in a methionine adspecies with respect to the Si surface (flat, tilt, twist) at specific Si adatom

| | |
|---|-----|
| sites, with the double bar () indicating the second adspecies H-bonded across the dimer wall. The configuration that is supported by XPS and STM measurements is marked with an asterisk..... | 157 |
| Figure C11 Top and side view of equilibrium configuration of a methionine trimer via formation of triple O··H–O hydrogen bonds in a ring configuration at the center of faulted half unit cell on a supercell including four Si ₂₀₀ H ₄₉ slabs, i.e., a Si ₈₀₀ H ₁₉₆ slab, as a model for a Si(111)7×7 surface obtained by DFT-D2 calculations..... | 158 |

List of Tables

| | |
|--|-----|
| Table 5.1 Binding energies (in eV) of fitted peak maxima for various XPS core-level features and their assignments for three growth stages on Si(111)7×7 surface for glycine (G), D-alanine (A), L-cysteine (C), L-methionine (M), and glycyglycine (GG). The values apply to all five benchmark proteinogenic biomolecules unless otherwise the application to specific biomolecules is indicated by superscripts. | 77 |
| Table 6.1 Binding energies (in eV) of fitted peak maxima for various XPS core-level features and their assignments for different exposures of L-cysteine on Au(0.004 ML)/Si(111)7×7..... | 110 |
| Table 6.2 Binding energies (in eV) of fitted peak maxima for various XPS core-level features and their assignments for different exposures of L-cysteine on Au(0.76 ML)/Si(111)7×7..... | 112 |
| Table 6.3 Binding energies (in eV) of fitted peak maxima for various XPS core-level features and their assignments for different exposures of L-cysteine on Au(3.97 ML)/Si(111)7×7..... | 115 |

List of Appendix Tables

| | |
|---|-----|
| Table B1 Binding energies (in eV) of fitted peak maxima for various XPS core-level features and their assignments for different exposures of L-cysteine on Si(111)7×7 and for powder cysteine..... | 129 |
| Table B2 Binding energies (in eV) of fitted peak maxima for various XPS core-level features and their assignments for a multilayer film of L-cysteine on Si(111)7×7 after storage at room temperature under ultrahigh vacuum condition and upon annealing to 85, 175, and 285 °C for 10 min. | 130 |
| Table C1 Binding energies (in eV) of fitted peak maxima for various core-level features and their assignments for different exposures of L-methionine on Si(111)7×7 and for L-methionine powder. | 141 |
| Table C2 Classification of plausible di-molecular adsorption structures into three main primary groups for five proteinogenic biomolecules adsorbed on Si(111)7×7. The calculated structures are identified by their corresponding figure numbers shown in Figure C5 to C19. The structures not supported by our XPS results are greyed out. The structures observed by our STM results for the initial growth stage are underlined. | 146 |

List of Schemes

| | |
|--|----|
| Scheme 1.1 Schematic diagram depicting ejection of the 1s electron as the result of absorption of an incident X-ray photon. | 12 |
| Scheme 4.1 Ball-and-stick models of (a) neutral, and (b) zwitterionic structures of cysteine, and (c-g) dimer structures resulting from formation of various H-bonds (marked by the dashed lines) between different types of functional groups of two cysteine molecules in the gas phase. These models are generated by DFT calculations. | 48 |
| Scheme 5.1 Ball-and-stick models of neutral and zwitterionic equilibrium structures of isolated aliphatic proteinogenic biomolecules: Glycine, D-alanine, L-cysteine, L-methionine, and glycylglycine. These structures are generated by DFT-D2 calculations and the molecular lengths (i.e. the separation between the hydroxyl O atom and the farthest non-H atom along the carbon chain backbone) are shown in angstrom (Å). No change in the molecular length of the zwitterionic structure from that of the neutral structure is found for all biomolecules, except for methionine with a 3% increase. | 70 |

Chapter 1

Introduction

1.1 Surface Science

The field of “surface science” provides understanding of surface and interfacial processes and their connection to bulk processes in the traditional research disciplines of chemistry, physics, and materials science at the atomic and molecular level. The concept of surface science goes back historically to the 18th century, when the properties of oil monolayers on water surfaces were first studied by Benjamin Franklin in 1774.¹ The explosive development of the field of surface science has been driven by a series of key events. It is quite obvious that the invention and development of a wide range of surface-sensitive analytical techniques during past two centuries have played a significant role to advance the goals of surface science and to provide important fundamental information about surfaces and interfaces. First, the development of ultrahigh vacuum (UHV) techniques that attain pressure from 10^{-7} to 10^{-11} Torr in the late 1950s has enabled preparation and maintenance of clean single-crystal surfaces to keep them uncontaminated for a sufficiently long period of time for experimentation. With the reduction of pressure, individual gaseous molecules collide only with the chamber wall due to its large inelastic mean free path that is thousands of times that of the dimension of the UHV chamber. Moreover, photons, electrons, and ions can also travel in UHV chamber without any direct contact or interaction with residual gas molecules, which is a critical requirement for many surface analytical methods. The second major event in surface science occurred in the 1980s with the invention of scanning probe techniques² that propel scanning tunneling microscopy (STM) and atomic force microscopy (AFM) as the only techniques capable of studying surfaces and interfaces with atomic resolution for the first time. Achieving atomic-level information by using these techniques has revolutionized surface science and amplified its impact to almost all areas of chemistry, physics, biology, and materials science, and to the emerging areas in nanotechnology and nanoscience.

Indeed, we can recognize the power of “surfaces” not only in our field of study but also in our daily life. One of the most powerful motivations for surface science is the goal of understanding catalytic reactions, which dated back to 1823 when Dobereiner studied combustion of hydrogen and oxygen on a platinum surface, acting as a catalyst, at room temperature.³ Nowadays, the scanning probe family of techniques can be used to provide atomically resolved information and direct insights into the active sites of catalysts, which ultimately improves the catalytic processes.⁴ Another main area of application of

surface science and vacuum technology is the semiconductor and microelectronic industry that is responsible for the research and development, fabrication and manufacturing of semiconductor devices and appliances that greatly improve the quality of life.^{5,6} In recent years, new opportunities in surface science have led to the development of biosurfaces and biointerfaces, which rely on functionalization of single-crystal metal or semiconductor surfaces with biochemical materials. Fundamental studies of chemical attachment of organic/bio molecules on different surfaces are very important to modifying the chemical and physical properties of solid surfaces. Typically, the interactions between organic adsorbates and surfaces can generally be categorized into two types: (a) weak, noncovalent interactions that result in molecular self-assembly on single-crystal metal surfaces, and (b) strong, chemical binding commonly found between adsorbed organic components and semiconductor surfaces.^{7,8} To design new semiconductor devices, silicon-based bio/nano sensors, nanopatterning templates, and molecular electronic devices, strong and selective chemical binding of organic/bio materials on semiconductor surfaces is practically required.

1.1.1 Surface Chemistry of Silicon

Of all the semiconductors, silicon is the most prominent material not only in both microelectronics and nanoelectronics applications, but also as the support/substrate for nanolithography and other applications.⁹ Among the advantages of silicon are high-temperature stability, high chemical resistance to acids and organic solvents, and well-established bonding process. In the diamond structure of crystalline silicon, one $2s$ orbital and three $2p$ orbitals are hybridized to form four sp^3 orbitals, which bond to four nearest neighboring atoms with a separation of 2.35 \AA in a tetrahedral configuration and with a bond strength of 226 kJ/mol . Depending on how the bulk is truncated, each silicon atom at a specific surface plane could have spare electrons in non-bonding sp^3 orbitals referred to as “dangling bonds”. In order to reduce the number of dangling bonds and the surface energy, the atoms at the surface reconstruct into a wide variety of non-ideal geometries and rearrange the surface bonding. Silicon surfaces that have attracted the most interest are Si(100) and Si(111). Truncation of the bulk Si structure at the (100) plane cuts through two Si-Si bonds for each surface silicon atom and leaves the surface atoms with two dangling bonds, each with one electron. To achieve a lower surface energy, Si(100) will undergo surface reconstruction with pairing of two adjacent surface silicon atoms together to form silicon dimers. This gives rise to the Si(100) 2×1 reconstruction with parallel rows of silicon dimers, which was first probed by using low-energy electron diffraction (LEED) over five decades ago.¹⁰ Each surface dimer contains a strong σ -bond and a weak π -bond, and it exhibits similar chemical reactivity as alkenes, allowing the

attachment of organic molecules in [2+2] and [4+2] cycloaddition reactions. Furthermore, the reconstructed Si(100)2×1 surface has thermodynamically tilted silicon dimers in an asymmetric manner, which was observed at low temperature (120 K) by STM, in contrast to the symmetric dimers observed at room temperature.¹¹ As a result of an electrophilic down-Si-atom and a nucleophilic up-Si-atom for a surface silicon dimer, there is an electronic charge transfer from the down-atom to the up-atom, which causes the addition of zwitterionic character to the Si(100)2×1 surface.¹² The surface interactions between organic/bio materials and Si(100)2×1 can be categorized into three different types of reactions: (a) dissociative addition reactions found for acetonitrile,¹³ aniline,¹⁴ benzenethiol and diphenyl disulfide,¹⁵ ethanol¹⁶ and formic acid,¹⁷ (b) dative bonding for trimethylamine¹⁸ and N-methylpyrrolidine,¹⁹ and (c) cycloaddition reaction for cyclopentene, ethylene, acetylene, 3-pyrroline and pyrrolidine,²⁰ benzaldehyde,²¹ trans-2-butene, and cis-2-butene.²²

On the other hand, each silicon atom of the Si(111) surface is cleavage face of silicon for which the covalent bonds along [111] direction are cut. Simple counting of the number of broken bonds suggests one dangling bond for each silicon surface atom, which is energetically favored to be oriented perpendicular to the surface. The 2×1 reconstruction of Si(111) has been observed at low temperature after cleavage in UHV condition by STM²³ and LEED,²⁴ which was described by Pandey in a π -bonded chain model.²⁵ Perhaps an even more famous reconstruction of the Si(111) surface is the 7×7 reconstruction, which has been prepared at high temperature after cleavage in UHV condition. The Si(111)7×7 has been regarded as one of the most important, well-ordered “perfect” templates in surface science for many decades.

1.1.2 Si(111)7×7 Surface

Since the discovery and investigation of the Si(111)7×7 surface by Schlier and Fransworth at the end of the 1950s using LEED method,¹⁰ the 7×7 surface has been widely studied by a variety of experimental techniques and modelled by many theoretical calculations. Just one year after the invention of STM, the Si(111)7×7 surface was imaged in real space with atomic resolution in 1983.²⁶ Furthermore, atomically-resolved AFM has also been used to study this surface.²⁷ These studies confirmed for the first time the generally accepted dimer-adatom-stacking (DAS) fault model, first proposed by Takayanagi after evaluating intensity distribution of the spots in transmission electron diffraction patterns along with LEED results obtained in UHV condition.^{28,29}

Figure 1.1a and Figure 1.1b show high-resolution filled-state and corresponding empty-state STM images of pristine Si(111)7×7 surface obtained at a sample bias of -2 V (so-called filled-state STM

image) and +2 V (so-called empty-state STM image), respectively, and with a tunneling current of 200 pA. These images are acquired with the sample held at room temperature using the variable-temperature STM system in the Waterloo Advanced Technology Laboratory (WATLab). The difference between two faulted and unfaulted half unit cells can be easily distinguished by imaging with a negative sample bias voltage. The protrusions in the faulted half unit cell in the filled-state image obtained with a negative bias voltage are brighter than those in the unfaulted half unit cell due to the presence of the stacking fault (Figure 1.1a), while the protrusions in both faulted and unfaulted half unit cells in the empty-state image obtained with a positive bias voltage have the same brightness (Figure 1.1b). The existence of 12 bright protrusions are very obvious in both filled-state (Figure 1.1a) and empty-state (Figure 1.1b) STM images of the Si(111)7×7 surface. Each protrusion corresponds to one of 12 silicon adatoms of the unit cell. At a sample bias of −2.0 V, the silicon restatoms are not observed in these images. At a less negative sample bias of −1.5 V, the corresponding filled-state STM image so obtained reveal discernible contrast between adatoms and restatoms, particularly with the lower intensities corresponding to restatoms located at the centers of three adjacent adatoms (Figure 1.1c). This also suggests that the emergence of restatom features (and indeed any local density of state feature) is highly dependent on appropriately chosen sample bias voltage.³⁰

Top and side views of the DAS model of the layer-by-layer unit cell structure (consisting of a top adatom layer, a restatom layer, a dimer bilayer, a base Si layer, and a layer of H atoms used for terminating the base Si layer) for the Si(111)7×7 reconstruction are shown schematically in Figure 1.1d and Figure 1.1e, respectively. The model is obtained by large-scale ab-initio quantum mechanical calculations based on the Density Functional Theory (DFT) using the VASP/MedeA platform in the Xeon computer cluster at WATLab. The DAS model consists of two triangular half unit cells, one with and another without a stacking fault referred to as “faulted half unit cell” and “unfaulted half unit cell”, respectively. The 7×7 unreconstructed unit cell of the Si(111) surface contains 49 atoms. To reduce the surface energy, the 49 dangling bonds are decreased to 19 dangling bonds, which are located on the 12 silicon adatoms, with three corner (*angulus* in Latin) adatoms (AAs) and three center (*centrum* in Latin) adatoms (CAs) on each of the faulted and unfaulted half unit cells, 6 silicon restatoms (RAs) placed between adatoms in the layer just below the adatom layer, and 1 silicon atom in the corner hole located three layers below the adatom layer that is shared among four adjacent unit cells. The dangling bonds on the silicon surface provide the interesting source of surface chemical activity with not only metal atoms, nanoclusters and nanocrystallites, but indeed organic and biochemical materials.

As a result of the 7×7 surface reconstruction, the silicon atoms are categorized into corner adatoms, center adatoms, and restatoms, each with its own characteristic local electron density of states. In particular, each adatom has a formal charge of $+7/12$, while both the restatom and the corner hole each has a formal charge of -1 .^{31,32} As each AA is surrounded by only one adjacent RA while each CA has two neighboring RAs, the amount of charge transferred from AA to RA is almost half that from CA to RA. The resulting electron density of AA is therefore higher than that of CA, which is consistent with the brighter protrusion at AA than that at CA in the STM image (Figure 1.1a). Because of the existence of both electrophilic sites (i.e., AA and CA) and nucleophilic sites (i.e., RA), Si(111) 7×7 is a fascinating surface with dangling bonds located at a variety of sites with different reactivities and selectivities to interact with incoming multifunctional organic/bio molecules. Furthermore, based on the DAS model of Si(111) 7×7 obtained with DFT calculations, a dangling bond pair between adjacent Si sites can be categorized into the following two groups, with their respective separations between two Si atoms indicated in parentheses:

(A) Two Si sites within a half unit cell: CA-AA (7.72 Å), CA-CA (7.66 Å), CA-RA (4.55 Å), AA-RA (4.46 Å), and AA-corner hole (8.25 Å); and

(B) Two Si sites across the dimer wall of adjacent half unit cells: CA-CA' (6.77 Å), AA-AA' (6.71 Å), and CA-AA' (10.25 Å).

We use a prime symbol to denote a substrate atom in the adjacent half unit cell. These site-to-site separations provide a set of natural metrics for multi-point attachment of a multifunctional admolecule and/or combinatorial interactions with several different admolecules for nanotemplating and nanopatterning applications.

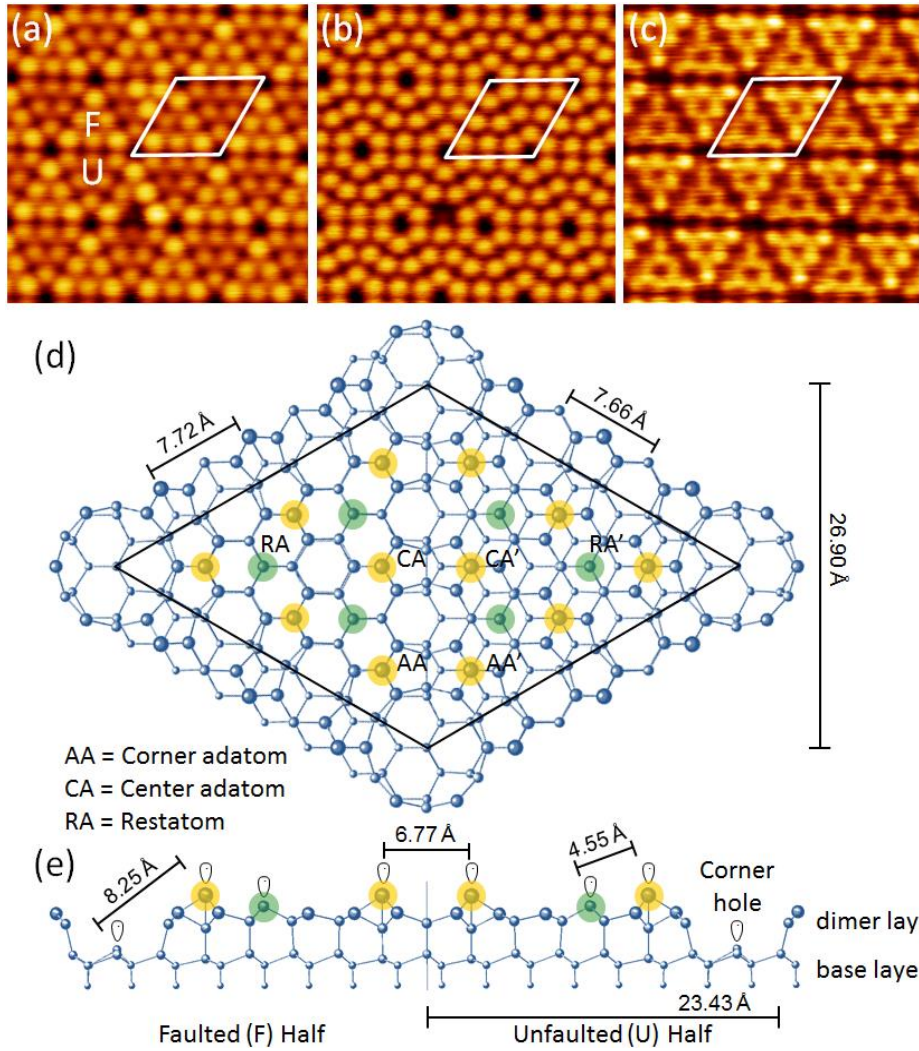


Figure 1.1 (a) Filled-state and (b) corresponding empty-state STM images ($10 \times 10 \text{ nm}^2$) of a clean Si(111) 7×7 surface obtained at a sample bias of -2 and $+2$ V, respectively, and a tunneling current of 200 pA. The faulted and unfaulted half unit cells are marked by F and U, respectively, in (a). (c) Filled-state STM image ($10 \times 10 \text{ nm}^2$) obtained at a less negative sample bias of -1.5 V shows discernible contrast between restatoms and adatoms. (d) Top view and (e) side view of the equilibrium dimer-adatom-stacking fault (DAS) model of a $\text{Si}_{200}\text{H}_{49}$ cluster (consisting of a top adatom layer, a restatom layer, a dimer bilayer, a base Si layer, and a layer of H atoms used for terminating the base Si layer) obtained by large-scale DFT calculations used as the model surface for Si(111) 7×7 . The sizes of the spheres used to represent the Si atoms are smaller with increasing distance from the surface (the top adatom layer). The adatoms, both corner adatoms (AAs) and center adatoms (CAs), and the restatoms (RAs) are highlighted by larger yellow and green circles for clarity, respectively. A prime symbol is used to denote a substrate atom in the adjacent half unit cell. The dangling bonds on the top of adatoms, restatoms, and corner hole are identified in (e). All STM images are collected by using a variable-temperature scanning probe microscope, manufactured by Omicron Nanotechnology, at WATLab and the model surface is generated by large-scale ab-initio quantum mechanical calculations using a Xeon computer cluster at WATLab.

1.2 Adsorption of Metals on Si(111)7×7

The formation of metal-semiconductor hybrid materials and their novel properties are strongly dependent on the chemical interactions between the metal deposit and the semiconductor substrate. Since its discovery, Si(111)7×7 surface has attracted much attention for studying the adsorption of various metal materials because of its directional dangling bonds for anchoring and supporting adsorbates, and its electronic properties for building hybrid properties. To date, a very broad range of metal materials, including univalent group IA metals (Li, Na, K, and Cs),^{33,34,35,36} trivalent group IIIA metals (Al, Ga, In and Tl),^{37,38,39,40} VIIB group metals (Mn),^{41,42} 3d ferromagnetic group VIIIB metals (Co, Fe, and Pt),^{43,44,45,46,47} IB group metals (Cu, Ag, and Au),^{48,49,50,51,52,53,54,55,56,57} bivalent group IIB metal (Zn),⁵⁸ and tetravalent group IVA metals (Ge, Sn, and Pb),^{30,59,60} on Si(111)7×7 surface has been investigated by various surface-sensitive analytical techniques and ab-initio quantum mechanical calculations. These studies indicate that the 7×7 surface provides a powerful versatile platform to develop a wide range of potential technological applications from next-generation nanoelectronics to nanocatalysis.

Among these metals, gold is the best known noble metal because of its very stable, non-reactive metallic properties. Since the first report on a Au/Si interface at room temperature some four decades ago,⁶¹ the Au/Si(111) interface has been investigated by a wide range of surface science techniques,⁶² including more recently Auger electron spectroscopy,⁶³ synchrotron-radiation photoemission spectroscopy,⁶⁴ and high-resolution medium energy ion scattering,⁶⁵ focusing on the growth, atomic and electronic properties of Au/Si interface for both fundamental and technological interests. In spite of these efforts, the growth evolution of nanofilms and layers of critical-thickness for the Stranski-Krastanov growth mode for gold silicide on a clean Si(111) surface at room temperature remains largely unexplored. Many of the intriguing questions, fundamental and otherwise, could be addressed by a complementary three-pronged approach that combines the chemical-state composition and surface bonding information obtained from XPS, and the site-specific local-density-of-state imaging information from STM, with molecular models generated by large-scale ab-initio quantum mechanical calculations.

1.3 Adsorption of Organic/Bio Molecules on Si(111)7×7

Molecular interactions of organic components and biomaterials with semiconductor surfaces have attracted much recent attention because of their potential applications in biosensors, biocompatible materials, and biomolecule-based electronic devices.^{66,67,68,69} Organic functionalization of Si(111)7×7 surface has been reported for organic molecules, with nitrogen-containing functional group (amines and amides) such as dimethylamine,⁷⁰ pyrrole,⁷¹ N-methylpyrrole,⁷² methylhydrazine,⁷³ trimethylamine,¹⁸ and

acetonitrile,⁷⁴ and oxygen-containing functional groups (carboxylic acids and alcohols) connected to an aliphatic backbone or an aromatic ring structure (benzene and their derivatives) such as methacrylic acid,⁷⁵ acetaldehyde,⁷⁶ geranyl acetone,⁷⁷ phenol,⁷⁸ cyclohexene,⁷⁹ and pyridine.⁸⁰ Among the surface-sensitive analytical techniques, STM is a very powerful tool to probe adsorbate-surface interactions, particularly site-specific chemistry, on Si(111)7×7. Based on STM observation of organic molecules with different functional groups chemisorbed on both the nucleophilic and electrophilic sites of the 7×7 surface, the interactions can be categorized into four different types of reactions: (1) [2+2]-like cycloaddition or di- σ binding; (2) [4+2]-like or Diels-Alder cycloaddition; (3) covalent attachment (via dissociative chemisorption); and (4) dative-bonded adduct formation. An early STM study of acetylene⁸¹ and ethylene⁸² adsorption shows a di- σ bonded product (i.e., a [2+2]-like product) bridging the pair of adjacent Si adatom-restatom sites. Furthermore, similar four- σ bonded products with two neighboring adjacent adatom-restatom pairs have been reported for several chain-dienes, such as 1,6-heptadiene, 1,7-octadiene and 1,13-tetradecadiene.⁸³ The [4+2] cycloaddition reaction has been observed for unsaturated hydrocarbon (1,3-butadiene⁸⁴) at adatom-adatom pairs, while aromatic hydrocarbons (benzene^{85,86,87,88} and toluene⁸⁶), aromatic heterocycles (thiophene^{89,90}), and DNA base (thymine⁹¹) are found at adjacent adatom-restatom pairs, both by using high-resolution STM imaging. These STM studies show that the center adatom has more opportunity to react with organic molecules than the corner adatom. Moreover, a wide range of covalent attachment from nitroxyl-free radicals⁹² and aromatic molecules (pyrrole,⁷¹ naphthalene,⁹³ tetracene,⁹⁴ and pentacene⁹⁵) to biomolecules, such as amino acids (glycine,⁹⁶ alanine,⁹⁷ and cysteine⁹⁸) and peptide (glycylglycine⁹⁹), have also been investigated by STM, which show that the adjacent or individual adatom-rest-atom pairs could react to form the σ -bonds. In a recent STM study, donating the lone-pair charge density of the N atom to the Si atom could lead to dative bonding in one of DNA base molecules (adenine¹⁰⁰). In contrast to direct bonding of the aforementioned neutral organic moieties to various Si surface sites, adsorption and patterning of zwitterionic molecular films on the Si(111)7×7 surface has also been investigated by STM imaging.¹⁰¹

Among the most fundamental biomolecules, amino acids and nucleotides are the basic building blocks of the larger biological materials such as proteins, peptides, and DNAs. The amino acids found in proteins are generally classified according to their structures: (a) aliphatic amino acids, including monoamino-monocarboxylic acids, monoamino-dicarboxylic acids and their amides, basic amino acids, and sulfur-containing amino acids; (b) aromatic amino acids; and (c) heterocyclic amino acids.¹⁰² Alpha amino acids are bio-organic molecules containing a carboxylic acid ($-\text{COOH}$) group and an amino ($-\text{NH}_2$) group, which are separated by at least one carbon segment (α -carbon). There are twenty different

standard amino acids ($\text{NH}_2\text{C}_\alpha\text{HRCOOH}$), which differ from one another by a unique functional group in the side chain (*R* group) attached to the α -carbon. Adsorption of aliphatic amino acids (glycine,^{103,104,105} alanine,^{106,107,108,109,110,111} glutamic acid,^{112,113,114,115} and lysine^{116,117,118}), sulfur-containing amino acids (cysteine^{119,120,121} and methionine^{122,123,124,125,126}), aromatic amino acids (tyrosine^{127,128}), and heterocyclic amino acids (proline^{129,130}) on various well-ordered single-crystal metal surfaces in UHV condition have attracted much attention in surface science and nanotechnology in the two past decades. This information is important not only to understanding fundamental interactions of larger biochemical molecules (such as proteins and peptides), but also to fabricating bio/nano-devices for biomedical sensing and molecular electronics. The development of future hybrid organic-inorganic interfaces also critically depends on understanding the nature of the substrate surface and particularly the type of available bonding interactions that are responsible for producing stable chemical states of amino acids, and ultimately for controlling the orientation, conformation, and two-dimensional organization of the bio-organic adspecies on the inorganic surface.

Our recent studies in WATLab have focused on the surface chemistry of organic components and biochemical materials, including DNA-bases (thymine⁹¹ and adenine¹⁰⁰), peptides (glycylglycine^{99,131}), and the simplest amino acids (glycine^{96,131,132,133} and alanine). Furthermore, our group has studied the surface chemistry of a series of aliphatic organic molecules, including di and perchloroethylene,¹³⁴ dibromoethylene,¹³⁵ acrylic acid and propanoic acid,¹³⁶ allyl alcohol and allyl aldehyde,¹³⁷ allylamine,¹³⁸ ethanolamine,¹³⁹ acetic acid,¹⁴⁰ 1,2-dihalogenated benzenes,¹⁴¹ toluene and benzene¹⁴² on Si(100)2×1 surface, and 1,1-difluoroethylene,¹⁴³ monochloroethylene, dichloroethylene, perchloroethylene and trichloroethylene,^{144,145,146} acetic acid,¹⁴⁷ and tetrachloride¹⁴⁸ on Si(111)7×7 surface using XPS, STM and ab-initio quantum mechanical simulations. These studies reveal the wide varieties of interactions of aliphatic organic molecules with the silicon surfaces, leading to reactions either via simple hydrogen dissociation, dative bonding, or cycloaddition with the surface Si atoms. All these past investigations by our group set the stage for the present study on more biologically important multifunctional materials, including sulfur-containing amino acids (cysteine and methionine), with a special focus on the reactivity and selectivity of different functional groups in these benchmark proteinogenic biomolecules towards specific sites on the Si(111)7×7 surface.

1.4 Molecular Interactions of Biomolecules with Metal Clusters Supported on Si(111)7×7

Understanding the adsorption features and molecular interactions of bio-organic molecules with metal superstructures (clusters, templates, nanocrystallites) on a semiconductor surface is important to developing potential applications involving hybrid bio-organic-metal interfaces for biosensors and biomolecular electronic devices. To date, studies of biomolecules interaction with supported metallic nanostructures have not received much attention, despite the importance of metallic nanostructures supported on a semiconductor surface. One notable study has focussed on “coadsorption” of the Au and L-cysteine on rutile TiO₂(110) by XPS.¹⁴⁹ When L-cysteine is exposed to gold clusters on TiO₂(110), cysteine was found to interact with both gold deposits and the substrate surface (likely at the defect sites) through the thiol group with the formation of S–Au and S–Ti bonds, respectively.

As one of two sulphur-containing standard amino acids, cysteine is especially interesting because it contains three-functional groups: amino (–NH₂), carboxylic acid (–COOH) and thiol (–SH) groups, which provide a wide variety of bonding possibilities and configurations with the surface. In this context, understanding the adsorption and molecular features of cysteine with gold nanostructures supported on silicon surface is fundamentally interesting. While there is a large volume of work on the adsorption of cysteine on Au surfaces^{119,121,150,151,152,153,154,155,156,157} and one recent complementary study of cysteine on Si(111)7×7,⁹⁸ molecular interactions of cysteine with Au nanostructures and nanotemplates supported on Si(111)7×7 surface remain challenging and unexplored.

1.5 Methodologies of Surface Sensitive Techniques

A number of different surface analytical techniques have been used in surface science to understand the properties and reactivity of a surface and also to provide fundamental information and understanding about the surface structure (physical topography), chemical composition, electronic structure, and kinetic and energetic mechanisms. Of all the technologies that have been developed to study the surface, low-energy electron diffraction (LEED), reflection high energy electron diffraction (RHEED), ion scattering methods, and STM are the most widely used to investigate the surface structure. Auger electron spectroscopy (AES), photoelectron spectroscopy (including XPS and ultraviolet photoelectron spectroscopy or UPS), high-resolution electron energy loss spectroscopy (HREELS), near-edge X-ray absorption fine structure spectroscopy (NEXAFS), and secondary ion mass spectrometry (SIMS) are the common surface-sensitive techniques to acquire elemental and chemical-state composition and chemical

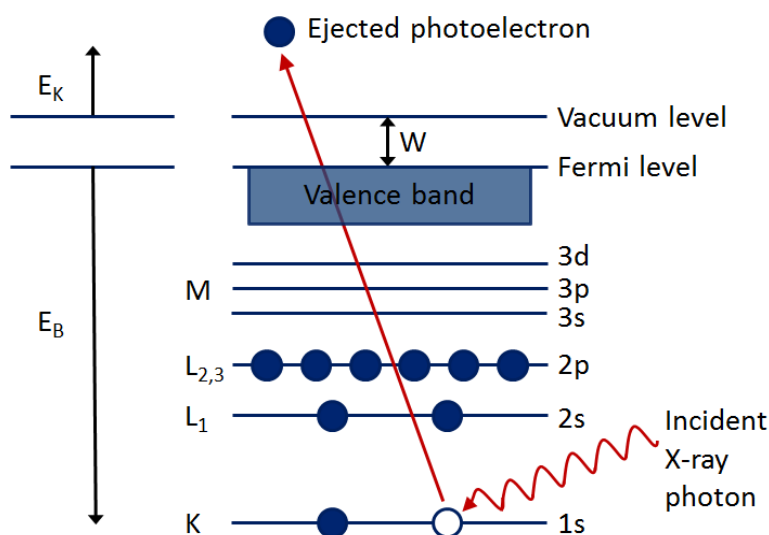
bonding information about the surface and adlayers. Among these surface analytical methods, surface-sensitive XPS and STM techniques are used for the present research.

1.5.1 X-ray Photoelectron Spectroscopy

One of the most widely used surface characterization methods is XPS, also known as electron spectroscopy for chemical analysis (ESCA), which provides quantitative (and qualitative) chemical-state composition, and electronic structural information of the surface. Not only is XPS a very useful surface-sensitive technique to measure elemental composition, empirical formula, oxidation state, and electronic state for inorganic materials, it is also very powerful in the analysis of organic layers. Among the many fundamental discoveries made in the early years of the 20th century was the discovery of the photoelectric effect. XPS technique is based on this important effect, first explained by Einstein in 1905¹⁵⁸ using Planck's quantization of energy, and was later developed further with the discovery of core-shell chemical shifts by Siegbahn and coworkers in 1957.¹⁵⁹ The minor displacement of a core-level photoline in a photoelectron spectrum as a result of changing local chemical environment (or the oxidation state) is known as the chemical shift. In a photoelectric process, an electron is ejected from an occupied energy level of the material, upon absorption of an X-ray photon of energy $h\nu$. The X-ray photon can be generated by high energy electron excitation of a metal target (as K_α line emissions of Mg and Al at 1253.6 eV and 1486.6 eV, respectively) or from a synchrotron radiation source. The kinetic energy (E_K) of the emitted electrons depends on the energy of the exciting photons through the Einstein equation.

$$E_K = h\nu - (E_B + W) \quad (1.1)$$

where E_B is the binding energy of the electronic energy level of the electron before photoejection, measured with respect to the Fermi level, and W is the work function of the electron spectrometer that is required to bring the electron from the Fermi level to the vacuum level outside the surface. Only photons with energy greater than the work function (i.e. $h\nu > W$) can be used to generate photoelectrons. The Fermi level corresponds to the highest energy level occupied by an electron in a neutral (metallic) solid at absolute zero temperature. Scheme 1.1 depicts the photoemission process, in which a photoelectron is ejected from the K shell (i.e. 1s energy state) of an atom (in a molecule), upon absorption of a photon. The binding energy of a core-level photoline, along with its chemical shift, can be used to provide unique signature of individual element in specific chemical environment, while the corresponding spectral intensity provides quantitative composition of specific chemical state, after appropriate consideration of the relative sensitivity factors.



Scheme 1.1 Schematic diagram depicting ejection of the 1s electron as the result of absorption of an incident X-ray photon.

A typical XPS instrument system includes a monochromatized X-ray source, an electron energy analyzer, and an electron detector, and one such commercial instrument is shown in Figure 1.2. Our XPS experiments are conducted under UHV condition to avoid contamination of the sample, and to minimize unwanted collisions of the photoelectrons with residual gaseous particles during transport from the sample through the analyzer to the detector. X-rays are generated by impinging a high-energy electron beam of ~ 10 keV kinetic energy onto an anode target (made of Al or Mg), and the resulting radiative decay via X-ray emission leads to X-ray photons with well-defined photon energies specific to the target material. Although the X-ray photons penetrate the sample to a depth on the order of a micrometer, the XPS spectrum contains information only about the top 10-100 Å of the sample due to the limited inelastic mean free paths of the photoelectrons in solids. Furthermore, an X-ray monochromator, consisting of one or more quartz crystals, provides the best way to produce a monochromatized X-ray beam because the quartz monochromator system diffracts the Bremsstrahlung X-ray radiation and removes the satellite lines of X-rays. The sample area illuminated by the monochromatized X-ray beam is usually less than a few millimeters in diameter. The photoelectrons generated from the sample surface are collected by an electrostatic lens system, and are focussed onto the entrance slit of the electrostatic hemispherical energy analyzer. The hemispherical energy analyzer consists of an inner and an outer concentric hemispheres with respective positive and negative applied potentials to mean pass energy. Electrons with kinetic energy corresponding to the pass energy of the analyser are allowed to pass through the energy analyser

onto the electron detector system. An array of electron multipliers (channeltrons), each of which amplifies a single electron by a factor of 10^8 , is used as the electron detector to register the number of photoionization events.¹⁶⁰

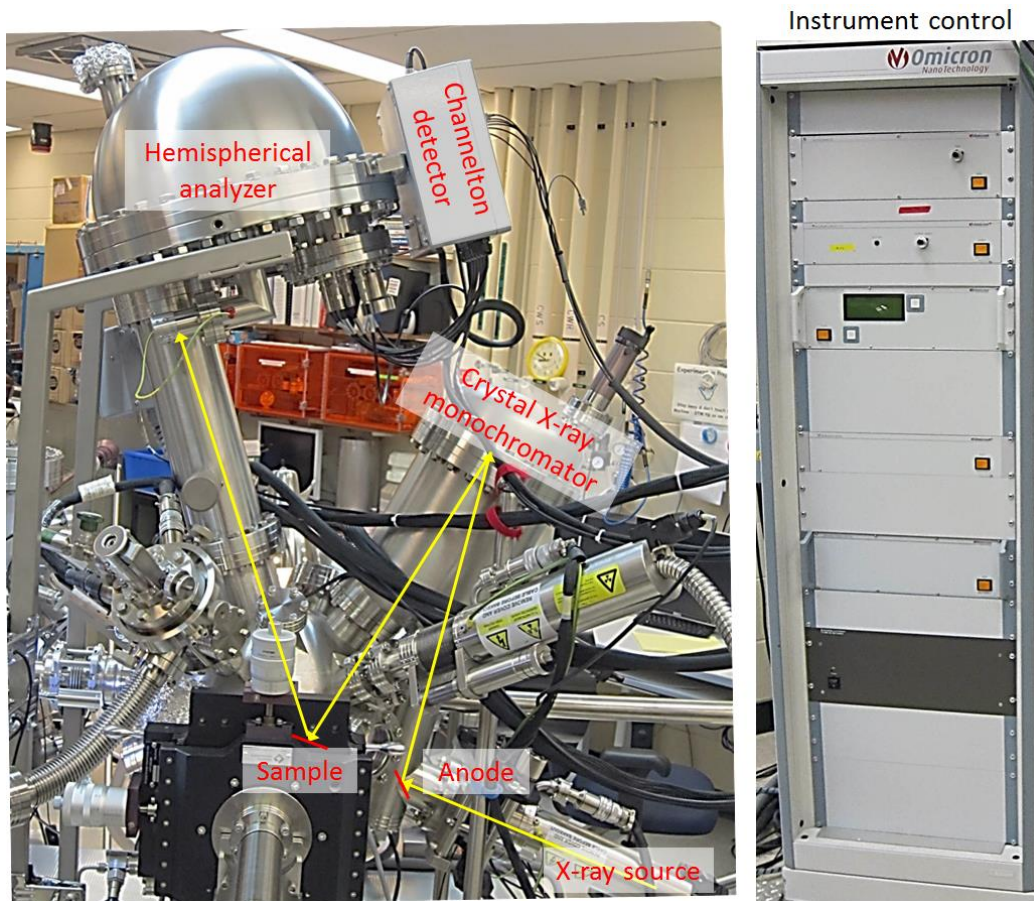


Figure 1.2 Left panel shows a photograph of a typical XPS system, consisting of an X-ray cathode, an X-ray anode, and a quartz-crystal X-ray monochromator, sampling position of the illuminating X-ray (approximate), an electrostatic lens system, a hemispherical analyzer, and a seven-channeltron electron detector. Right panel shows the corresponding control electronics of the XPS instrument.

1.5.2 Scanning Tunneling Microscopy

Scanning tunneling microscopy (STM) has evolved into one of the most powerful modern research tools for the study of a broad range of surface phenomena and processes, providing information about surface topography, film growth, electronic and vibrational properties, as well as molecular manipulation at atomic resolution. Developed by Binnig, Rohrer, and Gerber in the early 1980s, STM has used the

concept of quantum mechanical electron tunneling to open new door into the nanoworld of surface atoms in real space.^{2,161}

STM is an example of practical exploitation of a strictly quantum mechanical phenomenon, i.e. quantum mechanical tunneling. Quantum mechanical tunneling involves the penetration of a potential barrier by an electron wavefunction. In principle, tunneling can occur between two conductors simply by bringing them sufficiently close together, since the electron wavefunctions at the Fermi level extend out of their confining (classical) potential wells with a characteristic exponential inverse decay length K (in \AA^{-1}) given by:

$$K = (2m\phi)^{1/2}(2\pi/\hbar)^{-1} \approx 0.51(\phi)^{1/2} \quad (1.2)$$

where m is the electron mass, \hbar is the Planck constant and ϕ (in eV) is the effective local work function (Figure 1.3b). If two such wells are brought sufficiently close together (about 4\AA) and a potential V applied between them, then overlap of the electron wavefunctions permits quantum mechanical tunneling and a current I will flow across the gap (Figure 1.3c). The magnitude of the tunneling current is given by:

$$I \propto \exp(-2Kd) \quad (1.3)$$

where d is the separation between the electrodes. For example, when $\phi \approx 4$ eV, $K \approx 1 \text{\AA}^{-1}$, $e^2 \approx 7.4$, this means tunneling current will reduce by 7.4 times per \AA . While the tip is positioned two atoms away (i.e., $d \approx 3 \text{\AA}$, assuming a hypothetical atomic diameter of 1\AA), it will detect ~ 55 less current than when positioned one atom away (i.e. $d \approx 1 \text{\AA}$). This effect provides the basis for the surface sensitivity of STM, in which an electrode in the form of an atomically sharp point or tip is scanned mechanically across the surface of the other electrode.

The principle of the microscope is shown schematically in Figure 1.4. Piezo-electric elements are used to provide the tip movement at great precision. By employing appropriate voltages, the z piezo is used to adjust the tip-to-surface separation, while the x and y piezos provide scanning in the two lateral directions. The resolution of the STM depends simply on the diameter of the smallest attainable tip and tip-to-sample separation.

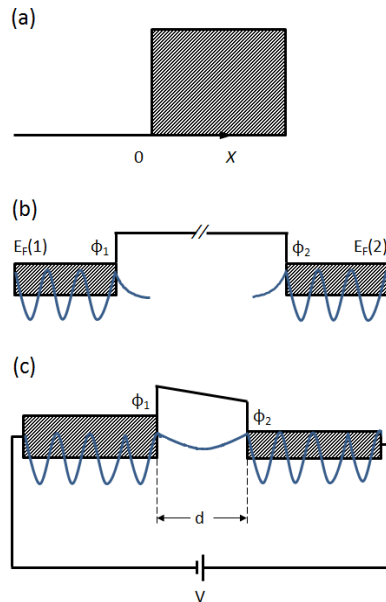


Figure 1.3 (a) An infinitely thick potential barrier where the potential is V for $x > 0$ and 0 for $x < 0$. (b) Electron wavefunctions for two metal electrodes 1 and 2 with work function Φ_1 and Φ_2 separated by a large distance. (c) As the separation between the electrodes becomes sufficiently small, the electron wavefunctions from both electrodes become connected. With the electron wavefunction overlapping each other, tunneling through the barrier may now proceed especially when assisted by the application of a bias potential difference.

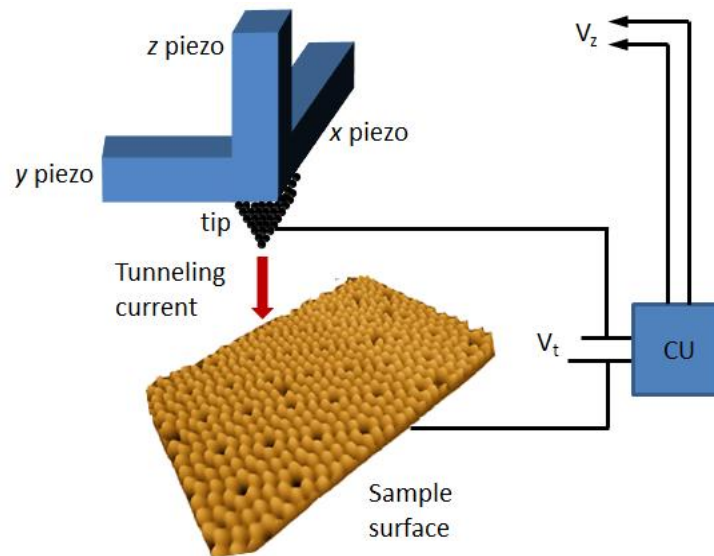


Figure 1.4 Principle of operation of a STM, where V_t is the sample bias voltage between the tip and the sample and V_z is the voltage applied to the z -piezo. In the constant current imaging mode, this z -piezo voltage is used to adjust the tip-to-sample separation so as to maintain a constant tunneling current. The control unit (CU) is used for the feedback loop.

There are three basic modes of operation: constant-current imaging, constant-height imaging, and spectroscopy modes. In both imaging modes (Figure 1.5), the tip is brought close to the surface (a few Å) and a potential difference is applied to produce a current flow. The resulting tunneling current is monitored as the tip is scanned laterally across the surface. In the constant current mode of operation (Figure 1.5a), the tip is brought close enough to the surface at a convenient z-piezo voltage so that the tunneling current is measurable. The tunneling current is usually of the order of a nanoampere. A feedback network is then used to change the z-piezo voltage and therefore the separation d between the tip and the surface in order to maintain a constant current while the tip is scanned laterally over a small area of the surface. Owing to the exponential dependence of the tunneling current on d , this has the effect of using the tip to trace out the topography of the surface at an essentially constant electron density of states. A plot of d (or the z-piezo voltage) versus the x and y coordinates of the tip provides a map of the physical topography of the surface.

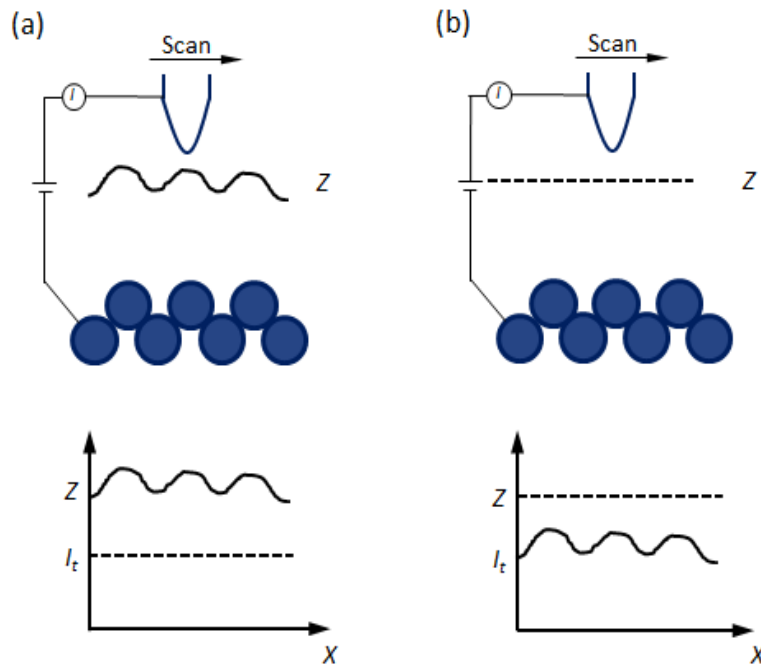


Figure 1.5 Schematic diagram of different scanning modes for STM imaging. (a) Constant current mode where the z-piezo voltage (corresponding to the height z) is adjusted to maintain a constant tunneling current I_t , and (b) constant height mode, where the z position (i.e., the z-piezo voltage) is kept fixed and the tunneling current is measured.

Alternatively, in the constant height mode (Figure 1.5b), the tip is scanned across the surface at nearly constant height obtained by using an appropriately selected z-piezo voltage, while the tunneling

current is measured. In this case, the feedback network response is made rather slow (or completely off) so that only the average current is maintained constant. A map of the resulting current versus x , y coordinates provides surface contours of different electron density of states (at a preselected distance above the surface).

There are two experimental parameters: the tunneling current and the sample-bias voltage. The resistance of the tunneling gap gives a measure of the separation between the tip and the surface. If the tip is close to the surface, the gap resistance will be relatively small. The separation between the tip and the surface is in turn determined by the set-point for the tunneling current. For a small separation, the tunneling current set-point value will be large. Typically, the tunneling current is set in the range 10 pA-1 nA. For values much greater than 1 nA, there is an increased risk that the tip-to-surface interactions will become strong enough to change the surface morphology, depending on the nature of the sample. Furthermore, the tip-induced damage to the surface can also be quite severe. It is therefore important to set an appropriate upper limit on the magnitude of the tunneling current. On the other hand, spatial resolution often becomes better at a higher tunneling current, and clearly a balance needs to be struck between the desired resolution of the recorded image on the one hand, and the likelihood of damage to the surface on the other. While tunneling currents of the order of tens of pA may be employed for molecular and biological systems, larger currents of the order of several nA could be acceptable when imaging metallic surfaces. The sample bias voltage (a potential applied to the sample with respect to the tip potential usually set at ground) also has a strong effect on the nature of the image recorded. At very high sample bias voltage values, alterations to the surface structure may be induced. This has made it possible to etch the sample surface, thus enabling the possibility of nanopatterning and nanolithography. If the tip is moved in a controlled fashion across the surface while a high bias voltage is maintained, it is possible to create nanometer scale topographical features on the surface.

The images generated by STM are determined by the electronic states at the surface and in the tip. STM can, therefore, in principle map out the electronic structure of a surface with atomic resolution, facilitating detailed studies of local, site-specific phenomena. As the STM image is dependent on the sample bias potential in a complex fashion, it is possible to take advantage of this dependence to probe the local electron density of states spectroscopically with STM. Figure 1.6 shows a hypothetical one-dimensional system. When the tip potential is negative with respect to the sample (by applying a positive sample bias voltage), electrons tunnel from the occupied states of the tip to the unoccupied states of the sample (Figure 1.6a). On the other hand, when the tip potential is positive with respect to the sample (by applying a negative sample bias voltage), electrons tunnel from the occupied states of the sample to the

unoccupied states of the tip (Figure 1.6b). Since states with the highest energy have the longest decay lengths into the vacuum, most of the tunneling current arises from electrons lying near the Fermi level of the negatively biased electrode. By varying the sample bias, it is therefore possible to sample the local electron density states over a specified energy region. In the present work, we will employ both positive sample bias and negative sample bias to obtain, respectively, complementary empty-state images and filled-state images of the sample, in order to provide more reliable assignment of STM features to specific adsorption moieties.

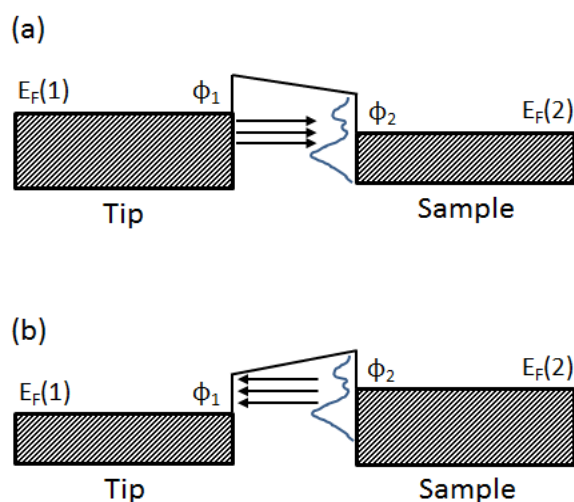


Figure 1.6 (a) By applying a positive bias to the sample (with respect to the tip), tunneling occurs from the occupied states of the tip to the empty-states of the sample (empty-state imaging). (b) By applying a negative bias to the sample, tunneling is reversed from the occupied states of the sample to the empty states of the tip.

1.6 Scope of Thesis

In the present work, we follow the growth evolution of gold, and two proteinogenic sulfur-containing amino acids (L-cysteine and L-methionine) on the Si(111)7×7 surface, with the ultimate goal to examine the molecular interaction of these aliphatic amino acids with gold clusters and other nanostructures supported on the 7×7 surface. Using the three-pronged approach of combining chemical-state information provided by XPS and the site-specific local density-of-state images from STM with large-scale quantum mechanical modelling, we seek to investigate their detailed growth and self-organization mechanisms, particularly site-specific surface chemistry on the 7×7 surface. We have outlined here in Chapter 1 the motivation and background for the present work, along with brief literature survey about

adsorption of organic and inorganic materials on Si(111)7×7 surface and the basic principles of the two primary experimental techniques (XPS and STM) used for the present work. Chapter 2 provides an overview of the experimental setups for XPS and STM measurements for gold and amino acids on silicon substrates, and computational details used for modeling the adsorption of these adsorbates on a Si₂₀₀H₄₉ slab used as a model 7×7 surface. The experimental and theoretical results are given in the next four chapters. In particular, Chapter 3 presents STM/XPS study of growth evolution of Au on Si(111)7×7 from single atom to clusters to self-organized honeycomb nanostructures to nanocrystallites and finally nanofilms in the Stranski-Krastanov mode. These STM results illustrate, for the first time, the intriguing surface dynamics and the formation of self-assembled nanostructures (honeycombs), the chemical identity of which (gold silicide) is supported as by our XPS results. The companion Appendix (Appendix A) presents optimized Au nanostructures based on large-scale DFT calculations for the early growth stage up to the formation of the first gold silicide layer. Chapter 4 and Chapter 5 describe the adsorption and thermal evolution of two sulphur-containing standard amino acids, L-cysteine and L-methionine, respectively. The results found for these amino acids fit the universal three-stage growth mechanism that we hypothesize based on the XPS and DFT-D2 data that we obtain from five benchmark proteinogenic biomolecules on the 7×7 surface. Moreover, the site-specific adsorption of L-cysteine on Si(111)7×7 surface at low exposure as observed by STM is also presented in Chapter 4. These STM results show, for the first time, the formation of novel self-organized Y-shaped trimer of L-methionine, which we propose as a plausible “magic-number” cluster supported on Si(111)7×7 also in Chapter 5. Chapter 6 presents a preliminary study on the molecular interactions of cysteine with three distinct gold nanodeposits on Si(111)7×7, including single/dimer Au adatoms, Au honeycomb nano-networks, and Au nanocrystallite film that are obtained at different growth stages of Au. Finally, the summary and future outlook of the present work are given in Chapter 7. Appendices A, B, and C provide supporting information for Chapters 3, 4 and 5, respectively.

Chapter 2

Experimental and Computational Details

The experiments were carried out in a custom-built, multi-chamber, multi-technique ultrahigh vacuum system (Omicron Nanotechnology, Inc.), shown in Figure 2.1. This system consisted of an analysis chamber for X-ray photoelectron spectroscopy (XPS) for chemical-state composition and depth-profiling analysis, scanning tunneling microscopy (STM) for atomic-resolution imaging, and low energy electron diffraction (LEED) for determination of surface structures; two molecular beam epitaxy (MBE) chambers for inorganic and organic materials deposition, one of which is equipped with a reflection high-energy electron diffraction (RHEED) system for in-situ growth monitor of crystalline materials; a fast-entry-lock (FEL) chamber for sample loading and introduction; and a center transfer chamber (CTC) connecting the other chambers for sample interchange and storage. The base pressure in the MBE chambers were lower than 1×10^{-10} mbar, while that in the FEL chamber, the center transfer chamber, and the analysis chamber were better than 2.1×10^{-7} , 2.0×10^{-11} and 1.6×10^{-11} mbar, respectively. The MBE chambers were each pumped by a turbomolecular pump, an ion pump and a titanium sublimation pump. The chamber wall was lined inside with a cooling shroud that, when filled with liquid nitrogen, acted as an additional cryogenic pump during MBE material growth. Single-side polished n-type Si(111) chips (11×2 mm², 0.3 mm thick, from Virginia Semiconductor Inc., USA), with a resistivity of 0.005 Ω cm were used as the substrates for all the experiments. The pre-cleaned Si(111) samples were mounted on sample transfer rod in the FEL chamber for subsequent transport to the center transfer chamber. Sample transfers between the chambers were performed by using magnetic transfer rods.

2.1 Generation of 7×7 Reconstructed Surface of Si(111)

The single-side polished n-type Si(111) chips were washed with ethanol and acetone in an ultrasonic cleaner, and then mounted on a sample holder as shown in Figure 2.2 before introduction to the FEL chamber. A contaminant-free Si(111) 7×7 reconstructed surface was prepared in the analysis chamber by direct-current resistive heating at ~ 400 °C overnight in ultrahigh vacuum (UHV) condition followed by a flash-annealing procedure, which involved rapidly increasing the sample temperature to ~ 1200 °C and holding it at that temperature for ~ 10 s, and then cooling rapidly to ~ 800 °C to be followed by slowly reducing the temperature back to room temperature at a rate of 4-5 °C/s. This flash-annealing process was repeated until a clean 7×7 reconstructed Si(111) surface (with a sharp 7×7 LEED pattern) was obtained, and validated by STM and XPS techniques.

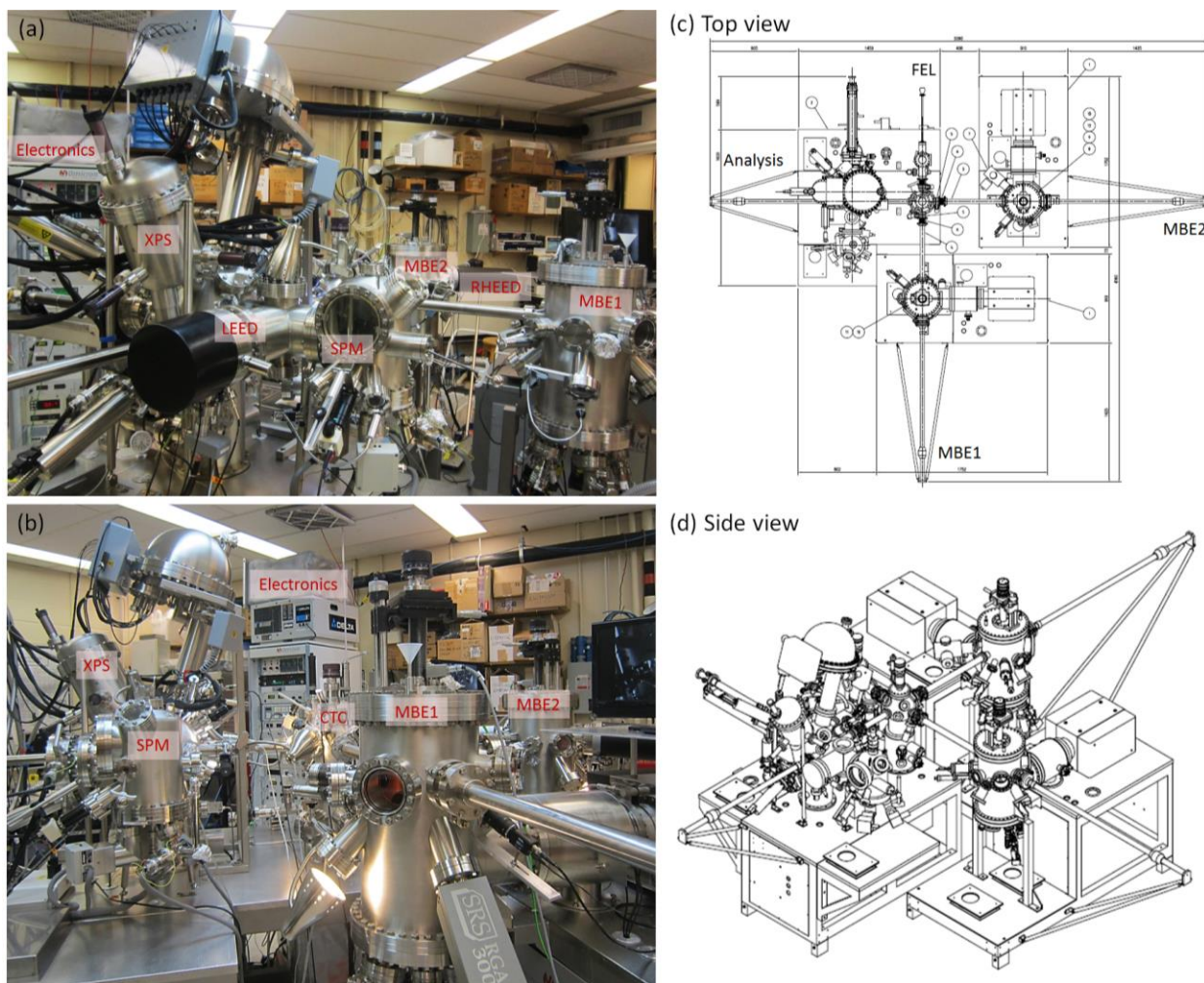


Figure 2.1 (a) and (b) Photographs of the Omicron multi-technique UHV system taken from two different angles. This five-chamber UHV system consists of two molecular beam epitaxy chambers: MBE1 for low-temperature organic material deposition and MBE2, equipped with a RHEED system, for high-temperature metal and inorganic material deposition; and an analysis chamber equipped with a X-ray photoelectron spectrometer (XPS), a variable-temperature scanning probe microscope (SPM), and a low energy electron diffractometer (LEED); as well as a fast entry lock (FEL) chamber (out of view) and a center transfer chamber (CTC). (c) and (d) The machine drawings showing the top and side view, respectively.

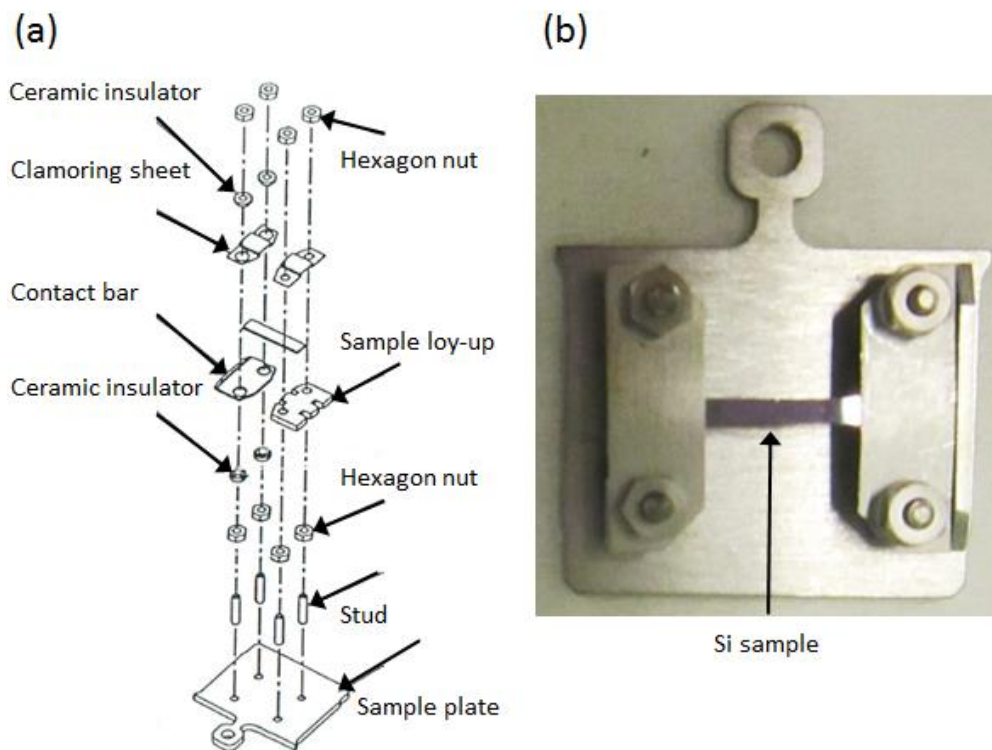


Figure 2.2 (a) The schematic diagram of the sample holder assembly (Omicron User Manual), and (b) photograph of a Si(111) chip ($11 \times 2 \text{ mm}^2$, 0.3 mm thick, from Virginia Semiconductor Inc., USA) mounted on the assembled sample holder.

2.2 Molecular Beam Epitaxy of Metal and Organic Materials

The MBE1 chamber, shown in Figure 2.3a, was used to deposit bio/organic materials, often in powder form, and was equipped with four specially designed, water-cooled, low-temperature effusion cells (Dr. Ebert MBE-Komponenten GmbH). Effusion cells OME1 and OME2, shown in Figure 2.3b, were used for evaporating organic powders at a relatively low temperature range (15-350 °C), while effusion cells NTEZ1 and NTEZ2, shown in Figure 2.3c, were used for evaporating materials at a higher temperature (80-700 °C). In order to assure the identity and integrity of the gas-phase biomolecules during exposure, the MBE1 chamber was also equipped with a 1-300 amu quadrupole mass spectrometer (Stanford Research Systems, RGA-300), shown in Figure 2.3a. After preloaded the crucible of the effusion cell with a biomaterial powder, the effusion cell was outgassed in vacuum overnight to remove any residual absorbants (e.g. water) in the powder. The powder inside the crucible of the effusion cell was heated uniformly along the entire length by a hot Ta-wire heater (Figure 2.3d-e). The temperature of the crucible was measured by using a thermocouple in direct contact with the crucible wall, and all

effusion cells were each equipped with a stainless steel double-wall water cooling shroud (Figure 2.3e) for homogenous heating and uniform temperature control. As a routine procedure, the cooling shroud of the MBE chamber was filled with liquid nitrogen before exposure of the bio/organic materials to minimize outgassing from the chamber wall. L-cysteine and L-methionine powders (99.5% purity, Fluka) with a normal melting point at 240 °C and 280 °C, respectively, were used as the bio/organic materials in the present work.

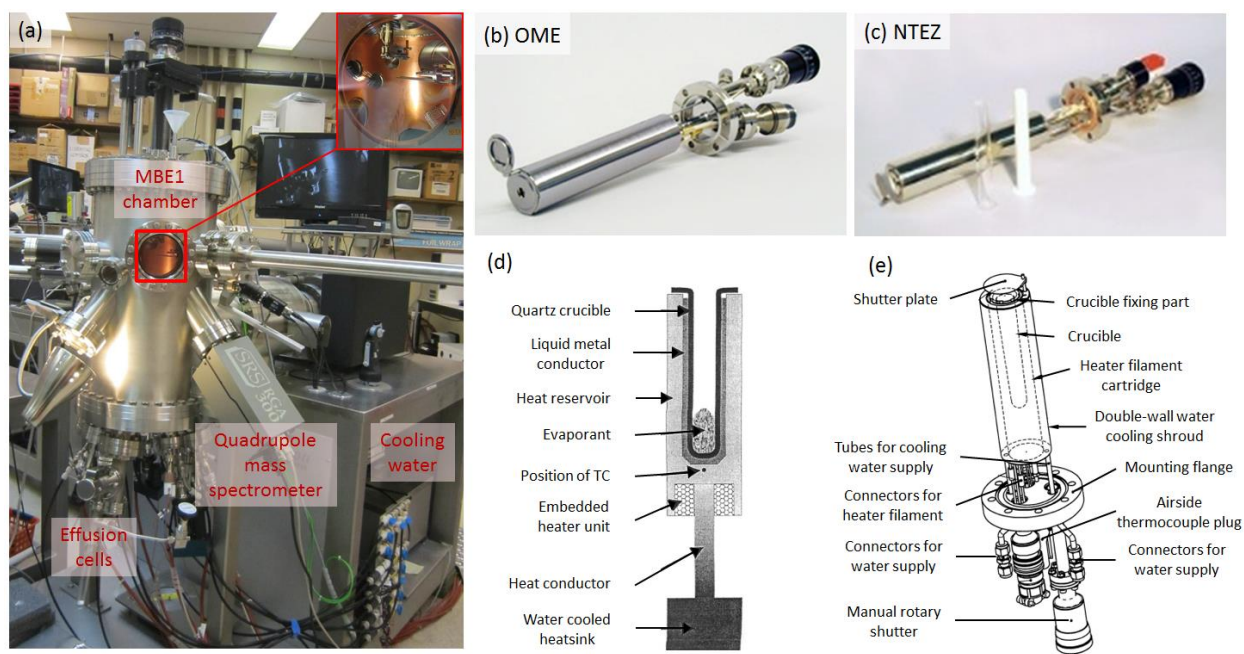


Figure 2.3 (a) Photograph of MBE1 chamber for deposition of bio/organic materials, which was equipped with four low-temperature precision effusion cells (two OME and two NTEZ cells), a quadrupole mass spectrometer, and a cooling water recirculator. The inset in (a) shows a magnified inside view of the MBE1 chamber, in which the sample stage was attached on a magnetic transfer rod. Photographs of (b) an OME effusion cell, and (c) a NTEZ effusion cell, along with a quartz and a polytetrafluoroethylene crucibles. Schematic diagrams of (d) the OME cell and (e) NTEZ cell, depicting the crucible, heating system, evaporant (powder), thermocouple and water-cooling mechanism.

The MBE2 chamber, shown in Figure 2.4a, was used to deposit metals (such as Au, Ag, Cu, and Fe) and high-temperature materials such as silicon and oxides. It was equipped with two medium-temperature WEZ effusion cells (200-1300 °C, Figure 2.4b) and two high-temperature effusion cells EFM (300-2000 °C, Figure 2.4c). A RHEED system was also installed to allow real-time monitoring of the crystalline growth. Gold was the metal material used in the present study.

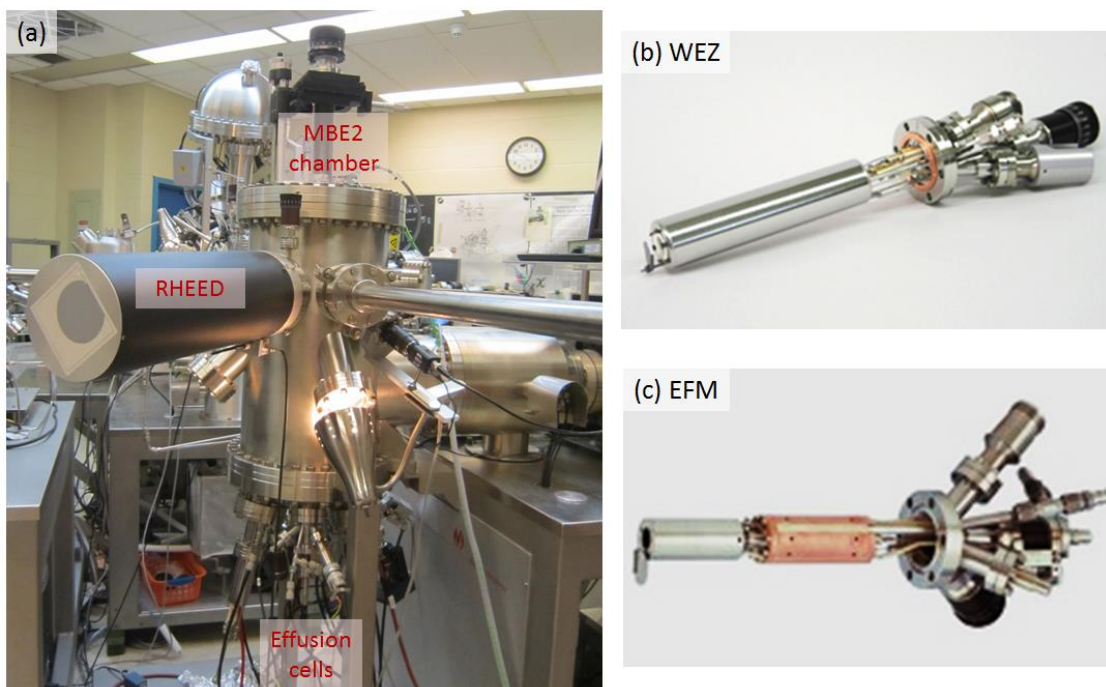


Figure 2.4 Photographs of (a) MBE2 chamber for deposition of metals and inorganic materials equipped with two medium temperature (WEZ) and two high-temperature (EFM) effusion cells and a RHEED system, (b) WEZ effusion cell and (c) EFM effusion cell.

2.3 Analysis Chamber

The multi-technique Omicron system in WATLab was equipped with XPS, SPM, and LEED facilities, used, respectively, for quantitative chemical-state composition analysis, atomic-resolution real-space imaging, and surface crystallography characterization. Together with our large-scale quantum mechanical modelling, the XPS and SPM provide a three-pronged approach for the present study.

2.3.1 X-ray Photoelectron Spectroscopy for Chemical-State Composition Analysis

X-ray photoelectron spectroscopy has been performed on various supported Au templates obtained with different Au exposures on Si(111)7×7 surface in order to follow the evolution of chemical-state composition with growth. XPS has also been employed for the nanofilm growth experiments of sulfur-containing aliphatic amino acids, i.e., L-cysteine and L-methionine, which were deposited cumulatively on the same Si(111)7×7 substrate at room temperature under UHV conditions, and for the thermal evolution experiments of the as-deposited thick amino acid films upon annealing to 85°C, 175°C and 285°C to investigate the thermal stability of the biofilms. XPS spectra of the Si 2p and Au 4f regions

were collected after deposition of Au on Si(111)7×7 surface, while those of the Si 2p, N 1s, C 1s, O 1s, S 2p and S 2s regions were obtained after deposition of cysteine and methionine on Si(111)7×7 surface as a function of exposure time. All XPS spectra were recorded with a pass energy of 20 eV, which gave an effective linewidth of 0.7 eV full width at half maximum (FWHM) for the Ag 3d_{5/2} photoline at 368.3 eV binding energy. Besides the Ag 3d_{5/2} peak, Au 4f_{7/2} peak at 83.9 eV and Cu 2p_{3/2} peak at 932.6 eV have also been used to calibrate the binding energy scale of the XPS spectrometer. Housed in the analysis chamber, the high-performance XPS spectrometer used for these measurement consisted of a monochromatized Al K α source (1486.7 eV photon energy), a SPHERA hemispherical electron energy analyzer (operated with a pass energy of 20 eV), and a 7-channeltron detector assembly (Figure 2.5a). Figure 2.5b shows a schematic diagram of the X-ray monochromator with its three major components: electron source and alignment manipulator of the cathode, X-ray anode, and quartz-crystal mirror assembly. Along with the sample, the positions of the X-ray anode and quartz-crystal mirror were positioned appropriately on the Rowland circle. As Figure 2.5c schematically illustrates, the relative orientation of the monochromator axis (photon direction) and the entrance lens direction of the analyzer (photoelectron emission direction) was fixed at the magic angle (54.7°). The X-ray source (XM 1000 MkII) had a water-cooled aluminum-coated anode surface, and a short and a long filament, acting as the cathodes for diffused and focused operations, respectively (Figure 2.5d). The long cathode was normally operated at a lower power density that led to a less focused X-ray spot on the sample (~4 mm), while the short cathode could produce a higher electron power density that gave rise to a smaller, brighter X-ray emitting spot (~1 mm) on the sample. The resulting photoemission signal was directly proportional to the brightness of the X-ray spot illuminating on the sample. The maximum emission was 300 W at 15 kV for the shorter filament and 600 W at 15 kV for the longer filament, which were controlled by the X-ray source power supply. The control electronics, including the X-ray control unit and the analyzer lens and counting electronics, was fully software-controlled by using a Windows XP computer. After acquisition of the XPS data, the spectra were fitted with Gaussian–Lorentzian lineshapes (70% Gaussian and 30% Lorentzian) along with the Shirley background using the Casa-XPS software, and the binding energies were referenced to the Si 2p_{3/2} peak of bulk Si at 99.3 eV.

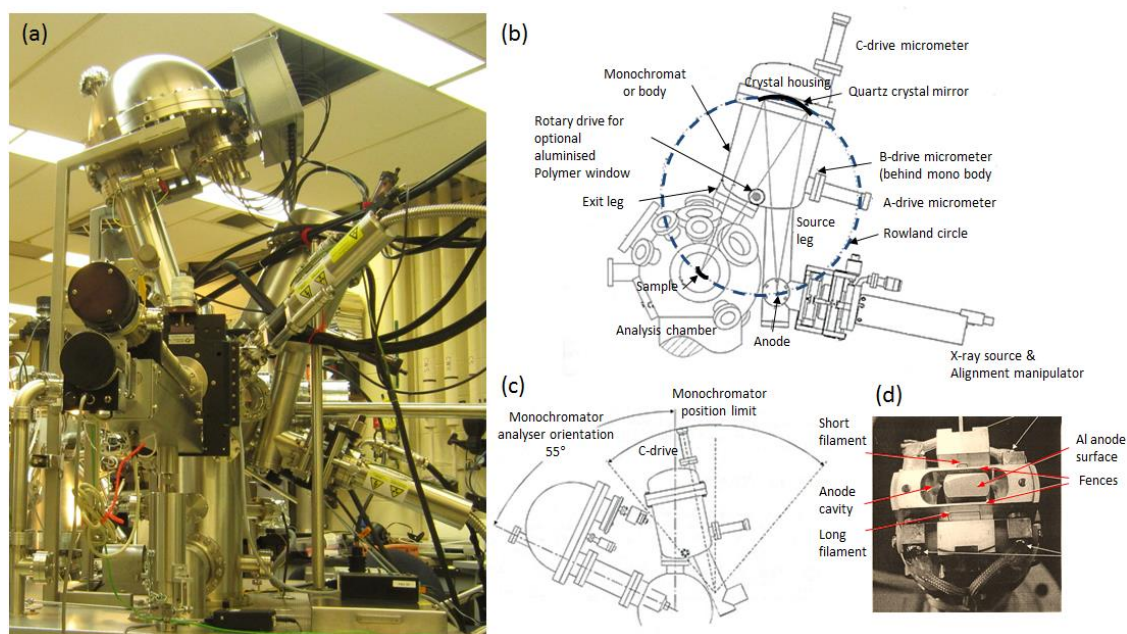


Figure 2.5 (a) Photograph of the X-ray photoelectron spectrometer, consisting of an X-ray source with a monochromator, and a hemispherical electron energy analyser with an entrance lens and an exit detector systems. (b) Schematic diagram of the X-ray monochromator with individual components: X-ray source and manipulator, and a quartz crystal mirror monochromator. The X-ray anode, monochromator and the sample position are appropriately aligned on the Rowland circle. (c) Schematic diagram of the relative orientation of the photon emission direction of the monochromator with respect to the entrance lens direction of the analyser (i.e. the photoelectron emission direction). (d) Photograph of an X-ray source (XM 1000MKII) with the short and long filament cathodes, and the aluminum-coated anode surface.

2.3.2 Scanning Tunneling Microscopy for Atomic Resolution Imaging

Figure 2.6 shows the variable-temperature scanning probe microscope (VT-SPM), manufactured by Omicron Nanotechnology, installed in the analysis chamber. A magnified and more detailed view of the VT-SPM taken outside the chamber is shown in Figure 2.6b. The VT-SPM was capable of both high-performance STM and AFTM measurements at a temperature range of -223 - 227 °C (or 50-500 K) when combined with cooling and heating facilities. Sample heating in the microscope was achieved by an indirect radiative heating facility integrated into the sample stage, while sample cooling was accomplished by using a continuous liquid helium flow cryostat. The VT-SPM employed a unique vibration decoupling mechanism to provide effective noise reduction. The base plate was suspended by four springs (with a resonance frequency of 2 Hz) and vibrations of the suspension system were prevented by using a non-periodic eddy current damping mechanism. To achieve this, the VT-SPM base plate was surrounded by a ring of copper plates seating in between permanent magnets. The sample or tip transfer

was performed by first locking the spring suspension with the push-pull motion feedthrough (PPM, Figure 2.6b), and then exchanging the sample by using a wobble stick (Figure 2.6a). The STM stage was then released and spring-loaded with the push-pull feedthrough. As shown in Figure 2.6c, the scanner stage with a STM tip could be moved vertically upward to reach the sample surface with the use of piezo motors. The STM tip could be commanded to approach the surface with the help of a remote control box (Figure 2.6d). After the STM tip reached the set position, applying appropriate bias voltage and setting the tunneling current set-point were fully controlled to obtain an STM image using the MATRIX software. A single tube scanner with a maximum scan range of $10\ \mu\text{m} \times 10\ \mu\text{m}$ and a z-travel of $1.5\ \mu\text{m}$ was used in the VT-SPM microscope and a z resolution better than $0.1\ \text{nm}$ could be achieved.

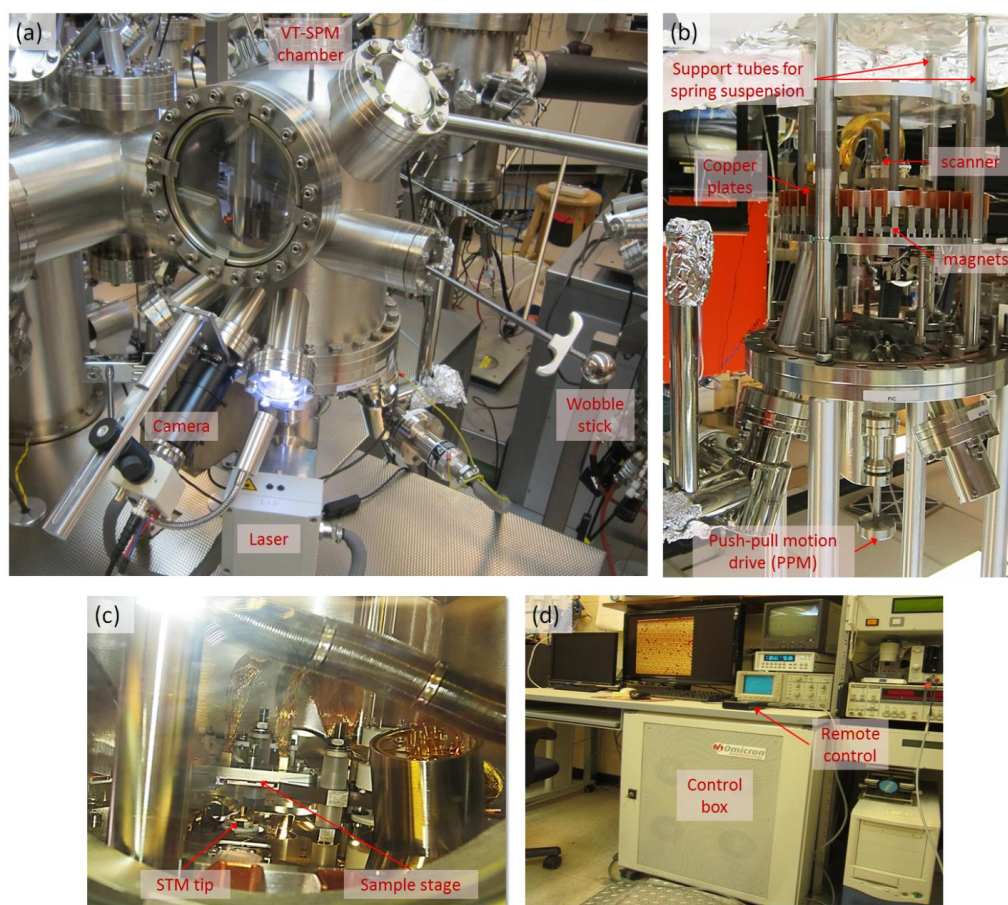


Figure 2.6 Photographs of the Omicron VT-SPM system: (a) SPM chamber with a wobble stick, the laser electronics for AFM operation, and a camera; (b) VT-SPM microscope outside the chamber; (c) STM scanner stage with a STM tip; and (d) data acquisition computer with control electronics.

2.4 Computational Details

In addition to the two aforementioned surface-sensitive analytical methods used to provide complementary information about specific properties of the surface, biomolecular surface reactions and film growth processes, computational chemistry with comprehensive ab-initio quantum mechanical molecular modelling is also employed to provide more comprehensive understanding of the experimental findings. This three-pronged approach has allowed us to acquire more fundamental insights into the systems on hand and to make predictions about other larger systems on the basis of the present results.

In computational chemistry, three general types of calculations: molecular mechanics, semi-empirical calculations, and ab-initio calculations, have been applied to study the problem on hand. While molecular mechanics employs classical physics to interpret the behavior of atoms and molecules using force-fields with empirical parameters, semi-empirical methods combine quantum physics with experimentally derived empirical parameters and approximations. These methods are particularly useful for describing approximate behaviour and trends of large systems, where accuracy is perhaps not the primary goal. On the other hand, ab-initio quantum mechanical method provides accurate calculations of total energies and other fundamental material properties, including atomic and electronic structures of molecules and solids, based entirely on quantum mechanics. Generally recognized as one of the most popular ab-initio methods, Density functional theory (DFT) has been applied to a wide range of systems from atoms, molecules and solids to nuclei and quantum and classical fluids. DFT can be used to predict various molecular properties such as molecular structure, electronic and magnetic properties, reaction paths, and vibrational frequencies in chemistry. The idea of using the electron density instead of a wavefunction to obtain information about chemical systems originated in the early days of quantum mechanics in the 1920s through the studies of Thomas¹⁶² and Fermi.¹⁶³ After three decades, Slater¹⁶⁴ in 1951 simplified the Hartree-Fock theory^{165,166,167,168} using ideas from the electron gas, which was first developed for electronic structural calculations for solids. The modern DFT formalism began in the mid 1960 based on two mathematical theorems proven by Hohenberg and Kohn¹⁶⁹ and Kohn and Sham.¹⁷⁰ The first Hohenberg and Kohn theorem, which states that “*The ground state energy from Schrodinger’s equation is a unique functional of the electron density.*” lay the foundation for DFT calculations. The ground-state energy E can be expressed as $E[n(\mathbf{r})]$, where $n(\mathbf{r})$ is the electron density of the wave function $|\Psi\rangle$ at spatial coordinates \mathbf{r} of the N electrons and is given by:

$$n(\mathbf{r}) = \int |\Psi(\mathbf{r}_1, \mathbf{r}_2, \dots, \mathbf{r}_N)|^2 d\mathbf{r}_1 d\mathbf{r}_2 \dots d\mathbf{r}_N \quad (2.1)$$

For a closed shell single determinant consisting of individual electron wave function (ψ_i), $n(\mathbf{r})$ is given by:

$$n(\mathbf{r}) = 2 \sum_i \psi_i^*(\mathbf{r})\psi_i(\mathbf{r}) \quad (2.2)$$

Although this theorem rigorously proves that a functional of the electron density exists and that it can be used to solve the Schrodinger's equation, the theorem says nothing about what the functional actually is. The second Hohenberg and Kohn theorem defines an important property of the functional and it states that “*The electron density that minimizes the energy of the overall functional is the true electron density corresponding to the full solution of the Schrodinger's equation.*” The energy functional defined by the Hohenberg and Kohn theorem in terms of the individual electron wave function can be written as in terms of an “known” total energy functional E_{known} and exchange-correlation functional $E_{\text{XC}}[\{\psi_i\}]$:

$$E[\{\psi_i\}] = E_{\text{known}}[\{\psi_i\}] + E_{\text{XC}}[\{\psi_i\}] \quad (2.3)$$

$$E_{\text{known}}[\{\psi_i\}] = -\frac{\hbar^2}{2m} \sum_i \int \psi_i^* \nabla^2 \psi_i d^3r + \int V(\mathbf{r})n(\mathbf{r})d^3r + \frac{e^2}{2} \iint \frac{n(\mathbf{r})n(\mathbf{r}')}{|\mathbf{r} - \mathbf{r}'|} d^3r d^3r' + E_{\text{ion}} \quad (2.4)$$

The terms on the right hand side correspond, from left to right, to the electron kinetic energies, the Coulomb interactions between the electrons and the nuclei, the Coulomb interactions between pairs of electrons, and the Coulomb interactions between pairs of nuclei.

Kohn and sham showed that the task of finding the right electron density can be expressed in a way that involves solving a set of equations, each of which only involves a single electron. The Kohn-Sham equation has the form:

$$\left[-\frac{\hbar^2}{2m} \nabla^2 + V(\mathbf{r}) + V_H(\mathbf{r}) + V_{\text{XC}}(\mathbf{r}) \right] \psi_i(\mathbf{r}) = \epsilon_i \psi_i(\mathbf{r}) \quad (2.5)$$

where V defines the interaction between the electron and the collection of atomic nuclei; V_H (the Hartree potential) describes the Coulomb repulsion between the electron and the total electron density and also involves the Coulomb interaction between the electron and itself; and V_{XC} can formally be defined as a “functional derivative” of the exchange-correlation energy:

$$V_{\text{XC}}(\mathbf{r}) = \frac{\delta E_{\text{XC}}(\mathbf{r})}{\delta n(\mathbf{r})} \quad (2.6)$$

To solve the Kohn-Sham equation, the exchange-correlation functional, $E_{\text{XC}}[\{\psi_i\}]$ must be specified, which is very difficult. Fortunately, there is one case where this functional can be derived exactly: the

uniform electron gas. In this case, the electron density is constant at all points in space, i.e., $n(\mathbf{r}) = \text{constant}$. The exchange-correlation potential at each position can be set to the known exchange-correlation potential for the uniform electron gas at the electron density observed at that position:

$$V_{XC}(\mathbf{r}) = V_{XC}^{electron\ gas}[n(\mathbf{r})] \quad (2.7)$$

This approximation uses only the local density to define the approximate exchange-correlation functional and it is known as the local density approximation (LDA). LDA defines the approximate exchange-correlation functional which can be derived exactly from the uniform electron gas, but the accuracy of the LDA is insufficient for most applications in chemistry.

$$V_{XLC}^{LDA}(\mathbf{r}) = V_{XC}^{electron\ gas}[n(\mathbf{r})] \quad (2.8)$$

After the LDA, development of functionals introduced the best known class of functionals, known as the generalized gradient approximation (GGA).¹⁷¹ GGA uses information about both the density and the gradient of the charge density at a particular point, and reduces the LDA errors. In GGA, the exchange-correlation functional is expressed using both the local electron density and the gradient of its electron density:

$$V_{XLC}^{GGA}(\mathbf{r}) = V_{XC}[n(\mathbf{r}), \nabla n(\mathbf{r})] \quad (2.9)$$

There are a large number of different GGA functionals arising from various ways that form the gradient of the electron density. The Perdew-Wang functional (PW91) and Perdew-Burke-Ernzerhof functional (PBE)¹⁷² are two of the most popular functionals.

Despite the great efforts in developing the DFT method in the past decade, there were lingering problems in describing van der Waals interactions or London forces (dispersion interactions) in intermolecular interactions, which are especially important in biochemical materials and in bio- or nanoarchitectures, and to the electronic structure of strongly correlated systems. To improve the electron correlation treatment, an additional term has been added to the conventional Kohn-Sham DFT energy.¹⁷³ The relationship between electron correlation and long-range forces between atoms was initially examined in the 1930s by London, who showed that the general form of the interaction between two spherically symmetric atoms at large distances was

$$V^{dispersion} = -\frac{C}{r^6} \quad (2.10)$$

where r is the separation between the atoms and C is a collection of physical constants.

In DFT-D calculations, the total energy of a collection of atoms as calculated with DFT, E_{DFT} , is augmented as follows:

$$E_{DFT-D} = E_{DFT} - S \sum_{i \neq j} \frac{C_{ij}}{r_{ij}^6} f_{damp}(r_{ij}) \quad (2.11)$$

Here, r_{ij} is the separation between atoms i and j , C_{ij} is a dispersion coefficient for atoms i and j , which can be calculated directly from tabulated properties of individual atoms, and $f_{damp}(r_{ij})$ is a damping function to avoid unphysical behavior of the dispersion term for small separations. The empirical parameter, S , corresponds to a scaling factor that is applied uniformly to all pairs of atoms.¹⁷⁴

Dispersion effects included via semiempirical atom pairwise interactions using the DFT-D2 or DFT-D3 methods by Grimme have been shown to give quite accurate thermochemistry for both covalently bonded systems and systems dominated by dispersion forces.^{175,176,177} Unless stated otherwise, we employ the DFT-D2 approach for the calculations presented in the present work.

2.4.1 Slab Model

In this study, we used an optimized structure of the dimer-atom-stacking fault (DAS)^{29,28} model for the Si(111)7×7 substrate, which contains a faulted and an unfaulted half unit cells, each with three corner adatoms and three center adatoms in the topmost layer and three restatoms in the second layer (Figure 1.1d). A periodic repeating slab consisting of 200 Si atoms, distributed in two Si bilayers and a reconstructed layer (topmost layer) with a 5.419 Å lattice constant of the Si bulk, and a vacuum gap of 12 Å was used to represent the Si(111)7×7 surface. The bottom layer of the slab was terminated by 49 H atoms. The Vienne Ab-initio Simulation Package (VASP, version 5.3.3)^{178,179,180,181} and the Materials Exploration and Design Analysis platform (MedeA, version 2.16, Materials Design, Inc.) were used for the calculations. During the equilibrium structure optimization, all the coordinates of the H-terminated Si atoms were relaxed until the forces at individual atoms were less than 0.01 eV/Å, with the coordinates of all the Si atoms fixed. With the coordinates of the H atoms now frozen, the coordinates of the Si adatoms and the two Si bilayers were then relaxed until the forces on each atom were less than 0.01 eV/Å.

The first-principle total energy calculations were performed within the generalized gradient approximation^{171,182} as defined by Perdew, Burke, and Ernzerhof (GGA-PBE),¹⁷² based on the exchange-correlation functional and projector augmented-wave (PAW) potentials^{183,184} to describe the effect of core electrons on the valence shells together with a plane-wave basis set used to span the valence electronic states. The plane-wave expansion cutoff energy was set to 250 eV (for Au) and 400 eV (for bio-organic adsorbates). The surface Brillouin zone was sampled at only Γ point with k-point spacing of 0.5/Å for all DFT and DFT-D2 calculations, due to the large unit cell and limited computing resources. Conjugate-gradient algorithm was employed to optimize the geometry of the atomic structure, and all Si atoms were

completely relaxed until the forces on all the atoms were less than 0.02 or 0.01 eV/Å, depending on the size of system. The energy convergence of the self-consistent field was set to 1.0×10^{-5} eV, with Methfessel-Paxton smearing of 0.2 eV.

The adsorption energy E_{ad} for adsorbates is defined as,

$$E_{ad} = (E_{nM+Si_{200}H_{49}} - E_{Si_{200}H_{49}} - nE_M) \quad (2.12)$$

where $E_{nM+Si_{200}H_{49}}$, $E_{Si_{200}H_{49}}$ and E_M are the total energies of the adsorbed species (i.e. a gold atom or a biomolecule) on the $Si_{200}H_{49}$ slab, the $Si_{200}H_{49}$ slab, and the isolated species, respectively, and n is the number of species making up the cluster nM . The more negative is the adsorption energy E_{ad} , the more stable is the corresponding adsorption.

In the case of adsorption of Au on the $Si(111)7 \times 7$ surface, we calculated the adsorption energy of a single Au adatom on the top of various sites, such as center adatom, corner adatom, restatom, pedestal atom of the restatom, pedestal atom of the corner adatom, and pedestal atom of the center adatom, on both the faulted and unfaulted half unit cells using DFT calculations. These calculations enabled us to determine the most stable position for anchoring individual Au atoms and also to discover the trajectory of hopping for a single Au atom. Furthermore, we did DFT calculations for the adsorption of two Au atoms on various sites of the $Si(111)7 \times 7$ surface (not reported in the present study). Moreover, we also calculated the adsorption energy of n Au adatoms on the top of $Si(111)7 \times 7$ in order to evaluate the stability of the proposed supported Au cluster structures.

In order to calculate the adsorption energy of bio-organic molecules on the $Si(111)7 \times 7$ surface, the DFT-D2 calculations were performed. A large variety of gas-phase conformations of the two S-containing biomolecules (i.e., L-cysteine and L-methionine) adsorbed in unidentate and/or bidentate configurations [through different functional groups: carboxylic acid ($-COOH$), amino ($-NH_2$), and thiol ($-SH$)] on different sites of $Si(111)7 \times 7$ surface (adatoms and restatoms sites on both faulted and unfaulted half unit cells) were evaluated. A selection of the most stable geometry was then made on the basis of their adsorption energy after optimization. To understand the formation of transitional and zwitterionic layers, the underlying driving forces, and growth modes of the adsorbed biomolecules on Si surface, additional molecules were also included to determine the equilibrium structure of the interfacial layer. The coordinates of all adsorbed molecules and Si atoms were relaxed during the DFT-D2 calculations.

Due to the importance of hydrogen bonding interactions in the formation of proteins and larger biochemical materials, quantitative studies are very useful to explain a number of supramolecular self-assembly and biological processes in physiochemical terms. For this reason, we employed DFT-D2 calculations for di-molecular configurations, which arise as a result of formation of various H-bonds, for a

number of benchmark aliphatic amino acids in the gas phase and also on the Si(111)7×7 surface. The total energy for adsorption of biomolecule or metal adspecies on the Si surface includes covalent bonds, H-bonds, long-ranged interaction energy between adsorbates and the Si surface (if it is applicable), and relaxation energy of Si surface.

Chapter 3

Two-dimensional Self-assembled Gold Silicide Honeycomb Nanonetwork on Si(111)7×7^{‡‡}

3.1 Introduction

As a noble metal, Au is well known for its stability and inertness even at high temperature. However, Au has been found to readily react with Si, with the first report of an intermixed Au/Si interface dated back to four decades ago.⁶¹ This unusual reactivity of Au toward Si is of fundamental interest. Furthermore, the catalytic property of Au in the nanoscale has also attracted a lot of attention because of its many potential technological applications. A large variety of preparation techniques have therefore been employed to grow Au on Si surface, from single Au adatoms to clusters to nanoparticles to thick films. Growing Au on clean, single-crystalline Si surface in ultrahigh vacuum is considered to be the best way to study the Au-Si reaction and the extent of this interaction, because complications due to oxide formation and grain boundaries could be minimized. Previous ultrahigh vacuum studies have focused exclusively on either the very early stage of formation of Au/Si interface⁵⁴ or a large Au coverage on Si.¹⁸⁵ Single Au adatoms,⁵² dimers,¹⁸⁶ and clusters with a proposed Au₆Si₃ structure⁴⁸ have been observed on Si(111)7×7 at room and lower temperatures by using scanning tunneling microscopy (STM).⁵⁰ On the other hand, at a high Au coverage three-dimensional Au^{187,188} or gold-silicide islands have been found by using photoemission¹⁸⁹ and medium energy ion scattering.^{64,190} Along with the formation and location of the gold silicide in the growth stage, the growth mode of Au on Si is also of great interest in the literature. In general, the common growth mode of heteroepitaxial growth of metals on Si surfaces is the Stranski-Krastanov mode. In this so-called mixed growth mode, the initial two-dimensional layer-by-layer growth is switched to three-dimensional island growth at a certain critical thickness.¹⁹¹ While the growth mode of Au on Si(111) (with various post-annealing temperatures) has been generally accepted to follow the Stranski-Krastanov mode,¹⁸⁸ details about the growth evolution particularly near the critical thickness region remains unclear. In spite of the earlier efforts and this seemingly simple metal-semiconductor “benchmark” system, a consistent picture about the formation and location of gold silicide in the growth stage of Au on Si has not been reached.^{62,64,65,189,190,192} This important information is of fundamental interest to silicon device fabrication, particularly in areas of metal and perhaps (bio)organic molecules

^{‡‡} This section is made from one of my publications: F.R. Rahsepar, L. Zhang, K. T. Leung, *J. Phys. Chem. C*, 2014, 118, pp 9051-5. Copyright (2014) by the American Chemical Society.

passivation. For example, the topmost layers of Au film on Si have been reported to be gold silicide,^{65,185,193} metallic Au,^{189,194} or Si-rich alloy.^{195,196} In the case of Au growth on Si(111)7×7 at room temperature, by using a combination of photoemission and ion scattering techniques, Hoshino et al. have reported the growth of two atomic layers (at an Au coverage of 5.2 monolayers) in the form of Au₃Si₂ on top of a metallic Au layer.⁶⁵ Even more surprising was their observation that an increase in the Au dosage only led to an increase in the metallic Au layer thickness, with the top Au₃Si₂ layers remaining unchanged.⁶⁵ In contrast, according to Kim et al.,¹⁸⁹ a complete monolayer of metallic Au was formed on the top of a gold silicide interfacial layer. They drew this conclusion from their results obtained by positron-annihilation-induced Auger electron spectroscopy that was sensitive to just the topmost layer, together with conventional Auger electron spectroscopy.

Here, we study the growth evolution of Au on Si(111)7×7 at room temperature under ultrahigh vacuum condition by correlating our STM images with our XPS spectra for the same coverage over a wide coverage range, from single adatoms to clusters to honeycomb nano-network and to islands. In particular, the morphology of Au (i.e., wetting layers vs islands) can be directly inferred from the STM images, while the chemical states of Au with well-defined chemical shifts (i.e., gold silicide vs metallic Au) can be obtained from the XPS spectra. Together, these results can be used to resolve the existing controversies about the formation and location of gold silicide in the growth stage near the critical thickness region.

3.2 Experimental Details

The experimental procedure has been discussed in detail in Chapter 2. Furthermore, Au (99.9999% purity) was deposited by thermal evaporation at 1040 °C with the 7×7 substrate held at room temperature. Different doses of Au were exposed onto the 7×7 surface, and each exposure was performed onto a freshly cleaned 7×7 surface. After each exposure, both STM and XPS measurements were performed on the same sample in the analysis chamber. For XPS, Si 2p and Au 4f spectra were recorded with an overall energy resolution of 0.7 eV FWHM (for the Ag 3d_{5/2} photoline at 368.3 eV) using monochromatised Al K_α X-ray (1486.7 eV) and an analyser pass energy of 20 eV. The Au coverage was given in monolayer (ML), for which 1 ML corresponds to 7.83×10¹⁴ atoms/cm² assuming the Si atomic density of an unreconstructed Si(111) surface. The calibration of Au coverage was carried out using the following procedure: (1) count the numbers of Au adatoms in the STM images where only single Au adatoms and dimers exist (i.e., those obtained at very low Au coverages, e.g. Figure 3.1a below); (2) measure the corresponding Au 4f XPS spectrum of the same sample; (3) establish a relation between the

Au surface number density (using the Si atomic density of an unreconstructed Si(111) surface) and the Au 4f peak area; and (4) use this relation to calculate the Au coverages for other samples using their respective Au 4f peak areas. This procedure allowed us to correlate the chemical state information obtained from XPS for a specific coverage with the corresponding morphology information provided by STM.

3.3 Results and Discussion

Figure 3.1 presents the STM filled-state images for various Au coverages from 0.004 to 3.97 ML on Si(111)7×7 at room temperature. At the lowest Au coverage (0.004 ML, with a magnified image shown in Appendix A, Figure A1), there are three notable features: sextets, triads, and scribbles. Briefly, the sextets (Figure 3.1a, circle) and the triads (Figure 3.1a, square), located respectively on the faulted (marked by F in Figure 3.1a) and unfaulted (marked by U in Figure 3.1a) half unit cells (HUCs), correspond to a single Au adatom rapidly moving among the six Si adatom sites within the respective HUCs.⁵¹ Closer examination of the sextet features shows that the corner-adatom protrusions appear brighter than the center-adatom protrusions, indicating a higher local density of states at the corner-adatom sites than the center-adatom sites. Similarly, in the unfaulted HUC the center-adatom protrusions forming the triad are brighter than the corner-adatom protrusions, as a result of a higher Au density of states at the center-adatom sites.⁵² The scribble feature (Figure 3.1a, up triangle) results from a fast moving Au dimer within a HUC.¹⁸⁶ An increase in the Au coverage to 0.05 ML leads to formation of new triangular clusters with threefold symmetry (Figure 3.1b, down triangle) located at the centers of the HUCs. We hypothesize that these triangle features correspond to Au_xSi_y clusters, including, e.g., Au₉Si₃ in accord with our large-scale calculations based on the Density Functional Theory (DFT) (Appendix A). At 0.20 ML (Figure 3.1c), larger clusters appear within the HUCs. The corresponding empty-state image (Appendix A, Figure A2) shows that these larger distorted triangle features have not covered the Si dimer walls. It should be noted that at this low coverage the 7×7 reconstruction remains clearly visible, with the dimer rows and corner holes unambiguously defining the registry of the original 7×7 surface.

Further increase in the Au coverage leads to larger clusters that completely fill the HUCs, some of which start to connect with clusters in neighboring HUCs. At 0.76 ML, the continued increase in size of these clusters and the merging of adjacent clusters eventually produce a complete Au layer with a honeycomb pattern that fills the entire Si(111)7×7 surface template with just the empty corner holes exposed. As demonstrated by the persistence of the 7×7 and related spots in the fast Fourier transform of the STM image (c.f. insets of Figure 3.1d and Figure 3.1a), this two-dimensional honeycomb nano-

network evidently follows the registry of the underlying 7×7 unit cell template. Indeed, the sharp spots in the fast Fourier transform of the honeycomb nano-network indicate its remarkably high degree of ordering. Si atoms in the third layer (i.e. the layer containing the corner hole) remain intact, preserving the otherwise disrupted 7×7 unit cell. Further Au exposure leads to growth of the second layer on the honeycomb nano-network (Figure 3.1e), at which Au atoms accumulate either on top of the existing Au clusters in the first layer or above the empty corner holes, as more and more Au atoms escape the confine of the underlying 7×7 HUCs. At higher coverage, the Au atoms continue to grow into patches of similar height, without any registry to the 7×7 unit cell. At 1.53 ML, patch growth continues and these Au patches evidently become larger and cover up any trace of the first-layer honeycomb clusters and corner holes (Figure 3.1f). It is noticeable that there is a thermodynamics spontaneous process to increase the particle size by increasing Au coverage (Figure 3.1e-h) because larger particles are more energetically favoured than smaller particles. Since Au still exists as gold silicide at this coverage (discussed below), this suggests that the Si atoms in the third layer (i.e., the corner hole layer) of the reconstruction are involved in the reaction of Au and Si atoms, with Au atoms covering displaced Si center adatoms (Appendix A, Figure A3). With further increase in the coverage to 1.80 ML (Figure 3.1g), the patches in the second Au layer join with one another and nearly cover the entire first Au layer. These STM images therefore show that the first two Au layers appear continuous and display a wetting property on the 7×7 surface.

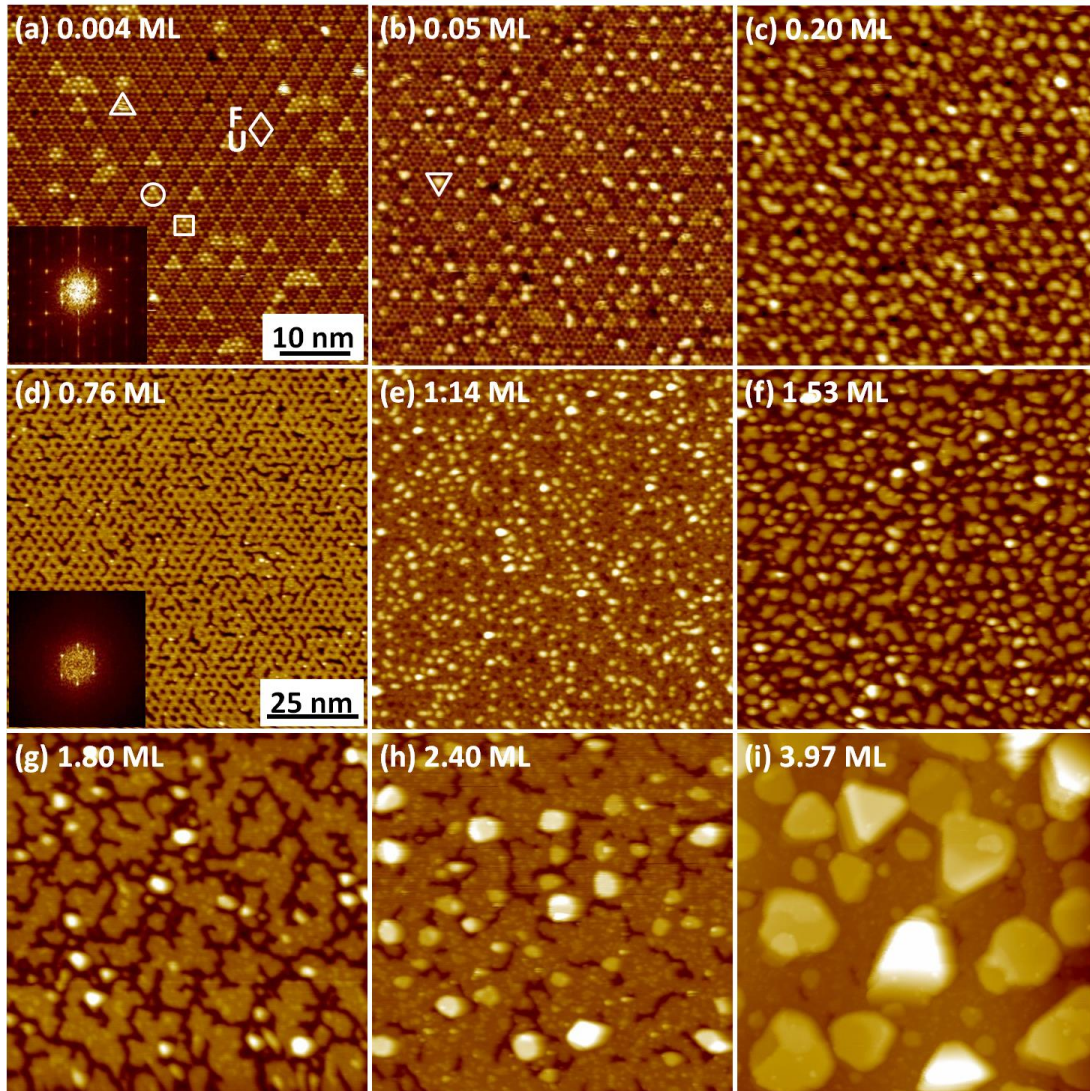


Figure 3.1 STM filled-state images of (a) 0.004, (b) 0.05, (c) 0.20, (d) 0.76, (e) 1.14, (f) 1.53, (g) 1.80, (h) 2.40, and (i) 3.97 ML of Au on Si(111)7 \times 7 at room temperature, all collected with a sample bias of -2.0 V and a tunneling current of 0.2 nA. The field of views for (a-c) and (d-i) are 50×50 nm 2 and 100×100 nm 2 , respectively. The faulted and unfaulted half unit cells are marked by F and U, respectively, in (a). Insets in (a) and (d) show the Fourier transforms of the respective images, in which the $1/7^{\text{th}}$ fractional spots corresponding to the periodic (7 \times 7) reconstruction are clearly evident.

As the coverage increases to 2.40 ML, individual three-dimensional islands as large as ~ 7.0 nm start to grow on the second layer. The replacement of layer-by-layer growth to island growth indicates a Stranski-Krastanov growth mechanism. The critical layer thickness, often used to mark the transition from layer-by-layer to island growth mode, depends on the strain and chemical potential of the deposited

film. For the present Au/Si(111)7×7 case, the critical layer thickness is found to be two physical layers equivalent to ~2 ML of Au coverage, which is in excellent agreement with our XPS results (discussed below) and with the Auger electron spectroscopy data reported by Kim et al.¹⁸⁹ With further increase in the coverage to 3.97 ML (Figure 3.1i), the metallic Au islands eventually exhibit regular triangular and polygon shapes, which indicates that these Au islands are single-crystalline and they prefer to grow along a specific direction (e.g. [111]).

To complement the above STM results on surface morphology during growth with the chemical-state information, we conduct XPS studies and show in Figure 3.2a the corresponding Au 4f spectra for the respective Au coverages shown in Figure 3.1. Evidently, the spectra are dominated by a prominent Au 4f_{7/2} (4f_{5/2}) peak near 84.6 eV (88.3 eV) over the entire coverage range. Above 2.90 ML, a second Au 4f_{7/2} (4f_{5/2}) feature emerges at 83.8 eV (87.4 eV) and appears to strengthen with increasing coverage. The primary and secondary features at their respective higher and lower binding energies are attributed to the gold silicide (Au_xSi for short) and metallic Au, respectively. This is in excellent accord with our earlier work on Au nanoparticles on Si(100),¹⁹⁷ which shows that the binding energy of Au 4f_{7/2} for gold silicide is 0.9 eV higher than that for metallic Au. Au therefore adsorbs on Si first in the form of Au_xSi at the interface, and then in the form of metallic Au with increasing coverage. It should be noted that in the early growth stage (0.05, 0.20, 0.37 ML), there appears a discernible Au 4f_{7/2} (4f_{5/2}) feature near 83.6 eV (87.4 eV). At 0.05 ML coverage and as illustrated in the corresponding STM image (Figure 3.1b), Au is found to adsorb as highly mobile single adatoms and dimers. The high mobility of these Au adatoms indicates weak electronic interactions between Au atoms and the Si adatoms and that these “metal-like” Au atoms are loosely bound. It is also of interest to note that while the peak position of the metallic Au component is essentially stationary at 83.8±0.1 eV for Au coverage above 2.4 ML, the metal-like Au feature found below 0.76 ML appears to be discernibly lower (83.6 eV). The minor shift in the Au_xSi component to lower binding energy could be due to the higher coordination of Au with Si before completing the first layer coverage and to less electron screening of the photon-excited core-level holes. The sharper Au 4f peaks of the Au_xSi component start at a coverage of 0.76 ML, which corresponds to the honeycomb nano-network shown in Figure 3.1d. At this Au coverage, the original Si(111)7×7 surface has, in effect, been transformed to a new two-dimensional honeycomb phase of Au_xSi component, which is not only structurally different (honeycomb vs 7×7) but also chemically different (Au_xSi vs Si). The relative intensities of Au 4f_{7/2} peaks for the Au_xSi and metallic Au 4f_{7/2} components (and their sum), along with that of the Si 2p_{3/2} peak, are plotted as functions of Au coverage in Figure 3.2b.

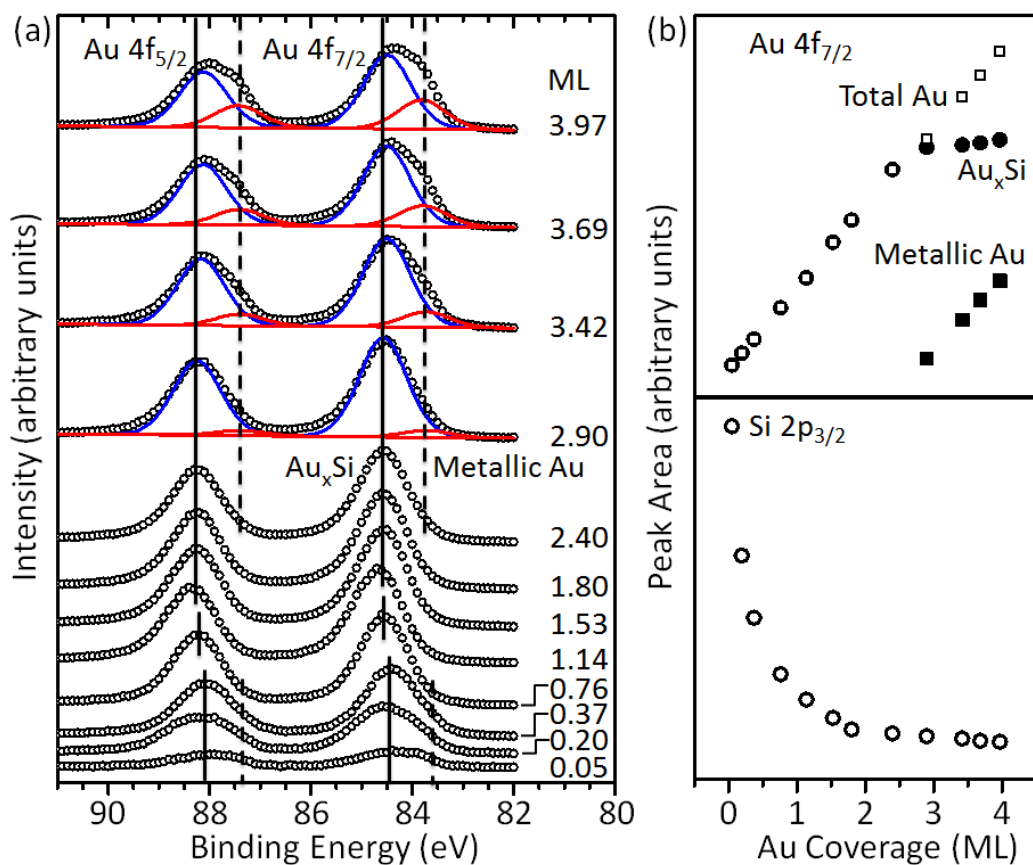


Figure 3.2 (a) XPS spectra of the Au 4f region for different Au coverages on Si(111)7×7 at room temperature. Solid and dashed lines mark the Au 4f peak positions for the gold silicide (Au_xSi) and metallic Au components, respectively. (b) Corresponding peak areas of the Au 4f_{7/2} peaks for Au_xSi and metallic Au components (along with their sum, marked as total), and of the Si 2p_{3/2} state at 99.3 eV.

By combining the information provided by the STM images and XPS spectra, we obtain a more complete picture of Au growth on Si(111)7×7 near the critical thickness region. We summarize the growth evolution of Au on Si(111)7×7 in a schematic model shown in Figure 3.3. At very low coverage (0.004-0.05 ML), Au exists as highly mobile, metal-like Au adatoms and dimers shared among the Si adatom sites in the HUCs. As the coverage increases to 0.76 ML, these Au clusters increase in size and begin to merge with neighboring clusters, which consist of both metal-like Au and Au_xSi adspecies. At 0.76 ML, only the Au_xSi component is found, and these Au silicide adspecies form a remarkably well-ordered honeycomb two-dimensional phase, completely blanketing the Si(111)7×7 surface template. As most of the further deposited Au atoms are adsorbed on the first Au_xSi layer and they grow into the second layer, they remain as Au_xSi . Further increase in the coverage leads to eventual filling of the

honeycombs to form a continuous first Au layer and to the growth of a second continuous Au_xSi layer. To understand the nature of the Au_xSi in the second layer, we perform large-scale DFT calculations and the details of this computational work are given in the Appendix A. For our calculations, we propose a Au_9Si_3 structure as a possible nucleation center for one of the six segments of the honeycomb unit, with each segment consisting of Au atoms located at three different Si sites (adatom, rest-atom and pedestal atom sites) as illustrated in Appendix A, Figure A3. The Au atoms in these segments essentially correspond to the majority of the first gold silicide layer, with some of center-adatom sites exposed. We believe that these unoccupied center-adatom sites are responsible for providing bonding to the Au atoms in the second Au_xSi layer. Above 2 ML coverage, the deposited Au atoms on top of the two continuous Au_xSi layers are sufficiently far from any Si atom, leaving them to react only with adjacent Au atoms, which leads to the formation of metallic Au islands. In agreement with the STM imaging is the coverage dependence of substrate Si $2p_{3/2}$ intensity shown in Figure 3.2b, which this information can be very helpful for device fabrication areas and also semiconductor industry. In particular, the Si $2p_{3/2}$ intensity decreases exponentially from 0 to 2 ML Au coverage, consistent with the layer-by-layer growth mode. The Si $2p_{3/2}$ intensity then increases at a much slower rate above 2 ML, indicative of the Au island growth. This also supports a critical thickness of 2 ML found for the Stranski-Krastanov growth. Our model is also consistent with the linear increase in the total Au $4f_{7/2}$ intensity with increasing Au coverage because the sampling depth of XPS is sufficiently large to cover the entire Au_xSi layers and the Au islands (Figure 3.2b).

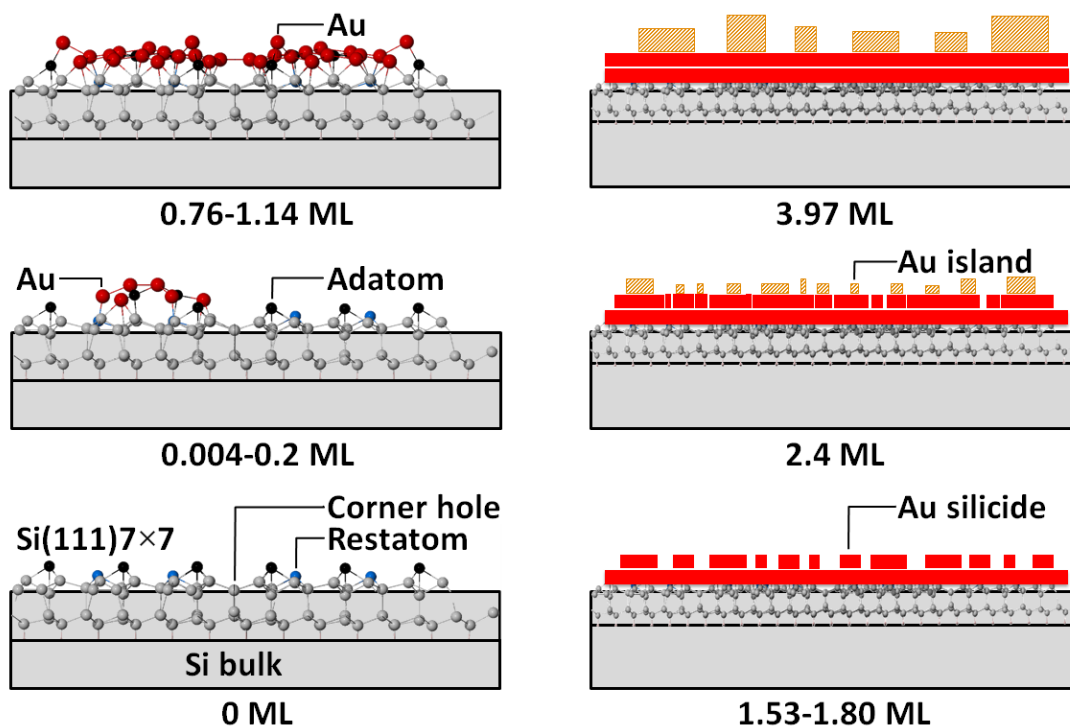


Figure 3.3 Schematic model of the growth evolution of Au on Si(111)7×7 at room temperature. Left column shows optimized structures based on DFT calculations for the early growth stage up to the formation of the first gold silicide layer. Right column shows the evolution to the second Au silicide layer and the formation of metallic Au islands.

3.4 Summary

We have studied the growth evolution of Au on Si(111)7×7 at room temperature under ultrahigh vacuum condition by using both STM and XPS. These combined results are crucial to provide support for the Stranski-Krastanov growth with the critical thickness of 2 ML that marks the formation of two Au_xSi layers followed by three-dimensional metallic Au island growth. It therefore seems unlikely that a metallic Au layer could form between the Au_xSi layers and the Si surface, as proposed by Hoshino et al. in their ion scattering study.⁶⁵ In the layer-by-layer growth below 2 ML, Au atoms react with the top three Si layers of the 7×7 reconstruction (Si adatom layer, restatom layer, and layer containing the dimer rows and the corner holes) and form two continuous Au_xSi layers. Above 2 ML, Au atoms form large individual metallic Au islands. The intricate STM images reveal not only the Stranski-Krastanov growth mode, but also the formation of a Au_xSi honeycomb nano-network at 0.76 ML. Given the conducting property of Au_xSi, this honeycomb nano-network on Si(111)7×7 could provide an important passivation

layer for device fabrication. Moreover, the Au_xSi honeycomb nano-network represents a unique nanoscale template of Au hexagonal grids (4 nm wide) and nanopores (~1 nm dia.). Upon functionalization by appropriate biomolecules such as cysteine or thiol-containing compounds, the Au_xSi honeycomb pattern also promises an important platform to build new applications for biosensing and molecular traps.

Chapter 4

Biofunctionalization of Si(111)7×7 by L-Cysteine^{§§}

4.1 Introduction

Site-specific chemistry of bio-organic molecules on semiconductor surfaces has attracted much recent attention in nanotechnology because it enables nanoscale conversion of an inorganic surface to an organic surface with opportunities for introducing multiple types of bonding. Incorporating functions by direct organic molecular attachment to semiconductor materials through both organic reactions in dry (vacuum) or wet conditions (solution) can lead to new emerging technological applications, as in the development of hybrid organic-semiconductor devices, three-dimensional memory chips, silicon-based nanoscale or biological sensors, and nanolithography.^{5,32,198–203} An important goal in organosilicon surface chemistry is to modify the electronic properties of the silicon surfaces and devices with organic molecules. Chemical attachment of organic molecules to a reconstructed silicon surface, i.e. organic functionalization, by taking advantage of the different reactivities of surface sites provides the necessary control. The Si(111)7×7 surface offers an ideal, two-dimensional template with directional dangling bonds not only for anchoring and supporting metallic adsorbates such as nanoclusters,²⁰⁴ but also for interacting with simple “benchmark” bio-organic molecules, including amino acids (e.g. glycine),²⁰⁵ peptide (e.g. glycylglycine),¹³¹ and DNA-base molecules (e.g. thymine and adenine).^{91,100} Our early studies have shown that bio-organic molecules including more than one functional group can be used to exploit site-specific chemistry of the Si(111)7×7 surface through competitive reactions among different functional groups with the Si surface dangling bonds.^{91,96,99,100} As these bio-organic molecules invariably contain moieties that can be linked to one another by intra- and interlayer hydrogen bonding, new opportunity of creating not just permanent but indeed semi-permanent (or renewable) biofunctionalization can be realized by manipulating these hydrogen bonds.

Fundamental understanding of the interactions of organic molecules with Si surface sites is the key to controlling the functionalization of semiconductor surfaces. These interactions at the interface can be typically categorized into longer-range noncovalent interactions and shorter-range covalent bonding. By using the weaker noncovalent interactions, including electrostatic interaction between statically charged species and/or molecular sites, hydrogen bonding, van der Waals forces, π - π interactions, and hydrophilic binding, many new self-assembled structures have been produced. In contrast to the longer-range

^{§§} This section is made from one of my publications: F.R. Rahsepar, L. Zhang, H. Farkhondeh, K. T. Leung, *J. Am. Chem. Soc.*, 2014, 136, pp 16909-18. Copyright (2014) by the American Chemical Society.

interactions in these weakly interacting systems, strong shorter-range chemical bonds provide the essential binding in many interfacial structures on semiconductor surfaces and in devices functionalized with bio-organic molecules.^{5,32,198,200}

Amino acids are ideal model molecules for investigating these long-range and short-range interactions with the Si surface, because they are the building blocks of proteins and as such representing one of the most important classes of biologically active molecules. They are also multifunctional molecules containing several different types of functional groups and they therefore provide ideal systems for comparative studies of the relative strengths of interactions arising from different functional groups. Of the twenty naturally occurring amino acids, only cysteine ($C_7OOHC_\alpha HNH_2C_\beta H_2SH$) contains a thiol ($-SH$) group, in addition to the carboxylic acid ($-COOH$) and amino ($-NH_2$) functional groups. Cysteine is a strong ligand for transition metals, making it a potential candidate of active materials for trace metal sensing. The adsorption of cysteine on (single-crystal) surfaces of a variety of metals, including copper,¹¹⁹ silver,¹²⁰ and gold,¹²¹ has been investigated. Cysteine was found to normally bind to the metal in the form of a thiolate.¹¹⁹⁻¹²¹ Depending on the nature of the surface, the other two functional groups also play an important role in attaching cysteine to the surface. For example, in a recent study of cysteine adsorption on a semiconductor surface, deprotonated carboxylic group was reported to be bound to the five-fold coordinated Ti surface sites on rutile $TiO_2(110)$.²⁰⁶ Furthermore, carboxylic acid and amino groups enable cysteine film growth through the formation of the intra- and interlayer hydrogen bonding.

To date, there is only one report on cysteine adsorption on the $Si(111)7\times 7$ surface. In particular, Huang *et al.* studied cysteine adsorption on $Si(111)7\times 7$ by high-resolution electron energy loss spectroscopy and X-ray photoelectron spectroscopy (XPS), and they concluded the coexistence of two chemisorption states, including a unidentate adspecies through the cleavage of an O-H bond and a bidentate adspecies with new Si-N and Si-O linkages (with two Si adatoms).²⁰⁷ However, the cysteine molecule, with a NH_2 to OH separation of 3.66 Å, reveals to be physically too small to realize the proposed bidentate structure, through the amino and hydroxyl groups, that bridges two adjacent Si adatoms across the dimer wall or in the same half unit cell, with a separation of 6.77 Å and 7.66 Å, respectively. Here, we present the first STM investigation of the adsorption configurations of cysteine on $Si(111)7\times 7$ as a function of coverage at room temperature under ultrahigh vacuum condition. By correlating this density of states images with the chemical state information provided by XPS, we determine the relative reactivity and selectivity of different surface sites towards the three functional groups in cysteine. We observe three different growth stages of cysteine, from chemisorbed adstructures in the interfacial layer (first adlayer) to transitional layer (second adlayer) to zwitterionic multilayers in

the nanofilm. We further study the room-temperature durability and thermal evolution, particularly the stability of the transitional layer and zwitterionic multilayer film, on the reconstructed Si(111) using XPS. Of particular interest is that the interlayer hydrogen bonding allows the transitional layer to be used as a renewable layer that can be removed and regenerated by manipulating the annealing-exposure cycle. By correlating, for the first time, the chemical-state information provided by XPS with the high-resolution filled-state STM images at very low exposure of cysteine, we show that the bidentate attachment of cysteine through Si-S and Si-N linkages with the (center-atom, center-atom) pair across the dimer walls of the 7×7 surface (in contrast to what was proposed earlier by Huang *et al.*).²⁰⁷ Furthermore, the empty-state STM images reveal the formation of intralayer horizontal hydrogen-bond (side-by-side) and interlayer vertical hydrogen-bond (head-to-tail), respectively, within and between adsorbed unidentate cysteine molecules in the interfacial and transitional layers. These site-specific surface interactions and intra- and inter-layer hydrogen bonding provide the important mechanism for different cysteine growth stages on the 7×7 surface. The biofunctionalization selectivity of silicon surface arising from these growth stages is easily controlled by cysteine exposure, which offers new opportunities for sensing and molecular trapping applications of other bio-organic molecules and trace transition metals.

4.2 Experimental Details

The experimental procedure has been discussed in detail in Chapter 2. Furthermore, cysteine (99.5% purity, Fluka), with a normal melting point at 240 °C, was exposed to the 7×7 substrate with the effusion cell held at 140 °C²⁰⁸ and the deposition chamber pressure at 2×10^{-9} mbar. The amount of deposited cysteine was controlled by the exposure time. The molecular identity and integrity of cysteine during exposure were confirmed by their cracking patterns, collected in-situ with a quadrupole mass spectrometer and found to be in good accord with the literature.²⁰⁹ Although the absolute coverage of cysteine could in principle be obtained directly from STM images for low exposure (for which the 7×7 pattern remains visible), deposition time was used here to indicate the relative exposure of cysteine due to the wide range of exposures employed in the present study.

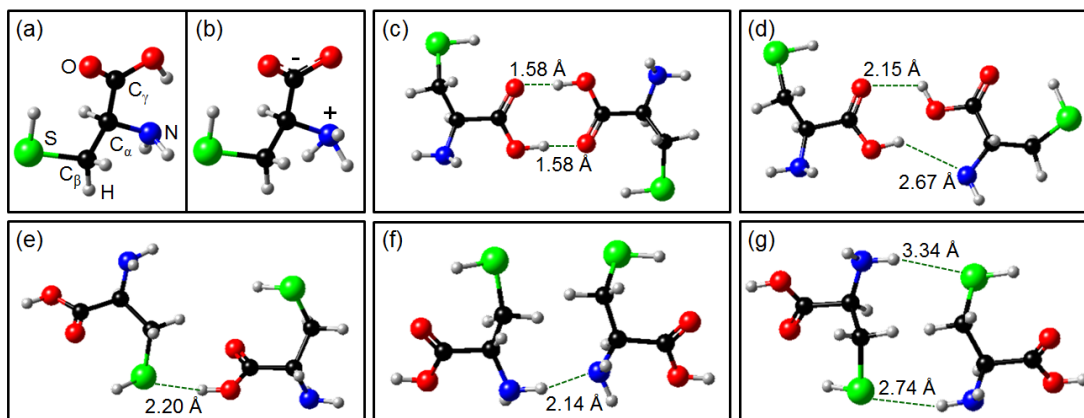
For the film growth experiments, cysteine was deposited cumulatively on the same Si(111)7×7 substrate, and their STM images were collected after each exposure. Their corresponding Si 2p, N 1s, C 1s, O 1s, S 2p and S 2s XPS spectra were recorded with a pass energy of 20 eV, which gave an effective linewidth of 0.7 eV full width at half maximum (FWHM) for the Ag 3d_{5/2} photoline at 368.3 eV. For the thermal evolution experiments, as-grown thick cysteine films were annealed sequentially by resistive heating of the sample holder from 85 °C up to 285 °C for 600 s, with the temperature monitored by a

thermocouple located a few millimeters from the sample. We have also measured the core-level spectra of cysteine powders, in which case an electron neutralizer was employed to compensate the minor charging during the measurement. The binding energy scale of the powder spectra was calibrated with respect to that of the corresponding multilayer films by aligning the main N 1s feature (Appendix B, Figure B1). After appropriate peak fitting of the observed spectral features, the ratios of peak areas could be used to determine the relative compositions of the chemical states.

4.3 Results and Discussion

While cysteine exists as the neutral form in the gas phase (Scheme 4.1a),²¹⁰ the zwitterionic structure (Scheme 4.1b), with the protonated amino group ($-\text{NH}_3^+$) and deprotonated carboxylic group ($-\text{COO}^-$), is the most stable form in both aqueous solution and solid state.²¹¹ To analyze the chemical state evolution of cysteine nanofilm growth from sub-monolayer to multilayers on Si(111)7×7 and to investigate their stability at the both room and evaluated temperatures in ultrahigh vacuum condition, we conduct XPS experiments. Figure 4.1 shows the O 1s, N 1s, C 1s and S 2s spectra of cysteine film as a function of exposure time, with their corresponding peak positions and assignments of the fitted features given in Table B1 and Table B2 (Appendix B). It should be noted that because the S 2p spectrum partially overlaps with one of the plasmon peaks of Si located at ~168.0 eV (Appendix B, Figure B2),²¹² we have chosen S 2s for the present work. At very low exposures of 5-15 s, the N 1s spectra (Figure 4.1b) show only one peak at 398.7 ± 0.1 eV, attributed to N–Si bond, which indicates that cysteine undergoes N–H dissociative adsorption on Si(111)7×7. This is in good accord with the N 1s feature at 398.8-399.1 eV found for chemisorption of dimethylamine,¹⁸ pyrazine,²¹³ hexylamine,²¹⁴ 1,4-phenylenediamine, aniline,²¹⁵ glycine²⁰⁵ and glycyglycine¹³¹ via N–H bond cleavage on Si surfaces. There is no sign of any neutral amino group ($-\text{NH}_2$) with a binding energy at ~400.0 eV.²⁰⁶ Our S 2s feature found at 227.4 eV in the present work is consistent with the Si–S linkage of chemisorbed cysteine, which indicates direct interaction of the S atom with the Si surface dangling bond. Because Si is less electronegative than H,²¹⁶ the S atom at the Si–S interface is anticipated to be more negatively charged than that in the thiol group, and consequently to have a smaller binding energy than the S atom in an intact thiol group, with S 2s at 228.4 eV. This is in marked contrast to the work by Huang *et al.*,²⁰⁷ who reported an intact thiol group for both physisorption and chemisorption of cysteine on Si(111)7×7. Furthermore, our assignment is also in good accord with Si–S species, with the S 2s feature at 227.3 eV, found for benzenethiol and diphenyl disulfide on the Si(001).¹⁵ The results of N 1s and S 2s spectra therefore clearly show that for the lowest exposure (i.e. the interfacial layer), cysteine anchors on the Si surface through dissociation of both amino

and thiol groups in a bidentate arrangement, because neither XPS feature corresponding to intact N–H nor that to S–H bond is observed. This bonding arrangement of the interfacial layer is also in good agreement with the information deduced from both filled-state and empty-state STM images (to be discussed below). Figure 4.1c shows three fitted C 1s peaks at 284.7, 286.3, and 289.2 eV, which can be attributed to the alkyl carbon atoms in C–S and C–N moieties and to the carbonyl C in the C=O group, respectively. The O 1s peak at 532.5 eV for the 5-15 s exposure is found to be broader (FWHM=1.9 eV) than that at 531.8 eV (FWHM=1.4 eV) for a thick film (5400 s). The larger width in the O 1s feature for a lower exposure is indicative of the existence of multiple components, including the carbonyl O at 532.1-532.9 eV and the hydroxyl O component at 532.8-534.4 eV.²¹⁷



Scheme 4.1 Ball-and-stick models of (a) neutral, and (b) zwitterionic structures of cysteine, and (c-g) dimer structures resulting from formation of various H-bonds (marked by the dashed lines) between different types of functional groups of two cysteine molecules in the gas phase. These models are generated by DFT calculations.

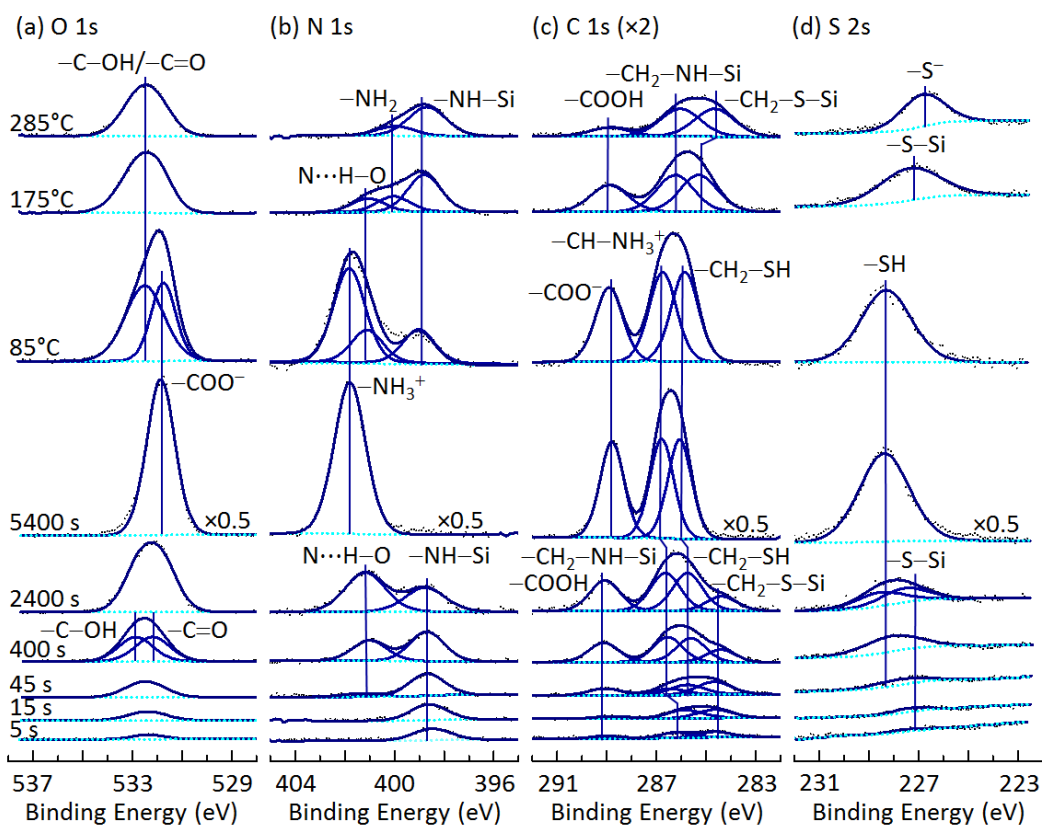


Figure 4.1 Evolution of (a) O 1s, (b) N 1s, (c) C 1s, and (d) S 2s XPS spectra of cysteine deposited on Si(111)7×7 as a function of exposure time (5 s to 5400 s); and of the as-deposited 5400 s cysteine film upon annealing to 85°C, 175°C and 285°C.

With increasing exposure to 45-2400 s, we observe the emergence and growth of a new N 1s feature at 401.1 eV (Figure 4.1b), attributable to $N\cdots H-O$ hydrogen bond (H-bond). Here we use “ \cdots ” to denote a H-bond. This feature therefore indicates the formation of interlayer vertical H-bond (head-to-tail) between a free carboxylic acid group of the interfacial layer (first adlayer) and a free amino group of the transitional layer (second adlayer), and that of intralayer horizontal (side-by-side) H-bond among two or more unidentate cysteine molecules (discussed below) in the interfacial layer. In Figure 4.2, we summarize the changes in the peak areas of the fitted XPS features. In particular, the N 1s intensity of the $N\cdots H-O$ feature for the 400 s exposure is ~6 times that for 45 s exposure, which is consistent with the increase in the amount of vertical H-bonds for the 400 s exposure from that for the 45 s exposure, the latter with mostly horizontal H-bonds. The presence of both types of H-bonds is supported by the emergence of a second S 2s feature at 228.4 eV (Figure 4.1d) and of a fourth C 1s feature at 285.5 eV

(Figure 4.1c) for the 45 s exposure, which are characteristic of the intact thiol ($-\text{SH}$) and thiol methyl ($-\text{C}_\beta\text{H}_2-\text{SH}$) groups, respectively. Moreover, there is a weak N 1s peak at ~ 401.0 eV, which can be assigned to $\text{N}\cdots\text{H}-\text{O}$ feature.^{131,133,205} For exposures in the transitional layer regime (i.e., above 45 s), the C 1s spectra have been fitted with four components at 284.5, 285.6, 286.6, and 289.2 eV, which are assigned to $-\text{CH}_2-\text{S}-\text{Si}$, $-\text{CH}_2-\text{SH}$, $-\text{CH}_2-\text{NH}-\text{Si}$, and $-\text{COOH}$, respectively.^{120,207} Further exposure to 2400 s increases the N 1s intensity of the $\text{N}\cdots\text{H}-\text{O}$ feature for transitional layer ~ 14 times with respect to that for the 45 s exposure (Figure 4.2a). Furthermore, close examination of Figure 4.2a represents that there is an increase in the N–H to S–H relative population from 50%:50% for 5 s exposure to 46%:54% for 45 s exposure. This is consistent with relative bond dissociation energies found for N–H (358.8 kJ/mol) and S–H bonds (353.6 kJ/mol).²¹⁸ Finally, the XPS spectra for the cysteine multilayers obtained for the 5400 s exposure on Si(111)7 \times 7 are found to be similar to those for cysteine powders in the solid phase (Appendix B, Figure B1). The shift of the peak maximum of the broad S 2s peak from 227.4 eV to that of the intact thiol peak at 228.4 eV (Figure 4.1d) further affirms the multilayer nature. The sharp O 1s peak at 531.9 ± 0.1 eV (FWHM=1.4 eV) (Figure 4.1a), and the single N 1s feature at 401.8 eV (Figure 4.1b) can only be assigned to, respectively, carboxylate ($-\text{COO}^-$) and protonated amino groups ($-\text{NH}_3^+$) in the zwitterionic structure ($\text{NH}_3^+\text{CHCH}_2\text{SHCOO}^-$, Scheme 4.1b) of the cysteine thick film (multilayers).²¹⁷ The corresponding C 1s spectrum (Figure 4.1c) consists of a broad band centered at 286.4 eV, attributable to the two alkyl carbons in $-\text{CH}_2-\text{SH}$ (at 285.9 eV) and $-\text{CH}-\text{NH}_3^+$ (at 286.8 eV), and a weaker feature at 288.8 eV corresponding to the carboxylate group.

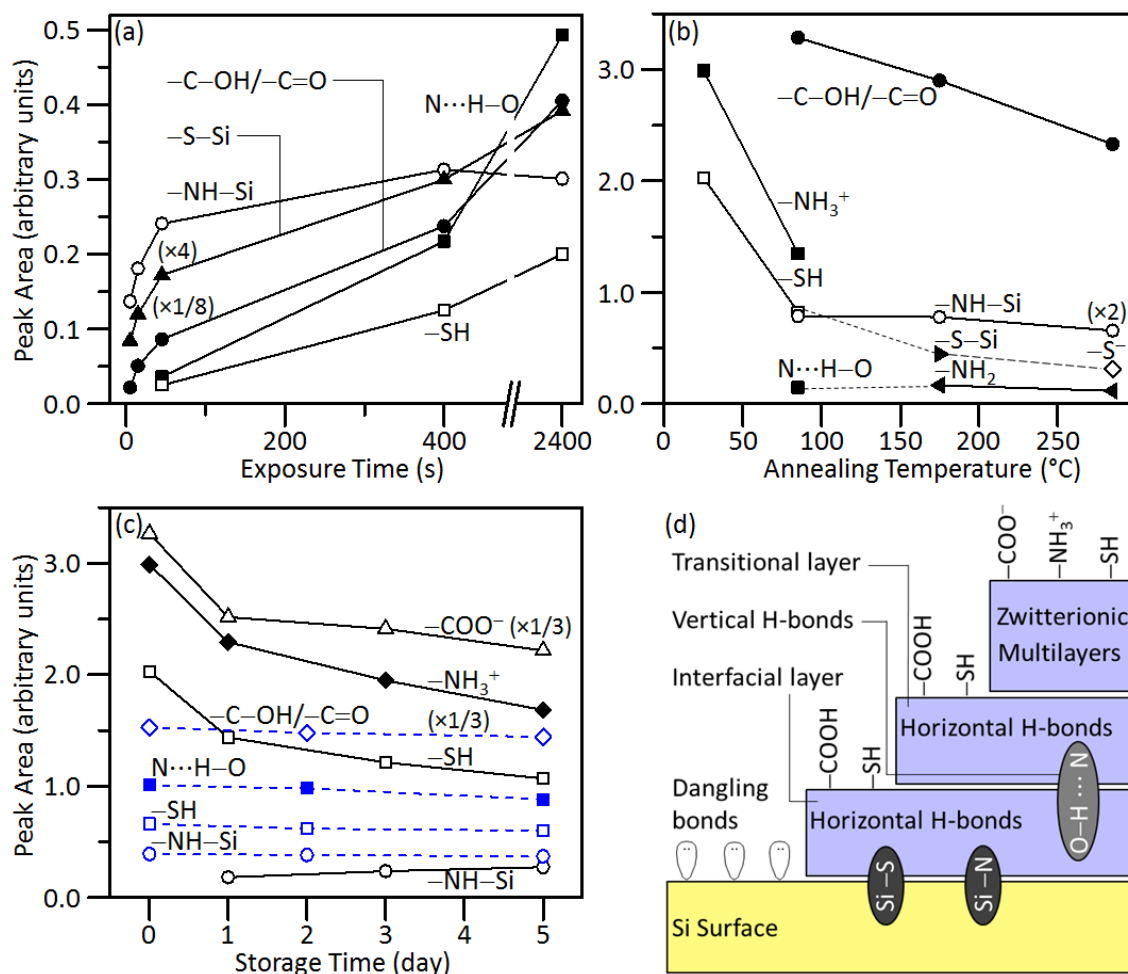


Figure 4.2 Peak areas of various O 1s, N 1s, C 1s, and S 2s features (a) for different cysteine exposure times; and for a multilayer cysteine film (obtained with 5400 s exposure, solid lines) and a transitional layer (obtained by annealing the multilayer film at 85 $^{\circ}C$ for 20 min, dashed lines) as functions of (b) annealing temperature, and (c) storage time in ultrahigh vacuum condition. (d) Schematic bonding model of available surface functional groups, and intra- and interlayer interactions for the interfacial layer, transitional layer and the multilayer film of cysteine on Si(111)7 \times 7.

To determine the thermal stability of the cysteine multilayer film (obtained with the 5400 s exposure) on the Si(111)7 \times 7 surface, we anneal the sample for 600 s at elevated temperatures (85, 175, and 285 $^{\circ}C$) and the sample is then cooled back to room temperature for XPS analysis. Annealing the sample at 85 $^{\circ}C$ evidently reduces the overall spectral intensities (Figure 4.2b), with the zwitterionic cysteine multilayer features significantly removed, which is indicated by the shifts of both the O 1s feature at 531.9 eV and the carboxyl C 1s feature at 288.8 eV to a higher binding energy and by the emergence of two N 1s features at 399.1 eV and 401.1 eV, corresponding to $-NH-Si$ (of the interfacial layer) and the $N\cdots H-O$ H-

bond, respectively (Figure 4.1). Furthermore, in the spectra evolution of the C 1s features of the cysteine film (Figure 4.1c), the position of the carboxyl C 1s feature is stable at 289.2 eV for the first and the second adlayers but it shifts by 0.4 eV to a lower binding energy in the multilayers, while the position of C_β 1s feature (for the thiol-related carbon of the chemisorbed cysteine) is stable at 284.6 ± 0.1 eV for the interfacial and transitional layers. On the other hand, the position of C_α 1s feature is found to shift by 0.5 eV to a higher binding energy for the transitional layer upon H-bond formation. The resulting substantial reduction on in the amount of physisorbed cysteine film is marked by the re-appearance of the N 1s peak at 399.1 eV and the O 1s feature at 532.5 eV, corresponding to the aforementioned chemisorbed adspecies in the transitional and interfacial layers. Further annealing to 175 °C leads to complete desorption of the physisorbed multilayers and the re-appearance of the chemisorption features, including the S 2s feature at 227.4 eV for S–Si bond, and N 1s features at 401.1 eV for N···H–O H-bond and at 400.0 eV for free amino group. Annealing at high temperature also leads to decomposition of the adspecies to S atoms and other dissociated products. Finally, upon annealing at 285 °C, the S 2s peak shifts further to 226.8 eV and the C 1s, N 1s and O 1s features closely resemble those found for the interfacial layer, i.e. those obtained with 45 s exposure. By analogy to the thermal evolution of thiophene on Si(100)²¹⁹ and Pt(111),²²⁰ we attribute the S 2s shift to the formation of atomic S on Si surface as a result of the C–S bond cleavage. By considering the stability of thick cysteine nanofilm, we conclude that the zwitterionic structure can exist up to 85 °C, at which temperature conversion to transitional layer occurs. The transitional layer is more stable and could withstand annealing up to 175 °C. Between 175°C and 285°C, the –HN–Si bond remains intact. At or above 285°C, the interfacial layer begins to break down, leading to dissociated S atoms on the Si surface. While the interfacial layer represents a very stable “permanent” adlayer, the transitional layer can be regarded as a renewable or “semi-permanent” one. The stabilities of these permanent and semi-permanent adlayers provide the key to some interesting potential applications for drug deliveries and medical applications.

We also obtain XPS spectra for the Si 2p feature of the substrate (Appendix B, Figure B3). As expected, these spectra show that the intensity of the Si 2p feature decreases with increasing exposure time of cysteine because of the growing organic layer. Annealing causes partial removal of the cysteine film, which recovers the Si 2p intensity (as the organic layer becomes thinner). Furthermore, the absence of silicon oxide feature at 103 eV confirms the cleanliness of the surface.

We further investigate the stability of the cysteine multilayer film (obtained with the 5400 s exposure) on Si(111)7×7 after storing at room temperature under ultrahigh vacuum condition for 24, 72, and 120 h (Figure B4, Appendix B, and Figure 4.2c). Evidently, after 24 h storage, there are 23%, 23%,

and 29% reductions in the overall intensities for the respective N 1s, O 1s, and S 2s features, when compared to the as-grown multilayer film (obtained with 5400 s exposure). These reductions indicate partial desorption of the thick zwitterionic film in ultrahigh vacuum over time. Interestingly, a weak N 1s feature is also observed at 399.1 eV, which corresponds to the emergence of the N–Si adstructures. By considering the intensity of protonated amino ($-\text{NH}_3^+$) peak, we conclude that the thickness of the zwitterionic cysteine film has been reduced to 44% after 120 h storage (Figure 4.2c). We repeat the same experiment for the transitional layer (obtained by annealing the multilayer film at 85 °C for 20 min) by storage under ultrahigh vacuum condition for 48 and 120 h. As we shown in Figure 4.2c (dash lines), only a 10% reduction after 120 h storage is observed. This confirms that the transitional layer is considerably more stable than the zwitterionic multilayer. The transitional layer therefore offers a potentially robust platform for device fabrication and other applications requiring high vacuum condition at room temperature.

Schematic 4.2d presents a summary of the bonding model of available surface functional groups and intra- and interlayer interactions for the interfacial layer, transitional layer and the multilayer film of cysteine on Si(111)7×7 under ultrahigh vacuum condition obtained by using molecular beam epitaxy technique. Both the interfacial and transitional layers have been saturated by carboxylic acid and thiol groups, which could be used for binding with other adspecies. Since covalent Si–S and Si–N bonds in interfacial layer are stronger than vertical $\text{N}\cdots\text{H}-\text{O}$ H-bond between the interfacial and transitional layers, the interfacial layer should therefore require higher temperature to remove than the transitional layer. In contract to interfacial and transitional layers, the surface of the zwitterionic multilayer is covered by thiol and protonated amino and deprotonated carboxylic acid groups, which leads to even weaker binding with other adspecies than the transitional layer.

To further investigate the nature and formation of these intra- and interlayer H-bonds in the interfacial and transitional layers, we conduct STM studies for the early growth stage. Figure 4.3 shows the corresponding filled-state and empty-state STM images ($45\times 45\text{ nm}^2$), collected, respectively, at -2 and $+2$ V sample bias with a 0.2 nA tunneling current, for a 3 s exposure of cysteine on Si(111)7×7. In these STM images, brightened features generally indicate saturation of the dangling bond sites with the addition of electron density from the adspecies. By comparing the filled-state image (Figure 4.3a, Inset) with the corresponding empty-state image (Figure 4.3b, Inset), we identify that each bright protrusion in a faulted half unit cell (up triangle) or an unfaulted half unit cell (down triangle) represents a single cysteine adspecies on the Si(111)7×7 surface. The line profiles in Figure 4.3c (L2) and 3e (L4) compare the local density of states (LDOS) differences at the marked positions of the corner adatom (AA), restatom (RA)

and center adatom (CA) along the long-diagonal in the reacted unit cell with those of the unreacted unit cell as indicated by the respective line profiles L1 and L3. Evidently, the bright protrusion in the magnified filled-state image (Figure 4.3a, Inset) appears to cover two adatoms across the dimer wall, suggesting a bidentate adsorption arrangement involving a (CA, CA') pair. We use parentheses to indicate a monomer in bidentate arrangement on two adatom sites, with a prime sign for the adatom in a different half unit cell. The corresponding LDOS profile of the bright protrusion along the long-diagonal of the unit cell (Figure 4.3c, L2) further reveals the asymmetric LDOS located at a CA in faulted half unit cell while clearly extending across the dimer wall to a CA in unfaulted half unit cell, when compared to that for an unreacted unit cell (L1). For the unreacted faulted half unit cell and unfaulted half unit cell (Figure 4.3a, Inset), the LDOS at the CA site on the faulted half unit cell side is generally higher than that on the unfaulted half unit cell side and that the LDOS of the AA is higher than that of the CA within either half unit cell (Figure 4.3c, L1). On the other hand, the empty-state image (Figure 4.3b, Inset) for the unreacted unit cell shows all adatoms with essentially the same LDOS (with similar brightness) on both faulted half unit cell and unfaulted half unit cell (Figure 4.3e, L3). A higher LDOS is, again, evident at CA and the intensity is clearly extending into the dimer wall in L4 when compared to L3 (Figure 4.3e). The protrusion for the occupied CA is however not dramatically brighter than other unoccupied atoms (e.g. AA). We will therefore concentrate our discussion on comparison between LDOS profiles along the long diagonals of the reacted (L2) and unreacted (L1) unit cells using the filled-state image in Figure 4.3c.

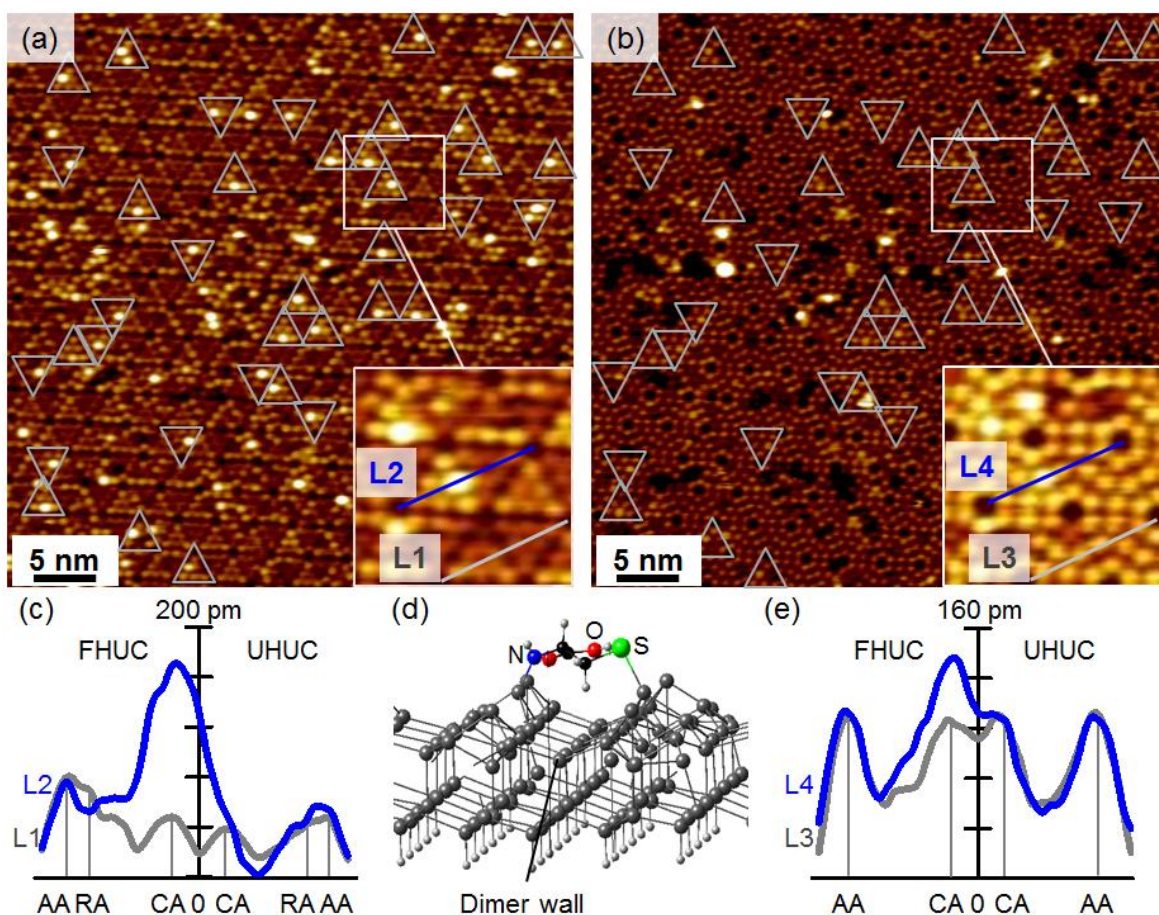


Figure 4.3 (a) Filled-state and (b) corresponding empty-state STM images ($45 \times 45 \text{ nm}^2$) for a 3 s exposure of cysteine on Si(111)7 \times 7 obtained with a sample bias of -2 and $+2$ V, respectively, and a tunneling current of 200 pA, with magnified views ($7.2 \times 7.2 \text{ nm}^2$) shown in insets; and corresponding LDOS profiles along long-diagonals [from corner atom (AA) to restatom (RA) and to center atom (CA)] (c) L1 and L2; and (e) L3 and L4; and (d) perspective view of the equilibrium geometry of a cysteine molecule adsorbed through N–H and S–H dissociation on adjacent center adatoms across a dimer wall on a $\text{Si}_{200}\text{H}_{49}$ slab as obtained by DFT calculation (Appendix B). Cysteine molecules in the faulted (FHUC) and unfaulted half unit cells (UHUC) are marked by up triangles and down triangles, respectively. The separation between two adjacent center adatoms across a dimer wall is 0.7 nm.

Evidently, the LDOS in the reacted unit cell is much higher (~ 135 pm) than the unreacted one (Figure 4.3c). This asymmetric LDOS distribution suggests that cysteine is attached in either a bidentate configuration on the (CA, CA') pair across the dimer wall through short-range interaction or a tilted unidentate configuration with a second longer-range interaction between a CA and one of the functional groups of the adsorbed cysteine molecule. This is consistent with the higher LDOS at the CA site in the reacted unfaulted half unit cell (L2) than that for the unreacted unfaulted half unit cell (L1), the

“spillover” of which into the dimer wall also obscures the “valley” in the dimer wall. On the other hand, our complementary XPS results (Figure 4.1b and Figure 4.1d) indicate a bidentate configuration through short-range interaction between the amino and thiol groups and Si adatoms at the lowest cysteine exposure (5-15 sec). Furthermore, our large-scale DFT study of cysteine adsorption on a model Si(111)7×7 surface as represented by a Si₂₀₀H₄₉ slab concludes that the bidentate adstructure resulting from N–H and S–H dissociative adsorption of cysteine is considerably more stable than any unidentate adstructure. These results therefore provide strong support for our proposed bidentate adsorption structures for cysteine on Si(111)7×7 at the lowest exposure. Given that the separation between the NH₂ and OH groups in cysteine (3.66 Å) is too short to bridge two adatom sites across the dimer wall (6.77 Å), a larger separation between N and S (4.18 Å), obtained via N–H and S–H dissociation, would make such a bidentate configuration quite viable (Appendix B, Figure B5-Figure B7). Figure 4.3d shows a plausible equilibrium adstructure obtained by our DFT calculation, in which the free carboxylic acid group located on the faulted half unit cell side produces an asymmetric LDOS distribution across the dimer wall with a higher LDOS on the faulted half unit cell side. In the corresponding empty-state image (Figure 4.3b), we can also identify similar bright protrusions for the adsorbed cysteine molecule, but with a lower LDOS than that in the filled-state image. Furthermore, statistical analysis of these bright protrusions obtained for the lowest cysteine exposure (3 s) shows that the population of adstructures with the free carboxylic acid group on the faulted half unit cell side is 1.9 times that on the unfaulted half unit cell side, which suggests that formation of the stronger Si–N bond occurs more favourably on the more reactive faulted half unit cell.

The hydrogen atoms resulted from dissociative adsorption of cysteine are believed to adsorb on the restatom sites. This is in accord with previous studies of H₂ and NH₃ adsorption on Si(111)7×7 by Razado et al.²²¹ and by Zang et al.,²²² who reported that the dissociated hydrogen atoms adsorb on restatom sites. As the topmost layer of the Si(111)7×7 surface (containing the adatoms) is more electrophilic in nature while the restatom layer is nucleophilic, the hydrogen atom would therefore adsorb on the nucleophilic restatom sites. The adsorption of hydrogen on restatom sites has also been observed for dissociative adsorption of other organic molecules, including glycine and glycyglycine, on Si(111)7×7.^{96,99}

To follow the self-assembly process of adsorbed cysteine molecules, we show a 30×30 nm² empty-state image for a 25 s exposure of cysteine on Si(111)7×7 in Figure 4.4. While both empty-state and filled-state images of adsorbed cysteine on Si(111)7×7 appear similar (Figure 4.3a and Figure 4.3b), the empty-state images are more straightforward to use for identifying the distribution of adspecies over the

unit cells for higher cysteine exposures than the filled-state images. Evidently, a higher cysteine exposure increases the population of multiple adjacent bright protrusions, from dimers to trimers to multimers (Figure 4.4a), when compared to very low exposure (Figure 4.3b). Closer examination reveals four types of dimers (D) and two types of trimer configurations (T) at this exposure: (D1) CA-CA and (D2) AA-CA, both within the same half unit cell (faulted half unit cell or unfaulted half unit cell); (D3) AA-AA' and (D4) CA-CA' across the dimer wall; (T1) CA-AA-CA (triangular trimer); and (T2) CA-CA-CA' (linear trimer). The formation of these clusters is clearly mediated by H-bonds. The CA-AA' (across the dimer wall) dimer configuration is not observed, which is consistent with the large separation between CA and AA' (10.25 Å) that is not conducive to H-bond formation.

Quite a few direct STM observations of the N···H–O H-bond in the self-assembly of amino acids have been reported in the literature.⁹⁶ The LDOS profiles along the long diagonals of the unit cells containing the (CA, CA') monomer (Figure 4.4c, L2), CA-CA' dimer (Figure 4.4g, L3), and CA-CA-CA' trimer (Figure 4.4j, L4), in comparison to that for an unreacted 7×7 unit cell (Figure 4.4a, L1), show the respective LDOS for one (L2), two (L3), and three (L4) cysteine molecules attached on adjacent CA adatoms. While the L2 profile of the (CA, CA') monomer (Figure 4.4m, similar to L4 in Figure 4.3e) shows one bidentate cysteine molecule covering a (CA, CA') pair across the dimer wall, the L3 profile of the CA-CA' dimer (Figure 4.4l) clearly shows a valley in the LDOS at the dimer wall, with nearly the same LDOS at the CA sites in both faulted half unit cell and unfaulted half unit cell.

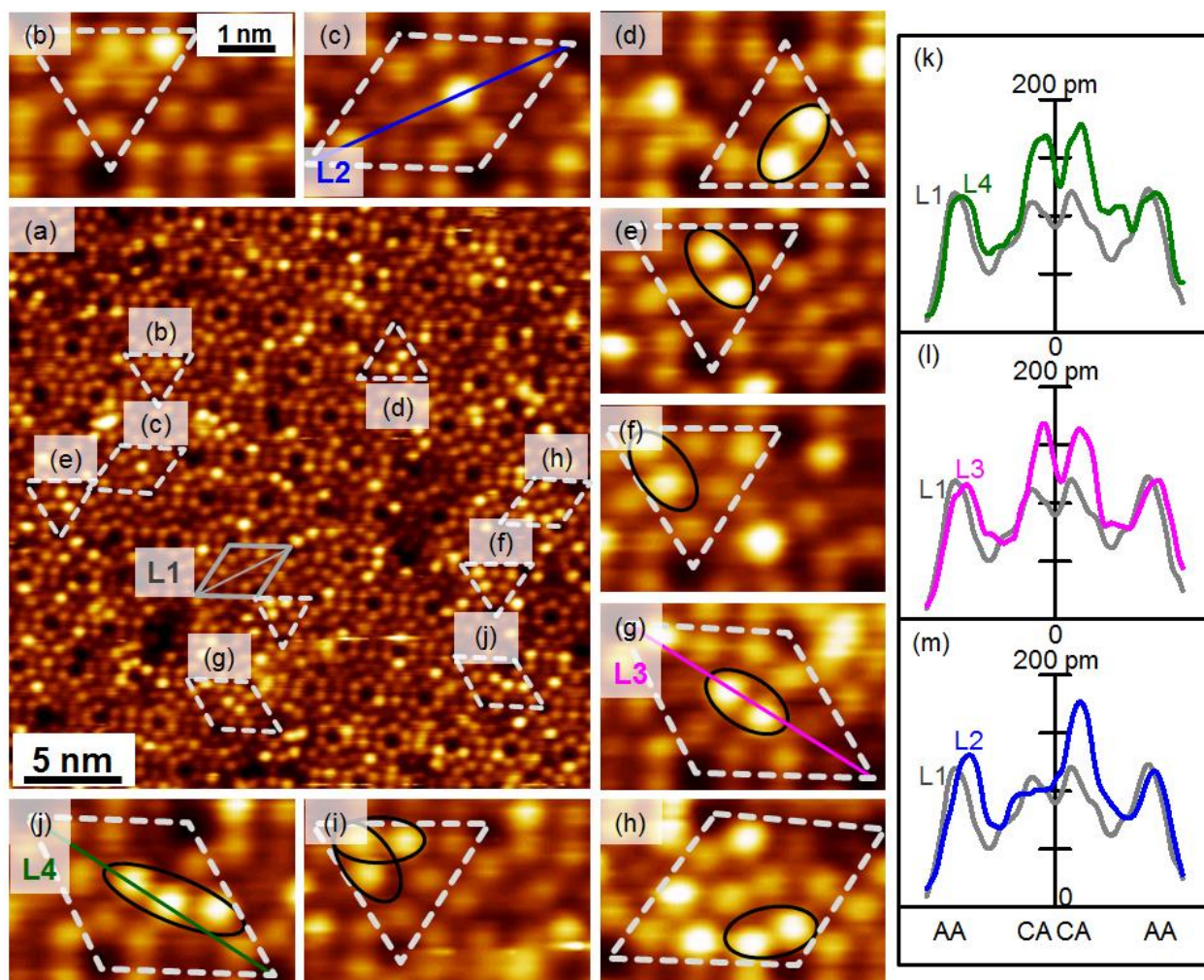


Figure 4.4 (Color online) (a) Empty-state STM image ($30 \times 30 \text{ nm}^2$) of a 25 s exposure of cysteine on Si(111) 7×7 recorded with a sample bias of +2 V and a tunneling current of 200 pA; magnified images of a bidentate cysteine molecule at (b) (AA, AA') and (c) (CA, CA') sites; H-bond mediated dimers formed from different unidentate cysteine molecules in (d) CA-CA in faulted half unit cell and (e) in unfaulted half unit cell, (f) AA-CA, (g) CA-CA' (across the dimer wall), and (h) AA-AA'; self-assembled cysteine trimers in (i) CA-AA-CA and (j) CA-CA-CA' sites on Si(111) 7×7 surface. LDOS profiles along the long-diagonals (m) L2 for monomer in (c), (l) L3 for dimer in (g), and (k) L4 for trimer in (j), all compared with the LDOS profile L1 of the unreacted unit cell in (a).

To complement our experimental finding, we also extended our large-scale DFT calculations to investigate different cysteine dimer adsorption configurations on Si(111) 7×7 surface (Appendix B). These dimer configurations are based in part on those of the gas-phase dimers, shown in the order of most stable to least stable in Scheme 4.1c-g. In particular, there are five possible configurations for gas-phase cysteine dimers produced by formation of two $\text{O} \cdots \text{H}-\text{O}$ H-bonds (Scheme 4.1c), two $\text{S} \cdots \text{H}-\text{N}$ H-bonds

(Scheme 4.1g), one O \cdots H–O and one N \cdots H–O H-bonds (Scheme 4.1d), and of one of the following two single H-bonds: S \cdots H–O (Scheme 4.1e), and N \cdots H–N (Scheme 4.1f) between two adjacent cysteine molecules. The most stable dimer involves double O \cdots H–O H-bonds between their carboxylic acid groups (Scheme 4.1c), while the least stable dimer contains just two S \cdots H–N H-bonds between the amino and thiol groups (Scheme 4.1g). (The bond energy for O \cdots H–O H-bond is 0.5 eV lower than that for S \cdots H–N H-bond). The nominal (donor-acceptor) bond distance for a H-bond categorized as strong (mostly covalent), moderate (mostly electrostatic), and weak (electrostatic) bonds are 2.2-2.5 Å, 2.5-3.2 Å, and 3.2-4.0 Å, respectively.²²³ As expected, the calculated H-bond distances in the most stable dimer formed by double O \cdots H–O H-bonds between their carboxylic acid groups are discernibly shorter than that of strong H-bond due to the formation of cyclic dimer.

On the Si(111)7 \times 7 surface, dimer formation is affected by steric hindrance on the adsorbed cysteine molecules exerted by the surface atoms, which rule out many of the gas-phase dimer configurations shown in Scheme 4.1. Our DFT calculations suggest that the N \cdots H–O H-bond is a favorable H-bond that would lead to acceptable cysteine dimer on adjacent CA-AA adatoms without torsion on the Si(111)7 \times 7 surface. We overlay plausible configurations of such a cysteine dimer on the corresponding STM images of a CA-CA (Figure 4.5a) and CA-AA pair (Figure 4.5b). Perspective views of the corresponding equilibrium structures of these “torsion-free” dimer adsorption configurations are shown in Figure 4.5c and Figure 4.5d. In these configurations, cysteine molecules are bound to the surface in unidentate fashion through S–H or N–H dissociative adsorption with the formation of the respective S–Si or N–Si bond. These unidentate adspecies allow the remaining unreacted functional groups free to interact with functional groups from a second cysteine adsorbed in an adjacent adatom site. This unidentate adsorption in effect leads to lateral interactions between a free amino group and a free carboxylic acid group, producing the N \cdots H–O H bond. Our DFT study further shows that the donor-acceptor distances for these N \cdots H–O H-bond configurations is 2.5-2.9 Å, in good accord with bond length of moderately strong H-bonds.

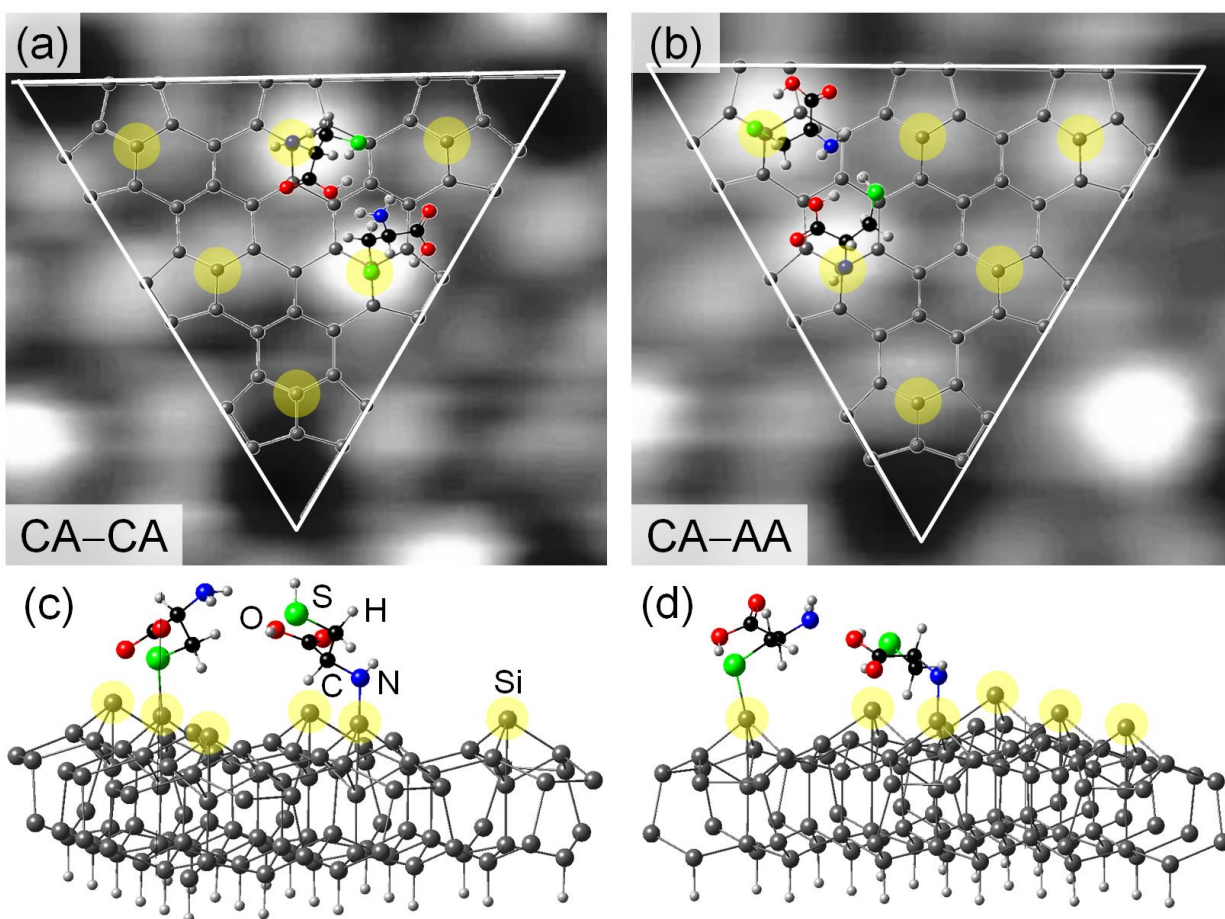


Figure 4.5 (a, b) Top views and (c, d) perspective views of equilibrium structures of cysteine dimer on (a, c) CA-CA and (b, d) CA-AA sites on a Si₂₀₀H₄₉ slab (used as a model Si(111)7×7 surface), as obtained from the DFT calculations, superimposed onto corresponding magnified empty-state STM images in (a, b). Si adatoms are highlighted by larger yellow circles for clarity.

Figure 4.6a-d show the empty-state images for four cysteine exposures on Si(111)7×7 in the build-up toward the transitional layer during the early growth stage (i.e. from 5 to 60 s exposure). Using the full 50×50 nm² images (of approximately 320 7×7 unit cells), we count the numbers of individual bidentate monomers, unidentate dimers and trimers in order to estimate their relative surface concentrations (i.e., the fractions of available surface sites that are occupied by the respective cysteine configurations) and the total coverage, shown in Figure 4.6e. Evidently, growth begins with just the monomer and dimer populations on the 7×7 surface for the 5 s exposure (Figure 4.6a), with the relative surface concentration for monomers being discernibly higher than that for dimers, until they become nearly equal for the 20 s exposure. The surface concentration of the monomers increases sharply by 64% from 5 s to 10 s

exposure and then decreases slowly by 10% from 10 s to 60 s exposure (Figure 4.6e, bottom panel). As the exposure increases, the relative surface concentrations for dimers and trimers increase gradually. The bar chart in Figure 4.6e (middle panel) shows the relative surface concentrations of various types of bidentate monomer configurations [corner adatom-corner adatom (AA, AA') vs center adatom-center adatom (CA, CA'), both across the dimer wall], with increasing cysteine exposure. At the initial growth stage (5 s exposure), the relative surface concentration of the monomers with the (CA, CA') configuration is found to be higher than that with the (AA, AA') configuration, suggesting that the former configuration is more stable. This is consistent with the results from our large-scale DFT calculation, which also shows that the calculated adsorption energy of the adsorbed bidentate cysteine monomer on (CA, CA') is 0.13 eV lower than that of the adsorbed cysteine on (AA, AA') (Appendix B, Figure B7). On the other hand, the population ratio of (CA, CA') to (AA, AA') is decreasing gradually as a result of formation of dimers and trimers configurations. For the lowest exposure (5 s) of cysteine, the relative surface concentrations of the more popular types of dimer configurations follow the ordering: CA-AA > CA-CA > CA-CA' > AA-AA' (Figure 4.6e, top panel). There are steady increases in the CA-AA and AA-AA' surface concentrations, while the CA-CA and CA-CA' surface concentrations appear to be leveling off with increasing exposure to above 10 s, which could be the result of increasing population of the trimer (CA-CA-CA') configuration. This evolution of the dimer growth is consistent with the more reactive CA sites being occupied first. Based on our STM and XPS results, the coverage-dependent adsorption configurations of cysteine molecules on the Si(111)7×7 surface play an important role in the observed evolution of the surface concentrations of these multimers. At very low cysteine exposure, preferential bidentate monomer adsorption on the (CA, CA') sites (across the dimer wall) is observed, while formation of H-bond between the unidentate cysteine molecules becomes predominant at higher exposure. Moreover, at higher exposure (60 s, marked by circles in Figure 4.6d), we can see the emergence of brighter, larger protrusions, which suggest the on-set of the translational layer growth, with larger clusters arising from formation of vertical H-bonds between a free carboxylic acid group from the first adlayer and an amino group of the second adlayer. Furthermore, the growth of the translational layer begins before formation of the complete interfacial layer.

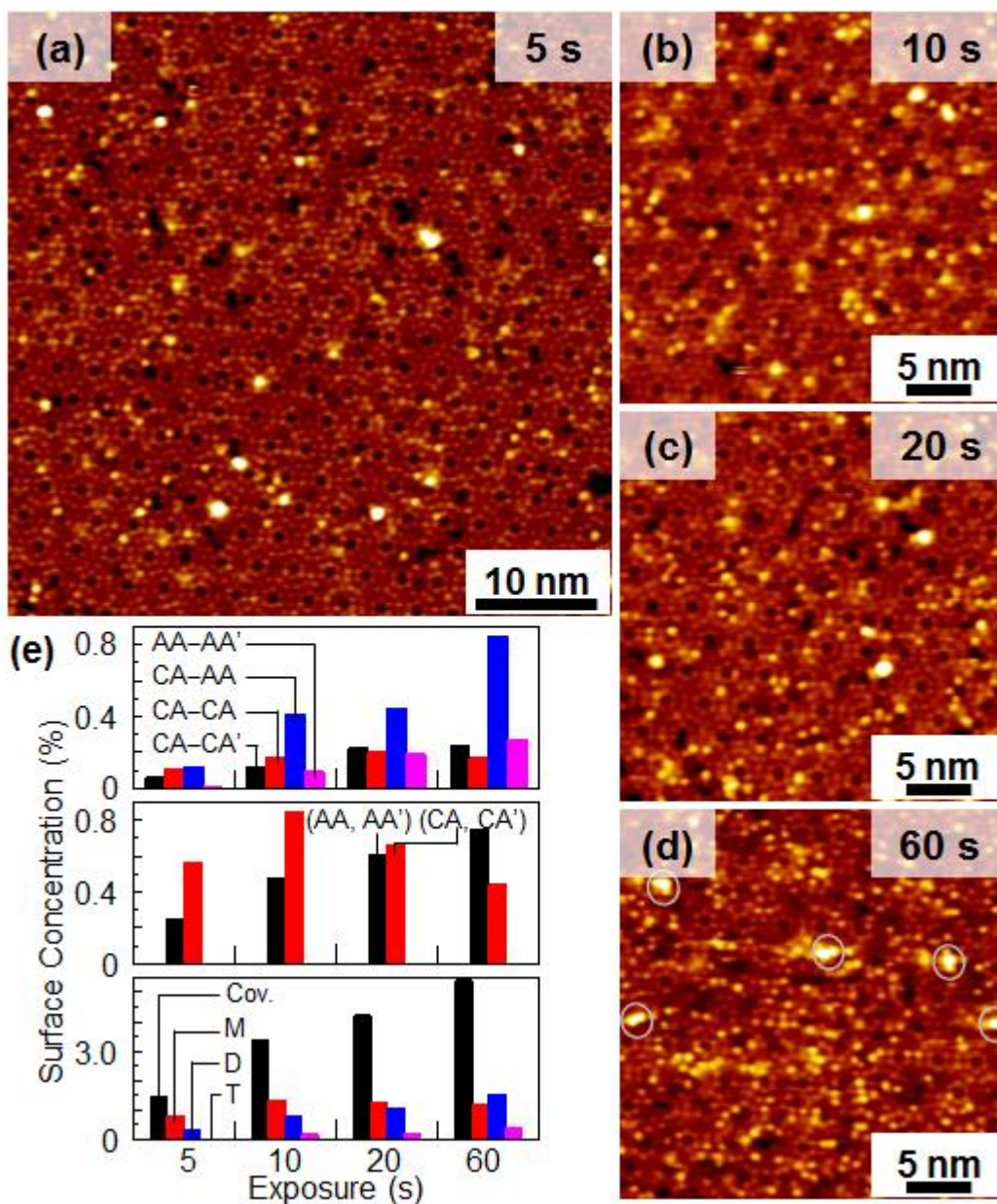


Figure 4.6 STM empty-state images collected at a sample bias +2 V and a tunneling current of 200 pA for cysteine exposures of (a) 5 s, (b) 10 s, (c) 20 s, and (d) 60 s on Si(111)7x7 surface; and (e) lower panel: the corresponding total coverage (Cov.) and the relative surface concentrations for monomer (M), dimer (D) and trimer (T) configurations, middle and upper panels: various type of respective M and D configurations on Si(111)7x7 sites.

4.4 Summary

The growth evolution of cysteine on Si(111)7×7 at room temperature in ultrahigh vacuum condition has been studied by combining XPS chemical-state data with STM LDOS images. Three N 1s features for N–Si at 398.9 eV, N··H–O at 401.1 eV, and –NH₃⁺ at 401.8 eV are found to emerge sequentially with increasing deposition time, which mark the onsets of three distinct growth stages. In the formation of the interfacial layer (first stage), cysteine is found to undergo N–H and S–H dissociative adsorption and form a bidentate adstructure across the dimer wall of the 7×7 surface. Both filled-state and empty-state STM images reveal the presence of bright protrusions over the (CA, CA') adatom sites across the dimer wall, which correspond to asymmetric LDOS resulting from the off-to-side orientation of the free carboxylic acid group. As the exposure increases, more unidentate cysteine adstructures bonded through Si–N or Si–S are found. The corresponding bright protrusions begin to self-assemble into dimer, trimer, and higher-order multimer configurations. The formation of these self-assembled arrangements is driven by horizontal H-bonding between a free carboxylic acid group and an amino group of adjacent cysteine molecules. These unidentate adstructures leave the carboxylic acid group free to engage other incoming moieties, and the interfacial layer is found to be very stable and break down only at 285 °C (the maximum annealing temperature employed in the present work). For a higher exposure, we observe the formation of vertical N··H–O H-bond, signaling the onset of a transitional layer (second stage),^{131,133,205} which is found to be stable to 175°C. The final stage is marked by formation of cysteine multilayer film in zwitterionic form (NH₃⁺CHCH₂SHCOO⁻). This study shows that a highly reactive Si surface, full of Si dangling bonds, can be easily converted to different types of bio-organic surfaces. These surfaces, with both carboxylic acid and thiol groups free to serve as receptor sites for incoming moieties, offer potential applications in biosensing and heavy metal detection. As the transitional layer is held to the interfacial layer by weak H-bonding, this layer offers a “renewable” platform for sensing application.

Chapter 5

Biofunctionalization of Si(111)7×7 by L-Methionine

5.1 “Universal” Three-Stage Growth of α -Amino Acids on Si(111)7×7 as Mediated by Surface Hydrogen Bonding

5.1.1 Introduction

Molecular interactions of biomaterials with semiconductor surfaces have attracted much recent attention because of their potential applications in biosensors, biocompatible materials, and biomolecule-based electronic devices.^{66,67,68,69} Among the most fundamental biomolecules, amino acids and nucleotides are the basic building blocks of the larger biological materials such as proteins, peptides, and DNAs. The amino acids found in proteins are generally categorized by their structures: (a) aliphatic amino acids, including monoamino-monocarboxylic acids, monoamino-dicarboxylic acids and their amides, amino acids with basic side groups, and sulfur-containing amino acids; (b) aromatic amino acids; and (c) heterocyclic amino acids.¹⁰² Alpha amino acids are bio-organic molecules containing a carboxylic acid ($-\text{COOH}$) group and an amino ($-\text{NH}_2$) group, which are separated by at least one carbon segment (α -carbon). There are twenty different standard amino acids ($\text{NH}_2\text{C}_\alpha\text{HRCOOH}$), which differ from one another with a unique functional group in the side chain (R group) attached to the α -carbon.

One of the most challenging questions when studying the behaviour of amino acids on a metal or semiconductor surface is “What is their chemical state upon adsorption?” Depending on the physical phase, the most stable chemical states of amino acids are zwitterionic state ($\text{NH}_3^+\text{CHR}\text{COO}^-$) for the solid and liquid phases, non-zwitterionic or neutral state ($\text{NH}_2\text{CHR}\text{COOH}$) for the gaseous phase, and cationic ($\text{NH}_3^+\text{CHR}\text{COOH}$) and anionic states ($\text{NH}_2\text{CHR}\text{COO}^-$) for solutions. On a metal or semiconductor surface under ultrahigh vacuum (UHV) condition, formation of these states during adsorption and film growth of amino acids depends on the surface reactivity and the growth conditions, notably the substrate temperature and dosage of the adsorbates.

Adsorption of aliphatic amino acids (glycine,^{103,104,105} alanine,^{106,107,108,109,110,111} glutamic acid,^{112,113,114,115} and lysine^{116,117,118}), sulfur-containing amino acids (cysteine^{119,120,121} and methionine^{122,123,124,125,126}), aromatic amino acids (tyrosine^{127,128}), and heterocyclic amino acids (proline^{129,130}) on various well-ordered single-crystal metal surfaces in UHV condition have attracted much attention in surface science and nanotechnology in the two past decades. These studies are important not only to understanding fundamental interactions of larger biological molecules (such as

proteins and peptides), but also to fabricating bio/nano-devices for biomedical sensing and molecular electronics. The development of future hybrid organic-inorganic interfaces also critically depends on the nature of the substrate surface and particularly the type of available bonding interactions that are responsible for producing stable chemical states of amino acids, and ultimately for controlling the orientation, conformation, and two-dimensional organisation of the bio-organic adspecies on the inorganic surface. For example, the bonding and orientation of adsorbed anionic form of glycine, as the simplest and non-chiral amino acid, on Cu(110)¹⁰³ at room temperature was found to depend on the coverage. Glycinate was initially bonded through both O atoms of the carboxylate group ($-\text{COO}^-$) at a low coverage, but it anchored through the N atom of the amino group and one O atom of the carboxylate group at higher coverage. Alanine, the simplest chiral amino acid, and lysine both adsorbed in anionic form on Cu(110)^{108,116,117} and Cu(001)^{106,118} surfaces at room temperature, which was structurally analogous to glycine adspecies with bonding via the O atom of the carboxylate group and the N atom of the amino group. The adsorption geometries of glutamic acid, with monoamino and dicarboxylic acid functional groups, on the less reactive Ag surface were also found to depend on the coverage. These included a mixture of the zwitterionic form, and neutral and anionic states on different Ag surface planes such as (100), (111), and (110).^{112,113,114}

Additional reactive side groups, such as those containing sulfur, in selected amino acids could contribute to bonding to the surface significantly. The room-temperature adsorption of cysteine, which contains a thiol ($-\text{SH}$) group, on Cu(111),¹¹⁹ Ag(111),¹²⁰ and Au(110)¹²¹ normally involved binding to the metal surface in the form of a thiolate. Methionine, which contains a thiol ether ($-\text{CH}_2-\text{S}-\text{CH}_3$) group, was found to adsorb on Au(111)^{122,125} and Ag(111)¹²³ surfaces in the zwitterionic form. The chemical state of the anchoring methionine on Cu(110)¹²⁶ surface also depended on the coverage. Analogous to most adsorbed amino acids on copper surfaces, methionine adsorbed in the anionic form ($\text{NH}_2\text{C}_\alpha\text{HCH}_2\text{CH}_2\text{SCH}_3\text{COO}^-$) through interaction of the S and/or O atoms or interaction of the O atom of the carboxylate group and the N atom of the amino group. Adsorption of tyrosine, an amino acid containing a phenol group, on a relatively unreactive Ag(111) surface exhibited a tilted orientation of the phenol moiety in the zwitterionic state.¹²⁸ As an amino acid containing a 5-membered ring, proline adsorbed on Au(111)¹³⁰ in a mixture of the neutral, zwitterionic, and anionic forms, while prolate adsorbed on Cu(110)¹²⁹ through a tridentate bonding interaction via two O atoms of the carboxylate and the N atom of the amino group.

In spite of the large number of studies of adsorbed amino acids on various surfaces of single-crystal metals, only a few investigations of their adsorption on semiconductor surfaces have been reported. A

major impetus behind the research in biological surface chemistry of semiconductors is their potential to convert biological information directly into electrical signals. Unlike the long-range, non-covalent interactions between adsorbed amino acids and metal surfaces, the availability of directional dangling bonds on semiconductor surfaces make feasible direct covalent bonding with biomolecules, thus providing the opportunity to create a highly stable, multifunctional interface. Furthermore, interactions of amino acids with metal surfaces lead to generally weak zwitterionic form or to binding through both amino and carboxylic acid groups in anionic state, which consumes all the free functional groups and therefore leaves little prospect in building a biological interface. Of all the semiconductors, silicon is by far the most heavily studied because of its widespread use in the microelectronic industry and nanotechnology applications.⁶⁹ The 7×7 reconstruction of the Si(111) surface is one of the most popular templates used for anchoring both organic and inorganic adsorbates via 18 directional dangling bonds, over six (electron-deficient) adatoms and three (electron-rich) restatoms per each of the faulted and unfaulted half unit cells, and one remaining dangling bond shared among the four corner-hole sites.²⁹ The Si surface therefore offers a variety of interesting reaction sites, with several different site-to-site separations relevant to bio-organic molecules, for exploring the reactivity and selectivity of site-specific processes especially for amino acids containing multiple functional groups.

The second challenging question when investigating amino acids is “What are the driving forces and film growth mechanisms for their adsorption on semiconductor surfaces?” In addition to covalent bonding with the dangling bonds of Si adatom sites, amino acids also offer novel hydrogen bonding among themselves due to the amino and carboxylic acid groups. Hydrogen bonding, both intralayer and interlayer, therefore introduces new film growth and biofunctionalization mechanisms. Our previous studies have focused on the early adsorption and growth processes from submonolayer to thin film of several benchmark proteinogenic biomolecules, including glycine (the simplest non-chiral amino acid), alanine (the simplest chiral amino acid), cysteine (the simplest amino acid with a thiol group), and glycylglycine (a dipeptide of glycine), on Si(111) 7×7 surface at room temperature under UHV conditions.^{98,131,205} Alanine ($\text{NH}_2\text{C}_\alpha\text{HCH}_3\text{COOH}$) corresponds to glycine ($\text{NH}_2\text{CH}_2\text{COOH}$) with the replacement of a methanediyl H atom by a methyl group, while methionine ($\text{NH}_2\text{C}_\alpha\text{HCH}_2\text{CH}_2\text{SCH}_3\text{COOH}$) represents a cysteine ($\text{NH}_2\text{C}_\alpha\text{HCH}_2\text{SHCOOH}$) with the thiol group replaced by a thiol ether group. The addition of methionine data presented here would provide a sufficient set of building-block biomolecules, in terms of the varieties of functional groups and of available molecular lengths, to allow us to deduce a common set of basic bonding rules operative on the 7×7 surface. If we define the molecular length as the separation between the hydroxyl O atom and the

farthest non-H atom along the carbon chain backbone in the molecule, then we have a wide range of molecular lengths from glycine (3.70 Å), alanine (3.68 Å), cysteine (4.96 Å), methionine (7.40 Å) and glycylglycine (6.10 Å). The lengths of these molecules are obtained for their most stable conformers in the isolated molecule case (i.e. the gas phase) by large-scale quantum mechanical calculations. Accommodating the different sizes of these aliphatic biomolecules (with molecular lengths ranging from 3.68 to 7.40 Å) geometrically to the separations as imposed by various Si surface adatom dangling-bond sites is expected to lead to simple restrictions for surface bonding on the 7×7 surface and therefore interesting biofunctionalization outcomes. For small aliphatic amino acids, e.g., glycine, alanine, and even cysteine, adsorption of more than one molecule within a half unit cell is physically viable, unlike the other larger biomolecules such as methionine and glycylglycine. This is expected to serve as an important criterion in guiding the long-range interactions.

To date, there is no study on the interaction of L-methionine with any semiconductor surface at any temperature. In the present study, we deposit L-methionine on Si(111)7×7 at room temperature under UHV conditions, and follow the early film growth from submonolayer to multilayers and the subsequent thermal evolution by using a surface-sensitive technique, X-ray photoelectron spectroscopy (XPS), to quantify the chemical-state composition. Together with large-scale ab-initio quantum mechanical computation, particularly based on density functional theory (DFT) with van der Waals corrections (D2), we develop precise models of the adsorption geometries at different growth stages. We demonstrate that the driving force behind this biomolecular film growth is surface-mediated hydrogen bonding. Along with results on the aforementioned benchmark proteinogenic biomolecules, our results for methionine also support a “universal” three-stage growth process, which involves initial N–H dissociative adsorption followed by an intermediate transitional layer formation involving hydrogen bond, and the final formation of a zwitterionic multilayer film. Like the other benchmark proteinogenic biomolecules, thermal evolution of a thick methionine film also follows the reverse trend, with the sequential desorption of weakly bonded zwitterionic multilayer, “semi-permanently bonded” transitional layer, and the strongly covalently bonded interfacial layer. Collectively, these results allow us to develop a set of basic surface bonding rules regarding these benchmark proteinogenic biomolecules.

5.1.2 Experimental Details and DFT Calculations

The experimental procedure has been discussed in detail in Chapter 2. Furthermore, the organic molecular beam epitaxy chamber was used to deposit L-methionine with a low-temperature organic effusion cell (Dr. Ebert MBE-Komponenten GmbH). After outgassing thoroughly overnight at 100 °C,

L-methionine powder (99.5% purity, Fluka), with a normal melting point at 280 °C, was exposed to the 7×7 surface at room temperature with the effusion cell held at 130 °C²⁰⁸ and the deposition chamber pressure at 2×10^{-9} mbar. After the methionine exposure on the Si surface, XPS spectra of the Si 2p, N 1s, C 1s, O 1s, S 2p and S 2s regions were recorded with an energy resolution of 0.7 eV full width at half maximum (for the Ag 3d_{5/2} photoline at 368.3 eV). We have also measured the core-level spectra of L-methionine powders, in which case an electron neutralizer was employed to compensate the minor charging during the measurement. The binding energy scale of the powder spectra was calibrated with respect to that of the corresponding multilayer films by aligning the main N 1s feature (Appendix C, Figure C1). For the thermal evolution experiments, as-grown thick methionine films (obtained with a 2400-s exposure) were annealed sequentially by resistive heating of the sample holder to 85 or 175 or 285 °C, each for 600 s. The chemical-state compositions of the remaining layers were then determined by XPS analysis.

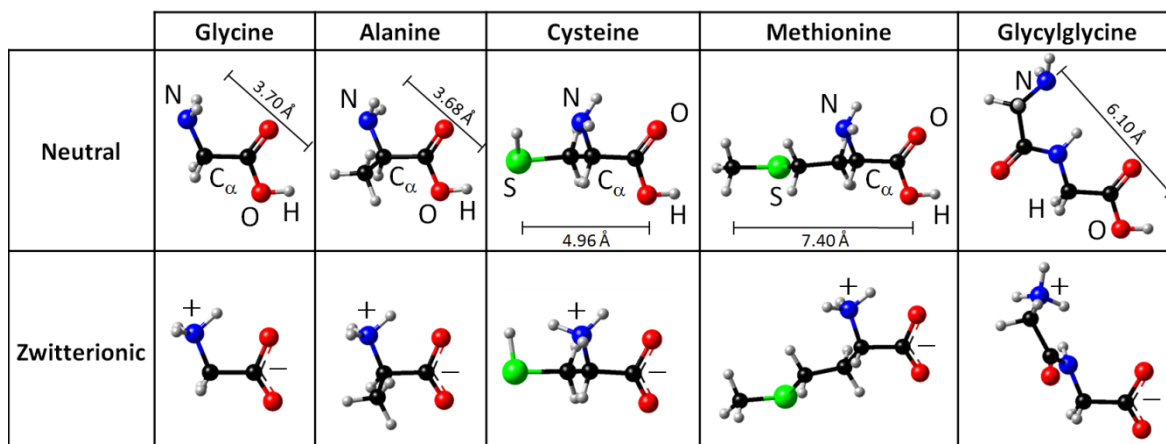
To complement the experimental results, we performed DFT-D2 calculations¹⁷⁶ with the inclusion of van der Waals interactions to model the equilibrium geometries of plausible adsorption structures of L-methionine on one complete unit cell of Si(111)7×7 at various growth stages, including the interfacial layer, transitional layer, and zwitterionic multilayer. The DFT-D2 calculations also provided more accurate simulation of hydrogen bonds involved in di-molecular configurations of the five benchmark proteinogenic biomolecules on the 7×7 surface (and in the gas phase). The details of DFT calculations have been discussed in detail in the Chapter 2.

In this study, we used an optimized structure of the dimer-atom-stacking fault (DAS) model for the Si(111)7×7 substrate,^{29,28} which contained a faulted and an unfaulted half unit cells, each included 3 corner adatoms (AAs) and 3 center adatoms (CAs) in the topmost layer, and 3 restatoms (RAs) in the second layer (Appendix C, Figure C2). A periodic repeating slab consisting of 200 Si atoms, distributed in the reconstructed topmost layer and two underlying Si bilayers with a 5.419 Å lattice constant of the Si bulk, and a vacuum gap of 12 Å was used to represent the Si(111)7×7 surface, and the bottom layer of the Si slab was terminated by 49 H atoms. An adsorbate molecule was placed on the topmost layer of the Si slab to simulate covalent binding to Si adatom in the interfacial layer. To find the most stable equilibrium configuration, we first calculated a large variety of plausible adsorption configurations of methionine (or other proteinogenic biomolecules) in unidentate geometry (bonding through the amino or carboxylic acid group) on specific sites on the Si(111)7×7 surface (AA and CA sites on both the faulted and unfaulted half unit cells, and across the dimer wall). A selection of the most stable geometries was then made on the basis of their adsorption energies after optimization (Appendix C). To understand the formation of

transitional and zwitterionic layers, additional molecules were included into the equilibrium geometry of the interfacial layer. The positions of all adsorbed molecules and Si atoms were relaxed during the DFT-D2 calculations. The adsorption energy E_{ad} is defined as $E_{\text{ad}} = (E_{n\text{M}+\text{Si}_{200}\text{H}_{49}} - E_{\text{Si}_{200}\text{H}_{49}} - nE_{\text{M}})$, where $E_{n\text{M}+\text{Si}_{200}\text{H}_{49}}$, $E_{\text{Si}_{200}\text{H}_{49}}$ and E_{M} are the total energies of the adsorbed molecule on the $\text{Si}_{200}\text{H}_{49}$ slab, the $\text{Si}_{200}\text{H}_{49}$ slab, and the isolated molecule, respectively, and n is the number of admolecules. The H-bond energy $E_{\text{H-bond}}$ for a di-molecule in the gas phase is defined as $E_{\text{H-bond}} = (E_{\text{M}\cdots\text{M}} - 2E_{\text{M}})/m$, where $E_{\text{M}\cdots\text{M}}$, and E_{M} are the total energies of the di-molecule and the isolated molecule, respectively; and m is the number of H bonds.

5.1.3 Results and Discussion

Scheme 5.1 shows the equilibrium geometries of neutral and zwitterionic forms of the five benchmark proteinogenic biomolecules: glycine, D-alanine, L-cysteine, L-methionine, and glycyglycine, in their isolated molecule state, that are obtained by DFT-D2 calculations. In our earlier study of glycine on $\text{Si}(111)7\times 7$,²⁰⁵ we observed the existence of a transitional layer between the interfacial layer and zwitterionic layer for the first time. In our follow-up study of glycyglycine on the 7×7 surface,¹³¹ we proposed a growth model involving sequential formation of the covalently bonded interfacial layer, the hydrogen-bond mediated transitional layer, and the zwitterionic multilayer. In our recent work on cysteine on $\text{Si}(111)7\times 7$,⁹⁸ we again observed a three-stage growth process, from chemisorbed interfacial layer (first stage) to transitional layer (second stage) and to zwitterionic multilayer film (third stage). For the smallest chiral α -amino acid, alanine, the same growth sequence prevailed and we found the formation of interlayer hydrogen bonding between the transitional and interfacial layers.⁹⁷ To further investigate the universality of the growth process of the aforementioned α -amino acids, we first provide XPS analysis of the other sulfur-containing proteinogenic amino acid, methionine, and follow the chemical-state evolution of its nanofilm growth from submonolayer to multilayers on $\text{Si}(111)7\times 7$. We then compare the experimental data of all five benchmark proteinogenic biomolecules (shown in Scheme 5.1) with the respective large-scale DFT-D2 calculations, in order to provide a complete description of the adsorption structures and the underlying nanofilm growth mechanism on the Si surface.



Scheme 5.1 Ball-and-stick models of neutral and zwitterionic equilibrium structures of isolated aliphatic proteinogenic biomolecules: Glycine, D-alanine, L-cysteine, L-methionine, and glycylglycine. These structures are generated by DFT-D2 calculations and the molecular lengths (i.e. the separation between the hydroxyl O atom and the farthest non-H atom along the carbon chain backbone) are shown in angstrom (Å). No change in the molecular length of the zwitterionic structure from that of the neutral structure is found for all biomolecules, except for methionine with a 3% increase.

5.1.3.1 Nanofilm Growth of Methionine on Si(111)7×7

Figure 5.1 shows the O 1s, N 1s, C 1s, and S 2s spectra of methionine as a function of exposure time at room temperature and upon annealing the thickest methionine film to elevated temperature. The corresponding peak positions and assignments obtained for the fitted features are summarized in Table C1 (Appendix C), while the changes in their relative intensities are given in Figure C3 (Appendix C). Instead of one dominant feature for the lowest exposure (30 s), a second N 1s peak is found to emerge at a higher binding energy for the 90 s exposure (Figure 5.1b). This is in good accord with the presence of the O–H···N hydrogen bond at 401.0 eV (where we use “···” to denote a H-bond), which is found to be common in the chemisorption of α -amino acids (e.g., cysteine, glycine, and alanine).^{98,205} The α -amino acids and peptides undergo N–H dissociative adsorption on Si(111)7×7 surface at room temperature via N–H bond cleavage, as indicated by the N–Si N 1s feature located at a lower binding energy (398.7 eV). The absence of any feature related to neutral amino group (–NH₂) at ~400.0 eV²⁰⁶ further supports the chemisorption. While bidentate chemisorption of cysteine via additional cleavage of the thiol group has been observed at very low exposure by us,⁹⁸ the same binding energy position of the corresponding S 2s feature for various methionine exposures is consistent with an intact thiol ether (–CH₂–S–CH₃) group (Figure 5.1d and Table C1). With two strong C–S bonds in the thiol ether group, the sulfur atom in

methionine, with its lone-pair electrons, could still undergo long-range interaction with a Si adatom or restatom nucleus, which could perturb the final equilibrium configuration. Furthermore, the best fit for the C 1s spectrum (Figure 5.1c) is obtained by using four components (from low to high binding energy): $-\text{CH}_2-$, $-\text{CH}_2-\text{S}-\text{CH}_3$, $-\text{CH}-\text{NH}-$, and $-\text{COOH}$, with atomic ratios of 1:2:1:1, in excellent accord with the stoichiometric composition and with the chemical state of the neutral dehydrogenated methionine adspecies. Finally, the O 1s spectrum for exposure below 90 s is consistent with the carbonyl component ($-\text{C}=\text{O}$) at 532.2 eV and hydroxyl oxygen ($-\text{OH}$) at 533.1 eV.

Given the XPS result for adsorbed methionine in the interfacial layer, we have considered a large variety of unidentate geometries involving bonding through the dehydrogenated amino group on specific sites within a half unit cell and across the dimer wall of the 7×7 surface and calculated their adsorption energies. The equilibrium unidentate adsorption configurations on the 7×7 model surface obtained by DFT-D2 calculations are shown in Figure C4 (Appendix C). Among the calculated adsorption configurations involving bonding through the dehydrogenated amino group with the rest of the adsorbate overhanging across the dimer wall, the geometry with the S atom closest to the CA' site across the dimer wall (Figure C4a1, with a separation of 2.55 Å between a Si adatom and S) is 0.189 eV and 0.335 eV more stable than that with the molecular plane (the plane containing the C-S-C backbone) near parallel (Figure C4a2, with a CA'-to-S separation of 4.26 Å) and near perpendicular to Si adatom surface plane (Figure C4a3, with a CA' to-S separation of 5.12 Å), respectively. (We use the prime sign to denote an adatom or a restatom in the unfaulted half unit cell.) For other unidentate configurations involving methionine on the CA site within a half unit cell (Figure C4b1-Figure C4b4), the configuration with the S atom atop of a Si restatom is the most stable (Figure C4b1, with a separation of 2.33 Å between a Si restatom and S). The adsorption energy of this configuration is also 0.224 eV lower than the unidentate configuration across the dimer wall (Figure C4a1). As expected, the results of unidentate methionine adsorbate on the CA site vs those on the AA site show that the adsorption energy on the CA site is generally slightly more negative than that on the AA site (Figure C4b5). While the S atom in methionine is not involved in direct covalent bonding with the 7×7 surface, the separation between the S atom and Si adatom/restatom controls the strength of the latter long-ranged weak interaction, which ultimately governs the final adsorption geometry. Furthermore, the plausible unidentate adsorption configurations observed by our companion STM study for the initial growth stage²²⁴ have identified by asterisks in Figure C4 (Appendix C). STM results are pivotal in identifying site-specific process and ab-initio calculations alone, even the large-scale one shown here, could not provide the complete picture. To understand the STM results, we must consider the importance of site-specific electric field density as

imposed by the surface registry in directing the initial adsorption of the incoming molecules. As the CA site (with a formal charge of $\sim+1$) is more electrophilic than the AA site (with a formal charge of $\sim+7/12$) while the RA site (with a formal charge of ~-1) is nucleophilic, the incident molecule would be preferentially guided by the electrostatic field provided by the CA site rather than AA site and would thereby orient itself appropriately to attach to the CA site. Furthermore, given that adsorption on the CA site in the faulted half unit cell is also more energetically stable than that on the unfaulted half unit cell (with an energy difference of 0.05-0.08 eV), the molecule would adsorb more favourably on the CA site than the CA' site, which is also corroborated by our STM results.

In contrast to single-crystal metal surfaces, such as Au(111)¹²⁵ and Ag(111) surfaces,¹²³ on which methionine adsorbs in zwitterionic form, methionine chemisorbs on Si(111)7 \times 7 in the neutral form to produce the interfacial layer for submonolayer coverage. This is similar to that found for other proteinogenic biomolecules. For cysteine with three functional groups,⁹⁸ we determine that the thiol group is generally more reactive than the amino group for interacting with the dangling bonds of the electrophilic Si adatom sites. Our studies also show that the carboxylic acid group remains intact for adsorption on the Si(111) surface,^{98,131,205} unlike copper surfaces.^{103,106,108,116,117,129} As the S atom is terminated with a methyl group in the thiol ether group and it appears not to play any role in direct covalent bonding, chemisorption of methionine via the amino group on Si surfaces is therefore the only viable pathway.

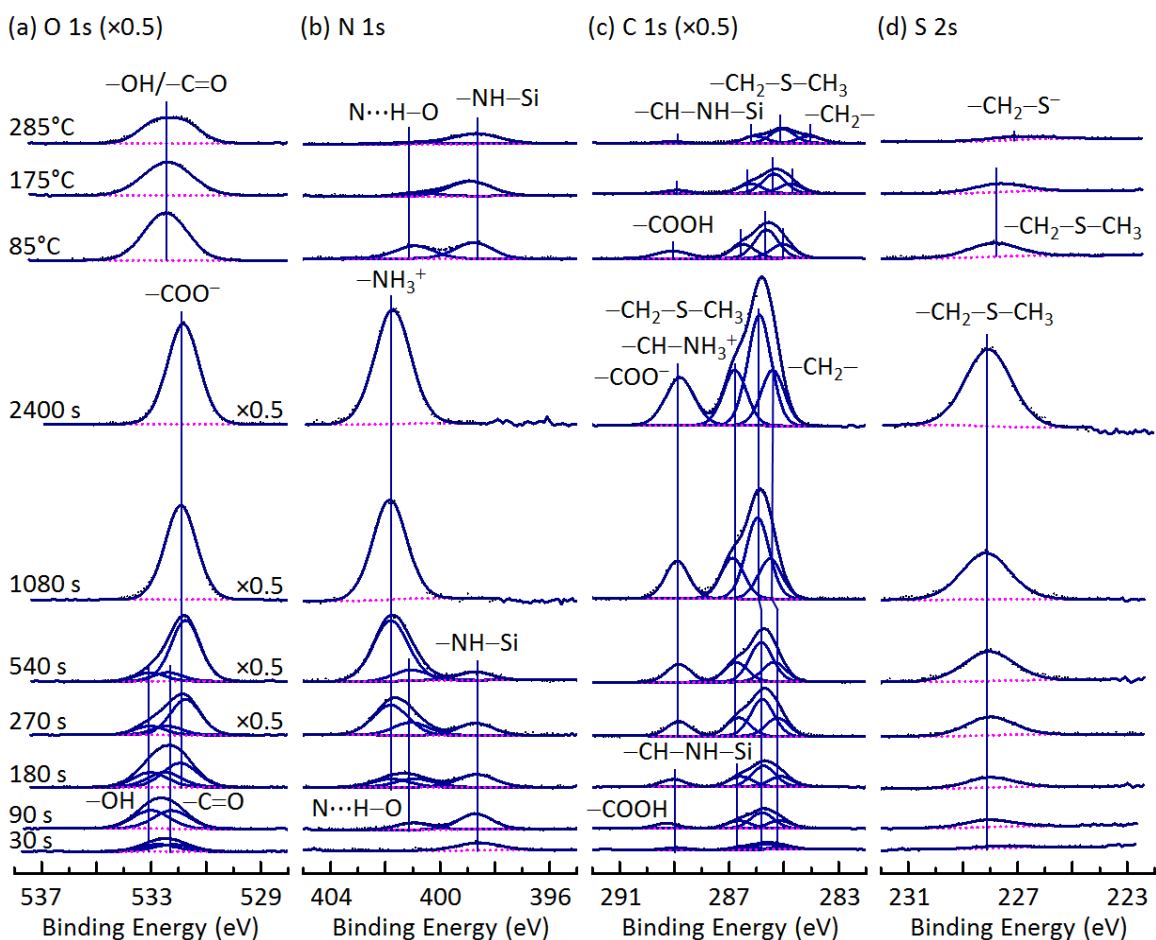


Figure 5.1 Evolution of (a) O 1s, (b) N 1s, (c) C 1s, and (d) S 2s XPS spectra of L-methionine deposited on Si(111)7×7 as a function of exposure time and of the as-deposited 2400-s film upon annealing to 85°C, 175°C and 285°C. XPS data are fitted with individual components (solid line) corrected with a Shirley background (dotted line).

Emergence of O–H···N hydrogen bonding feature in methionine with increasing exposure (180 s and above) has been observed (Figure 5.1b), as similarly found in the adsorption of other α -amino acids on the Si(111)7×7 surface. This feature indicates the formation of interlayer H-bond (head-to-tail) between a free carboxylic acid group of one amino acid molecule in the interfacial layer (first adlayer) and a free amino group of a second amino acid molecule in the second adlayer, the “transitional” layer. The observed respective increasing and decreasing N 1s intensities of the O–H···N and –NH–Si features from 90 s to 270 s (Figure C3, Appendix C) are consistent with the increasing thickness of the transitional layer. Since a methionine molecule unidentately anchors on a Si dangling bond site only through the

dehydrogenated amino group, in contrast to an adsorbed cysteine molecule that could unidentately attach through either the dehydrogenated amino or thiol group,⁹⁸ formation of intralayer O–H···N “flat” (head-to-tail) H-bonding among methionine molecules in the interfacial layer is therefore much less likely than cysteine molecules. In the methionine case, there is no free amino group to enable H-bonding with an adjacent carboxylic acid group, unlike the cysteine case, in which an intact amino group not involved in bonding to the surface is freely available to form a flat O–H···N H-bond.

Our calculations, however, show that the most stable configuration to accommodate “flat” H-bonds in the interfacial layer involves double O···H–O H-bonds between two vicinal carboxylic acid groups of two methionine molecules (head-to-head) at the CA-AA’ sites across the dimer wall (Figure C5a1, Appendix C). Similar dimerization of adsorbed cysteine on Au(110) surface has also been observed by STM.¹²¹ This double H-bond configuration is followed by a slightly less stable configuration containing a single O···H–O H-bond with one methionine molecule anchored to a CA while the second methionine molecule hovering over a CA’ site across the dimer wall (Figure C5a2, Appendix C). The low intensity of the broad O 1s spectrum for films obtained with low exposure (<30 s, Figure 5.1c), for which the presence of O···H–O H-bonds is expected, does not allow a definitive fit to isolate the O···H–O H-bond feature at 532.2 eV.²²⁵ Our STM results for the interfacial layer (obtained with a 5-s exposure) supports the presence of the single O···H–O H-bond configuration shown in Figure C5a2 (Appendix C).²²⁴ We have also evaluated other adsorption geometries with two methionine molecules in a single half unit cell and found that anchoring the second molecule to an adjacent Si adatom site within the same half unit cell is much less likely due to the considerable length of methionine (7.40 Å). We therefore conclude that aliphatic long-chain amino acids, such as methionine, that are unidentately adsorbed through Si–N linkage on the 7×7 surface, could only make intralayer O···H–O H-bonds across the dimer wall (flat configuration) due to size effect. In the other set of DFT-D2 calculations, we consider a large variety of interlayer H-bond with “lateral” and “near-vertical” configurations between two methionine molecules, corresponding to the molecular backbone of the second molecule oriented away from the first adsorbed molecule closer to the surface plane or the surface normal, respectively, and the more stable adsorption geometries are shown in Figure C5b1-Figure C5b12 (Appendix C). We designate these di-molecular geometries using CA or AA as the anchoring sites of the first adsorbed molecule, and a double bar (||) or semicolon (;) sign to indicate the position of a second adsorbed molecule in the adjacent half unit cell or in the same half unit cell, respectively. The orientation of the second adsorbed molecule relative to the first adsorbed molecule is identified in parentheses as “flat”, “twist” or “tilt”. Our DFT-D2 results show that the most stable lateral configurations to accommodate interlayer H-bonds include double O···H–O H-

bonds between two carboxylic acid groups of two methionine molecules that can be ruled out by our XPS results (Figure C5b1, Figure C5b2, Appendix C). These are followed by lateral and near-vertical configurations involving interlayer O–H···N H-bonds formed between a free carboxylic acid group in the interfacial layer and an amino group in the transitional layer similar to that found for the smaller amino acids (e.g. glycine) (Figure C5b3, Figure C5b4 and Figure C5b6, Appendix C). Table C2 (Appendix C) summarizes these di-molecular adsorption configurations, with the structures that are not supported by our XPS results grayed out. The adsorption energies of the lateral configurations are generally more negative than those of the near-vertical configurations due to possible long-range interactions with the surface in the former to form the transitional layer, while the adsorption energy of the flat configuration is the most negative one. On the other hand, an amino acid with a thiol group, such as cysteine, could produce O–H···N H-bonds through both flat and lateral/near-vertical configurations because of free amino groups in the interfacial layer within the half unit cell or/and across the dimer wall (Figure C6, Appendix C).

The XPS spectra for the methionine multilayers obtained for the 1080-s exposure on Si(111)7×7 (Figure 5.1) are found to be similar to those for methionine powder in the solid phase (Figure C1, Appendix C). The single O 1s and N 1s features represent, respectively, the carboxylate ($-\text{COO}^-$) and protonated amino groups ($-\text{NH}_3^+$) in the zwitterionic state for methionine ($\text{NH}_3^+\text{CHCH}_2\text{CH}_2\text{SHCH}_2\text{COO}^-$). Similar zwitterionic features have also been observed for the aforementioned benchmark proteinogenic biomolecules. The $-\text{NH}_3^+$ N 1s feature for the zwitterionic layer obtained for the 1080-s exposure also nearly doubles in intensity with respect to that for the transitional layer for the 540-s exposure (Figure C3a, Appendix C). Upon further doubling the methionine exposure from 1080 s to 2160 s, the intensity of the $-\text{NH}_3^+$ feature increases only by ~10% (Figure C3a, Appendix C), which indicates that the zwitterionic layer obtained for 1080 s has reached a sufficiently large film thickness above the electron mean free path of the photoelectrons.

In Table 5.1, we summarize the XPS peak positions and their assignments for the five proteinogenic biomolecules adsorbed on the Si(111)7×7 surface, in accord with their three-stage growth at room temperature. This reference table will provide an important guide to follow the adsorption of other amino acids and larger bio-organic molecules, such as proteins and peptides, on the reconstructed Si surfaces. For amino acids and peptides with only terminal amino and carboxylic acid groups, the biomolecule covalently bonds to appropriate Si adatom sites unidentately through dehydrogenated amino group, which builds up the interfacial layer. For the amino acid with additional terminal functional group, such as thiol, the molecule can also bind bidentately to adjacent Si adatom sites at very low coverage. Further exposure

produces the transitional layer, the formation of which is driven by O–H···N H-bonds between a free carboxylic acid group in the first adlayer and a free amino group in the second adlayer. Finally, zwitterionic structures are obtained with continued exposure upon completion of the transitional layer.

We also study the thermal stability of the methionine nanofilm (obtained with the 2400-s exposure) on the 7×7 surface by annealing the film for 600 s to elevated temperatures (85, 175, and 285°C) and perform XPS analysis after the sample has been cooled back to room temperature. Evidently, annealing the film at 85°C completely removes the zwitterionic methionine multilayer features, as indicated by re-emergence of two N 1s features related to the interfacial layer and to the H-bond formation and by the shift in the O 1s feature back to the position for the carboxylic acid group (Figure 5.1). The overall spectral intensities of O 1s and N 1s peaks (Figure C3b, Appendix C) decrease with increasing annealing temperature to 175°C, indicating reduction in the amount of physisorbed methionine in the film. For methionine, the S 2s position of thiol ether is unchanged for interfacial, transitional and zwitterionic layers, but it shifts to a lower binding energy upon annealing at 285°C, indicating dissociation of the methyl group. By analogy to the thermal evolution of thiophene on Si(100)²¹⁹ and Pt(111),²²⁰ we attribute the S 2s shift to the formation of atomic S on Si surface as a result of C–S bond cleavage. From the observed thermal stabilities of the thick amino acid nanofilms (methionine, cysteine, and glycine) on Si(111)7×7 surface, we conclude that the stabilities of zwitterionic multilayer and transitional layer depend on the extent and strength of the intralayer and interlayer hydrogen bonding. Moreover, the interfacial layer secured through the dehydrogenated amino group of proteinogenic biomolecules on Si dangling-bond sites is stable until decomposition of amino acids above 200°C, which confirm the strength of the –HN–Si covalent bond between the adsorbate and Si surface.

Table 5.1 Binding energies (in eV) of fitted peak maxima for various XPS core-level features and their assignments for three growth stages on Si(111)7×7 surface for glycine (G), D-alanine (A), L-cysteine (C), L-methionine (M), and glycylglycine (GG). The values apply to all five benchmark proteinogenic biomolecules unless otherwise the application to specific biomolecules is indicated by superscripts.

| Core level | Assignment | Interfacial layer | Transitional layer | Zwitterionic layer |
|------------|-------------------------------------|--------------------------|--------------------------------|--------------------------|
| O 1s | -OH -C=O | 532.5-533.0 | 532.2-533.0 | |
| | -NH-C=O | | | 532.7 ^{GG} |
| | -COO ⁻ | | | 531.8-531.9 |
| N 1s | -NH-Si | 398.6-399.1 | 398.7-399.1 | |
| | -NH ₂ -NH-CO- | 400.6 ^{GG} | | |
| | O-H···N | 401.0 ^C | 401.0-401.1 ^{G,A,C,M} | |
| | -NH ₃ ⁺ | | | 401.7-402.2 |
| C 1s | -CH ₂ -S-Si | 284.7 ^C | 284.5 ^C | |
| | -CH ₂ -SH | 285.6 ^C | 285.6 ^C | 285.9-286.0 ^C |
| | CH ₃ - | 285.3 ^A | 285.3 ^A | 285.3 ^A |
| | -CH ₂ - | 285.285.1 ^M | 285.2-285.4 ^M | 285.4-285.5 ^M |
| | -CH ₂ -S-CH ₃ | 285.7-285.8 ^M | 285.8-285.9 ^M | 285.9 ^M |
| | -NH-C=O | 288.1 ^{GG} | 288.4-288.7 ^{GG} | 288.9 ^{GG} |
| | -CH-NH- | 286.3-286.9 | 286.5-286.9 | |
| | -CH-NH ₃ ⁺ | | | 286.7-286.9 |
| | -COOH -COO ⁻ | 288.9-289.7 | 288.9-289.7 | 288.7-289.0 |
| S 2s | -S-Si | 227.4 ^C | 227.4 ^C | |
| | -SH | | 228.4 ^C | 228.4 ^C |
| | -CH ₂ -S-CH ₃ | 228.1 ^M | 228.1 ^M | 228.1 ^M |

5.1.3.2 “Universal” Three-Stage Growth Applicable to Methionine on Si(111)7×7

In Figure 5.2, we summarize our large-scale DFT-D2 calculations for the three-stage growth of methionine on a Si(111)7×7 supercell that consists of three complete 7×7 unit cells. In the interfacial layer, a methionine molecule binds covalently with the dangling bond of a Si CA via a dehydrogenated amino group, which gives rise to a large variety of unidentate adsorption geometries on specific sites of the 7×7 surface within a half unit cell and also across the dimer wall involving supplementary “weaker” long-range interactions of other functional groups (Figure C4, Appendix C). The magnified side-view of interfacial layer (Figure 5.2a) shows a methionine molecule anchored to a Si adatom with a covalent –

HN–Si bond, leaving the carboxylic acid (–COOH) group free to interact with a second methionine molecule. Similar to that found for methionine adsorption on Cu(110),¹²⁶ our DFT-D2 calculation suggests that the S lone-pair electrons could interact with other nearby Si adatom/restatom. Since the XPS result shows no detectable change in the position of S 2s peak over various methionine coverages, thus reinforcing our hypothesis that the thiol ether group is intact (without dissociation of the terminal methyl group), there is only weak long-range interaction between the lone-pair electrons of the S atom and the adjacent Si surface atom. Furthermore, the calculated equilibrium configuration of the transitional layer contains interlayer O–H···N H-bond (with a bond length of 1.62 Å) between the free carboxylic acid group of the first adsorbed methionine and a free amino group from a second methionine molecule (Figure 5.2b), which suggests that interlayer H bonding is the driving force in the formation of the transitional layer. Finally, both intralayer and interlayer O···H–N H-bonds lead to the formation of a stable zwitterionic layer (Figure 5.2c),²²⁶ which is weaker than the transitional layer held together by the O–H···N H-bonds. Our DFT-D2 results demonstrate that intralayer interactions via hydrogen bonding (O···H–N H-bonds) between neighboring negatively charged carboxylate groups (–COO[–]) and positively charged protonated amino groups (–NH₃⁺) lead to the formation of the zwitterionic layer. Furthermore, the zwitterionic layer is connected to the transitional layer through interlayer O···H–N H-bonding between the carbonyl group (–C=O) of a free carboxylic acid group in the transitional layer and the –NH₃⁺ group in the zwitterionic layer, and interlayer O–H···O H-bonding between the hydroxyl group (–OH) of the carboxylic acid in the transitional layer and the –COO[–] group in the zwitterionic layer. As the result of these weak interactions, the zwitterionic layer is not as stable as the transitional layer and interfacial layer, which is confirmed by the thermal evolution of XPS features shown in Figure 5.1 and Figure C3b (Appendix C).

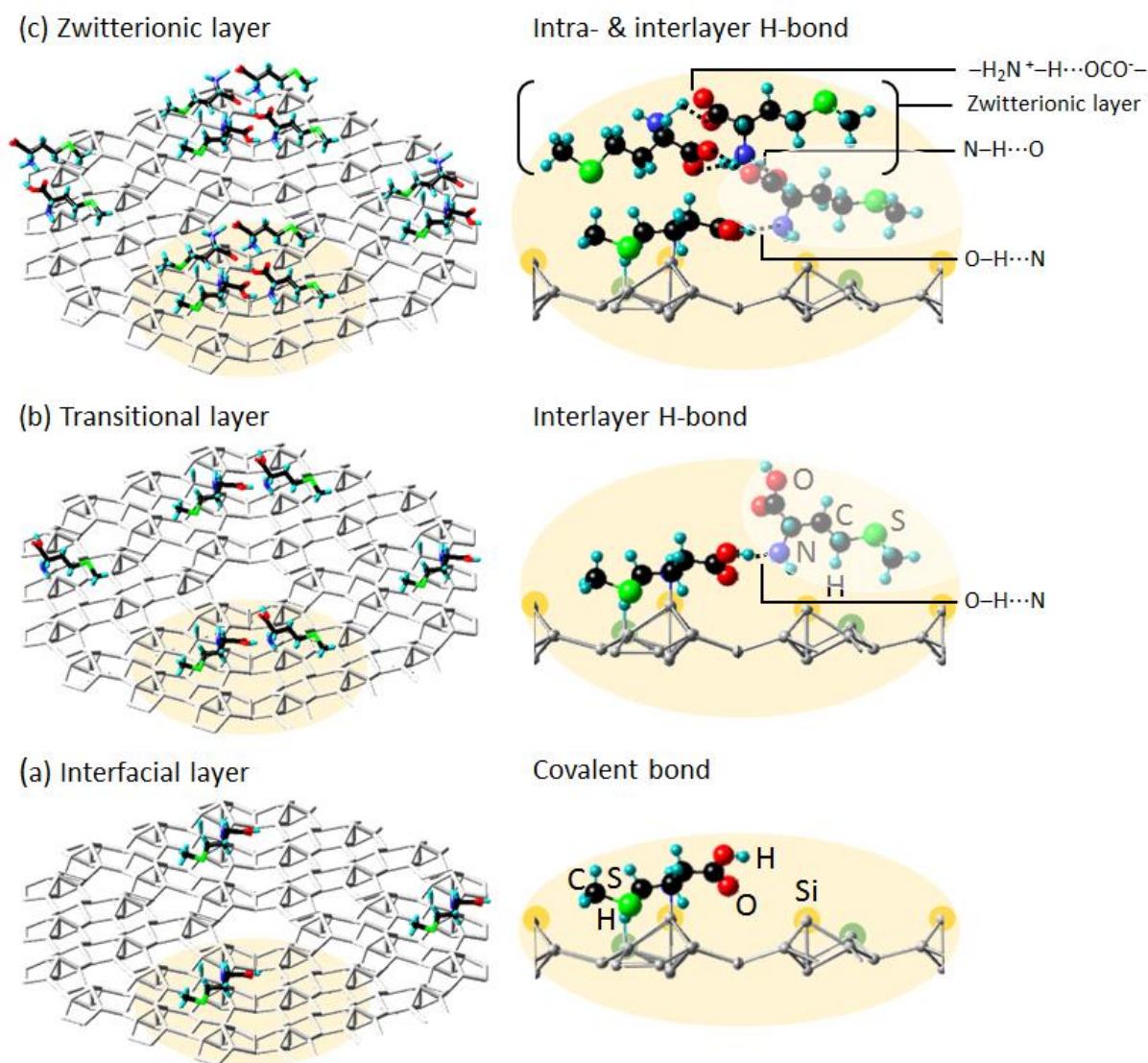


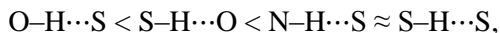
Figure 5.2 Three-stage growth model of L-methionine on Si(111)7×7 surface: Perspective views (left column) and magnified side views (right column) of (a) an interfacial layer, (b) transitional layer, and (c) zwitterionic layer. All of equilibrium configurations are obtained by DFT-D2 calculations using a supercell of three 7×7 unit cells, each of which is represented by a Si₂₀₀H₄₉ slab, to model the 7×7 surface. Magnified side-views show (a) a methionine molecule adsorbed on a Si center adatom, (b) an interlayer N···H–O H-bond between molecules in the interfacial and transitional layers, and (c) an additional interlayer O···H–N and O···H–O H-bonds between the transitional layer and zwitterionic layer, and intralayer zwitterionic hydrogen bonding (O···H–N H-bond). For clarity, only the topmost layers of Si adatoms and the first bilayers of the three unit cells are shown. Si adatoms and restatoms are highlighted by larger yellow and green circles, respectively. The molecules in the transitional layer are slightly whitened for easier identification.

5.1.3.3 Hydrogen Bonding in Universal Three-Stage Growth of Proteinogenic Nanofilm on Si(111)7×7

Hydrogen bonding represents the most important interactions in the formation of proteins and larger biological materials from the amino acid building blocks. Quantitative studies of these interactions are very useful not only for the understanding of a number of important film growth and biological processes in physicochemical terms, but also for self-organization and assembly of supramolecular nanostructures on the surface.²²⁷ Although there are a number of theoretical studies of intramolecular H-bonds of free glycine, alanine, and cysteine conformers in the gas phase in the past two decades,^{210,228,229,230,231,232} only a few have reported the bond strengths and bond lengths of intermolecular hydrogen bonding interactions.²³¹ With the data on methionine and additional calculations for the other proteinogenic biomolecules presented here, we could provide a more complete picture and particularly site-specific investigation on this important interaction, by using DFT-D2 calculations to discover optimized dimer configurations and common hydrogen bonding trends for the aforementioned benchmark proteinogenic biomolecules. Di-molecular structures resulting from formation of various H-bonds between different functional groups of isolated biomolecules are shown in Figure 5.3. The presence of two terminal functional groups, amino ($-\text{NH}_2$) and carboxylic acid ($-\text{COOH}$) groups, in glycine, alanine, and methionine could lead to the formation of four types of single H-bonds ($\text{O}-\text{H}\cdots\text{N}$, $\text{O}-\text{H}\cdots\text{O}$, $\text{N}-\text{H}\cdots\text{N}$, $\text{N}-\text{H}\cdots\text{O}$) and two types of double H-bond configurations [$2\times(\text{O}-\text{H}\cdots\text{O})$, $2\times(\text{N}-\text{H}\cdots\text{O})$]. The H-bonds in the dipeptide of glycine (glycylglycine) is similar to glycine, except for the missing double $\text{N}-\text{H}\cdots\text{O}$ H-bond configuration due to the steric hindrance effect. Furthermore, L-cysteine is a good representative of aliphatic amino acids with the added functionality of a thiol ($-\text{SH}$) group in the side chain to serve as a H-bond donor or acceptor. The thiol group gives rise to four additional types of single H-bonds ($\text{O}-\text{H}\cdots\text{S}$, $\text{S}-\text{H}\cdots\text{O}$, $\text{N}-\text{H}\cdots\text{S}$, $\text{S}-\text{H}\cdots\text{S}$) and one more type of double H-bond configurations [$2\times(\text{S}-\text{H}\cdots\text{N})$]. In the gas phase, additional stabilization is observed when double H-bonds between two $-\text{COOH}$ groups are formed to produce a cyclic di-molecular configuration. The H-bond energies for these double H-bond arrangements are 3.66-24.22 kJ/mol higher than twice the corresponding single H-bond arrangements formed between two $-\text{COOH}$ groups. Among the single H-bond configurations, the $\text{O}-\text{H}\cdots\text{N}$ bond is the strongest, which is in good accord with what makes the amino acids the basic building blocks in biomolecular systems. The H-bond length in di-molecular configurations of isolated aliphatic amino acids in the gas phase follows the increasing trend:



with the OH group being the stronger H-bond donor group than the NH group. When the side-chain –SH H-bond donor and/or acceptor in cysteine are included, the corresponding trend for the H-bond length becomes:



in which the O–H⋯S bond length for cysteine is discernibly longer than the O–H⋯O bond length for the other amino acids. As the H-bond length is inversely related to the H-bond energy, the corresponding trends for the bond energy follow the reverse trends for the bond length. It is clear that the O–H group is a stronger H-bond donor than N–H group, with the S–H group being the weakest. The reference structures shown in Figure 5.3 are expected to provide a useful guide to the type of plausible hydrogen bonding formation and their approximate bond strengths among larger bio-organic molecules, including other amino acids and different peptides and proteins. The general trends in H-bond strength obtained above should also offer insights to H-bond formation on surfaces, which are important to biofunctionalization and biodevice fabrication.

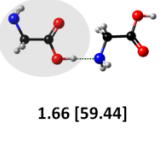
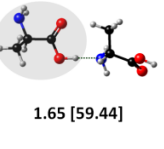
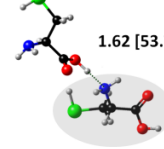
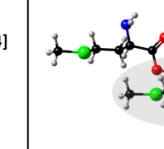
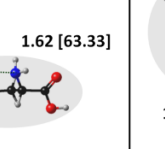
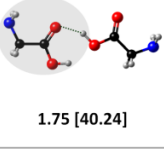
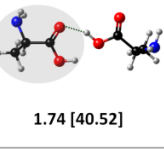
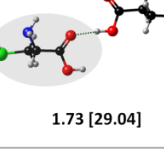
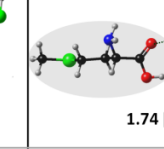
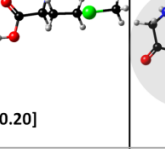
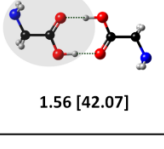
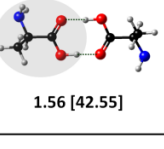
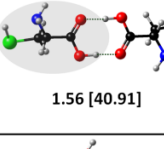
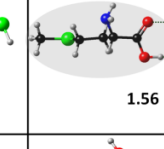
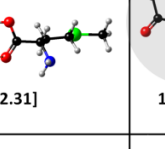
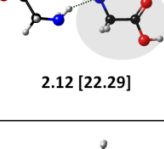
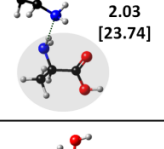
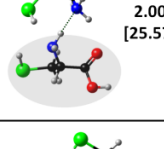
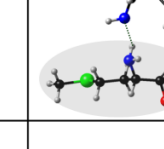
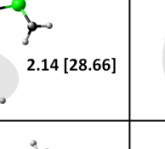
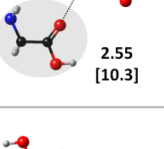
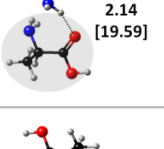
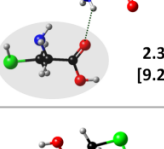
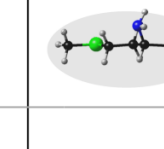
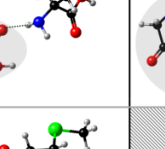
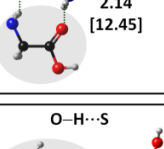
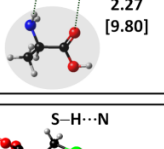
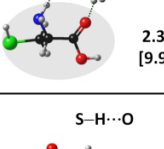
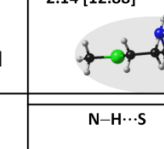
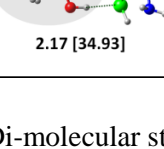
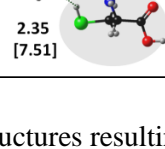
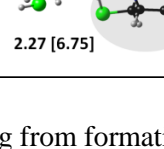
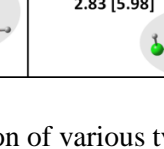
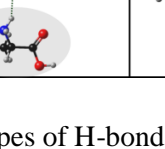
| H-Bond Bond Length (Å) [Bond Energy (kJ/mol)] | Glycine | Alanine | Cysteine | Methionine | Glycylglycine |
|--|---|---|--|--|---|
| O-H...N |  1.66 [59.44] |  1.65 [59.44] |  1.62 [53.74] |  1.62 [63.33] |  1.69 [53.55] |
| O-H...O |  1.75 [40.24] |  1.74 [40.52] |  1.73 [29.04] |  1.74 [30.20] |  1.70 [33.09] |
| O-H...O O-H...O |  1.56 [42.07] |  1.56 [42.55] |  1.56 [40.91] |  1.56 [42.31] |  1.55 [41.78] |
| N-H...N |  2.12 [22.29] |  2.03 [23.74] |  2.00 [25.57] |  2.14 [28.66] |  2.27 [23.16] |
| N-H...O |  2.55 [10.3] |  2.14 [19.59] |  2.31 [9.26] |  2.20 [15.24] |  2.16 [20.45] |
| N-H...O N-H...O |  2.14 [12.45] |  2.27 [9.80] |  2.30 [9.94] |  2.14 [12.88] | |
| Cysteine |  2.17 [34.93] |  2.35 [7.51] |  2.27 [6.75] |  2.83 [5.98] |  2.84 [5.60] |

Figure 5.3 Di-molecular structures resulting from formation of various types of H-bonds (marked by dashed lines) between different functional groups of isolated biomolecules. These models are generated by DFT-D2 calculations. The calculated bond length (Å) is depicted along with the corresponding bond energy (kJ/mol) shown in square parentheses. The molecule in the gray oval is shown with the >C-COOH group in plane in order to provide a reference orientation for the H-bond. The last row shows additional -SH donor or acceptor H-bonds in di-molecular configurations of cysteine.

On the surface, di-molecule formation is affected not just by the surface bonding used for anchoring the adsorbate to the surface through a preferred functional group but also by steric hindrance on the adsorbate as imposed by the surface atoms and other adsorbates. These constraints rule out many of the gas-phase H-bonded di-molecular structures shown in Figure 5.3. Furthermore, our DFT-D2 calculation shows that the available physical separations between specific adatom sites on the 7×7 surface can also be used to eliminate a number of gas-phase hydrogen bonding possibilities. Based on the dimer-adatom-stacking fault model of Si(111) 7×7 (Figure C2, Appendix C), we could categorize a dangling bond pair between adjacent Si sites into the following two groups, with their respective separations between two Si atoms indicated in parentheses:

- (A) Two Si sites within a half unit cell: CA-AA (7.72 Å), CA-CA (7.66 Å), CA-RA (4.55 Å), AA-RA (4.46 Å), and AA-corner hole (8.25 Å); and
- (B) Two Si sites across the dimer wall of adjacent half unit cells: CA-CA' (6.77 Å), AA-AA' (6.71 Å), and CA-AA' (10.25 Å).

These separations represent the available “pitch” spacings on the 7×7 surface registry for constructing covalent bonding with appropriate functional groups of the biomolecules.

In analogy to methionine, the H-bonded di-molecular structures of proteinogenic biomolecules on Si(111) 7×7 surface can also be categorized as either “flat” configurations for intralayer H-bonds in the interfacial layer or “lateral”/“near-vertical” configurations for interlayer H-bonds to form the transitional layer (Table C2, Appendix C). In the interfacial layer of the smallest amino acid, glycine, the molecule is bonded covalently through the –NH functional group to a Si adatom on the 7×7 surface as supported by our XPS data. It is therefore not possible to form O–H \cdots N, N–H \cdots N, and N–H \cdots O (single and double) H-bonds between a pair of glycine molecules (due to the use of N in the N–Si bond formation). This is in contrast to the transitional layer in which the formation of N–H \cdots N and N–H \cdots O (double) H-bonds becomes viable. Using large-scale DFT-D2 calculations, we obtain the equilibrium structures and adsorption energies of all other possible intralayer flat di-molecular hydrogen bonding configurations (in the interfacial layer) and interlayer lateral and near-vertical hydrogen bonding configurations (in the transitional layer) on our Si₂₀₀H₄₉ model surface. Altogether, a total of well over 120 optimized configurations have been successfully computed for the five proteinogenic biomolecules on the model surface, which represents the most comprehensive computational study for these biomolecules (supported on any surface) reported to date. Among all of these di-molecular flat configurations containing intralayer hydrogen bonding that are covalently bonded to the Si adatoms through the dehydrogenated amino group, the cyclic di-molecular structure with double O–H \cdots O H-bonds across the dimer wall

(Figure 5.4a1 and 5.4a2), single O–H···O H-bond across the dimer wall (Figure 5.4a4), and with O–H···N H-bond within a half unit cell (Figure 5.4a3) are found to be the most stable in the interfacial layer, while both lateral (Figure 5.4b1-5.4b4) or near-vertical (Figure 5.4c1-5.4c4) configurations of five proteinogenic biomolecules (except glycylglycine) involving interlayer O–H···N H-bond are the most stable structure in the transitional layer. The former flat arrangements including intralayer H-bonds are of 1.4-2.3 eV and 1.6-2.5 eV stronger than the lateral and near-vertical arrangements with interlayer H-bonds, respectively. For the near-vertical configurations that are supported by our XPS results (Table C2, Figure C5-Figure C9, Appendix C), the O–H···N H-bond length is shorter than the N–H···O H-bond length, which is in good accord with the trends found for di-molecule systems in the gas phase (Figure 5.3). For both glycine (Figure C7, Appendix C) and alanine (Figure C8, Appendix C), our DFT-D2 calculations show that the cyclic double O–H···O hydrogen bonding flat arrangements (Figure 5.4a1 and 5.4a2) provide the most stable interfacial bonding on the Si surface, while the O–H···N hydrogen bonding provides the best lateral (Figure 5.4b1 and 5.4b2) and near-vertical configurations (Figure 5.4c1 and 5.4c2) to form the transitional layer. These calculated configurations are supported by our XPS results.

Among the XPS studies on the adsorption of the aforementioned benchmark proteinogenic biomolecules, cysteine⁹⁸ is the only amino acid exhibiting a N 1s feature that corresponds to O–H···N H-bond in the interfacial layer. Our large-scale DFT-D2 calculation shows that the configuration with the lateral O–H···N H-bond (Figure 5.4a3, Figure C6a1) is only slightly more stable (by 0.015 eV) than that of the double O–H···O H-bond in cysteine (Figure C6a2), in contrast to other amino acids. For the other S-containing aliphatic amino acid, methionine, the most stable configurations with flat and lateral/ near-vertical hydrogen bonding are the single O–H···O H-bond configuration (Figure 5.4a4) and O–H···N H-bond configuration (Figure 5.4b4 and 5.4c4), respectively. However, methionine di-molecules are physically too large to form lateral hydrogen bonding within a half unit cell because of incompatibility of their size with respect to the separations of Si adatoms within a half unit cell.

For the simplest peptide, glycylglycine, with amino, amide and carboxylic acid groups, our XPS result provides strong evidence for bidentate configuration through either O–H and N–H dissociation or double N–H dissociation in the interfacial layer.¹³¹ The possibility of forming lateral H-bonds between two glycylglycine molecules adsorbed bidentately on the Si(111)7×7 surface is unlikely because of incompatible molecular dimensions with the separations between adjacent Si adatoms. Among all the configurations containing near-vertical H-bonds (Figure C9, Appendix C), our DFT-D2 results show that the configuration with the C=O···H–O hydrogen bonding is the most stable one in the transitional layer.

Our calculated results are consistent with our XPS data, which indicate the absence of any O–H···N H-bond in the transitional layer.¹³¹

The adsorption energy of the flat di-molecular structures involving intralayer H-bonds of the benchmark proteinogenic biomolecules on the Si(111)7×7 surface follows the trend:

Cysteine > Methionine > Alanine > Glycine,

with cysteine being 0.28, 0.46 and 0.60 eV more stable than methionine, alanine, and glycine, respectively. On the other hand, the corresponding trend for the adsorption energy of the near-vertical di-molecular structures involving interlayer H-bonds becomes:

Glycylglycine > Methionine > Alanine ≈ Glycine > Cysteine,

with the O–H···N H-bonds for the cysteine, glycine and alanine exhibiting essentially the same adsorption energy (within ~0.12 V) and those for glycylglycine and methionine discernibly stronger (by over 1.96 and 0.73 eV, respectively than the former). As these proteinogenic biomolecules contain various moieties with a wide range of adsorption energy on Si surface, the resulting interfacial layer and transitional layer offer new opportunity of creating not just “permanent” but indeed “semi-permanent” biofunctionalization, respectively.

From our DFT-D2 results of di-molecular configurations of the aforementioned proteinogenic biomolecules in the formation of the interfacial and transitional layers on the reconstructed 7×7 surface, we summarize a few general observations here to guide future investigations of the growth processes of other amino acids and larger biological molecules.

- (1) Most, if not all, aliphatic proteinogenic biomolecules follow the “universal” three-stage film growth process on Si(111)7×7. Of all the studies reported to date,^{98,205,131} we have not seen any exception.
- (2) The formation of intralayer H-bonds in the interfacial layer leads to a more stable configuration (flat configuration) than the formation of interlayer H-bonds in the transitional layer (lateral/near-vertical configurations), with the more parallel configuration with respect to the surface being more favorable than the tilted or more upright configurations.
- (3) The interlayer O–H···N H-bond between a free carboxylic acid group in the interfacial layer and a free amino group in the transitional layer is found to be the most common mechanism in the early growth stage of these aliphatic amino acids.
- (4) The formation of intralayer H-bonds between two adsorbed biomolecules in the interfacial layer depends on several factors: the size, nature and available variety of the functional groups, conformer configuration, nature of possible adsorption sites on the surface, and steric hindrance among adsorbates and between an adsorbate and the surface registry.

(5) In the case of interlayer H-bonds, not only do the orientations of both the first and second adsorbates play a crucial role on the adsorption energy, but also the site-specificity of the Si surface could affect the formation of a viable stable system.

These proposed rules inferred from our DFT-D2 results of the aforementioned benchmark proteinogenic biomolecules can be tested on other aliphatic amino acids and larger biomolecules. They can be used to provide practical guide to understand biofunctionalization of Si surface for the application development.

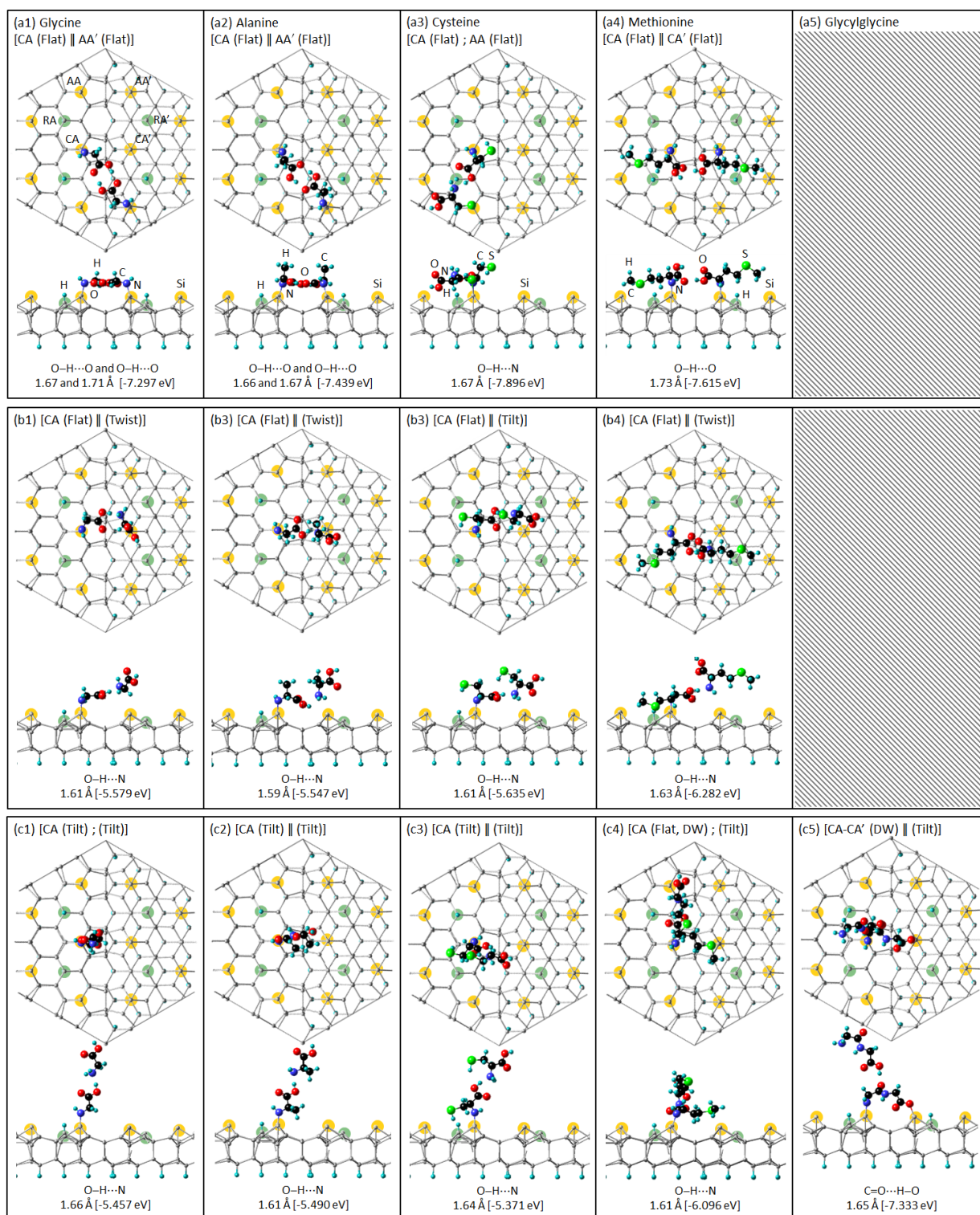


Figure 5.4 Top and side views of the most stable adsorption configurations for two proteinogenic biomolecules connected by (a1-a4) flat configurations with intralayer H-bond in the interfacial layer, (b1-

b4) lateral configurations with interlayer H-bond, and (c1-c5) near-vertical configurations with interlayer H-bond in the transitional layer on a $\text{Si}_{200}\text{H}_{49}$ model 7×7 surface, as obtained by DFT-D2 calculations. The lengths (in Å) of the respective H-bonds are indicated, along with the corresponding bond energies (in eV) shown in parentheses. The biomolecules are (a1/b1/c1) glycine, (a2/b2/c2) alanine, (a3/b3/c3) cysteine, (a4/b4/c4) methionine, and (c5) glycylglycine. For clarity, the Si adatoms [corner adatom (AA) and center adatom (CA)] and restatoms (RA) are highlighted by larger yellow and green circles, respectively. The Si unit cell used in the calculation is partially truncated in order to provide a higher magnification of the adsorption region. We use a prime symbol to denote a substrate atom in the adjacent half unit cell. Each panel heading denotes the orientation of the $>\text{C}-\text{COOH}$ backbone in the admolecules with respect to Si surface (as flat, tilt, or twist) at specific Si adatom sites, with the double bar (||) and semicolon (;) indicating the second molecule H-bonded, respectively, across the dimer wall or within the same half unit cell.

5.1.4 Summary

Nanofilm growth of five benchmark aliphatic proteinogenic biomolecules on $\text{Si}(111)7\times 7$ surface at room temperature under UHV conditions have been investigated by using XPS in our group.^{98,205,131} In the present study, three-stage growth is also observed for methionine on the 7×7 surface, closely following the adsorption characteristics of all of the amino acids (cysteine, glycine, and alanine) and peptide (glycylglycine) studied to date. Our previous investigations show that N–H dissociative adsorption provides the initial impetus in the formation of N–bonded adsorption structure of these biomolecules on the Si adatom sites. Methionine is another example of an amino acid that follows the same binding pathway via the N–Si bond formation in the interfacial layer, thus reinforcing our hypothesis that the amino ($-\text{NH}_2$) group is more reactive than the carboxylic acid group ($-\text{COOH}$) on the 7×7 surface. Our XPS results further reveal that the driving force to produce the transitional layer is interlayer $\text{N}\cdots\text{H}-\text{O}$ H-bonding between a free carboxylic acid group in the interfacial layer and an amino group in the second adlayer (transitional layer). This is also supported by our large-scale DFT-D2 calculations (that include van der Waals corrections) for the aforementioned proteinogenic biomolecules. Finally, at higher exposure, the formation of a zwitterionic layer is evident. We conclude that the thermal stability of the zwitterionic layer is much lower than the interfacial and transitional layers because of the weaker intralayer and interlayer $\text{O}\cdots\text{H}-\text{N}$ H-bonds than the $\text{O}-\text{H}\cdots\text{N}$ H-bonds, as illustrated by DFT-D2 calculations for di-molecule systems in the gas phase or on the reconstructed Si surface. Based on these results, we propose a “universal” three-stage growth model for α -amino acids ($\text{NH}_2\text{CHR}\text{COOH}$) on $\text{Si}(111)7\times 7$ surface at room temperature. We expect that such a growth model can be applied to larger biological molecules, such as peptides and proteins, which will provide basic understanding in constructing silicon biological interface for bio-devices and biomedical applications. Our results also

enable us to construct a reference XPS data table to guide future studies of biofilm growth on reconstructed Si(111) surface (Table 5.1). We also establish the trends in the H-bond length among different types of the hydrogen bonding for di-molecular structures in the gas phase (Figure 5.3) and on Si(111)7×7 surface (Figure 5.4). The trend for the H-bond length ($\text{O-H}\cdots\text{N} < \text{O-H}\cdots\text{O} < \text{N-H}\cdots\text{N} < \text{N-H}\cdots\text{O}$) in the gas phase can be applied to biomolecular surface interaction, except for the $\text{N-H}\cdots\text{N}$ H-bond because the amino group is occupied by covalent bonding with the surface. Finally, five simple rules of thumb are developed to summarize the adsorption properties of these proteinogenic biomolecules, and they are expected to provide helpful guide to studies of larger biomolecules and their potential applications.

5.2 Novel Self-Organized Y-shaped Trimer of L-methionine: A Magic-Number Cluster Supported on Si(111)7×7

5.2.1 Introduction

Fundamental understanding of the interactions of various types of organic molecules with semiconductor surfaces has attracted much attention in the past two decades, because of the wide range of potential applications in the design and fabrication of hybrid organic-inorganic electronic devices, particularly in the functionalization and molecular processing of silicon substrates.^{69,199} Compared to inorganic materials, organic molecules, with the availability of a large variety of functional groups, offer powerful chemical and physical properties as well as potential biological compatibility. Of all the semiconductors, silicon is the best known substrate for fabricating electronic devices because of its unique electronic and surface properties, with Si(111)7×7 and Si(100)2×1 being two of the most studied semiconductor surfaces to date. With 18 directional dangling bonds (at 6 center and 6 corner electrophilic adatom sites, and 6 nucleophilic restatom sites) plus one dangling bond shared among the four corner-hole sites per unit cell,²⁹ the Si(111)7×7 surface provides a highly reactive surface for adsorption of both inorganic and organic materials. Since observation of the 7×7 surface reconstruction with atomic resolution²⁶ by scanning tunneling microscopy (STM)² shortly after its invention, adsorption of a wide variety of organic molecules on Si(111)7×7 have been studied by STM. These molecules, from small molecules with a single functional group to larger biomolecules with multiple functional groups, have provided a rich test bed for investigating not just molecule-surface reactions but also surface-mediated intermolecular processes such as self organization.

Based on STM observation of organic molecules, with different functional groups, chemisorbed on both the nucleophilic and electrophilic sites of the 7×7 surface, the molecule-surface interactions can be categorized into four general types of reactions: (a) [2+2]-like cycloaddition or di- σ binding, (b) [4+2]-like or Diels-Alder cycloaddition, (c) covalent attachment via dissociative chemisorption, and (d) formation of dative-bond adducts. Early STM studies of acetylene⁸¹ and ethylene⁸² adsorption showed a [2+2]-like product di- σ bonded on a pair of adjacent Si adatom-restatom sites. Similarly, quad- σ bonded products on two neighboring pairs of adjacent adatom-restatom sites were found for several aliphatic dienes, including 1,6-heptadiene, 1,7-octadiene and 1,13-tetradecadiene.⁸³ These [4+2] cycloaddition reactions have been observed for unsaturated hydrocarbon (1,3-butadiene⁸⁴) at adatom-adatom pairs, and for aromatic hydrocarbons (benzene^{85,86,87,88} and toluene⁸⁶), aromatic heterocycles (thiophene^{89,90}), and DNA base (thymine⁹¹) at adjacent adatom-restatom pairs by high-resolution STM imaging. These STM

studies showed that the center adatom was more reactive with these organic molecules than the corner adatom. Moreover, a wide range of the covalent attachments, from nitroxyl free radicals⁹² and aromatic molecules (pyrrole⁷¹, naphthalene⁹³, tetracene⁹⁴, and pentacene⁹⁵), amines (dimethylamine⁷⁰) to benchmark amino acids (glycine,⁹⁶ alanine,⁹⁷ and cysteine⁹⁸) and peptide (glycylglycine⁹⁹), have also been investigated by STM. These molecules were found to react with adjacent adatom-restatom pairs, usually with the dissociated hydrogen atom bonded at a nearby restatom site. Finally, STM studies showed that donating the lone-pair charge density of the N atom in one of DNA bases (adenine¹⁰⁰) and amines (trimethylamine⁷⁰) to the Si atom could lead to long-range dative bonding. In contrast to direct bonding of the aforementioned neutral organic moieties to various Si surface sites, adsorption and nanoscale patterning of zwitterionic molecular films on the Si(111)7×7 surface has also been investigated by STM.¹⁰¹

Of all the organic and biological molecules, amino acids represent the building blocks of proteins and peptides. Understanding their adsorption on and interactions with semiconductor surfaces will enable the use of biofunctionalization to convert a potentially hostile inorganic surface like silicon to a more biologically friendly substrate. Such biofunctionalization process is the first step of building any biocatalysts and biodevices. Of the twenty amino acids, methionine ($\text{COOHC}_\alpha\text{HNH}_2\text{CH}_2\text{CH}_2\text{SCH}_3$) is one of the two sulfur-containing aliphatic amino acids, and it contains a terminal thioether ($-\text{CH}_2\text{SCH}_3$) group, unlike the other sulfur-containing amino acid, cysteine, that contains a thiol ($-\text{SH}$) group. As an essential amino acid, methionine plays several important roles in cell metabolism in the human body, and an abnormal level of methionine could indirectly cause a variety of health problems. The adsorption of L-methionine on the Si(111)7×7 surface is therefore of particular interest to both surface science and biomedical research. In contrast to a few studies on self-assembly of methionine on single-crystal metal surfaces, there has been no report on the interaction of methionine with any semiconductor surface at any temperature. Of particular interest is the availability of strong directional dangling bonds on Si(111)7×7, which could play a significant role in changing the nature of surface functionalization that involves strong bonds in neutral form, in marked contrast to metal surfaces on which the zwitterionic form is the norm. On Au(111),^{122,125} D- and L-methionine were found to form parallel chain or zipper-like dimer rows in the formation of hydrogen-bonded zwitterionic layer at room temperature. L-methionine was reported to form nano-gratings by self-assembly with tunable periodicity in the zwitterionic chemical state on a Ag(111) surface held at 320 K during deposition.¹²³ Furthermore, steering chiral organization of L-methionine on Cu(111)¹²⁴ was found to be strongly affected by the substrate reactivity and thermal activity. Unlike metal surfaces, the availability of directional dangling bonds on Si(111)7×7 offers a new

paradigm in understanding the formation and evolution of surface chemical bonds of these building-block biomolecules, including methionine.

Here, we study the early growth stage of L-methionine monomers into dimers and trimers on Si(111)7×7 at room temperature in UHV conditions by high-resolution STM imaging. We illustrate the formation of a unique Y-shaped trimer through self-organization of chemisorbed methionine. Using large-scale ab-initio quantum mechanical computations, based on the density functional theory (DFT) with van der Waals corrections (D2), we provide precise structural models for the observed methionine features, including the “delta or Δ-shaped” monomers in a half unit cell or across a dimer wall, “oval-shaped” dimer across a dimer wall, and “Y-shaped” trimer within of a half unit cell on the 7×7 surface. Understanding fundamental intermolecular interactions of biological relevant molecules will be useful to developing bio-inspired applications involving nanoscale engineering and biofunctionalization of semiconductor surfaces. Observed for the first time, the methionine Y-shaped trimer represents a novel adsorption structure, not only because it results from formation of a stable planar arrangement of a triple (O···H–O) H-bonded cyclic network with three-fold symmetry, but also because of its near-perfect match of the occupied space in the 7×7 half unit cell. These networks of H-bonds and their corresponding interaction energies are the cornerstones of molecular recognition and self-organization and they remain poorly understood.

5.2.2 Experimental Details

The experimental procedure has been discussed in detail in Chapter 2. Furthermore, in the organic molecular beam epitaxy chamber, the 7×7 surface held at room temperature was exposed to L-methionine vaporized from its powder. The absolute coverage of methionine could be determined directly from the STM images for low exposure, for which the 7×7 registry remained visible. We counted the numbers of methionine adspecies in the STM images at these low exposures and estimated the methionine surface number density, assuming the surface number density of the substrate to be that of an unreconstructed Si(111) surface [i.e. 7.83×10^{14} atoms/cm² for 1 monolayer (ML)]. All STM measurements were performed at room temperature in a constant tunneling current mode using an atomically sharp W tip obtained by electrochemical etching.

The DFT-D2 calculations¹⁷⁶ were based on the exchange-correlation functional and projector augmented-wave (PAW) potentials,^{183,184} with the inclusion of van der Waals interactions. Full structural optimization using the generalized gradient approximation,^{182,171} as defined by Perdew, Burke, and Ernzerhof (GGA-PBE),¹⁷² were performed for L-methionine molecules adsorbed on a model Si(111)7×7

surface as represented by a $\text{Si}_{200}\text{H}_{49}$ slab using the dimer-atom-stacking fault (DAS) model.^{29,28} All five layers of Si atoms and all of the methionine molecules were relaxed until the total residual force was below $0.01 \text{ eV}/\text{\AA}$ using the conjugate-gradient algorithm, with details given elsewhere.²³³ The Vienna Ab initio Simulation Package (VASP, version 5.3.3)^{178,180,181} with the MedeA platform (Materials Design)²³⁴ was used to implement the calculations.

5.2.3 Results and Discussion

In our recent XPS study on L-methionine on the $\text{Si}(111)7\times 7$ surface,²³³ we observe N–H dissociative adsorption of a methionine molecule through a dehydrogenated amino group, producing a unidentately N-bonded adspecies (along with a dissociated H atom) in the interfacial layer. To further investigate specific adsorption geometries of methionine on various 7×7 sites, we conduct STM studies for the very early growth stage of the interfacial layer. Figure 5.5 shows the corresponding filled-state and empty-state STM images ($35\times 35 \text{ nm}^2$) collected, respectively, at -1.7 and $+1.7 \text{ V}$ sample bias with a 0.2 nA tunneling current, for a 0.01 ML coverage (corresponding to 5 s exposure) of methionine on $\text{Si}(111)7\times 7$ at room temperature. Three dark depression features with “delta”, “oval” and “Y” shapes can be identified on the 7×7 surface registry from the filled-state image (Figure 5.5a). Dark depression features usually correspond to saturation of the dangling bond sites in a similar way as adsorbed organic molecules such as multicyclic aromatic molecules⁸³ or long-chain dienes.^{93,94,95} Figure 5.5c shows that there are two distinct delta features for the darkest depression within a half unit cell, each with a less dark depression feature on the other (complementary) half unit cell with a different intensity. We attribute the first delta feature M1 to a localized monomer within a half unit cell, the presence of which causes the intensity reduction in the protrusion of the center adatom across the dimer wall. The brighter appearance of the center adatom and corner adatom on the left of the delta feature is due to reverse charge transfer from the restatom location at which adsorption of the dissociated H atom occurs. The second delta feature M2 can be assigned to a monomer bonded to a center adatom with the overhanging moiety undergoing long-range interaction with the center adatom across the dimer wall, which causes the observed depression in the adjacent half unit cell. Similarly, the brighter center adatom and corner adatom on the right side of the second delta feature is caused by adsorption of the dissociated H atom at the restatom. Evidently, the corresponding empty-state image (Figure 5.5f) shows a “ Λ -shaped” depression feature (a missing bright spot) at the center adatom for both delta depression features M1 and M2 (Figure 5.5c). The localization of the Λ -shaped empty-state feature at a single center adatom site confirms the covalent bonding interaction from a single methionine monomer adspecies. These two features M1 and M2 are found on

both faulted and unfaulted half unit cells, with the faulted half unit cell being more populated by these monomer features than the unfaulted half unit cell (Figure 5.5a).

The oval depression feature shown in Figure 5.5d may be considered as an overlap of two M1 delta features, each located at the adjacent center adatom across the dimer wall in the unit cell. We can also identify the adsorption sites of the dissociated H atoms at the two restatoms next to the respective pairs of brighter protrusions for the center-adatom and corner-adatom. The corresponding empty-state image (Figure 5.5g) also shows an oval-shaped depression (located at the two center adatom sites) surrounded by eight equally bright protrusions at neighbouring adatom sites. These oval features can therefore be attributed to methionine dimer consisting of two monomers unidentately bonded at center adatoms, likely in the M1 configuration, in adjacent half unit cells.

Similarly, the filled-state Y depression feature shown in Figure 5.5e can be regarded as the overlap of three M2 delta features, each located at the center adatom of a half unit cell. The discernibly minor intensity reduction at the center adatom across the dimer wall in the adjacent half unit cell is consistent with the presence of the monomer “overhanging” on the other side of the dimer wall. In the corresponding empty-state image (Figure 5.5h); a large bright protrusion at the center of the half unit cell is connected to three smaller bright protrusions at the apices of the half unit cell, forming a three-point star configuration within the half unit cell. The three-fold symmetry of both the filled-state and empty-state images indicates the presence of three methionine molecules symmetrically organized in the form of a trimer, located at the center of the half unit cell. As expected, the population of the oval (dimer) features is found to be generally less than the monomer features. Interestingly, the population for the Y (trimer) features is larger than that of the dimer features (but less than that of the monomer features), which suggest that anomalous stability could result from the formation of trimer. Furthermore, the trimer appears to be dimensionally commensurate with the 7×7 half unit cell, making the methionine trimer the first supported “magic-number” cluster observed to date. Recently, the adsorption of a synthesized molecule [4-methoxy-N-(3-sulfonatopropyl) pyridinium] as a model of zwitterion has also led to a triangular tri-molecule nanostructure binding electrostatically through the S atom over three restatom sites in a half unit cell of Si(111) 7×7 surface.¹⁰¹ Since DFT calculations suggest that the interaction between 4-methoxy-N-(3-sulfonatopropyl) pyridinium and the substrate is driven by electrostatic forces, these triangular nanostructures start to desorb from the surface at around 375 K. However, the methionine Y trimers are found to be considerably more stable and stay on the surface till 550 K.²³³ This unusual stability is due to the formation of N–Si bonds in the adsorbed methionine moieties of the trimer and is not found in previously reported self-assembled zwitterionic nanostructures.

A statistical analysis of the STM image (of approximately 165 7×7 unit cells) shows that there are more depression features at the center adatoms than the corner adatoms and on the faulted half unit cell (60%) than the unfaulted half unit cell (40%). In the 7×7 reconstruction, the restatom and corner-hole sites have a -1 formal charge each, while the formal charge of the adatom site is $+7/12$. Since each center adatom is surrounded by two restatoms instead of only one restatom for the corner adatom, the electron density of the center adatom is therefore lower than the corner adatom.^{31,32} Consequently, the higher reactivity of the center adatom than the corner adatoms accounts for the observed higher occupancy of all features at the center adatom sites. Similarly, the higher electrophilicity of the adatom sites on the faulted half unit cell than that on the unfaulted half unit cell may explain the observed greater occupancy on the faulted half unit cell.

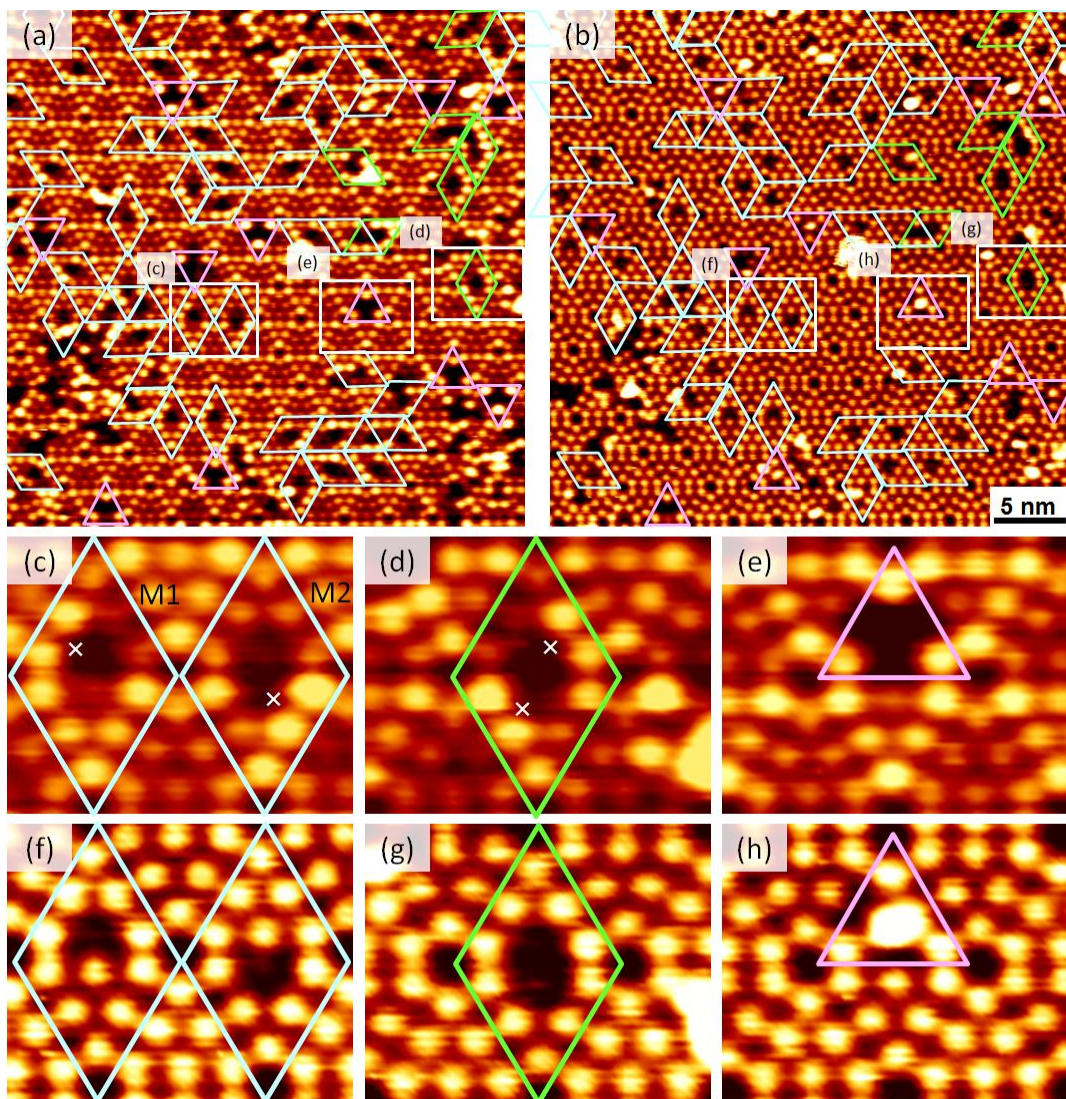


Figure 5.5 (a) Filled-state and (b) empty-state STM images ($35 \times 35 \text{ nm}^2$) for 0.01 ML coverage of L-methionine on Si(111) 7×7 obtained with a sample bias of -1.7 and $+1.7 \text{ V}$, respectively, and a tunneling current of 0.2 nA ; and magnified views ($6 \times 5 \text{ nm}^2$) of filled-state images for (c) monomer “delta” dark depression features, (d) dimer “oval” dark depression feature, and (e) trimer “Y” dark depression feature, along with their corresponding empty-state images shown in (f), (g) and (h), respectively. The locations of the dissociated H atoms are marked by crosses in (c) and (d). In (a) and (b), the unit cells containing methionine monomers and dimers are marked by light cyan and green diamonds, respectively, while the faulted and unfaulted half unit cells containing the trimers are marked by light magenta up and down triangles, respectively.

To further investigate the nature and orientation of the methionine adspecies on specific 7×7 sites, we evaluate the corresponding line profiles of the local density of states (LDOS) of a delta, an oval and a Y features. In the magnified filled-state STM image for the M1 delta feature (Figure 5.6a1), the line

profiles along the long diagonals of the unreacted (L01) and the reacted cells (L11) illustrate the marked differences in LDOS at the positions of the center adatom (CA) and the similarities in LDOS at the restatom (RA), and corner adatom (AA) in both half unit cells (Figure 5.6a2). The line profiles along the three adatoms on the opposite sides of the dimer walls in the reacted unfaulted (L12, Figure 5.6a3) and the adjacent faulted half unit cells (L13, Figure 5.6a4) are also compared with the respective line profiles for the unreacted 7×7 unfaulted (L02) and faulted half unit cells (L03). The dark depression in the magnified empty-state image (Figure 5.5f) appears to cover only one CA, in contrast to two CA sites across the dimer wall in the magnified filled-state image (Figure 5.6a1). The corresponding LDOS profile along the long diagonal of the unit cell (Figure 5.6a2, L11) reveals that the reacted center adatom in the unfaulted half unit cell (CA', where a prime superscript is used here to designate for Si atoms in the unfaulted half unit cell) can no longer be seen because of saturation of the dangling bond with the anchored methionine adspecies. Evidently, the LDOS line profile along the side of the reacted unfaulted half unit cell (Figure 5.6a3, L12) shows that the LDOS at the CA' site becomes greatly reduced while that at the adjacent AA' becomes slightly enhanced, when compared with the respective sites of the unreacted unfaulted half unit cell (Figure 5.6a3, L02). This suggests that the adsorption of the dissociated H atom at the restatom site in the reacted unfaulted half unit cell (RA') may cause a reverse charge transfer from RA' back to the surrounding adatoms (left AA' in L12). The LDOS line profile along the side of the adjacent faulted half unit cell on the other side of the dimer wall (Figure 5.6a4, L13) shows a lower LDOS at the CA site while that at neighboring AA sites remain essentially unchanged, when compared to those of the unreacted faulted half unit cell (Figure 5.6a4, L03). We show a schematic diagram of the delta feature in Figure 5.6a5 to illustrate the positions of dissociated H atom adsorbed on a RA' site and the anchored methionine adspecies (marked by a smaller and larger black solid circles, respectively), and the resulting LDOS changes in the affected adatoms in the rest of the unit cell. In contrast to the M1 delta feature in Figure 5.5c, the LDOS profile in the half unit cell adjacent to reacted half unit cell across the dimer wall for M2 delta feature is evidently darker (not shown).

To determine plausible adsorption geometries for the M1 and M2 delta features and to understand the nature of the interactions between the methionine adspecies and the surface, we conduct large-scale DFT-D2 calculations. Our recent XPS study of methionine adsorption on Si(111) 7×7 ²³³ has shown that methionine undergoes N–H dissociative adsorption on the 7×7 surface, resulting in N–Si bond formation through the dehydrogenated amino group. We therefore put an isolated dehydrogenated methionine molecule on various “test” combinations of selected 7×7 sites (e.g., CA and AA in both faulted and unfaulted half unit cells, and also across the dimer wall), with the dissociated H atom located

appropriately at a nearest restatom site. Optimized equilibrium geometries and their corresponding adsorption energies are then obtained from the DFT-D2 calculations (Figure C4, Appendix C). As a methionine adspecies could adopt a wide variety of orientations with respect to the 7×7 surface site registry, a selection of the most stable adsorption configurations over a total of 20 test configurations is made on the basis of their total energies after optimization. Among the calculated adsorption configurations that involve bonding through the dehydrogenated amino group with the rest overhanging across the dimer wall, the geometry with the S atom closest to the CA' site across the dimer wall (Figure C4a1, with a separation of 2.55 Å between S and Si adatom) is 0.189 eV and 0.335 eV more stable than that with the molecular plane (the plane containing the C–S–C backbone) near parallel (Figure C4a2, with a S-to-CA' separation of 4.26 Å) and near perpendicular to the Si adatom surface plane (Figure C4a3, with a S-to-CA' separation of 5.12 Å), respectively. For other unidentate configurations that involve methionine adspecies bonding completely within a half unit cell, the configuration with the S atom atop of the Si restatom gives the most stable geometry (Figure C4b1, with a separation of 2.33 Å between S and Si restatom), with its adsorption energy 0.224 eV lower than the unidentate configuration across the dimer wall (Figure C4a1). Among the calculated adsorption configurations considered here, the geometry with the S atom closest to a Si adatom or restatom (Figure C4), i.e. with the shortest S-to-CA', S-to-CA, or S-to-RA separation, is found to be more stable than other configurations.

For the M1 delta depression feature (Figure 5.7a), our large-scale DFT-D2 calculation therefore shows that the most favorable adsorption configuration of methionine monomer adspecies within a half unit cell corresponds to a dehydrogenated methionine N-bonded on the center adatom site with its S atom undertaking long-range interaction with a restatom through the lone-pair electrons, along with the dissociated H atom on other restatom site in the same half unit cell (Figure C4b1). The M2 delta depression feature (Figure 5.7b) then corresponds to the second most stable configuration (Figure C4a1), which involves a dehydrogenated methionine N-bonded on a center adatom site in a half unit cell with long-range interaction between the lone-pair electrons of the S atom and a center adatom site in an adjacent half unit cell across the dimer wall, along with the dissociated H atom on a restatom in the first half unit cell. This configuration (Figure 5.7b) accounts for the discernibly darker depression in the adjacent half unit cell when compared with the M1 configuration (Figure 5.7a). Our previous STM and XPS studies on adsorption of L-cysteine on Si(111) 7×7 surface at a very low coverage have supported dissociative adsorption via the amino and thiol functional group to form a bidentate adsorption configuration across the dimer wall.⁹⁸ Unlike cysteine, dissociative adsorption via the $-\text{CH}_2-\text{S}-\text{CH}_3$ group in methionine is not possible.²³³ The S atom in methionine could, however, still be sufficiently

nucleophilic to exert long-range interaction with electrophilic sites (such as CA). Although the calculated adsorption energy for the M1 configuration located at the corner adatom (-5.544 eV, Figure C4b5) is only slightly less negative than that located at the center adatom (-5.573 eV, Figure C4b1) but is discernibly more negative than the M2 configuration (-5.349 eV, Figure C4a1), we do not observe any M1-like delta feature located at a corner adatom but find M2 delta feature by STM. The higher electron charge of the center adatom than the corner adatom makes it more reactive and therefore provides a “kinetically favored” mechanism for the initial adsorption.

For the oval depression feature that covers two center adatom sites across the dimer wall (Figure 5.6b1), the LDOS line profile along the long diagonal of the reacted unit cell (Figure 5.6b2, L24) clearly shows missing LDOS at the CA and CA' sites, which is also in accord with greatly reduced LDOS at CA' along the short diagonals L25 (Figure 5.6b3) and at CA along L26 (Figure 5.6b4), all relative to the long diagonal L04 in the unreacted unit cell. Higher LDOS are also found along the short diagonal L25 at AA' (Figure 5.6b3) and along L26 at AA (Figure 5.6b4), all relative to their respective short diagonal L05 and L06 in the unreacted cell. This is due to reverse charge transfer from a reacted restatom site back to an adjacent corner adatom site as a result of adsorption of the dissociated H atom on the restatom site. In Figure 5.6b5, we illustrate schematically the LDOS distribution of the oval feature for dissociative adsorption of two methionine molecules on adjacent CA and CA' sites across the dimer wall, with the dissociated H atoms adsorbed on the respective nearest RA and RA' sites. Our DFT-D2 calculation for the oval feature shows that the most stable dimer corresponds to adsorption of dehydrogenated methionine at adjacent CA and CA' sites across the dimer wall (Figure C10b). This dimer is formed by a single $\text{O}\cdots\text{H}-\text{O}$ H-bond between two vicinal carboxylic acid groups of two dehydrogenated methionine adspecies (in a head-to-head configuration). Interestingly, a slightly more stable calculated dimer configuration, consisting of adsorption of two dehydrogenated methionine at CA and RA' sites diagonally across the dimer wall and formed by two $\text{O}\cdots\text{H}-\text{O}$ H-bonds (Figure C10a), is not supported by our STM data. This is consistent with our hypothesis that the lower electron charge at the corner adatom than the center adatom makes it less reactive and therefore less kinetically favored for the initial adsorption. An overlay of the most probable dimer structure on the oval feature is shown in Figure 5.7c.

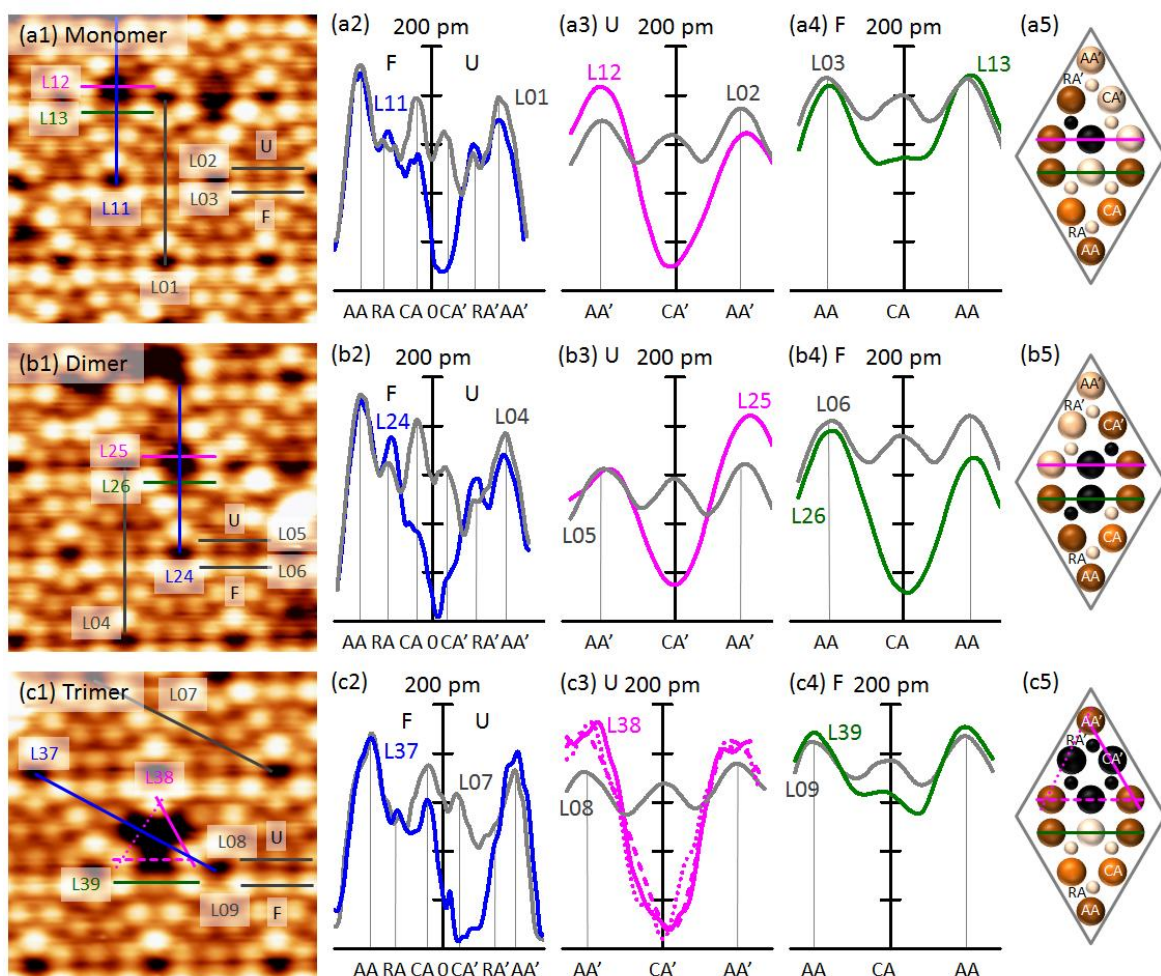


Figure 5.6 High-magnification STM filled-state images ($7.8 \times 7.8 \text{ nm}^2$) of (a1) “delta”, (b1) “oval” and (c1) “Y-shaped” dark depression features for L-methionine adspecies on Si(111) 7×7 surface at room temperature. LDOS profiles for the delta feature (a2) along the long-diagonal L11, and short-diagonals of the reacted (a3) unfaulted half unit cell (L12) and (a4) faulted half unit cell (L13), all compared with the corresponding profiles for the unreacted complete unit cell and half unit cell (a2) L01, (a3) L02, and (a4) L03, respectively. LDOS profiles for the oval features (b2) along the long-diagonal L24, and short-diagonals of the reacted (b3) unfaulted half unit cell (L25) and (b4) faulted half unit cell (L26), all compared with the corresponding profiles for the unreacted complete unit cell and half unit cell (b2) L04, (b3) L05, and (b4) L06, respectively. LDOS profiles for the Y features (c2) along the long-diagonal L37, and short-diagonals of the reacted (c3) unfaulted half unit cell (L38) and (c4) faulted half unit cell (L39), all compared with the corresponding profiles for the unreacted complete unit cell and half unit cell (c2) L07, (c3) L08, and (c4) L09, respectively. The silicon corner atom (AA) to restatom (RA) to center adatom (CA) on the faulted (F) half unit cell and the corresponding AA', RA' and CA' on the unfaulted (U) half unit cell are used as reference points for the linescans of the LDOS profiles. The separation between two adjacent center adatom across the dimer wall (i.e. the CA-to-CA' separation) is 0.68 nm and that between adjacent center adatom and corner adatom (i.e. the CA-to-AA separation) is 2.34 nm. The STM images are obtained with a sample bias of -1.7 V and a tunneling current of 0.2 nA. (a5)-(c5) depict the corresponding schematic diagrams of delta, oval and Y STM features, with the large and small black solid circles indicating the anchored locations of the dehydrogenated methionine and the dissociated hydrogen atom, respectively.

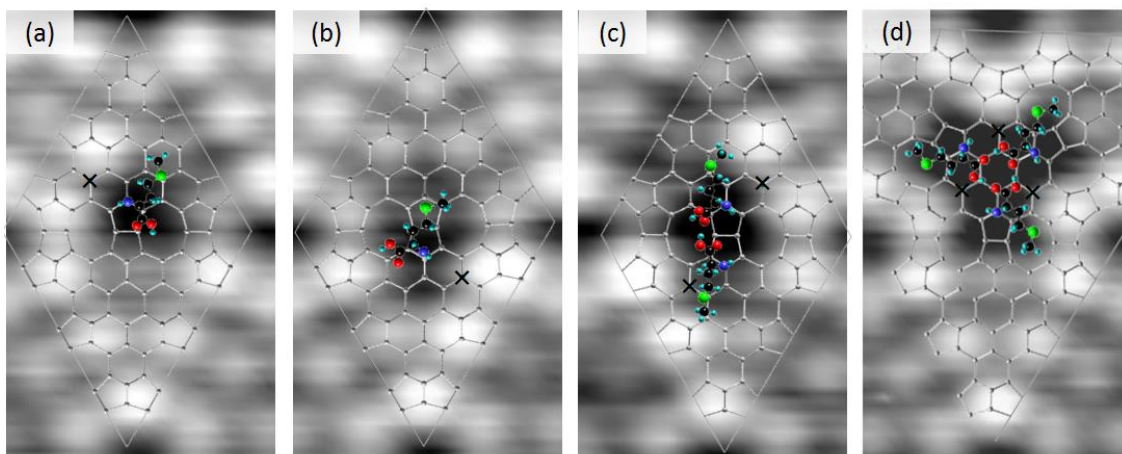


Figure 5.7 Overlays of the most stable equilibrium configurations of methionine adspecies on (a) M1 and (b) M2 “delta”, (c) “oval”, and (d) “Y-shaped” dark depression features of the STM filled-state images. The adsorption configurations have been obtained for methionine monomers, dimer and trimer on a supercell consisting of four $\text{Si}_{200}\text{H}_{49}$ slabs (used as a model of the $\text{Si}(111)7\times 7$ surface) by DFT-D2 calculations. Only the top most Si layer is shown for clarity. The locations of the dissociated H atoms are marked by crosses.

In the magnified filled-state STM image for the Y dark depression feature (Figure 5.6c1), the Y feature evidently covers all three center adatom sites and three restatom sites within the unfaulted half unit cell. This is also illustrated by considerable LDOS deficit at CA' along the long diagonal of the reacted half unit cell (L37), relative to that of the unreacted half unit cell (L07) in Figure 5.6c2. N–H dissociative adsorption of methionine also produces a dissociated H atom adsorbed at an adjacent RA' site, which causes a reverse charge transfer from RA' back to a neighbouring CA' site. This leads to a higher LDOS at AA' , as observed in L38, when compared to that for the unreacted unit cell, L08 (Figure 5.6c3). The nearly identical LDOS profiles along L38 and its two other equivalent AA' to CA' to AA' directions (marked as solid, dashed and dotted lines) in the unfaulted half unit cell (Figure 5.6c3) confirm the three-fold symmetry of the Y dark depression feature. In Figure 5.6c5, we show schematically that the Y feature corresponds to three methionine adspecies on three CA' sites and three dissociated H atoms on adjacent RA' sites, all within a half unit cell. The LDOS profile along the parallel AA to CA to AA direction in the adjacent faulted half unit cell across the dimer wall (L39) exhibits discernible LDOS deficit at the CA site when compared with the profile of the unreacted faulted half unit cell along the same direction (L09), which suggests charge transfer from CA' to an adjacent reacted CA site or the presence of overhang of the tail ends of methionine adspecies across the dimer wall (Figure C11, Appendix C). Our ultra-large-scale DFT-D2 calculations suggest trimer formation of methionine adspecies within the unfaulted half unit cell. Unlike the calculations for the monomer and dimer features

where we use only one $\text{Si}_{200}\text{H}_{49}$ slab, we employ a supercell of four $\text{Si}_{200}\text{H}_{49}$ slabs, i.e. a $\text{Si}_{800}\text{H}_{196}$ cluster, as a model for the 7×7 surface, and then strategically position three methionine adspecies and their corresponding dissociated H atoms at the respective CA' and RA' sites. The present ultra-large-scale calculation involving over 1000 atoms therefore represents the largest quantum simulation for surface science reported to date, and it provides us with a reliable, precise platform, for the first time, to explore site-specific chemistry of these proteinogenic biomolecules on the 7×7 surface. Each methionine adspecies is covalently N-bonded to the Si center adatom site through the dehydrogenated amino group, with the carboxylic acid group pointing toward the center of the half unit cell and the thiol ether group toward the dimer wall (Figure C11, Appendix C). Interestingly, this molecular orientation is in marked to the monomer M1 and dimer adsorption configurations, in which the carboxylic acid group is pointed towards the dimer wall and the thiol ether group towards the center. It is compelling to suggest that the combination of three M2 monomers (with the surface orientation opposite in alignment to that of M1) in a single half unit cell leads to the formation of the Y trimer. With the free carboxylic acid functional groups of three methionine adspecies pointing toward the center of the half unit cell, formation of triple $\text{O}\cdots\text{H}-\text{O}$ hydrogen bonding is possible, which enables the creation of a cyclic ring structure and thereby significantly stabilizes the adsorption geometry. Figure 5.7d shows an overlay of this plausible calculated configuration of methionine trimer in the 7×7 half unit cell on the corresponding STM image.

5.2.4 Summary

Methionine chemisorbed on $\text{Si}(111)7\times 7$ at room temperature under ultrahigh vacuum condition has been studied by combining high-resolution STM images (and XPS studies) with large-scale DFT-D2 calculations. Both filled-state and empty-state STM images reveal surface clustering from monomers (delta features) to dimer (oval feature), and to trimer (Y feature) at very low methionine coverage. Large-scale DFT-D2 calculations attribute the two delta features to coexistence of two N-Si bonded monomer configurations within a half unit cell on CA (M1) and with overhang across the dimer wall on CA' (M2), along with the respective dissociated H atoms located on RA or RA' sites. A dimer configuration of two methionine adspecies (head-to-head) across the dimer wall containing a single $\text{O}\cdots\text{H}-\text{O}$ H-bond between two vicinal carboxylic acid groups corresponds to the oval feature. The Y feature corresponds to a methionine trimer formed similarly with three methionine adspecies in a head-to-head, ring configuration within a 7×7 half unit cell. Observed for the first time, formation of this supported “magic-number” methionine cluster could be due to the near-perfect match between the dimension and geometry of methionine and the surface registry. Our ultra-large-scale DFT-D2 calculation shows that the Y trimer is

driven by the formation of three O··H–O hydrogen bonds, in a ring configuration, among the unattached carboxylic acid groups from three methionine adspecies, covalently attached to the center adatom sites of Si surface via the N–Si bond. In marked contrast to zwitterionic structures reported for other molecules earlier, the mix of covalent and hydrogen bonding in this configuration accounts for the anomalous stability of the trimer. Fundamental understanding of site-specific interfacial chemistry, including molecular orientation and self-organization, of methionine adspecies on semiconductor surfaces, such as the Si(111)7×7 surface, is useful not only to understanding the growth of component biomolecules into organized nanoarchitectures but also to design of biodevices for biosensors, drug delivery carriers, and bio-inspired nanosystems and appliances.

Chapter 6

Molecular Interaction of Cysteine on Gold Templates Supported on Si(111)7×7

6.1 Introduction

Understanding the molecular interactions of multifunctional bio-organic molecules such as L-cysteine on a single-crystal metallic or semiconductor solid surface is important to developing potential applications in biosensors and biomolecular electronic devices. As one of two sulphur-containing standard amino acids, cysteine is especially interesting because it contains three functional groups: amino ($-\text{NH}_2$), carboxylic acid ($-\text{COOH}$) and thiol ($-\text{SH}$) groups, and they provide a wide variety of bonding possibilities and configurations with the surface and/or with other coadsorbates. The interest in cysteine adsorption on single-crystal metal surfaces stems from their importance in bioanalytical and drug delivery protocols, surface patterning, biofunctionalization, and molecular electronics.^{235,236,237} Cysteine adsorption on different single-crystal surfaces of gold,^{119,121,150,151,152,153,154,155,156,157} silver,^{120,238} and copper^{119,239} both in vacuum and in the solution have been studied by using X-ray photoelectron spectroscopy (XPS), scanning tunneling microscopy (STM), near-edge X-ray absorption fine structure spectroscopy, and computational modelling by density functional theory (DFT) calculations.^{240,241,242} Among all of metal surfaces, gold is known to be the most inert metal. On the nanoscale, Au becomes rather reactive and its unique properties have attracted a lot of attention particularly as nanocatalysts and plasmonic nanoparticles. Cysteine was found to normally bind to the metal in the form of a thiolate through the thiol group.^{119,120,121,243} Depending on the nature of the surface, the other two functional groups, i.e. amino and carboxylic acid groups, could also play an important role in attaching cysteine to the surface.⁹⁸

In spite of the large number of studies on adsorbed cysteine on various single-crystal surfaces of metals,^{119,120,121,150,151,152,153,154,155,156,157,238,239} only a few investigations of its adsorption on semiconductor surfaces have been reported.^{98,206,207} The 7×7 reconstruction of the Si(111) surface is one of the most popular templates used for anchoring both organic and inorganic adsorbates via 18 directional dangling bonds, over six (electron-deficient) adatoms and three (electron-rich) restatoms per each of the faulted and unfaulted half unit cells, and one remaining dangling bond shared among the four corner-hole sites.²⁹ In our recent work on L-cysteine on Si(111)7×7 surface,⁹⁸ we conclude that cysteine can be anchored to the Si substrate through Si–N and/or Si–S covalent linkages in unidentate and/or bidentate arrangement,

thereby providing “permanent” biofunctionalization in this interfacial layer. This interfacial layer (first adlayer) can be used to build a “semi-permanent” transitional layer (second adlayer) of cysteine mediated by interlayer hydrogen bonding between an amino group and a carboxylic acid group. Further exposure of cysteine eventually leads to a zwitterionic multilayer film involving electrostatic interactions between cation ($-\text{NH}_3^+$) and anion moieties ($-\text{COO}^-$). The 7×7 surface also provides an important substrate for a wide range of materials from inert gold and other inorganic adsorbates and/or superstructures to bio/organic molecules, and it therefore offers an ideal testing ground for studying the interaction between a trifunctional biomolecule like cysteine and gold nanoassemblies.

To date, studies of biomolecular interaction with supported metallic nanostructures have not received much attention, despite the importance of metallic nanostructures supported on a semiconductor surface. One notable study has focussed on “coadsorption” of Au and L-cysteine on rutile $\text{TiO}_2(110)$ by XPS.¹⁴⁹ When L-cysteine was exposed to gold clusters on $\text{TiO}_2(110)$, cysteine was found to interact with both the gold deposits and the substrate surface (particularly the defect sites) through the thiol group with formation of S–Au and S–Ti bonds, respectively. Here, we present the first investigation of the interactions of L-cysteine with various gold nanoassemblies deposited on $\text{Si}(111)7\times 7$ at three different coverages, including Au monomers and dimers, Au honeycomb nanonetwork, and Au nanocrystallite film, at room temperature under ultrahigh vacuum condition.

6.2 Experimental Details

The experimental procedure has been discussed in detail in Chapter 2. Furthermore, to obtain the various Au nanoassemblies on the $\text{Si}(111)7\times 7$ surface, the clean 7×7 substrate was transferred to a molecular beam epitaxy growth chamber, in which Au (99.9999% purity, Alfa Aesar) was deposited by thermal evaporation at $1040\text{ }^\circ\text{C}$ with the 7×7 substrate held at room temperature. Appropriate doses of Au were exposed to a freshly cleaned 7×7 surface as described above to produce (a) Au monomers and dimers (nanoclusters), (b) Au honeycomb nanonetwork, and (c) Au nanocrystallite film.²⁰⁴ After each exposure, both STM and XPS measurements were performed on the same supported Au nanoassembly in the analysis chamber. Each of the Au nanoassemblies was then introduced to the organic molecular beam epitaxy chamber to be deposited with L-cysteine using a low-temperature organic effusion cell. After the cysteine exposure on the Si surface, XPS spectra of the Si 2p, Au 4f, N 1s, C 1s, O 1s, and S 2s regions were recorded with an energy resolution of 0.7 eV full width at half maximum (for the Ag $3d_{5/2}$ photoline at 368.3 eV).

6.3 Results and Discussion

Figure 6.1 shows the STM images of three Au nanoassemblies obtained with appropriate exposures on Si(111)7×7: clusters (0.004 ML), honeycomb nanonetwork (0.76 ML), and nanocrystallite film (3.97 ML). Details of the growth evolution of Au nanoassemblies obtained at room temperature under ultrahigh vacuum condition have been described elsewhere.²⁰⁴ Briefly, at the lowest Au coverage, there are only sextet and triad STM features located, respectively, on the faulted and unfaulted half unit cells, and these features correspond to individual Au adatoms translocating among all six adatoms or three center adatom sites. There are also scribble STM features that correspond to a fast-moving Au dimer within a half unit cell. Further increase in the Au coverage to 0.76 ML leads to the formation of a complete gold silicide layer with a honeycomb nanonetwork that covers the entire Si(111)7×7 surface except for the corner holes. In effect, this new gold silicide nanonetwork represents a two-dimensional template of nanopores (~1 nm in pore size) that could be used for molecular trapping and nanotemplating application. The gold silicide honeycomb nanonetwork also offers a new conducting phase of fundamental interest to silicon device fabrication and to a number of interesting applications in biofunctionalization. The presence of gold silicide has been observed for coverage up to ~2 ML. At a higher coverage of 3.97 ML, a thin film of Au nanocrystallites exhibiting regular triangular and polygonal faces, likely the (111) planes, is observed. The corresponding chemical-state compositions for specific Au coverages have been determined in our recent XPS study and are summarized in Figure 6.2a.²⁰⁴ Evidently, the spectra are dominated by a prominent Au 4f_{7/2} (4f_{5/2}) peak near 84.5 eV (88.1 eV) and 84.7 eV (88.3 eV) for clusters (0.004ML) and honeycomb nanonetwork (0.76 ML), respectively, attributed to gold silicide. A second Au 4f_{7/2} (4f_{5/2}) feature emerged at 83.8 eV (87.4 eV) at higher Au coverage corresponds to metallic Au.

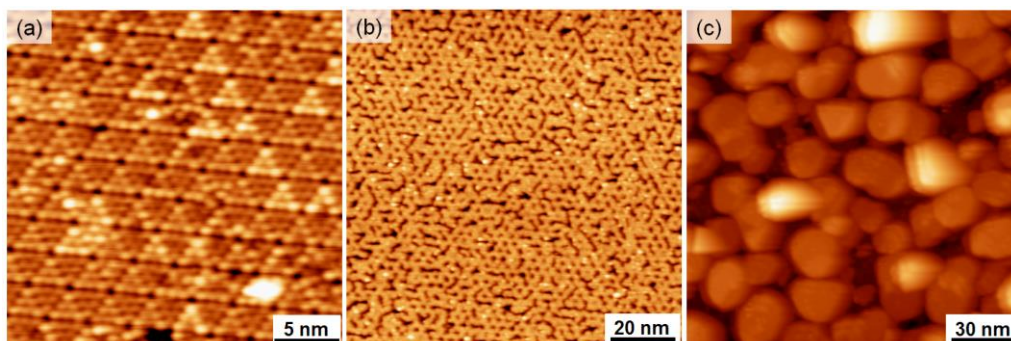


Figure 6.1 Filled-state STM images of (a) 0.004, (b) 0.76, and (c) 3.97 ML coverages of Au on Si(111)7×7 surface at room temperature, all collected with a sample bias of -2.0 V and a tunneling current of 0.2 nA. The fields of view for (a), (b), and (c) are 25×25 nm², 75×75 nm² and 150×150 nm², respectively.

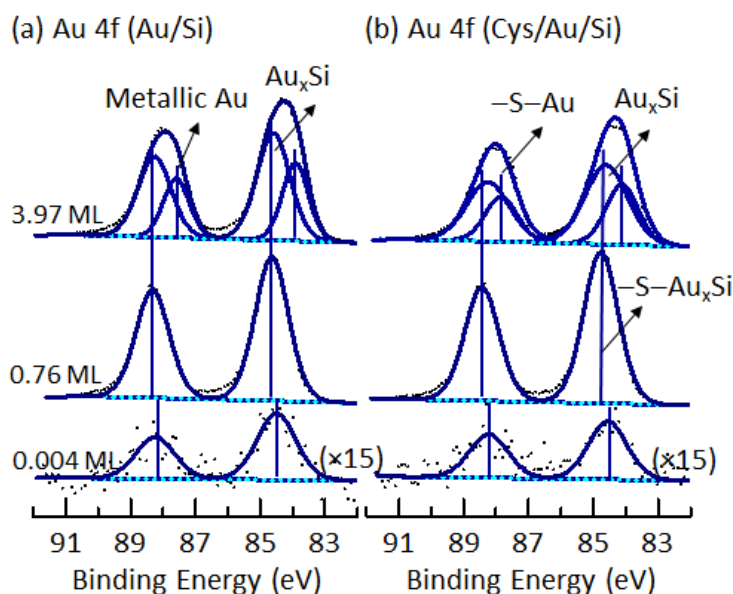


Figure 6.2 XPS spectra of the Au 4f region for three Au nanoassemblies obtained with coverages of 0.004, 0.76 and 3.97 ML on Si(111)7×7 at room temperature, (a) without and (b) with 20 min post-exposure of cysteine.

6.3.1 Interaction of Cysteine with Supported Gold Monomers and Dimers (0.004 ML)

Figure 6.3 shows the O 1s, N 1s, C 1s, and S 2s spectra of cysteine deposited at room temperature on 0.004 ML of Au supported on Si(111)7×7 surface as a function of cysteine exposure time, with their

corresponding peak positions and assignments of the fitted features given in Table 6.1. The corresponding filled-state STM image for this supported Au nanoassembly (Figure 6.1a) shows a very low surface density of Au adatoms (i.e., 0.004 ML coverage of Au), with the majority of the 7×7 reconstruction remaining clearly visible. We therefore expect that the cysteine growth evolution should follow closely that on a pristine Si(111) 7×7 surface, but with some added contribution due to the presence of Au monomers and dimers. Not surprisingly, then, there is a three-stage growth process for cysteine, from chemisorbed interfacial layer (first stage, 0.5-1.5 min) to transitional layer (second stage, 4.5-60 min) and to zwitterionic multilayer film (third stage, 150 min). The coexistence of the N 1s feature at 398.8 eV (Figure 6.3b) and the S 2s feature at 227.1 eV (Figure 6.3d) at the lowest exposure (0.5 min), attributed to N–Si and S–Si bonds respectively, indicates unidentate and/or bidentate chemisorption of cysteine at the interfacial layer through the respective N–H and S–H dissociative adsorption on the 7×7 surface. The second N 1s feature emerged at a higher binding energy upon higher exposures (1.5 min and above) is in good accord with the presence of the O–H \cdots N hydrogen bond at 401.1 eV (Figure 6.3b) (where we use the triple-dot line “ \cdots ” to denote a H-bond). This feature therefore confirms the formation of interlayer H-bond (head-to-tail) between a free carboxylic acid group of cysteine in the interfacial layer (first adlayer) and a free amino group of cysteine in the transitional layer (second adlayer). Furthermore, the best fit for the C 1s spectrum (Figure 6.3c) is obtained by attributing four fitted peaks, located from low to high binding energy, to the $-\text{CH}_2-\text{S}-\text{Si}$, $-\text{CH}_2-\text{SH}$, $-\text{CH}-\text{NH}-\text{Si}$, and $-\text{COOH}$ moieties. The relative area ratios of 1:1:1:1 for these C 1s features found for 0.5-1.5 min exposure are consistent with the stoichiometric ratios expected for the first adlayer bonding. As the exposure increases into the transitional layer and zwitterionic multilayer regimes, the relative intensity of the $-\text{CH}_2-\text{S}-\text{Si}$ feature becomes reduced. Finally, the broad O 1s spectrum (Figure 6.3a) for exposure up to 60 min is consistent with the carbonyl component ($-\text{C}=\text{O}$) and hydroxyl oxygen ($-\text{OH}$).

The XPS spectra for the cysteine multilayer obtained at the 150-min exposure on the 7×7 surface pre-exposed with 0.004 ML of Au (Figure 6.3) are also found to be similar to those for cysteine multilayer on a pristine Si(111) 7×7 surface.⁹⁸ The chemical shift of O 1s feature for $-\text{C}=\text{O}/-\text{OH}$ at 532.6 eV to a lower binding energy can be attributed to a carboxylate group ($-\text{COO}^-$), while the appearance of a new N 1s feature at a higher binding energy (401.7 eV) corresponds to a protonated amino group ($-\text{NH}_3^+$). These new features affirm the formation of zwitterionic structure in the multilayer ($\text{NH}_3^+\text{CHCH}_2\text{SHCOO}^-$). The weaker intensity of the $-\text{NH}-\text{Si}$ N 1s feature at 398.8 eV for the 150-min exposure than those for 1.5 min to 60 min exposures (Figure 6.3b) suggests that the thickness of the zwitterionic layer has exceeded the photoelectron escape depth. Furthermore, the S 2s peak at 228.4 eV

corresponds to an intact thiol group (Figure 6.3d), similar to that observed for cysteine powder and the multilayer cysteine film on a pristine Si(111)7×7 surface.⁹⁸ The corresponding C 1s spectrum (Figure 6.3c) consists of a broad band centered at 286.4 eV, attributable to the three alkyl carbons in $-\text{CH}_2-\text{S}-\text{Si}$, (at 284.6 eV), $-\text{CH}_2-\text{SH}$ (at 286.0 eV) and $-\text{CH}-\text{NH}_3^+$ (at 286.7 eV), and a weaker feature at 288.8 eV corresponding to the carboxylate group.

We also obtain the Au 4f spectra for a 20-min cysteine exposure deposited on Si(111)7×7 pre-deposited with 0.004 ML of Au (Figure 6.2b). The presence of cysteine appears to cause only a 0.1 eV shift in the Au 4f_{7/2} peak to a higher binding energy (84.6 eV), when compared to the corresponding pristine supported Au nanoassembly shown in Figure 6.2a.

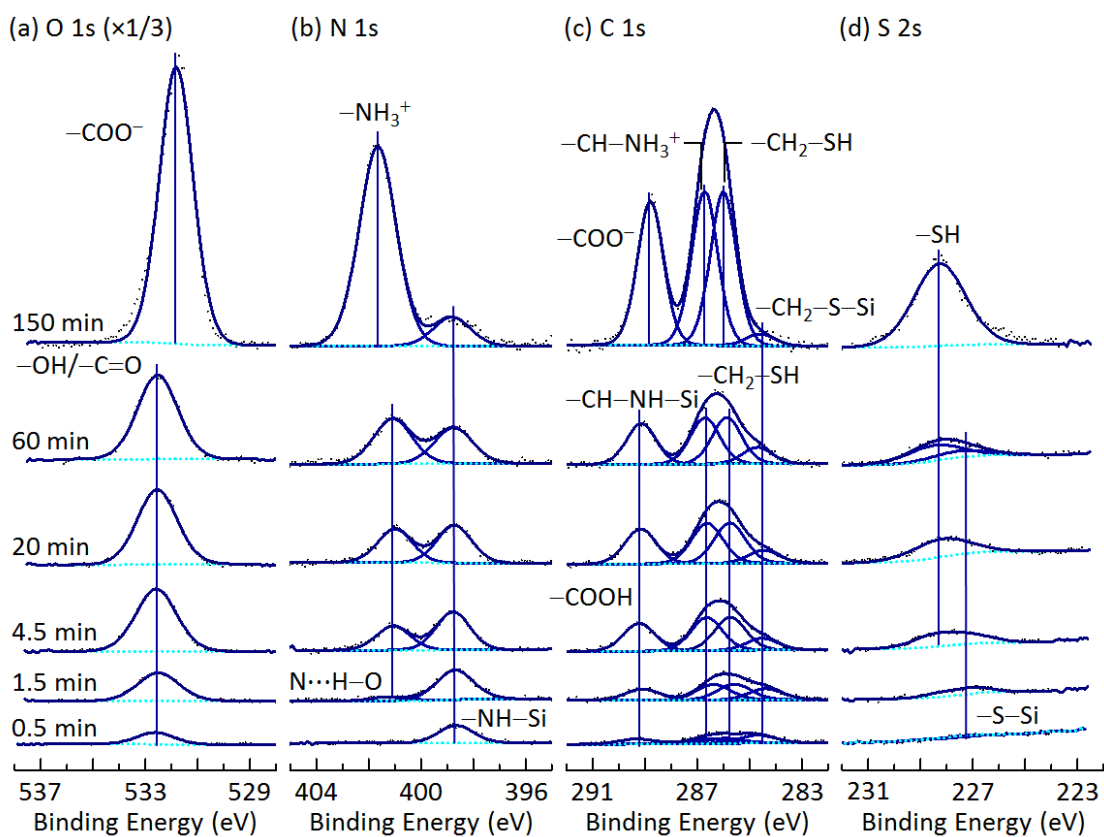


Figure 6.3 XPS spectra of (a) O 1s, (b) N 1s, (c) C 1s, and (d) S 2s regions of L-cysteine deposited on Au(0.004 ML)/Si(111)7×7 as a function of cysteine exposure time.

Table 6.1 Binding energies (in eV) of fitted peak maxima for various XPS core-level features and their assignments for different exposures of L-cysteine on Au(0.004 ML)/Si(111)7×7.

| Core level | 0.5 min | 1.5 min | 4.5 min | 20 min | 60 min | 150 min | Assignment |
|-------------|---------|---------|---------|--------|--------|---------|---|
| O 1s | 532.6 | 532.5 | 532.6 | 532.6 | 532.6 | 531.7 | -C-OH/-C=O |
| | | | | | | | -COO ⁻ |
| N 1s | 398.8 | 398.7 | 398.8 | 398.7 | 398.8 | 398.8 | -NH-Si |
| | | 401.1 | 401.1 | 401.0 | 401.1 | 401.7 | N··H-O -NH ₃ ⁺ |
| C 1s | 284.4 | 284.4 | 284.5 | 284.4 | 284.6 | 284.6 | -CH ₂ -S-Si |
| | | 285.6 | 285.7 | 285.7 | 285.8 | 286.0 | -CH ₂ -SH |
| | 286.3 | 286.4 | 286.4 | 286.4 | 286.4 | | -CH-NH-Si |
| | | | | | | 286.7 | -CH-NH ₃ ⁺ |
| | | | | | | 288.8 | -COO ⁻ |
| | 289.2 | 289.0 | 289.2 | 289.1 | 289.1 | | -COOH |
| S 2s | 227.1 | 227.1 | 227.2 | 277.2 | 227.2 | | -S-Si |
| | | | 228.2 | 228.2 | 228.2 | 228.3 | -SH |

6.3.2 Interaction of Cysteine with Supported Gold Silicide Honeycomb Nanonetworks (0.76 ML)

Figure 6.4 shows the O 1s, N 1s, C 1s, and S 2s spectra of cysteine deposited at room temperature on gold silicide honeycomb nano-network supported on Si(111)7×7 surface as a function of cysteine exposure time, with their corresponding peak positions and assignments of the fitted features given in Table 6.2. The filled-state STM image (Figure 6.1b) shows that the honeycomb nanonetwork is made up of six triangular Au clusters (surrounding each corner hole) interconnected to one another at the dimer rows of the Si(111)7×7 substrate, with each empty corner hole including one directional dangling bond. Our recent XPS study has ascertained that the honeycomb nanonetwork exhibits the gold silicide chemical states.²⁰⁴ Furthermore, our complementary DFT calculations suggest a Au₉Si₃ structure as a possible nucleation center for one of the six segments of the honeycomb unit, with each segment consisting of Au atoms located at three different Si sites (adatom, restatom and pedestal atom sites). The Au atoms in these segments essentially make up the majority of the first gold silicide layer, with some of center-adatom sites exposed. These unoccupied dangling bonds on the center adatom sites and also corner holes could therefore offer plausible anchoring points for inorganic/biomolecules adspecies on the top of the honeycomb nanonetwork.

At very low exposures of 0.5-1.5 min, the S 2s spectra (Figure 6.4d) show only one weak peak at 226.4 eV, attributed to the -S-Au bond, while the N 1s spectra (Figure 6.4b) reveal two weak peaks at

398.5 and 400.4 eV, attributed to $-\text{NH}-\text{Si}$ and $-\text{NH}_2$, respectively.²⁴⁴ These assignments indicate the coexistence of two unidentate adspecies (in the interfacial layer) that involve bonding through the thiol group ($-\text{SH}$) with Au atoms and through the amino group ($-\text{NH}_2$) with Si atoms. With increasing exposure above 5.0 min, we observe the emergence and growth of a new N 1s feature at 401.8 eV (Figure 6.4b), attributable to protonated amino group ($-\text{NH}_3^+$). The corresponding O 1s band centered at 533.0 eV (Figure 6.4a) consists of two O 1s peaks for the carbonyl group ($-\text{C}=\text{O}$) and hydroxyl group ($-\text{OH}$), and for the carboxylate group ($-\text{COO}^-$) at a lower binding energy and with lower intensity. Furthermore, the S 2s feature at 228.3 eV for exposures above 5 min indicates the presence of an intact thiol group (Figure 6.4d), which further confirms the existence of zwitterionic structures in the physisorbed layer. At the same time, there appears to be equal population of the $-\text{S}-\text{Au}$ moiety even for the higher cysteine exposure, which suggests that the thickness of the zwitterionic layer has not exceeded the photoelectron escape depth. The C 1s spectra shown in Figure 6.4c can be fitted with seven C 1s components, which can be attributed, respectively from low to high binding energy, to $-\text{CH}_2-\text{S}-\text{Au}$, $-\text{CH}_2-\text{SH}$, $-\text{CH}-\text{NH}-\text{Si}$, $-\text{CH}-\text{NH}_2$, $-\text{CH}-\text{NH}_3^+$, $-\text{COO}^-$, and COOH .

The complementary Au 4f spectrum for a 20-min exposure of cysteine to the Au honeycomb nanonetwork shown in Figure 6.2b indicates that the formation of $\text{S}-\text{Au}$ bond has evidently shifted the gold-silicide Au 4f_{7/2} peak to a higher binding energy (84.85 eV) from 84.7 eV for a pristine Au honeycomb nanonetwork. This shift to a higher binding energy is consistent with cysteine interaction through the $\text{S}-\text{Au}$ bonding that causes a more electron-withdrawing chemical environment that leads to a more positive Au ion core.

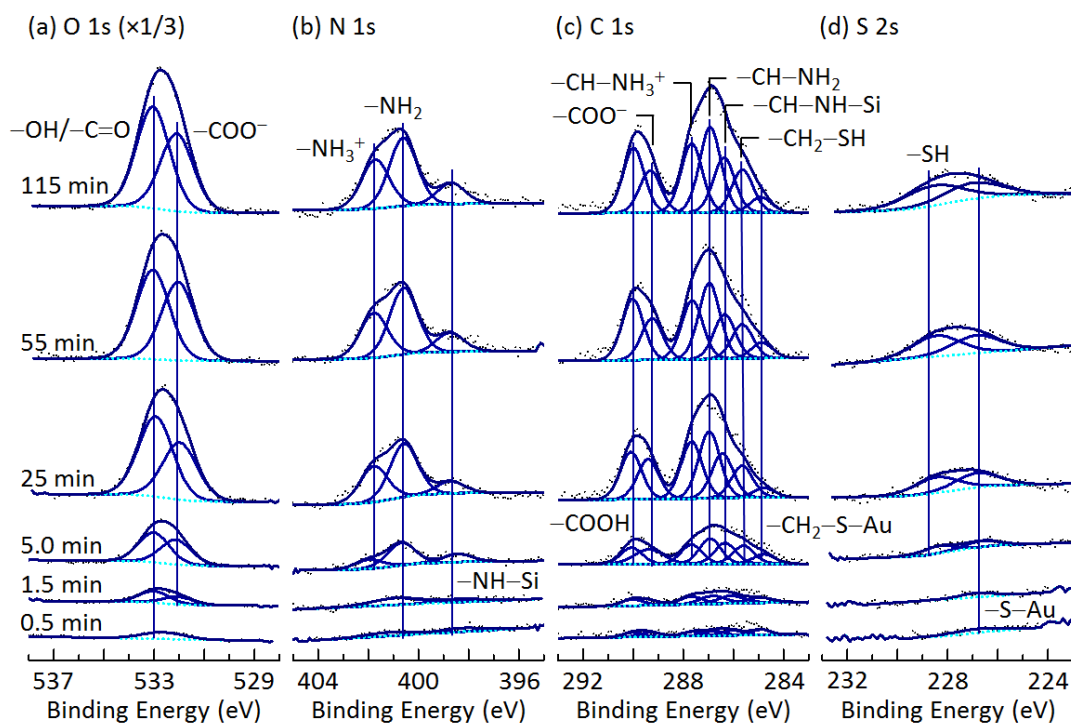


Figure 6.4 XPS spectra of (a) O 1s, (b) N 1s, (c) C 1s, and (d) S 2s regions of L-cysteine deposited on Au(0.76 ML)/Si(111)7×7 as a function of cysteine exposure time.

Table 6.2 Binding energies (in eV) of fitted peak maxima for various XPS core-level features and their assignments for different exposures of L-cysteine on Au(0.76 ML)/Si(111)7×7.

| Core level | 0.5 min | 1.5 min | 5.0 min | 25 min | 55 min | 115 min | Assignment |
|------------|---------|---------|---------|--------|--------|---------|----------------------------------|
| O 1s | 533.0 | 533.0 | 533.0 | 533.0 | 533.1 | 533.0 | -C-OH/-C=O |
| | | 532.2 | 532.2 | 532.0 | 532.1 | 532.2 | -COO ⁻ |
| N 1s | 398.5 | 398.5 | 398.6 | 398.7 | 398.7 | 398.7 | -NH-Si |
| | | | | | | | N...H-O |
| | 400.4 | 400.4 | 400.4 | 400.5 | 400.5 | 400.5 | -NH ₂ |
| | | | 401.8 | 401.8 | 401.8 | 401.8 | -NH ₃ ⁺ |
| C 1s | 284.6 | 284.7 | 284.8 | 284.9 | 284.9 | 284.9 | -CH ₂ -S-Au |
| | | | 285.7 | 285.8 | 285.7 | 285.7 | -CH ₂ -SH |
| | 286.3 | 286.4 | 286.5 | 286.4 | 286.4 | 286.4 | -CH-NH-Si |
| | 285.9 | 286.7 | 286.8 | 286.6 | 286.9 | 286.9 | -CH-NH ₂ |
| | 287.6 | 287.7 | 287.6 | 287.7 | 287.7 | 287.7 | -CH-NH ₃ ⁺ |
| | 289.2 | 289.2 | 289.3 | 289.4 | 289.3 | 289.3 | -COO ⁻ |
| 290.1 | 290.0 | 290.1 | 290.1 | 290.0 | 290.0 | -COOH | |
| S 2s | 226.5 | 226.5 | 226.5 | 226.7 | 226.7 | 226.7 | -S-Au |
| | | | 228.2 | 228.3 | 228.3 | 228.3 | -SH |

Figure 6.5 shows typical filled-state STM images ($75 \times 75 \text{ nm}^2$), collected at -2.0 V sample bias with a 0.2 nA tunneling current, for three cysteine exposures on the supported Au honeycomb nanonetwork. In these STM images, brightened features on top of the honeycomb nanonetwork generally indicate cysteine adspecies, and their number density appears to increase with increasing cysteine exposures. Furthermore, closer examination of STM images reveals that these cysteine adspecies could anchor on both Au hexagonal grids ($\sim 4 \text{ nm}$ wide) and nanopores ($\sim 1 \text{ nm}$ dia.). These primary results from both STM and XPS studies are therefore reinforcing our hypothesis that this novel gold silicide honeycomb nanonetwork, with its two-dimensional template of nanopores, offers a number of interesting potential applications for molecular trapping. For example, it is possible to fill all the nanopores with cysteine adspecies (with N–Si bonding) by removing cysteine adspecies on the Au honeycombs (with S–Au bonding) using simple annealing at an appropriate temperature. For larger molecules, adsorption will likely occur only on the Au honeycombs and the nanopores can then be used to trap a second type of (smaller) molecules. This provides a viable recipe of constructing a hybrid super-nanoarchitectures consisting of a single smaller molecule (attached to the nanopore) surrounded by larger molecules (attached to the Au honeycomb).

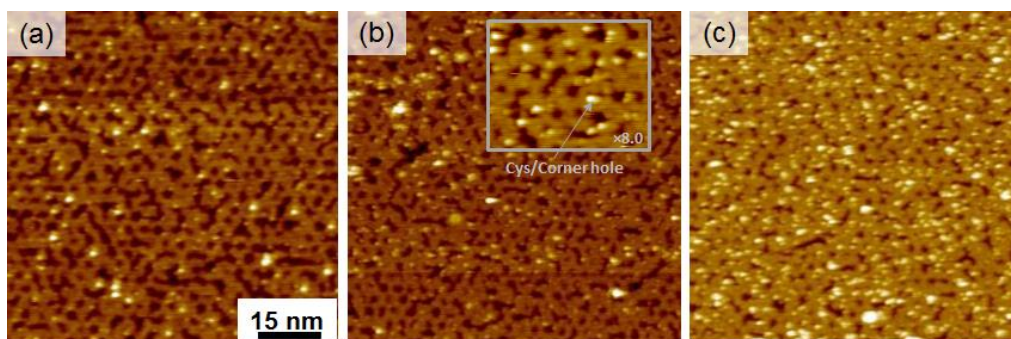


Figure 6.5. Filled-state STM images ($75 \times 75 \text{ nm}^2$), obtained with a sample bias of -2.0 V , for (a) 5 s, (b) 20 s, and (c) 65 s exposure of cysteine on Au honeycomb nanonetwork supported on Si(111) 7×7 surface. Inset in (b) shows a magnified view ($\times 8$) of a cysteine adspecies on the nanopore/corner hole.

6.3.3 Interaction of Cysteine with Au Nanocrystallite Film (3.97 ML)

Figure 6.6 shows the O 1s, N 1s, C 1s, and S 2s spectra of cysteine deposited at room temperature on a Au nanocrystallite film supported on Si(111) 7×7 surface as a function of cysteine exposure time, with their corresponding peak positions and assignments of the fitted features given in Table 6.3. The filled-state STM image (Figure 6.1c) shows the Au nanocrystallites with their regular triangular and polygonal

faces (likely the (111) plane) exposed, reflecting their single-crystalline nature. With 3.76 ML of Au coverage, there is no sign of any 7×7 registry from the Si(111) substrate. As the thiol group is known to interact strongly with noble metals (Au, Ag, Cu) and binds to them as thiolate,^{121,119,120,243} there is no evidence of any three-stage growth process (Figure 6.6), as is similarly found for the Au(0.76 ML)/Si(111) 7×7 nanoassembly. At the lowest exposure (0.5 min), the S 2s peak at 226.6 eV and the N 1s peak at 400.1 eV indicate adsorption of cysteine to Au via a thiolate group and leaving the amino group free. The corresponding O 1s feature consists mainly of a broad peak at 533.0 eV, which can be attributed to unattached -C=O and -OH . This further confirms that L-cysteine chemisorbs at room temperature via the sulfur atom on the supported Au nanocrystallites. With increasing exposure to 1.5-60 min, we observe the emergence of additional features for O 1s at 532.1 eV (Figure 6.6a), N 1s at 402.0 eV (Figure 6.6b), and S 2s at 228.2 eV (Figure 6.6c), which correspond to carboxylate group (-COO^-), protonated amino group (-NH_3^+), and intact thiol group (-SH), respectively. The corresponding C 1s spectra have been fitted with six components, from low to high binding energy, consistent with assignment to the $\text{-CH}_2\text{-S-Au}$, $\text{-CH}_2\text{-SH}$, -CH-NH_2 , -CH-NH_3^+ , -COO^- , and COOH moieties, respectively. When the coverage of cysteine is increased beyond a monolayer, cysteine molecules are expected to physisorb on top of the chemisorbed interfacial layer in zwitterionic form with a protonated amino group and carboxylate group. The absence of any XPS feature attributable to interlayer $\text{O-H}\cdots\text{N}$ H-bond at ~ 401.0 eV supports that there is no transitional layer in the cysteine growth process on both Au (0.76 ML) and Au (3.97 ML) nanoassemblies supported on the Si(111) 7×7 surface.

Analogous to adsorption of L-cysteine on Ag(111) surface,¹²⁰ we find that for the multilayer (150 min) cysteine exposure, only a single strong broad S 2s peak at 228.3 eV is observed (Figure 6.6d), which indicates an intact thiol group. The single O 1s feature at 532.0 eV (Figure 6.6a) and N 1s feature at 402.1 eV (Figure 6.6b) are also consistent with the carboxylate and protonated amino groups, respectively, in the zwitterionic multilayer. The broad C 1s band at 287.0 eV is due to a combination of $\text{-CH}_2\text{-SH}$ and, -CH-NH_3^+ moieties while the well-resolved feature at 289.3 eV corresponds to the -COO^- group (Figure 6.6c).

Similar to cysteine adsorption on the Au honeycomb nanonetwork, we also observe discernible chemical shifts (~ 0.2 eV) to higher binding energy for both the gold silicide $4f_{7/2}$ peak at 84.8 and Au metallic $4f_{7/2}$ peak at 84.1 eV after 20-min of cysteine deposition on the Au nanocrystallite film (Figure 6.2b), when compared to the respective Au 4f features for the pristine Au nanoassemblies. These small chemical shifts are due to their sulfur to Au interaction and confirms the reducing nature of the thiolate moiety.

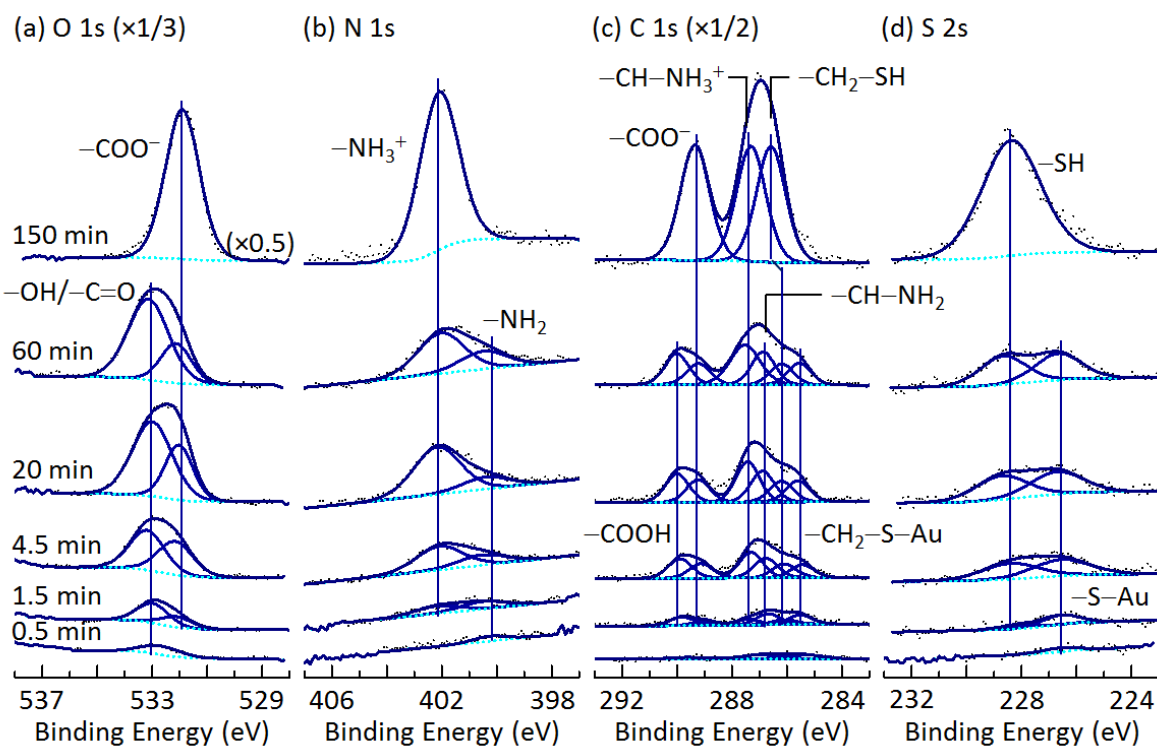


Figure 6.6 XPS spectra of (a) O 1s, (b) N 1s, (c) C 1s, and (d) S 2s regions of L-cysteine deposited on Au(3.97 ML)/Si(111)7×7 as a function of cysteine exposure time.

Table 6.3 Binding energies (in eV) of fitted peak maxima for various XPS core-level features and their assignments for different exposures of L-cysteine on Au(3.97 ML)/Si(111)7×7.

| Core level | 0.5 min | 1.5 min | 4.5 min | 20 min | 60 min | 150 min | Assignment |
|------------|---------|---------|---------|--------|--------|---------|----------------------------------|
| O 1s | 533.0 | 533.0 | 533.1 | 533.0 | 533.1 | | -C-OH/-C=O |
| | | 532.2 | 532.2 | 532.1 | 532.1 | 532.0 | -COO ⁻ |
| N 1s | 400.1 | 400.1 | 400.3 | 400.2 | 400.2 | | -NH-Si |
| | | 401.9 | 402.0 | 402.1 | 402.0 | 402.1 | N···H-O -NH ₂ |
| | | | | | | | -NH ₃ ⁺ |
| C 1s | 285.5 | 285.6 | 285.5 | 285.6 | 285.6 | | -CH ₂ -S-Au |
| | | 286.1 | 286.3 | 286.3 | 286.2 | 286.5 | -CH ₂ -SH |
| | 286.9 | 286.8 | 286.9 | 286.9 | 286.9 | | -CH-NH ₂ |
| | | 287.4 | 287.5 | 287.4 | 287.5 | 287.4 | -CH-NH ₃ ⁺ |
| | | 289.0 | 289.1 | 289.2 | 289.2 | 289.3 | -COO ⁻ |
| S 2s | 289.9 | 290.0 | 290.0 | 290.0 | 290.0 | | -COOH |
| | 226.6 | 226.6 | 226.6 | 226.5 | 226.6 | | -S-Au |
| | | | 228.2 | 228.2 | 228.2 | 228.3 | -SH |

6.4 Summary

The room-temperature growth evolution of cysteine on three gold nanoassemblies, from Au monomers and dimers to honeycomb nanonetwork to nanocrystallite film, supported on Si(111)7×7 surface has been studied by XPS and STM. The adsorption features in the adlayers are found to be strongly dependent on the nature of interface region. For low Au coverage (0.004 ML) that decorates the Si(111)7×7 with minor populations of Au monomers and dimers, we observe a three-stage growth process of cysteine, similar to that found for a pristine 7×7 surface. For higher Au coverages, the absence of any N 1s feature at 401.0 eV that corresponds to interlayer O–H···N hydrogen bond affirm the lack of a transitional layer for cysteine adsorbed on the supported Au honeycomb nanonetwork and nanocrystallite film. These primary results from both STM and XPS studies are therefore reinforcing our hypothesis that this novel gold silicide honeycomb nanonetwork, with its two-dimensional template of nanopores, offers a number of interesting potential applications for molecular trapping, with the bonding of unidentate cysteine adspecies on Si corner hole through the thiol group and on Au grids through the amino group.

Chapter 7

Conclusion and Future Work

The surface interactions of biological molecules, such as cysteine and methionine, and metal materials such as gold on a silicon surface, Si(111)7×7, are investigated by using a three-pronged approach of combining chemical-state information provided by X-ray Photoelectron Spectroscopy (XPS) and site-specific local density-of-state images from Scanning Tunneling Microscopy (STM) with large-scale quantum-mechanical modelling based on Density Functional Theory (DFT). In particular, the growth evolution and detailed nanofilm growth mechanisms of Au on Si(111)7×7 has been studied at room temperature under ultrahigh vacuum condition over a wide coverage range of Au, from single/dimer adatoms to nanoclusters to honeycomb nanonetwork and to nanocrystallites. Both STM filled-state and empty-state images show that on the 7×7 surface two distinct layers form one after another, each by connecting patches of adjoining Au clusters, before individual three-dimensional islands start to grow on top. XPS measurements of the same coverages reveal that Au exists as gold silicide (Au_xSi) in the two interfacial distinct layers and as metallic Au in the islands. The critical thickness of the gold silicide interface region is found to be two monolayers, which marks the transition from layer-by-layer to island growth. These results provide direct observation and chemical-state characterization of Au growth on Si(111)7×7 in the Stranski-Krastanov mode. Of special interest is the formation of the gold silicide honeycomb nanonetwork at 0.76 monolayer coverage, which is made up of six triangular Au nanoclusters (around each corner hole) interconnected to one another at the dimer rows of the Si(111)7×7 substrate. With the corner holes of the 7×7 surface exposed, this new gold silicide nanonetwork, in effect, forms a two-dimensional template of nanopores (~1 nm dia. pore size) for molecular trapping application. The gold silicide honeycomb nanonetwork also offers a new conducting phase of fundamental interest to silicon device fabrication and to a number of interesting potential applications in biofunctionalization. The nature of the Au_xSi has also been investigated by large-scale DFT calculations, and a Au_9Si_3 structure has been determined as a possible nucleation center for each triangular nanocluster (consisting of Au atoms located at three different Si sites: adatom, restatom and pedestal atom sites). Furthermore, a $\text{Au}_{25}\text{Si}_6$ structure has been determined as one of the six segments of the honeycomb pattern for each occupied 7×7 half unit cell.

With the ultimate goal to study the molecular interactions of sulfur-containing aliphatic amino acids with gold clusters and other nanostructures supported on the 7×7 surface, we first examine the adsorption of cysteine and methionine on pristine Si(111) 7×7 surface. The adsorption of L-cysteine, as the only standard amino acid containing a thiol ($-\text{SH}$) group, on Si(111) 7×7 at room temperature has been studied. Surface functionalization of an inorganic surface with bio-organic molecules is often aimed at creating a “permanent” bio-organic surface with receptor functional groups. We show here that cysteine can be used to transform a highly reactive Si(111) 7×7 surface to not just a permanent bio-organic surface but also a semi-permanent (or renewable) and a temporary bio-organic surfaces by manipulating the exposure. In the early growth stage, the strong bonding between the first cysteine adlayer and the Si substrate through Si–N and/or Si–S linkages in unidentate and/or bidentate arrangement provides permanent biofunctionalization by this interfacial layer, which produces very stable adlayer that breaks down above 285 °C. This interfacial layer can be used to build a transitional layer (second adlayer) mediated by interlayer $\text{N}\cdots\text{H}-\text{O}$ hydrogen bonding between an amino group of the second adlayer and a carboxylic acid group of the interfacial layer. The interlayer hydrogen bonding therefore provides temporary trapping of bio-organic molecules as the second transitional layer that is stable up to 175 °C. This transitional layer can be easily removed by annealing above this temperature and then regenerated with another molecular layer of the same molecule or a different one by “renewing” the interlayer hydrogen bonds. Further exposure of cysteine eventually leads to a zwitterionic multilayer film ($\text{NH}_3^+\text{CHCH}_2\text{SHCOO}^-$) involving electrostatic interactions between cation ($-\text{NH}_3^+$) and anion moieties ($-\text{COO}^-$). Another striking feature of cysteine adsorption observed in our experiments is the selectivity of the thiol ($-\text{SH}$) group and/or the amino ($-\text{NH}_2$) group in comparison to the carboxylic acid ($-\text{COOH}$) group towards reaction with the surface silicon atoms. The first adlayer is found to react with the 7×7 surface completely via the formation of Si–S and/or Si–N bonds, with no evidence of Si–O bond formation.

Coverage-dependent adsorption adstructures of cysteine, from bidentate to unidentate attachments and to self-assembled multimers, involving formation of intralayer horizontal $\text{N}\cdots\text{H}-\text{O}$ hydrogen-bond are observed for the first time by STM local density-of-state imaging. At the early adsorption stage of cysteine, the bidentate configuration through Si–S and Si–N linkages with the Si adatom pair across the dimer wall of the 7×7 unit cell has been found by both high-resolution filled-state and empty-state STM images. This bidentate configuration gives rise to asymmetric local density-of-state resulting from the off-to-the-side orientation of the free carboxylic acid group. The relative surface concentration of the monomers with the center adatom-center adatom (across the dimer wall) configuration is found to be

higher than that with the corner adatom-corner adatom (across the dimer wall) configuration, suggesting that the former configuration is more stable. STM images for higher exposures of cysteine reveal more unidentate cysteine adstructures bonded through Si–N or Si–S and also cysteine self-assembled into dimer, trimer, and higher-order multimer configurations. The formation of these self-assembled arrangements is driven by horizontal N··H–O H-bonding between a free carboxylic acid group and an amino group of adjacent cysteine molecules in the interfacial layer. The STM observations are in good accord with our XPS results that show N–H and/or S–H adsorption of cysteine and formation of the interfacial layer and transitional layer mediated by N··H–O H-bonding. Statistical analysis of the STM images collected at low exposures of cysteine shows that the relative surface concentration for monomers is discernibly higher than that for dimers. At higher exposures, the relative surface concentrations for dimers and trimers increase gradually with decreasing the population of monomers. Our large-scale DFT calculations show that the adsorption energy of cysteine monomer with the Si surface via the formation of bidentate product is lower than that via the formation of unidentate product. The calculated adsorption energy of the adsorbed bidentate cysteine monomer on center adatom-center adatom (across the dimer wall) is lower than that of the adsorbed cysteine on corner adatom-corner adatom (across the dimer wall). For dimer configurations, the calculated adsorption energy follows the trend: center adatom-corner adatom (within half unit cell) > center adatom-center adatom (within half unit cell) > center adatom-center adatom (across the dimer wall) > corner adatom-corner adatom (across the dimer wall), which is in good accord with the relative surface concentrations at the lowest exposure of cysteine as obtained by STM.

The room-temperature growth and thermal evolution data of methionine, as the remaining sulphur-containing standard amino acid (with a thiol ether group), from submonolayer to multilayer on Si(111)7×7 could be used to extend our current understanding of the general growth modes followed by other benchmark aliphatic amino acids (glycine, alanine, and cysteine) and the simplest peptide (glycylglycine). Our XPS results, combined with large-scale DFT calculations with van der Waals dispersion correction, show an “universal” three-stage growth process that is common to all the proteinogenic biomolecules on Si(111)7×7 surface studied to date. In comparison to cysteine, the surface chemistry of methionine on the 7×7 is found to be rather different at the interfacial layer due to terminated sulfur atom. In analogy to glycine and alanine, methionine follows the same binding pathway via the N–Si bond formation in the interfacial layer, thus reinforcing our hypothesis that the amino (–NH₂) group is more reactive than the carboxylic acid group (–COOH) on the 7×7 surface. This is then followed by the formation of a transitional layer (the second adlayer) and finally of a zwitterionic film

(multilayer), both of which are driven by intralayer and interlayer hydrogen bonding as well as structural compatibility as imposed by the surface registry. We conclude that the thermal stability of the zwitterionic layer is much lower than the interfacial and transitional layers because of the weaker intralayer and interlayer O \cdots H–N H-bonds than the O–H \cdots N H-bonds. Understanding this universal three-stage growth process, from interfacial to transitional to zwitterionic layers, and their underlying intermolecular interactions provides insight into the relative chemical and thermal stabilities of these biomolecular adlayers on the Si(111)7 \times 7 surface, which are essential to biofunctionalization and to designing bio-inspired materials and applications. Our results for all the adsorbed proteinogenic biomolecules on Si(111)7 \times 7 surface studied to date enable us to construct a reference XPS data table to guide future studies of biofilm growth on reconstructed Si(111) surface. We expect that such a growth model can be applied to larger biological molecules, such as peptides and proteins, which will provide basic understanding in constructing silicon biological interface for bio-devices and biomedical applications.

As a complementary computational study, the equilibrium structures and adsorption energies of all possible intralayer flat di-molecular hydrogen bonding configurations (in the interfacial layer) and interlayer lateral and near-vertical hydrogen bonding configurations (in the transitional layer) on our Si₂₀₀H₄₉ model surface have been obtained by DFT-D2 calculations. Altogether, a total of well over 120 optimized configurations have been successfully computed for the five proteinogenic biomolecules on the model surface, which represents the most comprehensive computational study for these biomolecules (supported on any surface) reported to date. The trend for the H-bond length (O–H \cdots N < O–H \cdots O < N–H \cdots N < N–H \cdots O) in the gas phase can be applied to biomolecular surface interaction, except for the N–H \cdots N H-bond because the amino group is occupied by covalent bonding with the surface. As these proteinogenic biomolecules contain various moieties with a wide range of adsorption energy on Si surface, the resulting interfacial layer and transitional layer offer new opportunity of creating not just “permanent” but indeed “semi-permanent” biofunctionalization, respectively. The adsorption energy of the flat di-molecular structures involving intralayer H-bonds of the benchmark proteinogenic biomolecules on the Si(111)7 \times 7 surface follows the trend: Cysteine > Methionine > Alanine > Glycine, while the corresponding trend for the adsorption energy of the near-vertical di-molecular structures involving interlayer H-bonds becomes: Glycylglycine > Methionine > Alanine \approx Glycine > Cysteine. We also develop five simple rules of thumb to summarize the adsorption properties of these proteinogenic biomolecules, and they are expected to provide helpful guide to studies of larger biomolecules and their potential applications.

- (1) Most, if not all, aliphatic proteinogenic biomolecules follow the “universal” three-stage film growth process on Si(111)7×7. Of all the studies reported to date,^{98,205,131} we have not seen any exception.
- (2) The formation of intralayer H-bonds in the interfacial layer leads to a more stable configuration (flat configuration) than the formation of interlayer H-bonds in the transitional layer (lateral/near-vertical configurations), with the more parallel configuration with respect to the surface being more favorable than the tilted or more upright configurations.
- (3) The interlayer O–H···N H-bond between a free carboxylic acid group in the interfacial layer and a free amino group in the transitional layer is found to be the most common mechanism in the early growth stage of these aliphatic amino acids.
- (4) The formation of intralayer H-bonds between two adsorbed biomolecules in the interfacial layer depends on several factors: The size, nature and available variety of the functional groups, conformer configuration, nature of possible adsorption sites on the surface, and steric hindrance among adsorbates and between an adsorbate and the surface registry.
- (5) In the case of interlayer H-bonds, not only do the orientations of both the first and second adsorbates play a crucial role on the adsorption energy, but also the site-specificity of the Si surface could affect the formation of a viable stable system.

For very low coverage of methionine on the Si(111)7×7 surface at room temperature, we also demonstrate surface clustering from monomers to dimers, and to trimers by using high-resolution STM. Coexistence of two monomer configurations within half unit cell and across the dimer wall has been obtained by STM and complementary DFT-D2 calculations. Evidence of N–H dissociative adsorption of methionine at the center adatom-restatom pair is also observed. A dimer configuration of two methionine adspecies (head-to-head) across the dimer wall containing a single O···H–O H-bond between two vicinal carboxylic acid groups corresponds to the observed oval STM feature. The Y-shaped STM feature is driven by hydrogen bonding among the unattached carboxylic acid groups from three methionine molecules adsorbed in a ring configuration. The stability of this trimer is verified by large-scale DFT-D2 calculations. The near perfect match of the Y-trimer with three-fold symmetry within the half-unit cell represents the first supported “magic-number” molecular cluster reported to date. Intralayer hydrogen bonding among appropriately oriented adsorbed biomolecules in the interfacial layer therefore plays a key role in the formation of self-organized molecular clusters on the Si(111)7×7 surface.

Preliminary XPS and STM results have been obtained for molecular interactions of cysteine with three distinct gold nanoassemblies on Si(111)7×7, including Au monomers and dimers, Au honeycomb nanonetworks, and Au nanocrystallite film. The presence of minor concentrations of Au monomers and

dimers appear not to perturb the general three-stage growth process of cysteine found on pristine 7×7 surfaces. The coexistence of two chemisorption states of cysteine on the Au honeycomb nanonetwork, including unidentate adspecies through the thiol ($-\text{SH}$) group with Au atoms and through the amino ($-\text{NH}_2$) group with Si atoms, illustrates site-selectivity of this novel Au honeycomb nanonetwork, which suggest potential applications for molecular trapping and hybrid surface functionalization. Cysteine chemisorbed via the sulfur in neutral form on the Au nanocrystallite film supported on the 7×7 surface in the interfacial layer at room temperature. There is no evidence of any transitional layer on the Au honeycomb nanonetwork and nanocrystallite films and the zwitterionic cysteine films are found for higher exposure.

The present work has provided the results that begin to address some of the fundamental questions about molecular interactions between benchmark biomolecules with supported metallic nanostructures and nanoassemblies on the 7×7 surface. Some of these future investigations include:

- (1) As an immediate extension of the present work, more detailed investigation of the surface chemistry of cysteine with other supported Au superstructures obtained between 0.004 ML and 0.76 ML would be of great interest. For example, the nanocluster and horseshoe nanoassemblies represent key turning points in the growth evolution of Au on the 7×7 surface (see Chapter 6.1.3, Figure 6.1). There are also sufficient large number densities for these nanoassemblies that would allow XPS detection of chemical shifts of features pertaining to the biomolecule to metallic-nanoassembly interactions. Individual nanoassemblies are also well dispersed within the surface registry of the 7×7 surface, thus potentially allowing easy differentiation between the cysteine adspecies and the metallic-nanoassembly.
- (2) Preliminary STM results for three cysteine exposures on the supported Au honeycomb nanonetwork have shown that these cysteine adspecies could anchor on both Au hexagonal grids (~ 4 nm wide) and nanopores (~ 1 nm dia.). However; a more systematic study supported by atomic-resolution Atomic Force Microscopy (which is feasible with our variable-temperature SPM system) could provide the much needed information about the “actual” topography or height of the adsorbate on the Au hexagonal grids and nanopores. Atomic-resolution AFM can also be used to study biomolecular interactions with other metallic-nanoassemblies.
- (3) Limited results using ultra-large-scale DFT-D2 calculations involving a supercell of four 7×7 unit cells (with over 800 Si atoms) have been obtained in the present work. Despite the inherent time-consuming nature of these calculations, these results are crucial to determining molecule-to-molecule interactions such as hydrogen bonding between two proteinogenic molecules (Chapter 5.1.3, Figure

5.4). Such type of ultra-large-scale calculations involving an appropriately large number of metal atoms (to model the metallic nanoassembly of interest) on one or more 7×7 unit cells will also be extremely beneficial to obtaining better insight into the molecular interactions of proteinogenic biomolecules with supported Au nanoassemblies (Appendix A, Figure A3). For example, one of the important outcomes of this type of study would be to demonstrate whether the Au silicide honeycomb nanonetwork could be used for molecular trapping of one or more types of biomolecules (e.g. cysteine with a molecular length of 4.96 Å vs methionine with a larger molecular length of 7.40 Å). Interfacial interactions of methionine (and other biomolecules) with gold silicide honeycomb nanonetwork (and other nanoassemblies) will be characterized experimentally by XPS, and they can be compared with the molecular models generated by the ultra-large-scale DFT-D2 calculations. Direct atomic-resolution STM and AFM imaging would also be useful for probing the surface arrangement of these biomolecules upon deposition on Au honeycomb nanonetwork and other nanoassemblies.

- (4) Gold nanoassemblies (clusters, nanonetworks, nanocrystallites) supported on a semiconductor surface could be used as the active materials for biosensors and biomolecular electronic devices. In this context, we have begun testing a small set of supported Au honeycomb nanonetwork samples for methanol electrochemical oxidation. Preliminary results show that the reactivity of the honeycomb nanonetworks obtained below 0.2 ML Au coverage is detectable. This type of experiments will be extended to other Au nanoassemblies and to other analyte systems.
- (5) To answer our hypothesis that the transitional layer could be used as a “renewable” or semi-permanent platform for sensing application outside the ultrahigh vacuum chamber under real world conditions remains one important challenge. Other site-specific techniques such as Scanning Tunneling Spectroscopy (potentially viable with our SPM system) can be used to further characterize the nature of interactions and stability of the transitional layer of benchmark proteinogenic biomolecules and to assess the feasibility of using these biomolecular transitional layers for sensing applications.

The growth evolution of benchmark aliphatic amino acids (glycine, alanine, cysteine, and methionine) and the simplest peptide (glycylglycine) exhibits the universal three-stage growth mode on $\text{Si}(111)7\times 7$ as mediated by surface hydrogen bonding. Our experiments will be extended to other standard amino acids and to other type of biomolecules such as aromatic amino acids to examine the “universality” of their growth processes. Many of the challenging questions, fundamental and otherwise, about surface interactions of biomolecules and metal adsorbates on specific sites of the $\text{Si}(111)7\times 7$

surface can be addressed by adopting a comprehensive three-pronged approach employed in the present work. This approach combines the chemical-state composition and surface bonding information obtained from XPS, and the site-specific local-density-of-state imaging information from STM, with molecular models generated by large-scale ab-initio quantum mechanical calculations in the present work. The present work shows that the Si(111) surface is remarkably flexible in providing a variety of adsorption sites and bonding arrangement possibilities not only for bio-organic molecules but also for metal adsorbates and their nanoassemblies. In particular, cysteine undergoes in a bidentate/unidentate dissociative adsorption reaction, while methionine reacts in selective unidentate dissociation reaction, and Au adatoms interact with Si dangling bonds to produce nanoassembled structures. As the results of our large-scale DFT calculations seek to illustrate, the combination of bio-organic materials with metallic nanostructures on a semiconductor surface (which could, in effect, be considered as an insulator-metal-semiconductor nanoarchitecture) provides a fertile testbed for exploiting fundamental new interactions and for development of new breakthrough applications involving these fascinating hybrid nanomaterials.

Appendix A

Two-dimensional Self-assembled Gold Silicide Honeycomb Nano-network on Si(111)7×7

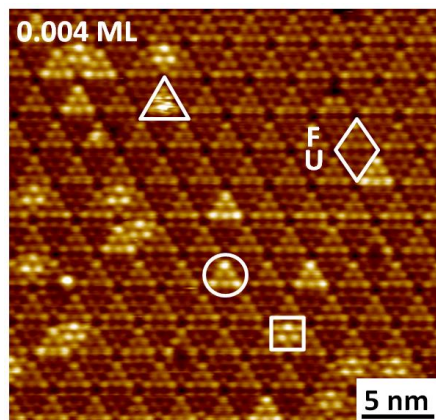


Figure A1 The magnified STM filled-state images of 0.004 ML of Au on Si(111)7×7 at room temperature, collected with a sample bias of -2.0 V and a tunneling current of 0.2 nA. The field of view is 30×30 nm². The faulted and unfaulted half unit cells are marked by F and U, respectively. The sextet (circle), triad (square), and scribble (upright triangle) features are located on the faulted, unfaulted, and faulted half unit cells, respectively.

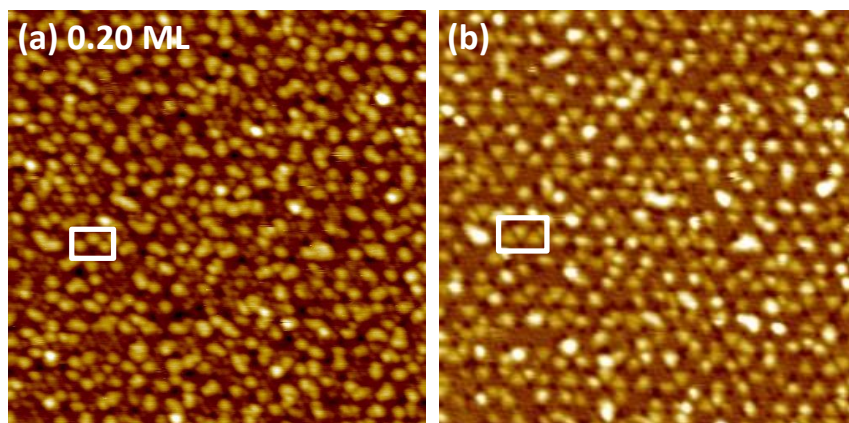


Figure A2 STM (a) filled-state and (b) corresponding empty-state images of 0.20 ML of Au coverage on Si(111)7×7 at room temperature, collected with a sample bias of -2.0 V and $+2.0$ V, respectively, and a tunneling current of 0.2 nA. The field of view is 50×50 nm².

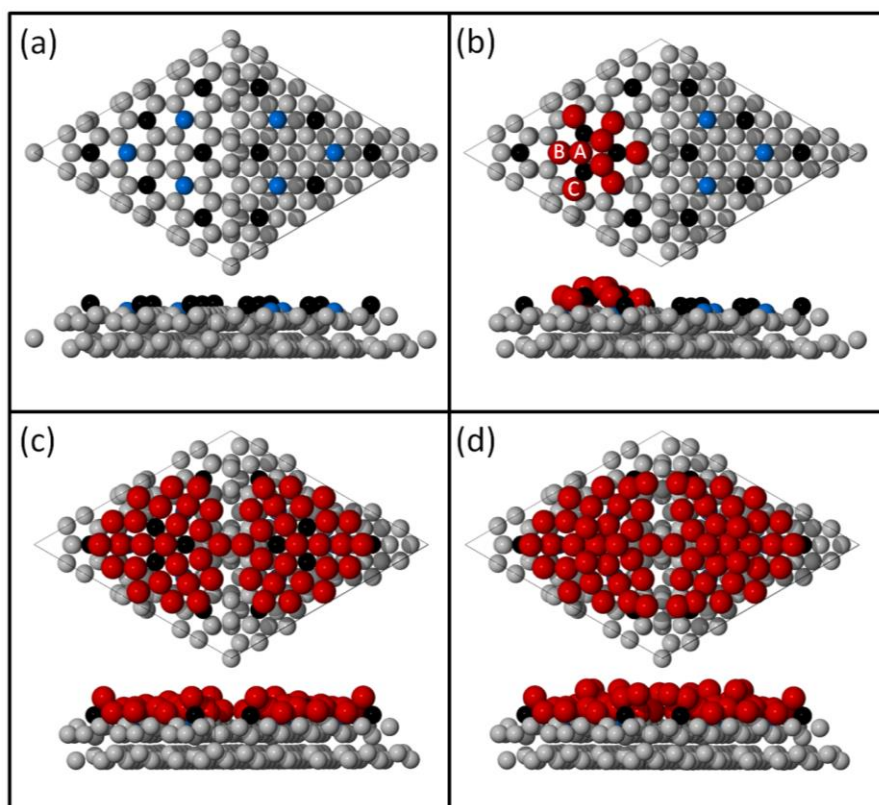


Figure A3 Top views (upper) and perspective side views (lower) of equilibrium structures obtained by large-scale DFT calculations for (a) a pristine Si(111)7×7 surface, and (b) a Au₉Si₃ cluster as a possible nucleation center, (c) a Au₂₅Si₆ cluster, with the center adatom sites exposed, for coverage below one monolayer, and (d) a Au₃₀Si₉ cluster for coverage between one and two monolayers, all for one half unit cell as one of the six segments of the honeycomb nano-network. The adatom and restatom sites are marked by black and blue circles while the Au atoms are marked in red.

Details of DFT Calculations

In order to determine the optimized equilibrium geometries and the adsorption energies, we used first-principle total energy calculations. These density functional theory (DFT)^{169,170} calculations were performed within the generalized gradient approximation^{171,182} as defined by Perdew, Burke, and Ernzerhof¹⁷² (GGA-PBE), based on the exchange-correlation functional and projector augmented-wave^{183,184} (PAW) potentials. The Vienna Ab initio Simulation Package^{178,180,181} (VASP, version 5.2) with the MedeA platform (Materials Design) was used. The plane wave cutoff energy was set to 250 eV and the surface Brillouin zone was sampled at the Γ point with k-point spacing of 0.5/Å. Conjugate-gradient algorithm was employed to optimize the geometry of the atomic structure, and all Si and Au

atoms were completely relaxed until the forces on all the atoms were less than $0.01 \text{ eV}/\text{\AA}$. The energy convergence of the self-consistent-field (SCF) was set to $1.0 \times 10^{-5} \text{ eV}$, with Methfessel-Paxton smearing of 0.2 eV . Based on these DFT results, we proposed a Au_9Si_3 model for the triangle Au cluster. The minimized structure shown in Figure A3b consists of three different types of adsorbed Au atoms: (A) three Au atoms placed on the top of pedestal atom sites of the Si restatoms, (B) three Au atoms located atop of the Si restatoms, and (C) three Au atoms located at the Si center adatom sites, which causes the three Si center adatoms to displace toward their pedestal atom sites. We also proposed a $\text{Au}_{25}\text{Si}_6$ cluster for one half unit cell, used as one of the six segments of the honeycomb nano-network. This cluster does not cover the three Si displaced center adatoms, which provides bonding with gold to form the second gold silicide layer.

Appendix B

Biofunctionalization of Si(111)7×7 by L-Cysteine

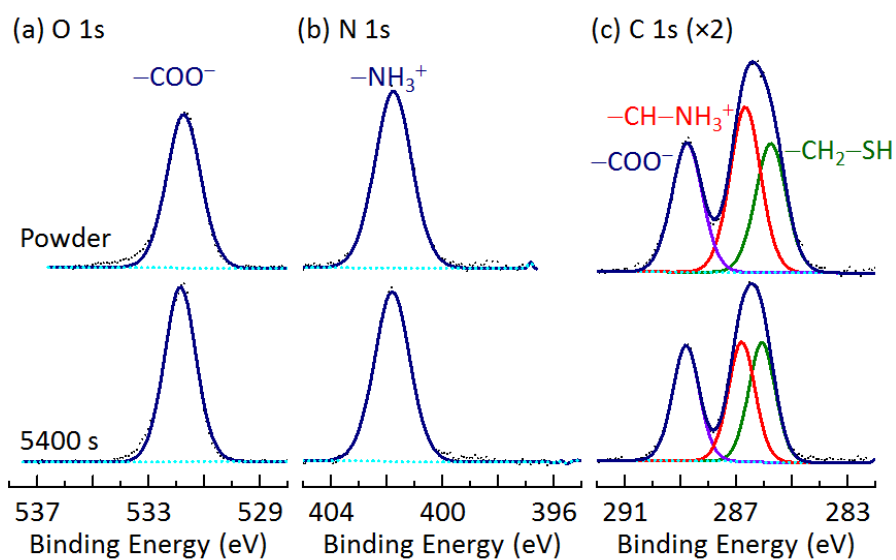


Figure B1 XPS spectra of (a) O 1s, (b) N 1s, and (c) C 1s regions for a multilayer film (with 5400 s exposure) on Si(111)7×7 and for cysteine powder. XPS data points are fitted with individual components (solid line) and a Shirley background (dotted line).

Table B1 Binding energies (in eV) of fitted peak maxima for various XPS core-level features and their assignments for different exposures of L-cysteine on Si(111)7×7 and for powder cysteine.

| Core level | Interfacial-layer | | | Transitional-layer | | Multi-layer | Powder | Assignment |
|-------------|-------------------------|-------------------------|----------------------------------|----------------------------------|----------------------------------|-------------------------|-------------------------|---|
| | 5 s | 15 s | 45 s | 400 s | 2400 s | | | |
| O 1s | 532.5 | 532.5 | 532.5 | 532.4 | 532.2 | 531.8 | 531.8 | -C-OH/-C=O -COO ⁻ |
| N 1s | 398.6 | 398.6 | 398.7 401.0 | 398.7 401.0 | 398.8 401.1 | 401.8 | 401.8 | -NH-Si N...H-O -NH ₃ ⁺ |
| C 1s | 284.7 286.3 289.2 | 284.7 286.3 289.2 | 284.7 285.6 286.6 289.2 | 284.5 285.6 286.6 289.2 | 284.5 285.6 286.6 289.2 | 286.0 286.8 288.8 | 285.9 286.8 288.8 | -CH ₂ -S-Si -CH ₂ -SH -CH-NH-Si -CH-NH ₃ ⁺ -COOH -COO ⁻ |
| S 2s | 227.4 | 227.4 | 227.4 228.4 | 277.4 228.4 | 228.4 | 228.4 | | -S-Si -SH |
| S 2p | | | | | | 164.1 | 164.1 | -SH |

Table B2 Binding energies (in eV) of fitted peak maxima for various XPS core-level features and their assignments for a multilayer film of L-cysteine on Si(111)7×7 after storage at room temperature under ultrahigh vacuum condition and upon annealing to 85, 175, and 285 °C for 10 min.

| Core level | Multi-layer | Storage Time at 25 °C | | | Annealing Temperature for 10 min | | | Assignment |
|-------------|-------------------------|-------------------------|-------------------------|-------------------------|----------------------------------|-------------------------|-------------------------|---|
| | | 24 h | 72 h | 120 h | 85°C | 175°C | 285°C | |
| | 5400 s | | | | | | | |
| O 1s | 531.8 | 531.9 | 531.9 | 531.9 | 532.5 531.8 | 532.5 | 532.4 | -C-OH/-C=O -COO ⁻ |
| N 1s | 401.8 | 399.1 401.8 | 399.1 401.8 | 399.1 401.8 | 399.1 401.1 401.8 | 398.8 401.1 400.0 | 398.8 400.0 | -NH-Si N...H-O -NH ₃ ⁺ -NH ₂ |
| C 1s | 286.0 286.8 288.8 | 286.0 286.8 288.8 | 286.0 286.8 288.8 | 286.0 286.8 288.8 | 285.9 286.8 288.8 | 285.2 286.2 289.1 | 284.6 286.2 289.1 | -CH ₂ -S-Si -CH ₂ -SH -CH-NH-Si -CH-NH ₃ ⁺ -COOH -COO ⁻ |
| S 2s | 228.4 | 228.4 | 228.4 | 228.4 | 228.4 | 227.4 | 226.8 | -S-Si -SH -S ⁻ |
| S 2p | 164.1 | | | | | | | -SH |

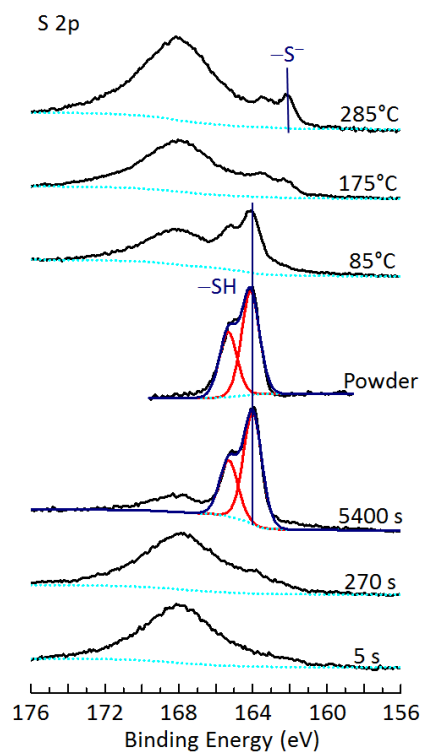


Figure B2 S 2p XPS spectra of cysteine deposited on Si(111)7×7 for 5 s, 270 s and 5400 s, and of cysteine powder, and the as-grown cysteine multilayer film (obtained with 5400 s) upon annealing at 85, 175, and 285 °C for 10 min. XPS data points are fitted with individual components (solid lines) on a Shirley background (dotted line). It should be noted that the S 2p spectrum partially overlaps with one of the plasmon peaks of Si (~ 168.0 eV).²¹² The S 2p_{3/2} peak is located at 164.1 eV binding energy for a thick cysteine film.¹²⁰

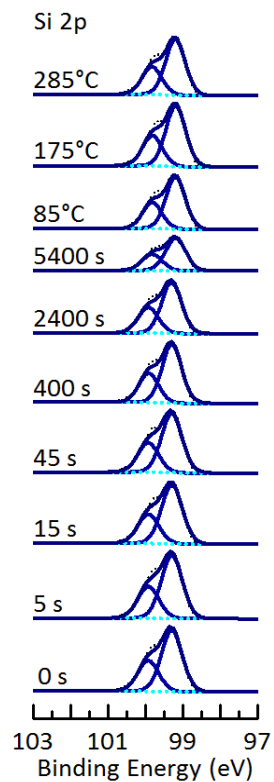


Figure B3 XPS spectra of the Si 2p region for cysteine deposited on Si(111)7×7 as a function of exposure time (5 s to 5400 s); and of the as-deposited 5400 s cysteine film upon annealing to 85°C, 175°C and 285°C. XPS data points are fitted with individual Si 2p_{3/2} and Si 2p_{1/2} components (solid lines) on a Shirley background (dotted line).

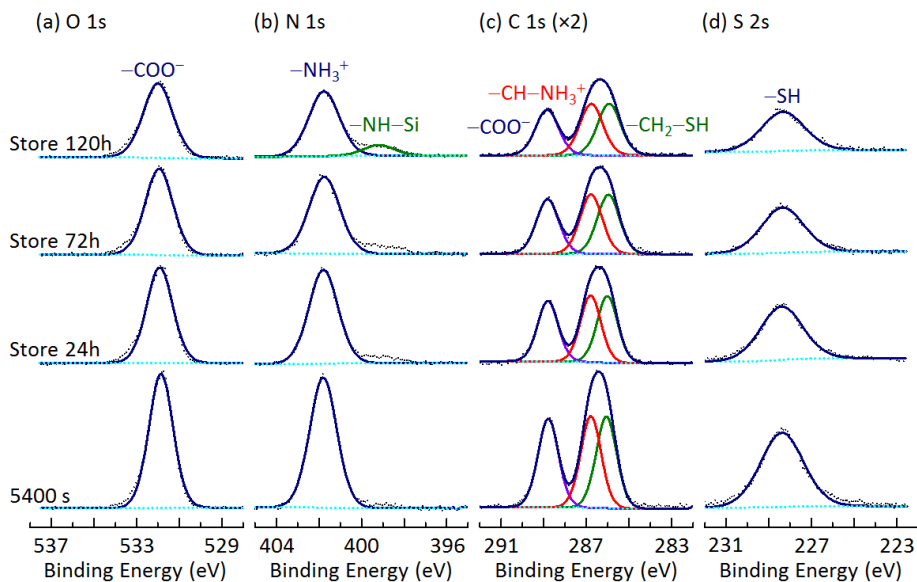


Figure B4 XPS spectra of the (a) O 1s, (b) N 1s, (c) C 1s, and (d) S 2s regions of a cysteine zwitterionic multilayer film (obtained with 5400 s exposure) on Si(111)7×7, and as a function of storage time in ultrahigh vacuum condition. XPS data points are fitted with individual components (solid lines) on a Shirley background (dotted line).

Detail of DFT Calculations

In order to determine the optimized equilibrium geometries and the adsorption energies for dissociative attachment of cysteine on Si(111)7×7, we use first-principle total energy calculations. These density functional theory (DFT)^{169,170} calculations and DFT-D2 calculations (the latter include van der Waals interactions) are performed within the generalized gradient approximation^{171,182} as defined by Perdew, Burke, and Ernzerhof (GGA-PBE),¹⁷² based on the exchange-correlation functional and projector augmented-wave (PAW) potentials.^{184,183} The Vienna Ab initio Simulation Package^{178,180,181} (VASP, version 5.2) with the MedeA platform (Materials Design) is used. The plane wave cutoff energy is set to 400 eV and the surface Brillouin zone is sampled at the Γ point with k-point spacing of 0.5/Å. Conjugate-gradient algorithm is employed to optimize the geometry of the atomic structure, and all Si atoms are completely relaxed until the forces on all the atoms are less than 0.01 eV/Å. The energy convergence of the self-consistent field is set to 1.0×10^{-5} eV, with Methfessel-Paxton smearing of 0.2 eV. In this study, we use an optimized structure of the dimer-adatom-stacking fault (DAS)²⁹ model for the Si(111)7×7

substrate (Figure B5a-B5b), which contains a faulted (F) and an unfaulted (U) half unit cells, with 12 adatoms on the topmost layer and 6 restatoms (RA) on the second layer. A periodic repeating slab consisting of 200 Si atoms, distributed in two Si bilayers and a reconstructed layer (topmost layer) with a 5.419 Å lattice constant of the Si bulk, and a vacuum gap of 12 Å is used to simulate the Si(111)7×7 surface, and the bottom layer of the slab is terminated by 49 H atoms. During the geometry optimization, first all the H atoms positions are relaxed with all the Si atoms positions fixed. Then, the Si adatoms and two Si bilayers are relaxed while the H atoms are frozen. An adsorbate molecule, cysteine, is placed on the top face of the Si slab. The equilibrium geometry of an isolated (i.e. free) cysteine molecule is shown in Figure B5c. The adsorption energy E_{ad} is defined as $E_{ad}=[E_{Total}-E_{Si\ Slab}]-E_{cysteine}$, where E_{Total} , $E_{Si\ Slab}$ and $E_{cysteine}$ are the total energies of the adsorbed cysteine on the Si slab, the Si slab, and the isolated cysteine molecule, respectively.

In the present calculation, a large variety of gas-phase conformations of cysteine adsorbed in unidentate and bidentate geometries (through three functional groups: carboxylic acid, amino and thiol) on specific sites on the Si(111)7×7 surface (corner and center adatom sites on both faulted and unfaulted half unit cells) are studied. The most stable equilibrium unidentate and bidentate configurations on the 7×7 model surface, as stimulated by the Si₂₀₀H₄₉ cluster, are shown in Figure B6 and Figure B7, respectively. Three kinds of upright adsorption configurations on the center adatom (CA) and corner adatom (AA) on both the faulted and unfaulted half unit cells of Si(111)7×7, via deprotonated functional groups (-SH, -NH₂, -COOH), are considered. The results of adsorbed unidentate cysteine molecule on the CA or AA site of the 7×7 surface show that the adsorption energy on the CA site is lower than that on the AA site on both half unit cells. Furthermore, bonding through the deprotonated thiol group (Figure B6a) is 0.44 eV and 0.23 eV more stable than bonding through the amino (Figure B6c) and carboxylic acid (Figure B6b) groups, respectively.

The other configuration considered here is cysteine adsorbed in a bidentate configuration on Si(111)7×7. Based on the DAS model of Si(111)7×7, two adjacent Si atoms with dangling bonds can be categorized as the following: (1) AA-CA, (2) CA-CA within a half unit cell; (3) CA-CA', (4) AA-AA', (5) AA-CA' across a dimer wall of adjacent half unit cells; (6) AA-corner hole, (7) AA-RA, and (8) CA-RA within a half unit cell. We use a prime symbol to denote substrate atom in the adjacent half unit cell. The corresponding separations between two Si atoms are 7.72, 7.66, 6.77, 6.71, 10.25, 8.25, 4.46, and 4.55 Å, respectively. Furthermore, typical bond lengths of Si-S, Si-N, and Si-O are 2.2, 1.7, and 1.7 Å, respectively. Given that the separation between the -NH₂ and -OH groups (3.66 Å) and that between the -OH and -SH groups (3.12 Å) in an isolated cysteine molecule are too short to bridge two neighboring Si

adatom sites, the only feasible choice for such a bidentate configuration to the Si surface is the larger separation between N and S (4.18 Å) (Figure B5c), which could be obtained via N–H and S–H dissociative adsorption of cysteine. To form covalent linkages of the deprotonated –SH and –NH₂ groups, the separation between two adjacent Si dangling bond sites should be close to 6.9 Å, assuming a Si-to-adsorbate bond angle of 45°. This rules out cases 5 and 6 because their separations are too large and cases 7 and 8 because they are too small. The above possibilities can therefore be limited to cases 1 to 4. The results from our large-scale DFT-D2 calculations for a large variety of possible bidentate adsorption configurations show that the calculated adsorption energy of the bidentate cysteine on Si adatom-adatom pair across the dimer wall (i.e. CA-CA' and AA-AA') is at least 0.57 eV lower than that of the bidentate cysteine on CA-CA and CA-AA within a half unit cell. Moreover, the calculated adsorption energy of the bidentate cysteine on a CA-CA' pair (Figure B7b) is 0.13 eV lower than that of the adsorbed cysteine on a AA-AA' pair (Figure B7a), both across the dimer wall. Our large-scale DFT-D2 study also shows that the bidentate adstructure resulting from N–H and S–H dissociative adsorption of cysteine (Figure B7) is considerably more stable (0.91 eV lower) than any unidentate adstructure (Figure B6).

Hydrogen bonding interaction between amino acids is one of most important interactions that lead to self-assembled structures. We also investigate complexes formed by hydrogen bonding interactions between two cysteine molecules (i.e., a cysteine dimer) on Si(111)7×7 by putting two cysteine molecules in unidentate adsorption configurations at adjacent Si dangling bond sites in our DFT-D2 calculations. On the Si(111)7×7 surface, dimer formation is affected by steric hindrance on the adsorbed cysteine molecules exerted by the surface atoms. We have obtained the adsorption energies and equilibrium structures for a large number of different bonding combinations on a variety of Si dangling bond sites. Our DFT-D2 calculations suggest that the N···H–O hydrogen bond is a favorable hydrogen bond that would lead to acceptable cysteine dimer on adjacent CA-AA sites without torsion on the Si(111)7×7 surface. We overlay plausible configurations of such a cysteine dimer on the corresponding STM images of a CA-CA (Figure 4.5a) and a CA-AA pairs (Figure 4.5b). Perspective views of the corresponding equilibrium structures of these “torsion-free” dimer adsorption configurations are shown in Figure 4.5c and Figure 4.5d.

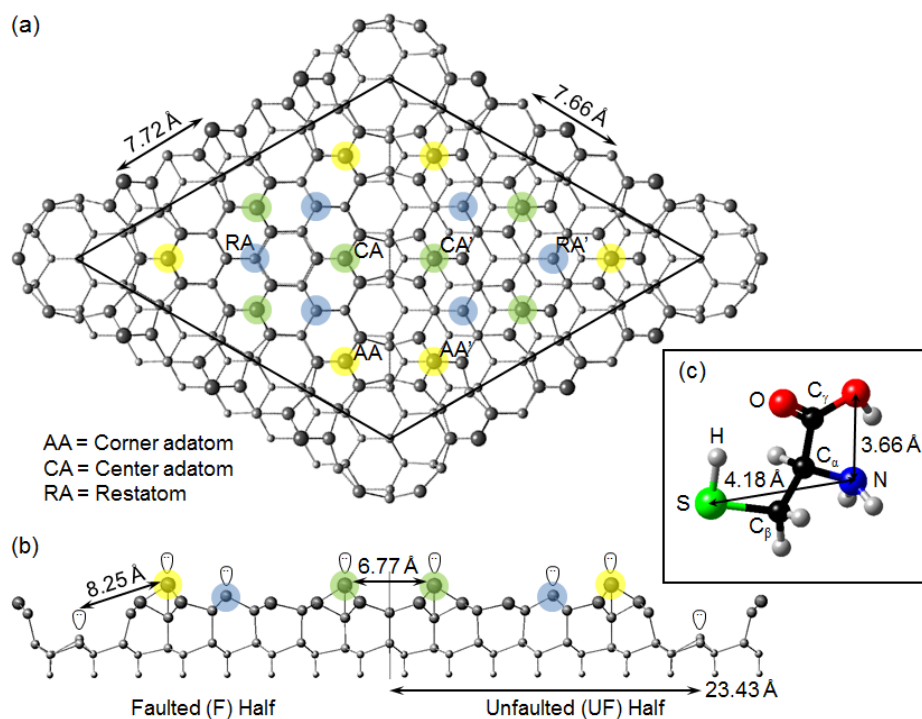


Figure B5 (a) and (b) Top view and side view of the equilibrium dimer-atom-stacking fault (DAS) model of a $\text{Si}_{200}\text{H}_{49}$ cluster (included top adatoms layer, two Si bilayers, and terminated by H atoms) obtained by large-scale DFT-D2 calculations used as the model surface for $\text{Si}(111)7\times 7$. With increasing the distance from the surface, the sizes of the spheres used to represent the Si atoms were decreased. Si corner adatoms (AA), center adatoms (CA), and restatoms (RA) are highlighted by larger yellow, green, and blue circles for clarity, respectively. The dangling bonds represent on the top of adatoms, rest atoms, and corner hole. (c) Stick-and-ball models of an isolated cysteine molecule in neutral form.

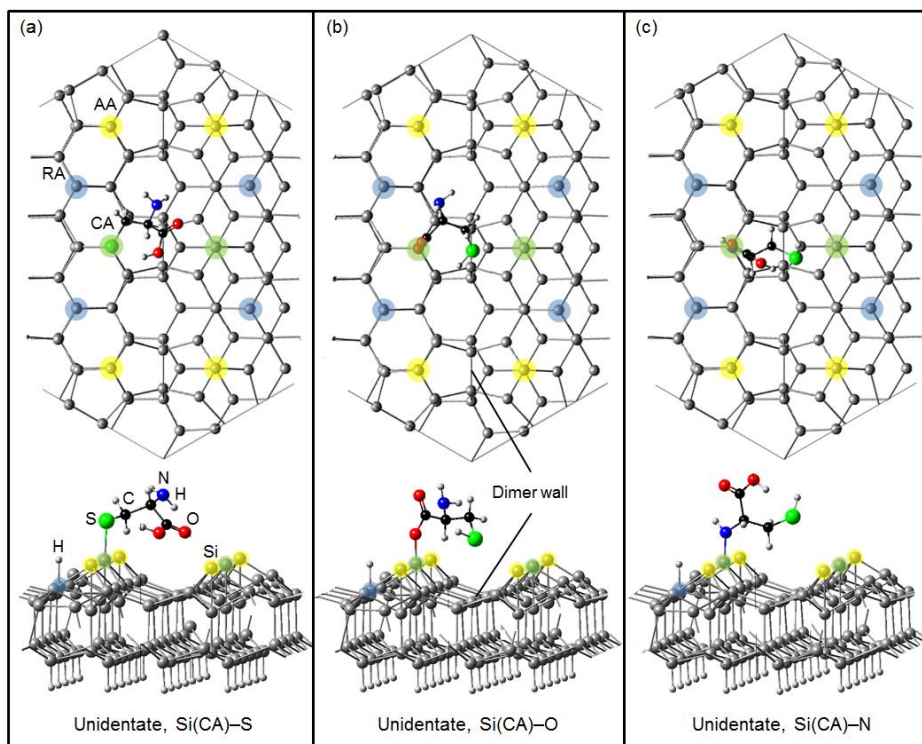


Figure B6 Top and perspective views of the most stable equilibrium adsorption geometries of an unidentate cysteine molecule bonded through (a) S, (b) O, and (c) N atoms to the model Si(111)7×7 surface, a $\text{Si}_{200}\text{H}_{49}$ cluster, obtained by large-scale DFT-D2 calculations. Si corner adatoms (AA), center adatoms (CA), and restatoms (RA) are highlighted by larger yellow, green, and blue circles, respectively. For clarity, only part of the unit cell with the relevant adatoms for bonding with cysteine is shown.

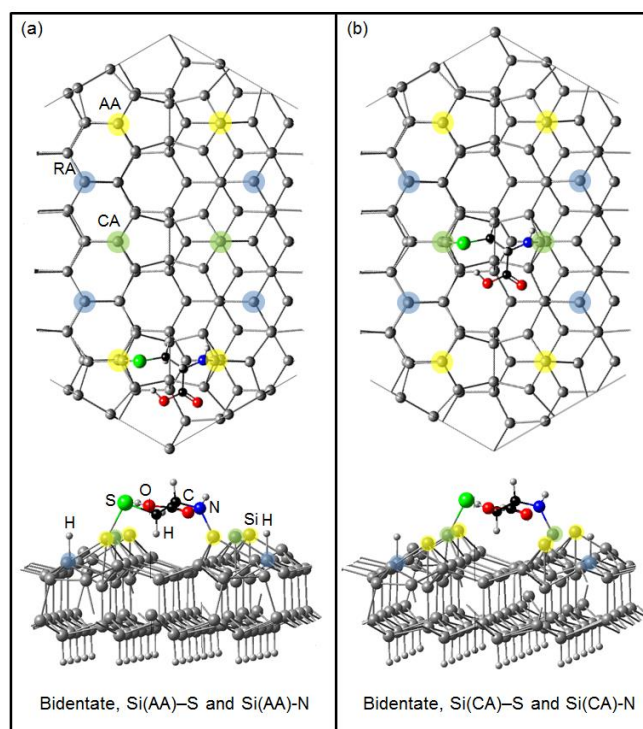


Figure B7 Top and perspective views of the most stable equilibrium adsorption geometries of a bidentate cysteine molecule bonded through the N and S atoms to the model Si(111)7×7 surface at an adatom-adatom pair across the dimer wall: (a) AA-AA', and (b) CA-CA'. Si corner adatoms (AA), center adatoms (CA), and restatoms (RA) are highlighted by larger yellow, green, and blue circles, respectively. For clarity, only part of the unit cell with the relevant adatoms for bonding with cysteine is shown.

Appendix C

Biofunctionalization of Si(111)7×7 by L-Methionine

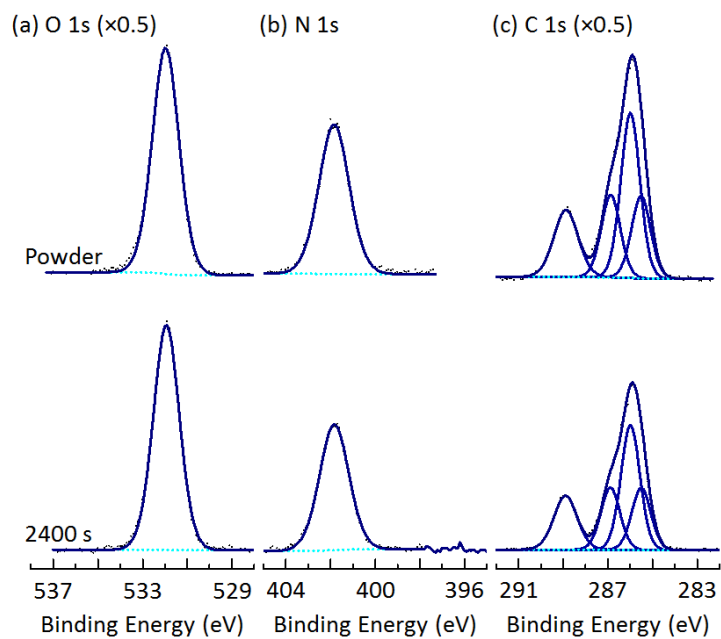


Figure C1 XPS spectra of (a) O 1s, (b) N 1s, and (c) C 1s regions for a methionine multilayer film (obtained with a 2400-s exposure) on Si(111)7×7 and for L-methionine powder. XPS data points are fitted with individual components (solid line) and a Shirley background (dotted line).

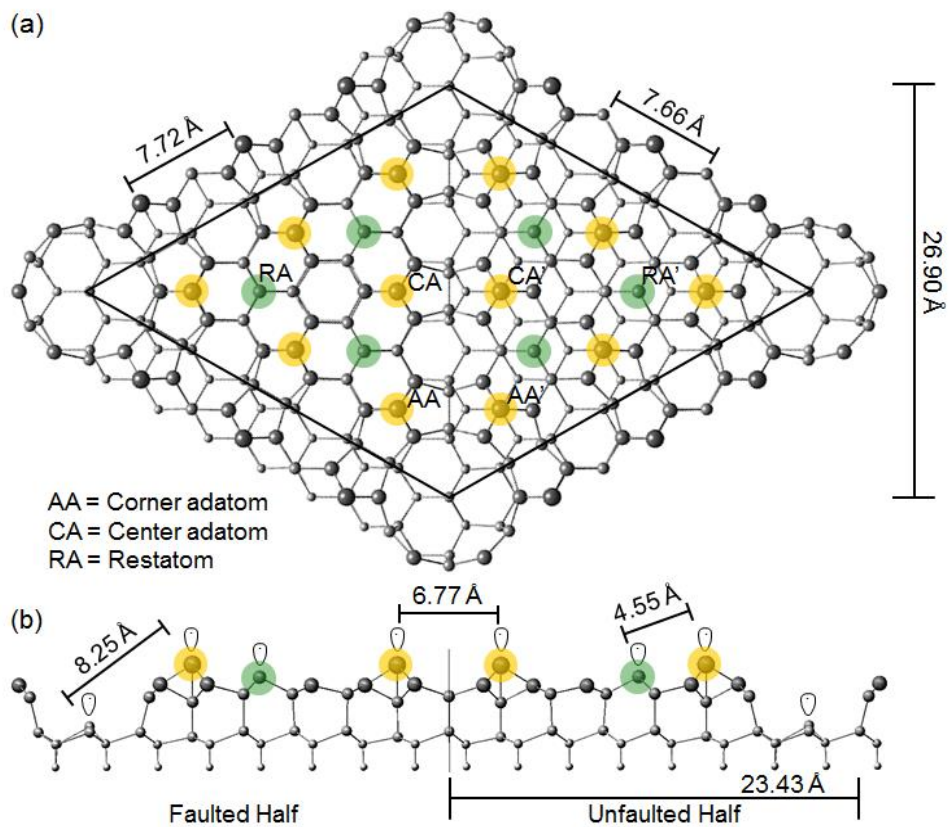


Figure C2 (a) Top and (b) side views of the equilibrium dimer-adatom-stacking fault (DAS) model of a $\text{Si}_{200}\text{H}_{49}$ cluster (consisting of a top Si adatom layer, two Si bilayers, and a bottom layer of terminating H atoms) obtained by large-scale DFT-D2 calculations used as the model surface for $\text{Si}(111)7\times 7$. Spheres with decreasing sizes are used to represent the Si atoms with increasing distance from the surface. Dangling bonds are identified on the top of the adatoms, restatoms, and corner holes. Silicon adatoms and restatoms are highlighted, respectively, by larger yellow and green circles for clarity.

Table C1 Binding energies (in eV) of fitted peak maxima for various core-level features and their assignments for different exposures of L-methionine on Si(111)7×7 and for L-methionine powder.

| Core level | Interfacial layer | Transitional layer | | | | Multilayer | | Powder | Assignment [#] |
|-------------|-------------------------|-------------------------|-------------------------|----------------------------------|----------------------------------|----------------------------------|----------------------------------|----------------------------------|--|
| | 30 s | 90 s | 180 s | 270 s | 540 s | 1080 s | 2160 s | | |
| O 1s | 532.5 | 532.6 | 532.5 531.9 | 532.4 531.8 | 532.2 531.8 | 531.9 | 531.8 | 531.9 | -OH / -C=O -COO ⁻ |
| N 1s | 398.7 | 398.7 401.0 | 398.7 401.0 401.8 | 398.7 401.0 401.8 | 398.7 401.1 401.8 | 401.8 | 401.8 | 401.8 | -NH-Si O-H...N -NH ₃ ⁺ |
| C 1s | 285.0 285.7 286.5 | 285.1 285.8 286.6 | 285.4 285.9 286.8 | 285.2 285.8 286.6 288.8 | 285.3 285.9 286.7 288.9 | 285.4 285.9 286.8 288.9 | 285.4 285.9 286.8 288.8 | 285.5 286.0 286.9 288.9 | -CH ₂ - -CH ₂ -S-CH ₃ -CH-NH-Si -CH-NH ₃ ⁺ -COOH -COO ⁻ |
| S 2s | | 228.1 | 228.1 | 228.1 | 228.1 | 228.1 | 228.1 | | -CH ₂ -S-CH ₃ |

[#] Triple-dot line is used to represent a hydrogen bond.

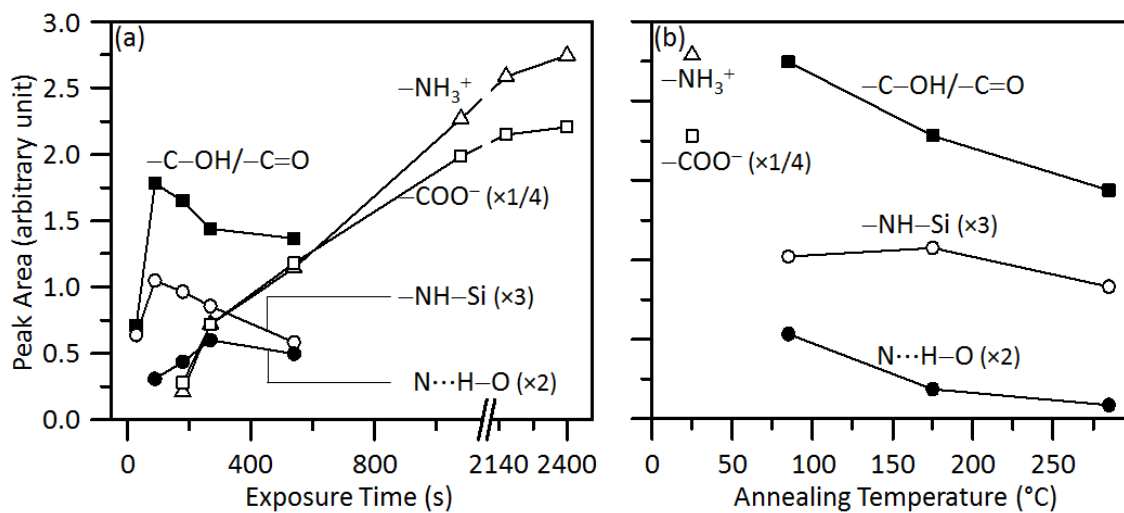


Figure C3 Peak areas of various O 1s and N 1s features (a) for different methionine exposure times and (b) for a multilayer methionine film (obtained with a 2400-s exposure) with increasing annealing temperature.

Details of DFT-D2 Calculations

Single and di-molecular adsorption structures of Methionine

In order to determine the most stable equilibrium adsorption geometry of the methionine molecule on the different sites of the Si(111)7×7 surface, we start with more than 20 initial geometries to achieve the present DFT-D2 results shown in Figure C4, which involve positioning the dehydrogenated amino group with various orientation at different Si sites within a half unit cell and across the dimer wall, in accordance with our XPS results. The H atom dissociated from the methionine upon N–H dissociative adsorption is commonly placed in the nearest adjacent restatom site. The calculated adsorption energy of unidentate methionine adsorbed within a half unit cell on the CA site (Figure C4b1) is 0.029 eV more negative than AA site (Figure C4b5) of the 7×7 surface. There is a clear correlation between the adsorption energy (indicated in square parentheses in Figure C4) and the separation between the S atom and the nearest Si adatom or restatom (indicated in round parentheses in Figure C4) across the dimer wall (Figure C4a1-C4a3) or within a half unit cell (Figure C4b1-C4b4). Among all of the adsorption configurations with various orientations of the thiol ether group, each involving a different S-to-Si separation, the most stable structure corresponds to a methionine molecule located entirely within a half

unit cell and anchored to CA through a dehydrogenated amino group with the smallest S-to-RA separation of 2.33 Å (Figure C4b1). The separation between the S atom and a Si adatom or restatom therefore plays a crucial role in the formation of stable adsorption structure of methionine. Furthermore, the configurations shown in Figure C4b2-C4b5 are not observed in our recent STM study and can be ruled out for early adsorption. Our DFT-D2 calculations therefore suggest that the configurations shown in Figure C4a1 and C4b1 are the most probable structures, while those shown in Figure C4a2 and C4a3 are also plausible. The configurations consistent with both XPS and STM results are marked by asterisks in the figures (and these are applicable only for very early growth stage).

To determine the di-molecular adsorption structures of methionine on Si(111)7×7 surface, we evaluate more than 20 complexes constructed by first using one of the two most stable adsorption configurations for methionine across the dimer wall (Figure C4a1) and within a half unit cell (Figure C4b1) as the methionine molecule anchored in the interfacial layer. We then put a second methionine molecule at an adjacent Si dangling-bond site, which could undergo N–H dissociative adsorption as the first adsorbed methionine molecule leading to the formation of “flat” configurations shown in Figure C5a1 and C5a2. These two configurations have the lowest adsorption energies but apparently with either double or single O–H···O H-bond (and a H-bond length above 1.7 Å), and they correspond to the interfacial layer. Alternatively, the second methionine molecule could also interact with the adsorbed methionine molecule primarily via hydrogen bonding and without direct (covalent) interaction with the Si surface, as shown in Figure C5b1-C5b12. We categorize these H-bonded di-molecular structures as either “lateral” (Figure C5b1-C5b5, C5b12) or “near-vertical” (Figure C5b6-C5b11), corresponding to the molecular backbone of the second molecule oriented away from the first adsorbed molecule closer to the surface plane or the surface normal (i.e. at greater or less than 45° from the surface normal), respectively. All the structural parameters of individual atoms in the two methionine molecules and of the Si atoms in the model surface have not been constrained in the energy optimization. The resulting different orientations for the second adsorbed methionine molecule (indicated as “twist” or “tilt” for the >C–COOH group with respect to the Si surface in the panel heading) lead to formation of various types of H-bonds such as O–H···O (single/double), O–H···N, and N–H···O H-bonds. In this notation, a double-bar (||) and a semicolon (;) are used to designate the second molecule positioned, respectively, across the dimer wall and within the same half unit cell. These “lateral” and “near-vertical” configurations represent possible configurations for the transitional layer. Not surprisingly, the adsorption energies of the “lateral” configurations are generally lower than those of the “near-vertical” configurations due to possible long-

range interactions with the surface in the former. As such, the “near-vertical” configurations are di-molecular complexes held together only by hydrogen bonding.

Given that our XPS data do not indicate the presence of free -NH_2 group, we could eliminate di-molecular structures shown in Figure C5b1, C5b2, C5b5, and C5b7-C5b9. The remaining di-molecular structures are therefore plausible configurations for the transitional layer. For the early growth stage, our STM result shows that only the structure in Figure C5a2 is plausible as the interfacial layer, which suggests that despite the lower adsorption energy for the structure in Figure C5a1, the less positive formal charge for AA' (Figure C5a1) than that for CA' (Figure C5a2) has made the formation of the adsorption structure involving the former site less favourable. It should be noted that the STM results for higher coverages (such as those in the transitional layer regime) do not provide further filtering for definitive structures in the transitional layer.

In separate calculations, we have also evaluated a number of possible adsorption geometries with both methionine molecules covalently bonded to Si sites and those with one methionine molecule covalently bonded to a Si site and H-bonded to a second methionine, all within a half unit cell. These calculations do not lead to stable structures, which indicate that it is physically unlikely to accommodate both methionine molecules within a single unit cell due to the length of the methionine molecule.

Di-molecular adsorption structures of Cysteine, Glycine, Alanine, and Glycylglycine

Similar large-scale DFT-D2 calculations have also been performed for a large number of possible di-molecular adsorption structures on Si(111)7×7 surface for cysteine (25), glycine (20), alanine (30) and glycylglycine (20). Of these possible configurations, we have shown the most stable configurations for these admolecules, respectively, in Figure C6, C7, C8, and C9. Following our approach for methionine, we categorize these structures into the following three groups:

- (A) “Flat” configurations involving two admolecules covalently bonded to two adjacent Si adatom sites, within a single half unit cell (A1) and across the dimer wall (A2);
- (B) “Lateral” configurations involving one admolecule covalently bonded to a Si adatom site while the second admolecule H-bonded to the first admolecule and weakly interacting with the surface, within a single half unit cell (B1) and across the dimer wall (B2); and
- (C) “Near-vertical” configurations involving one admolecule covalently bonded to a Si adatom site while the second admolecule H-bonded to the first admolecule without any interaction with the surface, within a single half unit cell (C1) and across the dimer wall (C2).

The “flat” configurations are important to the formation of interfacial layer while the “lateral” and “near-vertical” configurations represent plausible structures for the transitional layer. The absence of any N 1s feature corresponding to neutral amino group ($-\text{NH}_2$) in our XPS results for these molecules, except glycylglycine, allow us to rule out approximately a third of the di-molecular configurations. Table C2 summarizes these di-molecular adsorption configurations, with the structures that are not supported by our XPS results greyed out, for these three groups. Using STM results obtained for initial growth stage with the start of the interfacial layer, the remaining “flat” configurations (i.e. those not rejected by our XPS results) are all found to be viable. These structures are underlined in Table C2. One possible exception is found in methionine, where the most stable configuration involving covalent bonding at the CA and AA' sites (Figure C5a1) is not observed by STM. For glycylglycine, our STM results show bidentate adsorption configurations at CA-CA' and at CA-RA sites for the first admolecule, which eliminate the formation of “flat” configurations in the interfacial layer (i.e. Group A) due to steric hindrance and incompatibility with the separations between dangling bond sites. As the “near-vertical” di-molecular adsorption structures involving H-bonding of the second admolecule to the first admolecule are expected to produce essentially the same STM features, our STM results are not conclusive in differentiating between single admolecule bidentate adsorption and the di-molecular adsorption structures. Furthermore, the corresponding XPS results support the presence of free amino or amide group, which are consistent with the single admolecule and also the di-molecular adsorption structures.

Table C2 Classification of plausible di-molecular adsorption structures into three main primary groups for five proteinogenic biomolecules adsorbed on Si(111)7×7. The calculated structures are identified by their corresponding figure numbers shown in Figure C5 to C19. The structures not supported by our XPS results are greyed out. The structures observed by our STM results for the initial growth stage are underlined.

| | Methionine | Cysteine | Glycine | Alanine | Glycylglycine |
|---|--|---|--|---|--|
| (A1) Flat – within a single half unit cell | | <u>S6a1, S6a3</u> | <u>S7a3</u> | <u>S8a3</u> | |
| (A2) Flat – across a dimer wall | S5a1, <u>S5a2</u> | S6a2, S6a4, <u>S6a5, S6a6</u> | <u>S7a1, S7a2</u> , <u>S7a4</u> | <u>S8a1, S8a2</u> , <u>S8a4</u> | |
| (B1) Lateral – within a single half unit cell | | | | | |
| (B2) Lateral – across a dimer wall | <u>S5b1, S5b2</u> , <u>S5b3, S5b4</u> , <u>S5b5, S5b12</u> | S6b1, S6b4, <u>S6b7, S6b8</u> | S7b4, <u>S7b7</u> | <u>S8b1, S8b2</u> , S8b7, S8b8 | |
| (C1) Near-vertical – within a single half unit cell | <u>S5b6, S5b8</u> , | <u>S6b9, S6b10</u> , | <u>S7b1, S7b2</u> , S7b5, S7b6, S7b8, <u>S7b9</u> , <u>S7b10, S7b11</u> | <u>S8b3, S8b4</u> , <u>S8b5, S8b6</u> , S8b10, S8b11, S8b13, S8b14, <u>S8b15, S8b16</u> , S8b19, S8b20 | S9b4, S9b5, S9b6, S9b7, S9b8, S9b9, S9b10 |
| (C2) Near-vertical – across a dimer wall | <u>S5b7, S5b9</u> , S5b10, S5b11 | <u>S6b2, S6b3</u> , S6b5, S6b6, S6b11, S6b12, S6b13, S6b14 | <u>S7b3</u> | S8b9, S8b12, <u>S8b17, S8b18</u> | S9b1, S9b2, S9b3 |

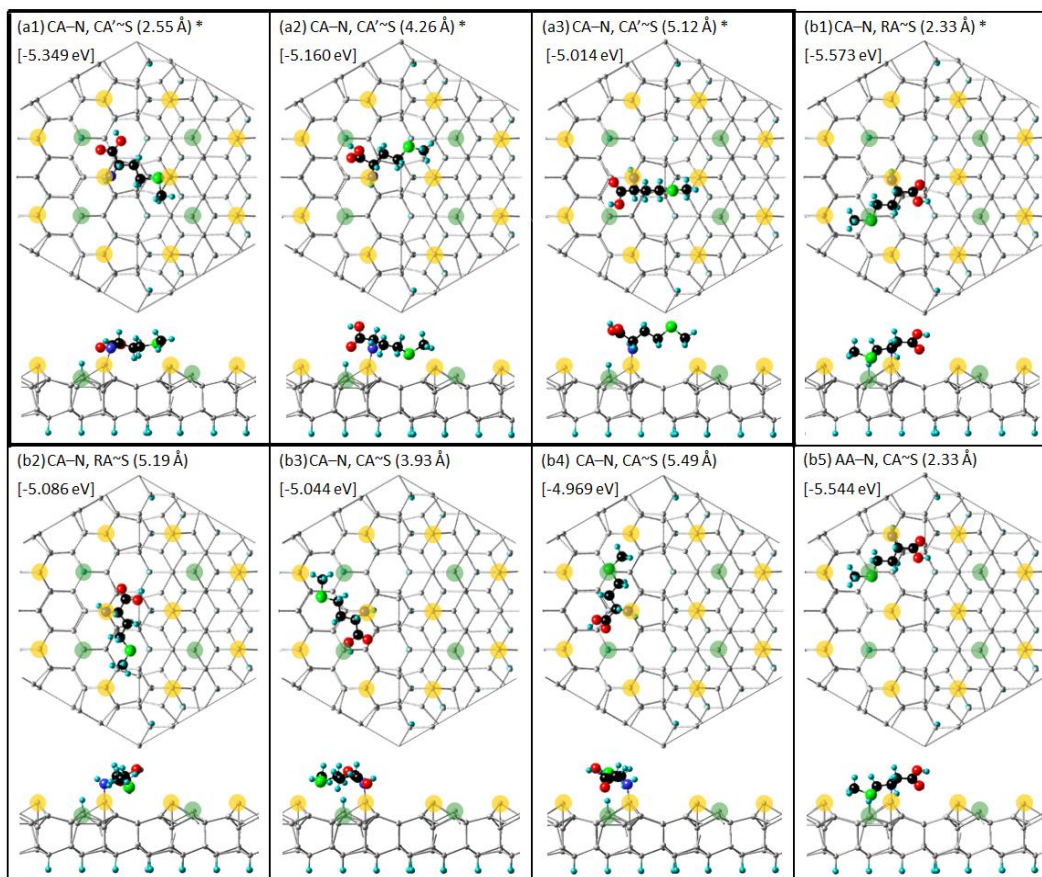


Figure C4 (a1-a3) Top and side views of the three most stable equilibrium adsorption geometries of an unidentate methionine molecule bonded through the N atom in accordance with our XPS results, with various orientations of the thiol ether group over the dimer wall on the model Si(111)7×7 surface, as represented by a Si₂₀₀H₄₉ cluster, obtained by large-scale DFT-D2 calculations. (b1-b5) Top and side views of the most stable equilibrium adsorption geometries of an unidentate methionine molecule bonded through N atom within a half unit cell with various thiol ether orientations at different Si CA and AA sites. For clarity, only part of the unit cell is shown, along with the Si adatoms and restatoms highlighted by yellow and green circles, respectively. The adsorption energies of the respective geometries are given in square parentheses while the S-to-Si separations are indicated in round parentheses. A straight (–) and a curly horizontal bars (~) are used to indicate covalent bonding between N and a Si surface atom and long-ranged interaction between S and a Si surface atom, respectively. The structures supported by STM results (only for early growth stage) are marked by asterisk.

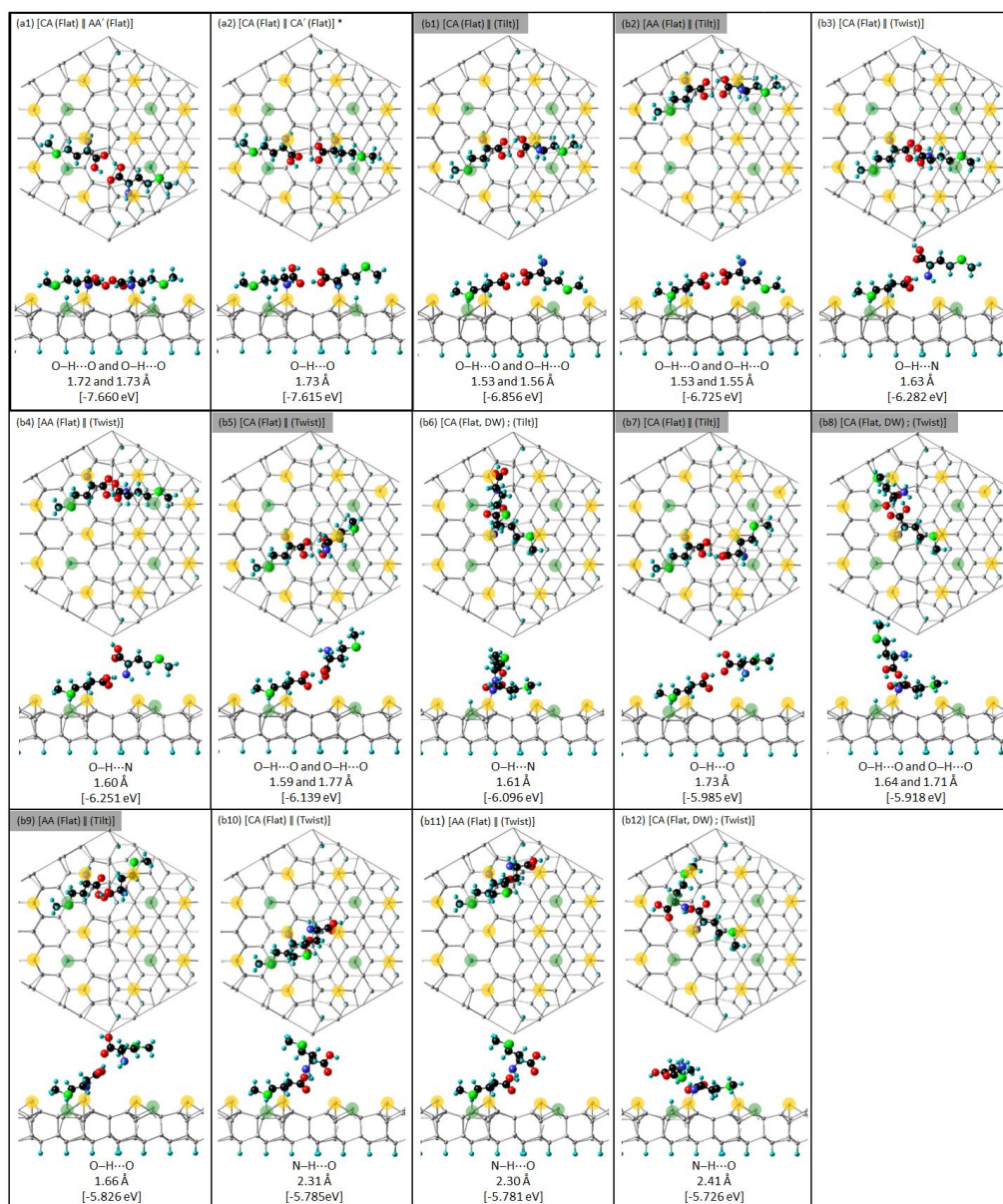
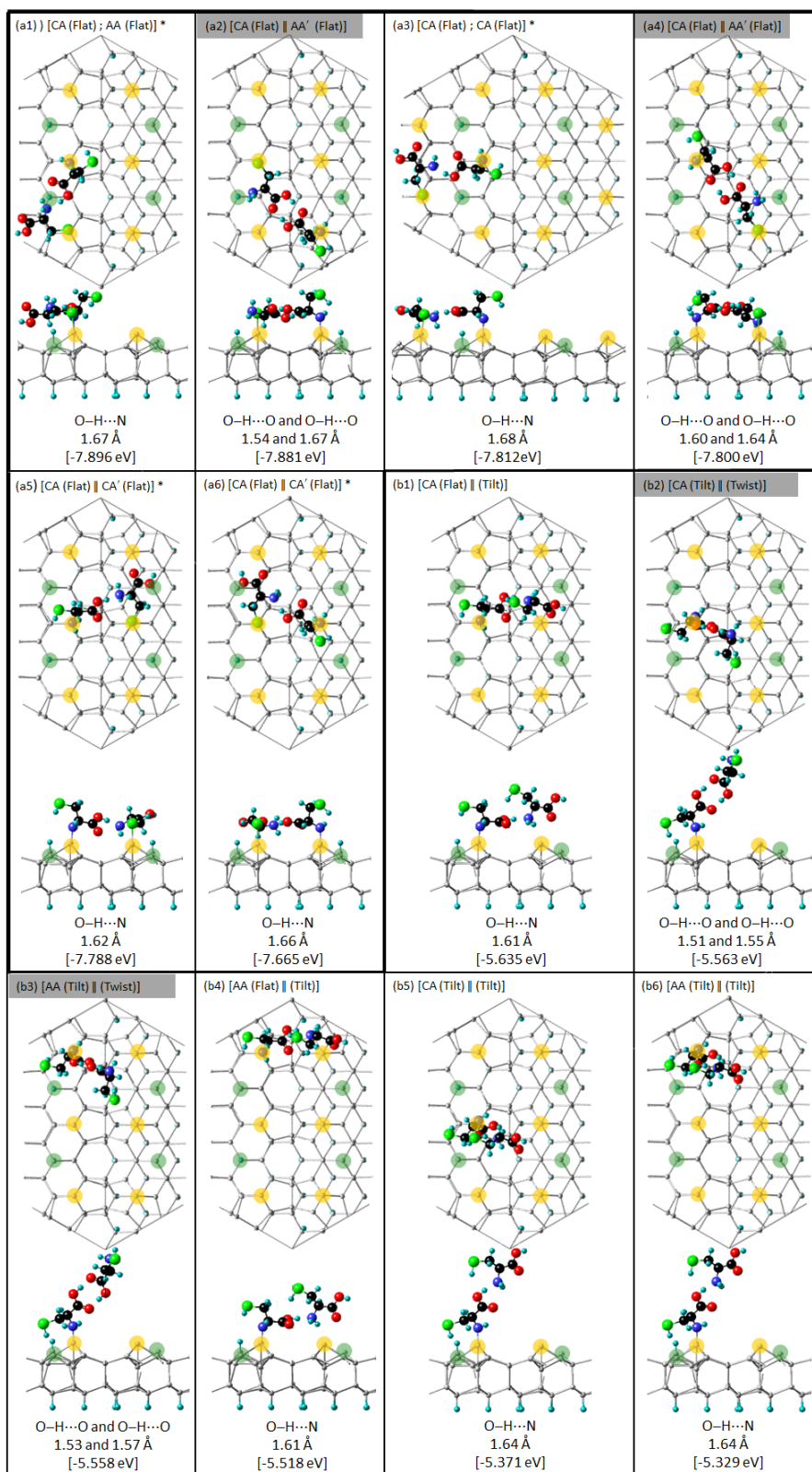


Figure C5 Top and side views of equilibrium di-molecular configurations of methionine molecules for various (a1-a2) “flat” and (b1-b12) “lateral” and “near-vertical” H-bonding on the $\text{Si}_{1200}\text{H}_{49}$ model 7×7 surface, obtained by DFT-D2 calculations. The lengths of the respective H-bonds are indicated, along with the corresponding adsorption energies shown in square parentheses. Si adatoms and restatoms are highlighted, respectively, by larger yellow and green circles for clarity. Each heading panel describes the orientation of the $>\text{C}-\text{COOH}$ backbone in the admolecules with respect to Si surface (flat, tilt, or twist) at specific Si adatom sites, with the double bar (||) and semicolon (;) indicating the second admolecule H-bonded across the dimer wall or within the same half unit cell. The structures not supported by XPS results are greyed out, while plausible configuration (for early growth stage) supported by STM results is marked by an asterisk.



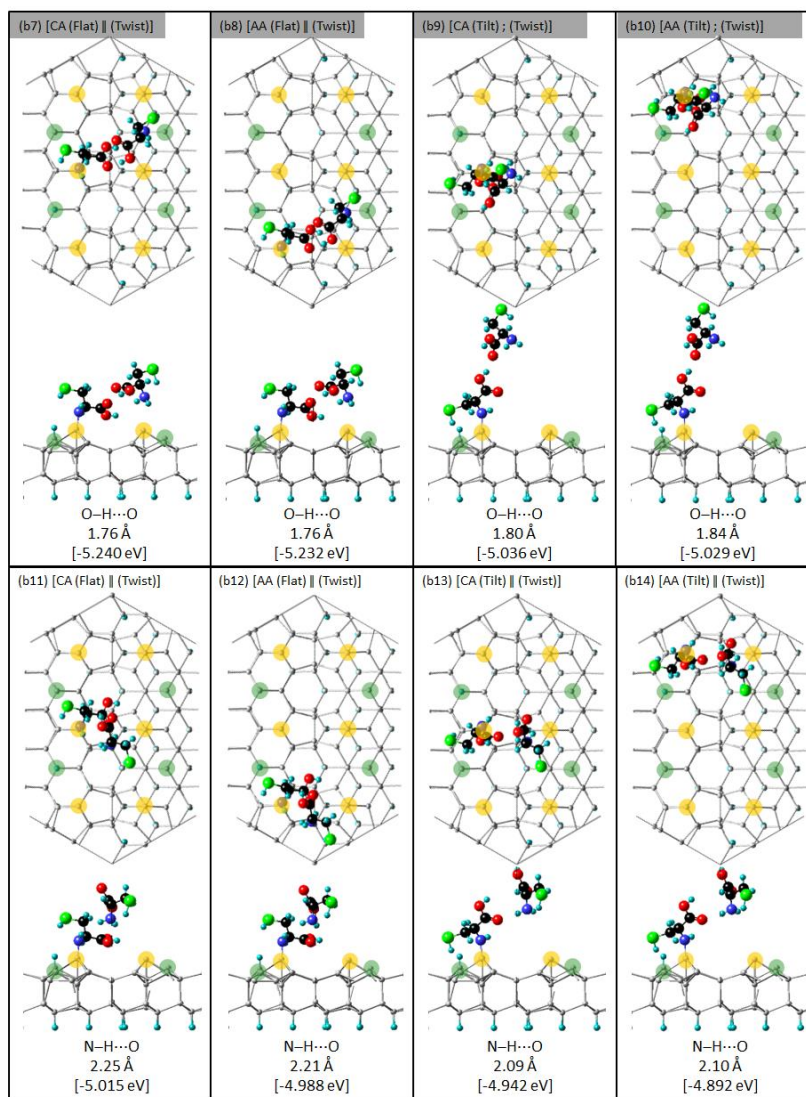


Figure C6 Top and side views of equilibrium di-molecular configurations of cysteine molecules for various (a1-a6) “flat” and (b1-b14) “lateral” and “near-vertical” H-bonding on the $\text{Si}_{200}\text{H}_{49}$ model 7×7 surface, obtained by DFT-D2 calculations. The lengths of the respective H-bonds are indicated, along with the corresponding adsorption energies shown in square parentheses. Si adatoms and restatoms are highlighted, respectively, by larger yellow and green circles for clarity. Each heading panel describes the orientation of the $>\text{C}-\text{COOH}$ backbone in the ad molecules with respect to Si surface (flat, tilt, or twist) at specific Si adatom sites, with the double bar (||) and semicolon (;) indicating the second ad molecule H-bonded across the dimer wall or within the same half unit cell. The structures not supported by XPS results are greyed out, while plausible configurations (for early growth stage) supported by STM results are marked by asterisks.

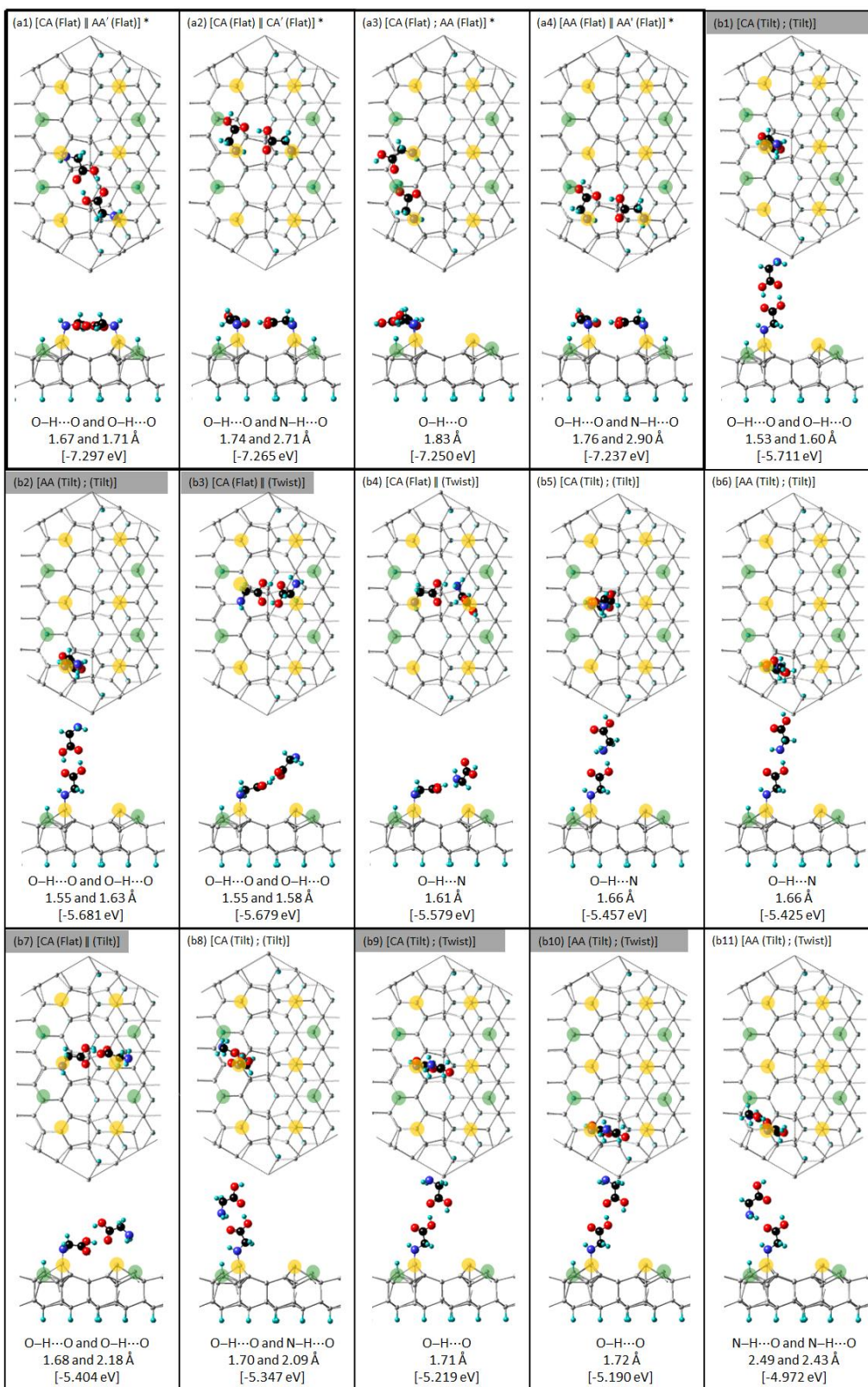
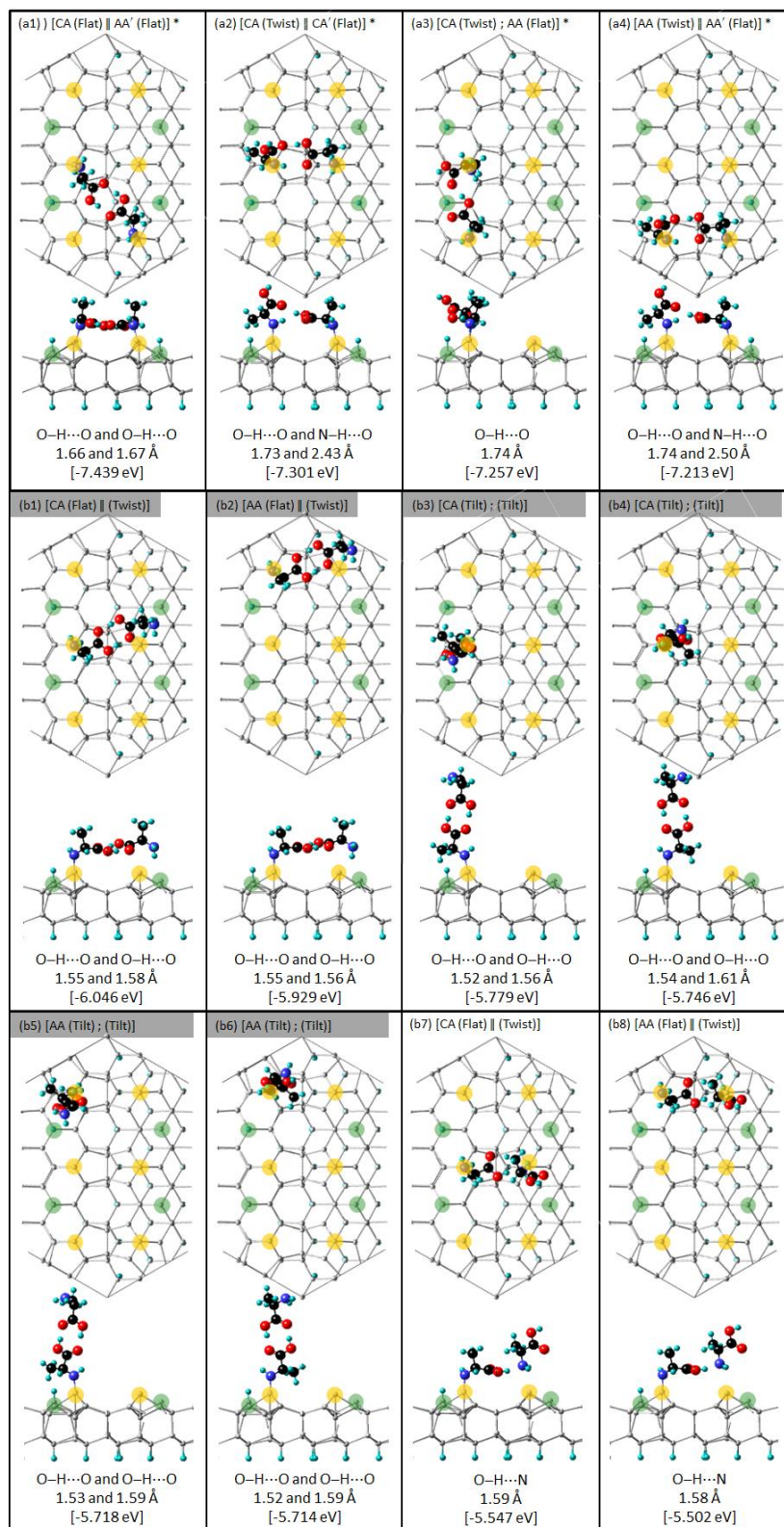


Figure C7 Top and side views of equilibrium di-molecular configurations of glycine molecules for various (a1-a4) “flat” and (b1-b11) “lateral” and “near-vertical” H-bonding on the $\text{Si}_{200}\text{H}_{49}$ model 7×7 surface, obtained by DFT-D2 calculations. The lengths of the respective H-bonds are indicated, along with the corresponding adsorption energies shown in square parentheses. Si adatoms and restatoms are highlighted, respectively, by larger yellow and green circles for clarity. Each heading panel describes the orientation of the $>\text{C}-\text{COOH}$ backbone in the admolecules with respect to Si surface (flat, tilt, or twist) at specific Si adatom sites, with the double bar (||) and semicolon (;) indicating the second admolecule H-bonded across the dimer wall or within the same half unit cell. The structures not supported by XPS results are greyed out, while plausible configurations (for the early growth stage) supported by STM results are marked by asterisks.



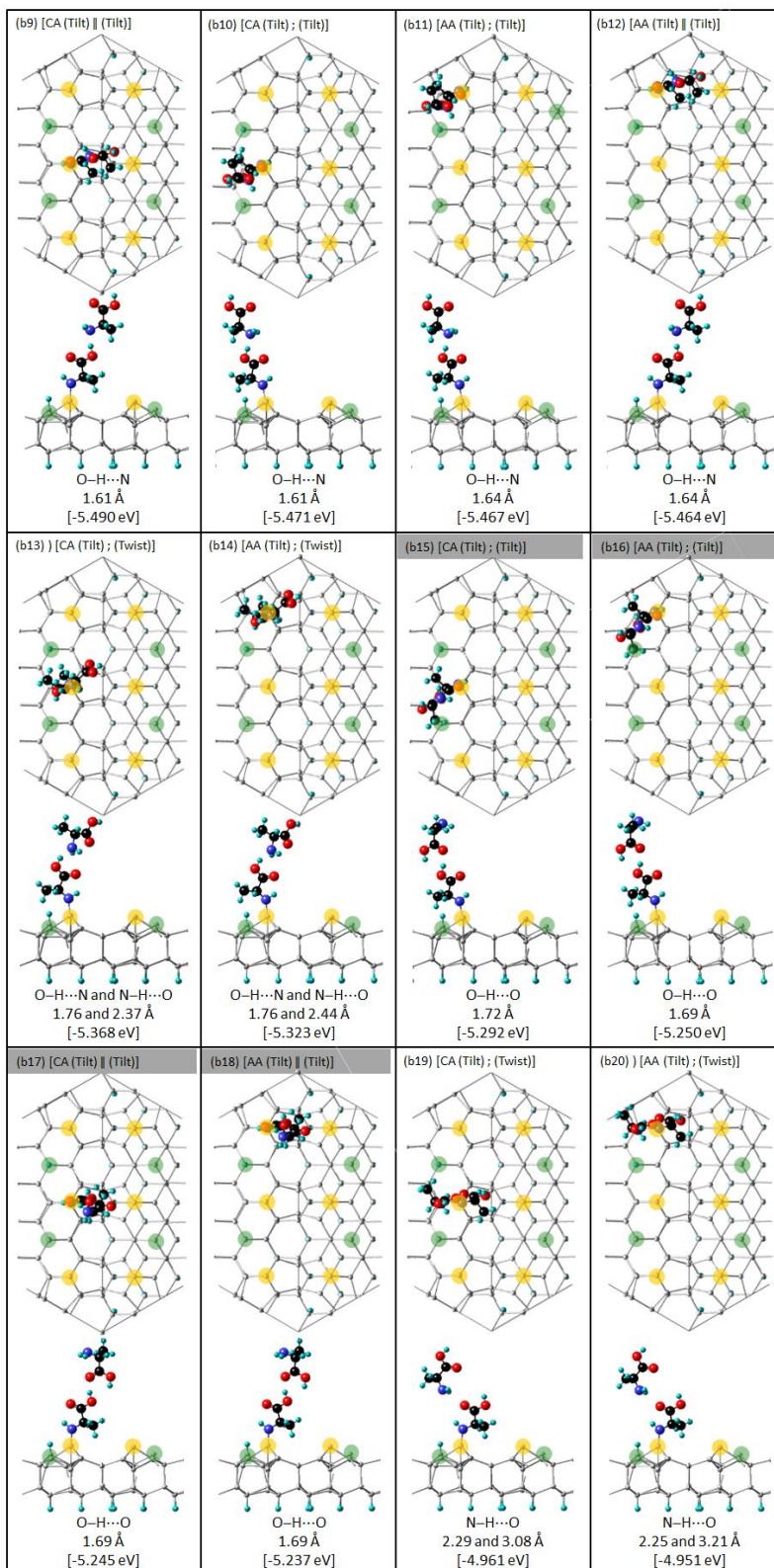


Figure C8 Top and side views of equilibrium di-molecular configurations of alanine molecules for various (a1-a4) “flat” and (b1-b20) “lateral” and “near-vertical” H-bonding on the $\text{Si}_{200}\text{H}_{49}$ model 7×7 surface, obtained by DFT-D2 calculations. The lengths of the respective H-bonds are indicated, along with the corresponding adsorption energies shown in square parentheses. Si adatoms and restatoms are highlighted, respectively, by larger yellow and green circles for clarity. Each heading panel describes the orientation of the $>\text{C}-\text{COOH}$ backbone in the admolecules with respect to Si surface (flat, tilt, or twist) at specific Si adatom sites, with the double bar (||) and semicolon (;) indicating the second admolecule H-bonded across the dimer wall or within the same half unit cell. The structures not supported by XPS results are greyed out, while plausible configurations (for early growth stage) supported by STM results are marked by asterisks.

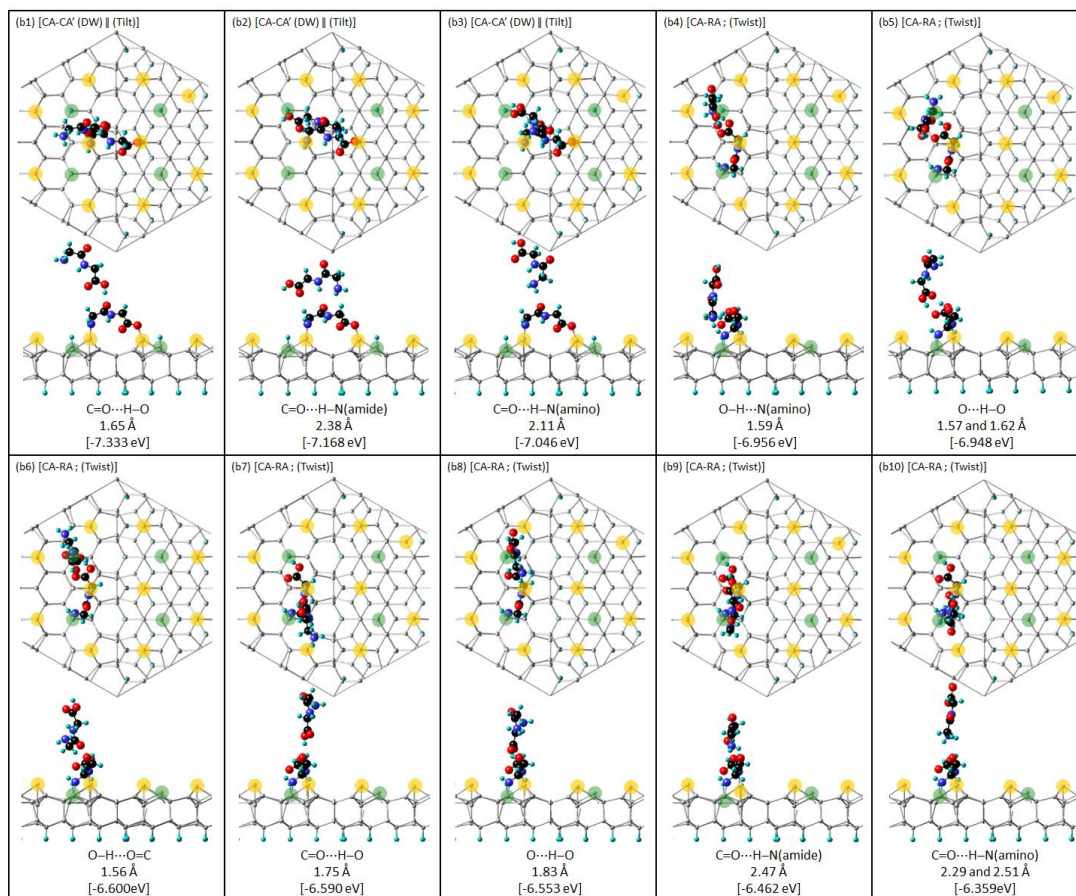


Figure C9 Top and side views of equilibrium di-molecular configurations of glycylglycine molecules for various (b1-b10) “lateral” and “near-vertical” H-bonding on the $\text{Si}_{200}\text{H}_{49}$ model 7×7 surface, obtained by DFT-D2 calculations. The lengths of the respective H-bonds are indicated, along with the corresponding adsorption energies shown in square parentheses. Si atoms and restatoms are highlighted, respectively, by larger yellow and green circles for clarity. Each heading panel describes the orientation of the $>\text{C}-\text{COOH}$ backbone in the admolecules with respect to Si surface (tilt, or twist) at specific Si adatom sites, with the double bar (||) and semicolon (;) indicating the second admolecule H-bonded across the dimer wall or within the same half unit cell.

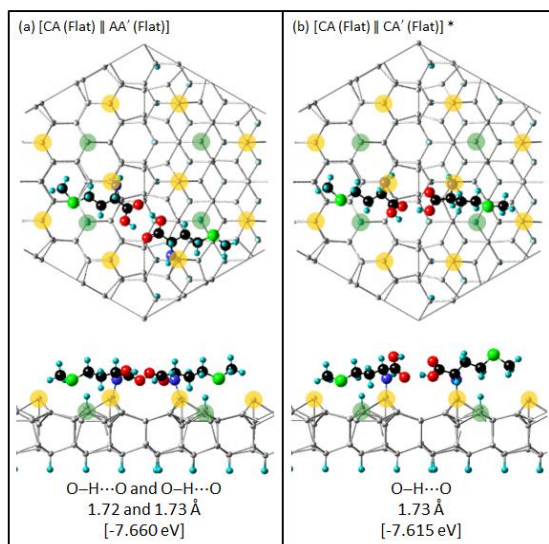


Figure C10 Top and side views of equilibrium di-molecular configurations of methionine adspecies involving (a) two and (b) one H-bond on the 7×7 $\text{Si}_{200}\text{H}_{49}$ model surface, obtained by DFT-D2 calculations. The lengths of the respective H-bonds are shown, along with the corresponding adsorption energies shown in square parentheses. Si adatoms and restatoms are highlighted, respectively, by larger yellow and green circles for clarity. Each heading panel describes the orientation of the $>\text{C}-\text{COOH}$ backbone in a methionine adspecies with respect to the Si surface (flat, tilt, twist) at specific Si adatom sites, with the double bar (||) indicating the second adspecies H-bonded across the dimer wall. The configuration that is supported by XPS and STM measurements is marked with an asterisk.

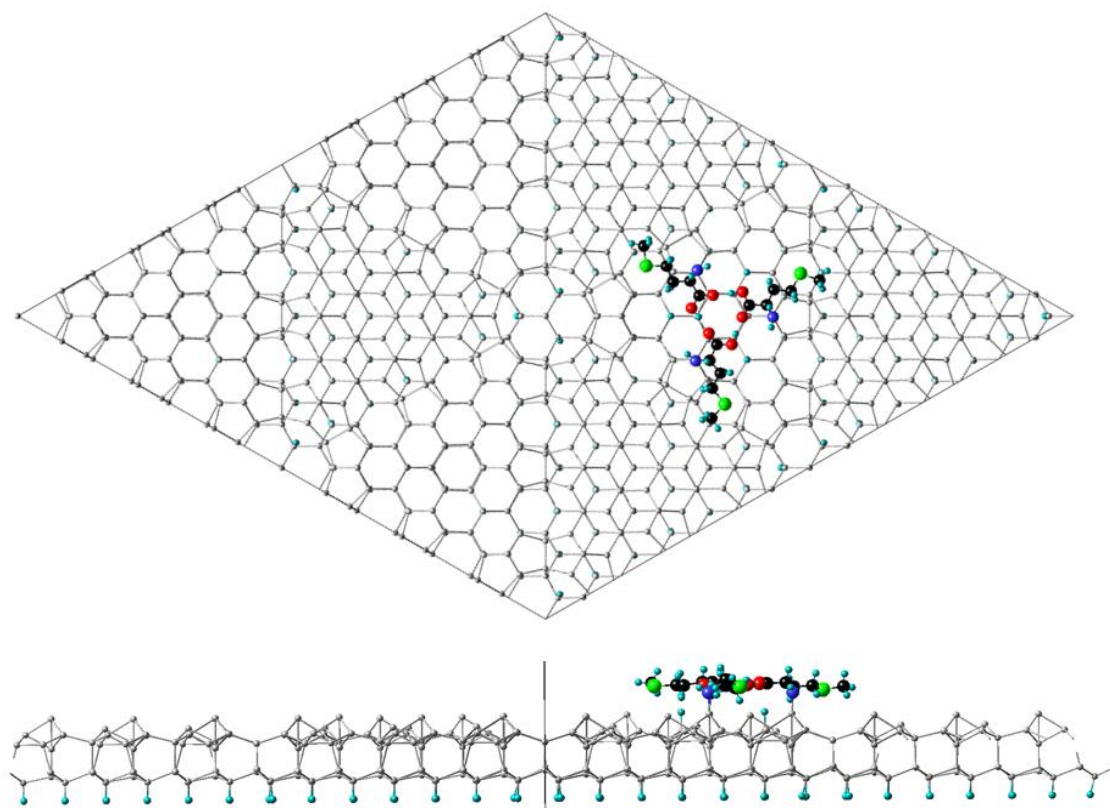


Figure C11 Top and side view of equilibrium configuration of a methionine trimer via formation of triple O···H–O hydrogen bonds in a ring configuration at the center of faulted half unit cell on a supercell including four Si₂₀₀H₄₉ slabs, i.e., a Si₈₀₀H₁₉₆ slab, as a model for a Si(111)7×7 surface obtained by DFT-D2 calculations.

Appendix D

Permissions



RightsLink®

Home

Account Info

Help



Title: Two-Dimensional Self-Assembled Gold Silicide Honeycomb Nanonetwork on Si(111)7×7

Logged in as:
Fateme Rahnemaye Rahsepar

Author: Fateme R. Rahsepar, Lei Zhang, K. T. Leung

LOGOUT

Publication: The Journal of Physical Chemistry C

Publisher: American Chemical Society

Date: May 1, 2014

Copyright © 2014, American Chemical Society

PERMISSION/LICENSE IS GRANTED FOR YOUR ORDER AT NO CHARGE

This type of permission/license, instead of the standard Terms & Conditions, is sent to you because no fee is being charged for your order. Please note the following:

- Permission is granted for your request in both print and electronic formats, and translations.
- If figures and/or tables were requested, they may be adapted or used in part.
- Please print this page for your records and send a copy of it to your publisher/graduate school.
- Appropriate credit for the requested material should be given as follows: "Reprinted (adapted) with permission from (COMPLETE REFERENCE CITATION). Copyright (YEAR) American Chemical Society." Insert appropriate information in place of the capitalized words.
- One-time permission is granted only for the use specified in your request. No additional uses are granted (such as derivative works or other editions). For any other uses, please submit a new request.

BACK

CLOSE WINDOW

Copyright © 2015 [Copyright Clearance Center, Inc.](#) All Rights Reserved. [Privacy statement](#). [Terms and Conditions](#). Comments? We would like to hear from you. E-mail us at customercare@copyright.com



RightsLink®

Home

Account
Info

Help



ACS Publications
Most Trusted. Most Cited. Most Read.

Title: Biofunctionalization of
Si(111)7×7 by "Renewable" I-
Cysteine Transitional Layer

Author: Fatemeh R. Rahsepar, Lei Zhang,
Hanieh Farkhondeh, et al

Publication: Journal of the American Chemical
Society

Publisher: American Chemical Society

Date: Dec 1, 2014

Copyright © 2014, American Chemical Society

Logged in as:
Fatemeh Rahnemaye
Rahsepar

LOGOUT

PERMISSION/LICENSE IS GRANTED FOR YOUR ORDER AT NO CHARGE

This type of permission/license, instead of the standard Terms & Conditions, is sent to you because no fee is being charged for your order. Please note the following:

- Permission is granted for your request in both print and electronic formats, and translations.
- If figures and/or tables were requested, they may be adapted or used in part.
- Please print this page for your records and send a copy of it to your publisher/graduate school.
- Appropriate credit for the requested material should be given as follows: "Reprinted (adapted) with permission from (COMPLETE REFERENCE CITATION). Copyright (YEAR) American Chemical Society." Insert appropriate information in place of the capitalized words.
- One-time permission is granted only for the use specified in your request. No additional uses are granted (such as derivative works or other editions). For any other uses, please submit a new request.

BACK

CLOSE WINDOW

Copyright © 2015 [Copyright Clearance Center, Inc.](#) All Rights Reserved. [Privacy statement](#). [Terms and Conditions](#).
Comments? We would like to hear from you. E-mail us at customercare@copyright.com

Bibliography

- (1) Frankline, B. Of the Stilling of Waves by Means of Oil. *Philos. Trans. R. Soc. Lond. B.* **1774**, *64*, 445–460.
- (2) Binnig, G.; Rohrer, H.; Gerber, Ch.; Weibel, E. Surface Studies by Scanning Tunneling Microscopy. *Phys. Rev. Lett.* **1982**, *49*, 57–61.
- (3) Somorjai, G. A.; Li, Y. *Introduction to Surface Chemistry and Catalysis*; 2nd ed.; Wiley, 2010; p. 800.
- (4) Bowker, M.; Davies, P. R. *Scanning Tunneling Microscopy in Surface Science*; Wiley-VCH, 2010; p. 258.
- (5) Tao, F.; Bernasek, S. L.; Xu, G.-Q. Electronic and Structural Factors in Modification and Functionalization of Clean and Passivated Semiconductor Surfaces with Aromatic Systems. *Chem. Rev.* **2009**, *109*, 3991–4024.
- (6) Stiévenard, D.; Legrand, B. Silicon Surface Nano-Oxidation Using Scanning Probe Microscopy. *Prog. Surf. Sci.* **2006**, *81*, 112–140.
- (7) Tao, F.; Bernasek, S. L. Understanding Odd–Even Effects in Organic Self-Assembled Monolayers. *Chem. Rev.* **2007**, *107*, 1408–1453.
- (8) Ma, Z.; Zaera, F. Organic Chemistry on Solid Surfaces. *Surf. Sci. Rep.* **2006**, *61*, 229–281.
- (9) Nejo, H. *Nanostructures–Fabrication and Analysis*; Springer, 2007; p. 292.
- (10) Schlier, R. E.; Farnsworth, H. E. Structure and Adsorption Characteristics of Clean Surfaces of Germanium and Silicon. *J. Chem. Phys.* **1959**, *30*, 917–926.
- (11) Wolkow, R. A. Direct Observation of an Increase in Buckled Dimers on Si(001) at Low Temperature. *Phys. Rev. Lett.* **1992**, *68*, 2636–2639.
- (12) Konečný, R.; Doren, D. J. Adsorption of Water on Si(100)-(2×1): A Study with Density Functional Theory. *J. Chem. Phys.* **1997**, *106*, 2426–2434.
- (13) Tao, F.; Wang, Z. H.; Qiao, M. H.; Liu, Q.; Sim, W. S.; Xu, G. Q. Covalent Attachment of Acetonitrile on Si(100) through Si–C and Si–N Linkages. *J. Chem. Phys.* **2001**, *115*, 8563–8569.

- (14) Rummel, R.; Ziegler, C. Room Temperature Adsorption of Aniline (C₆H₅NH₂) on Si(100)(2×1) Observed with Scanning Tunneling Microscopy. *Surf. Interface Anal.* **1998**, *418*, 303–313.
- (15) Coulter, S. K.; Schwartz, M. P.; Hamers, R. J. Sulfur Atoms as Tethers for Selective Attachment of Aromatic Molecules to Silicon(001) Surfaces. *J. Phys. Chem. B* **2001**, *105*, 3079–3087.
- (16) Silvestrelli, P. L. Adsorption of Ethanol on Si(100) from First Principles Calculations. *Surf. Sci.* **2004**, *552*, 17–26.
- (17) Tanaka, S.; Onchi, M.; Nishijima, M. The Adsorption and Thermal Decomposition of Formic Acid on Si(100) and Si(111) Surfaces. *J. Chem. Phys.* **1989**, *91*, 2712–2725.
- (18) Cao, X.; Hamers, R. J. Silicon Surfaces as Electron Acceptors: Dative Bonding of Amines with Si(001) and Si(111) Surfaces. *J. Am. Chem. Soc.* **2001**, *123*, 10988–10996.
- (19) Wang, G. T.; Mui, C.; Tannaci, J. F.; Filler, M. A.; Musgrave, C. B.; Bent, S. F. Reactions of Cyclic Aliphatic and Aromatic Amines on Ge(100)-2×1 and Si(100)-2×1. *J. Phys. Chem. B* **2003**, *107*, 4982–4996.
- (20) Liu, H.; Hamers, R. J. An X-Ray Photoelectron Spectroscopy Study of the Bonding of Unsaturated Organic Molecules to the Si (001) Surface. **1998**, *416*, 354–362.
- (21) Huang, H. G.; Zhang, Y. P.; Cai, Y. H.; Huang, J. Y.; Yong, K. S.; Xu, G. Q. Selective Attachment of Benzaldehyde on Si(100)-2×1: Structure, Selectivity, and Mechanism. *J. Chem. Phys.* **2005**, *123*, 104702.
- (22) Kiskinova, M.; Yates, J. T. Observation of Steric Conformational Effects in Hydrocarbon Adsorption and Decomposition: Cis- and Trans-Butene-2 on Si(100)-(2×1). *Surf. Interface Anal.* **1995**, *325*, 1–10.
- (23) Feenstra, R. M.; Thompson, W. A.; Fein, A. P. Scanning Tunneling Microscopy Studies of Si(111)-2×1 Surfaces. *J. Vac. Sci. Technol. A Vacuum, Surfaces, Film.* **1986**, *4*, 1315–1319.
- (24) Lander, J. J.; Gobeli, G. W.; Morrison, J. Structural Properties of Cleaved Silicon and Germanium Surfaces. *J. Appl. Phys.* **1963**, *34*, 2298–2306.
- (25) Pandey, K. C. New n-Bonded Chain Model for Si(111)-(2×1) Surface. *Phys. Rev. Lett.* **1981**, *47*, 1913–1917.
- (26) Binnig, G.; Rohrer, H.; Gerber, Ch.; Weibel, E. 7×7 Reconstruction on Si(111) Resolved in Real Space. *Phys. Rev. Lett.* **1983**, *50*, 120–123.

- (27) Erlandsson, R.; Olsson, L. Force Interaction in Low-Amplitude Ac-Mode Atomic Force Microscopy: Cantilever Simulations and Comparison with Data from Si(111)7×7. *Appl. Phys. A* **1998**, *66*, S879–S883.
- (28) Takayanagi, K.; Tanishiro, Y.; Takahashi, S.; Takahashi, M. Structure Analysis of Si(111)-7×7 Reconstructed Surface by Transmission Electron Diffraction. *Surf. Sci.* **1985**, *164*, 367–392.
- (29) Takayanagi, K.; Tanishiro, Y.; Takahashi, M.; Takahashi, S. Structural Analysis of Si(111)7×7 by UHV Transmission Electron Diffraction and Microscopy. *J. Vac. Sci. Technol. A* **1985**, *3*, 1502–1506.
- (30) Wang, Y.-L.; Guo, H.-M.; Qin, Z.-H.; Ma, H.-F.; Gao, H.-J. Toward a Detailed Understanding of Si(111)-7×7 Surface and Adsorbed Ge Nanostructures: Fabrications, Structures, and Calculations. *J. Nanomater.* **2008**, *2008*, 1–18.
- (31) Northrup, J. E. Origin of Surface States on Si(111)(7×7). *Phys. Rev. Lett.* **1986**, *57*, 154–157.
- (32) Tao, F.; Xu, G. Q. Attachment Chemistry of Organic Molecules on Si(111)-7×7. *Acc. Chem. Res.* **2004**, *37*, 882–893.
- (33) Ahn, J. R.; Yoo, K.; Seo, J. T.; Byun, J. H.; Yeom, H. W. Electronic States of Two-Dimensional Adatom Gas and Nanocluster Array: Na on Si(111)7×7. *Phys. Rev. B* **2005**, *72*, 113309.
- (34) Wu, K.; Fujikawa, Y.; Nagao, T.; Hasegawa, Y.; Nakatama, K. S.; Xue, Q. K.; Wang, E. G.; Briere, T.; Kumar, V.; Kawazoe, Y.; Zhang, S. B.; Sakurai, T. Na Adsorption on the Si(111)-(7×7) Surface: From Two-Dimensional Gas to Nanocluster Array. *Phys. Rev. Lett.* **2003**, *91*, 126101.
- (35) Wu, K. Unusual Diffusivity and Clustering of Alkali Metals on the Si(111)-7×7 Surface. *Sci. Technol. Adv. Mater.* **2005**, *6*, 789–794.
- (36) Watanabe, A.; Naitoch, M.; Nishigaki, S. Local Charge Redistribution at Potassium Adsorption on the Si(111)7×7 Surface: A Scanning Tunneling Microscopy Study. *Appl. Surf. Sci.* **1999**, *144-145*, 548–553.
- (37) Jia, J. F.; Liu, X.; Wang, J.-Zh.; Li, J.-L.; Wang, X. S.; Xue, Q.-K.; Li, Z.-Q.; Zhang, Zh.; Zhang, S. B. Fabrication and Structural Analysis of Al, Ga, and In Nanocluster Crystals. *Phys. Rev. B* **2002**, *66*, 165412.
- (38) Vitali, L.; Ramsey, M. G.; Netzer, F. P. Nanodot Formation on the Si Surface by Adatom Trapping. *Phys. Rev. Lett.* **1999**, *1*, 3–6.

- (39) Lai, M.Y.; Wang, Y. L. Self-Organized Two-Dimensional Lattice of Magic Clusters. *Phys. Rev. B* **2001**, *64*, 241404.
- (40) Li, J. L.; Jia, J.-F.; Liang, X.-J.; Liu, X.; Wang, J.-Zh.; Xue, Q.-K.; Li, Z.-Q.; Tse, J. S.; Zhang, Zh.; Zhang, S. B. Spontaneous Assembly of Perfectly Ordered Identical-Size Nanocluster Arrays. *Phys. Rev. Lett.* **2002**, *88*, 066101.
- (41) Wang, D. Y.; Chen, L.-J.; He, W.; Zhan Q.-F.; Cheng, Z.-H. Preferential Arrangement of Uniform Mn Nanodots on Si(111)-7×7 Surface. *J. Phys. D. Appl. Phys.* **2006**, *39*, 347–350.
- (42) Wang, D. Y.; Wu, H.-Y.; Chen, L.-J.; He, W.; Zhan, Q.-F.; Cheng, Z.-H. Growth of Honeycomb-Symmetrical Mn Nanodots Arrays on Si(111)-7×7 Surfaces. *J. Phys. Condens. Matter* **2006**, *18*, 6357–6363.
- (43) Zilani, M. A. K.; Xu., H.; Liu, T.; Sun, Y. Y.; Feng, Y. P.; Wang, X.-S.; Wee, A. T. S. Electronic Structure of Co-Induced Magic Clusters Grown on Si(111)-(7×7): Scanning Tunneling Microscopy and Spectroscopy and Real-Space Multiple-Scattering Calculations. *Phys. Rev. B* **2006**, *73*, 195415.
- (44) Zilani, M. A. K.; Sun, Y. Y.; Xu, H., Peng, G. W.; Feng, Y. P.; Wang, X.-S.; Wee, A. T. S. Formation and Stabilization of Fe-Induced Magic Clusters on Si(111)-(7×7) Template. *Surf. Sci.* **2007**, *601*, 2486–2490.
- (45) Zilani, M. A. K.; Sun, Y. Y.; Xu., H.; Liu, L.; Feng, Y. P.; Wang, X.-S.; Wee, A. T. S. Reactive Co Magic Cluster Formation on Si(111)-(7×7). *Phys. Rev. B* **2005**, *72*, 193402.
- (46) Hopfner, P.; Wisniewski, M.; Sandroock, J.; Schafer, J.; Claessen, R. Structural Components of the Pt/ Si(111) ($\sqrt{3}\times\sqrt{3}$) Surface from Scanning Tunneling Microscopy. *Phys. Rev.* **2010**, *82*, 075431.
- (47) Wawro, A.; Suto, S.; Kasuya, A. STM Studies of PtSi Formation on Si(111) by Solid State Epitaxy. *Phys. Rev. B* **2005**, *72*, 205302.
- (48) Wu, Y.; Zhou, Y.; Zhou, Ch.; Zhan, H.; Kang, J. Atomic Structure and Formation Mechanism of Identically Sized Au Clusters Grown on Si(111)-(7×7) Surface. *J. Chem. Phys.* **2010**, *133*, 124706.
- (49) Chizhov, I.; Lee, G.; Willis, R. F. STM Study of Room Temperature Adsorption of Au on the Si(111)-(7×7) Surface: Evidence for the Reaction of Au Atoms with Si Rest Atoms. *Appl. Phys. A* **1998**, *66*, 1003–1006.
- (50) Zhou, Y.; Wu, Qi-H.; Kang, J. STM Study of Au Adsorption on Si(111)-7×7 Surface: Voltage and Temperature Dependence. *J. Nanosci. Nanotechnol.* **2008**, *8*, 3030–3035.

- (51) Zhang, C.; Chen, G.; Wang, K.; Yang, H.; Su, T.; Chan, C. T.; Loy, M. M. T.; Xiao, X. Experimental and Theoretical Investigation of Single Cu, Ag, and Au Atoms Adsorbed on Si(111)-(7×7). *Phys. Rev. Lett.* **2005**, *94*, 176104.
- (52) Zhang, L.; Kim, Y.; Shim, H.; Lee, G. Adsorption of Au Atoms on Si (111)-(7×7) Studied by Using Scanning Tunneling Microscopy. *J. Korean Phys. Soc.* **2007**, *51*, 947–950.
- (53) Zhang, L.; Kim, Y.; Shim, H.; Lee, G. Influence of Substrate Temperature on Submonolayer Au Adsorption on an Si(111)-(7×7) Surface Studied by Scanning Tunneling Microscopy. *J. Phys. Condens. Matter* **2007**, *19*, 486004.
- (54) Chizhov, I.; Geunseop, L.; Willis, R. F. Initial Stages of Au Adsorption on the Si(111)-(7×7) Surface Studied by Scanning Tunneling Microscopy. *Phys. Rev. B* **1997**, *56*, 12316–12320.
- (55) Wang, K.; Zhang, C.; Loy, M. M. T.; Xiao, X. Time-Dependent Tunneling Spectroscopy for Studying Surface Diffusion Confined in Nanostructures. *Phys. Rev. Lett.* **2005**, *94*, 036103.
- (56) Zhang, Y. P.; Yang, L.; Lai, Y. H.; Xu, G. Q.; Wang, X. S. Formation of Ordered Two-Dimensional Nanostructures of Cu on the Si(111)-(7×7) Surface. *Surf. Sci.* **2003**, *531*, L378–L382.
- (57) Jarolimek, T.; Myslivecek, J.; Sobotil, P.; Ostadal, I. Adsorption and Diffusion of Ag Atoms on Si (111)-(7×7) Surface. *Surf. Sci.* **2001**, *482-485*, 386–390.
- (58) Zhou, C.; Xue, Q.; Jia, J.; Zhan, H.; Kang, J. Structural and Electronic Properties of Identical-Sized Zn Nanoclusters Grown on Si(111)-(7×7) Surfaces. *J. Chem. Phys.* **2009**, *130*, 024701.
- (59) Wang, Y. L.; Gao, H.-J.; Guo, H. M. Bonding Configurations and Collective Patterns of Ge Atoms Adsorbed on Si(111)-(7×7). *Phys. Rev. Lett.* **2005**, *94*, 106101.
- (60) Xie, Zh. -X.; Tanaka, K.-I. Tin Atoms Adsorbed on a Si(111)-(7×7) Surface. *Surf. Sci.* **2001**, *479*, 26–32.
- (61) Narusawa, T.; Komiya, S.; Hiraki, A. Diffuse Interface in Si (substrate) Au (evaporated Film) System. *Appl. Phys. Lett.* **1973**, *22*, 389–390.
- (62) Landree, E.; Grozea, D.; Collazo-Davila, C.; Marks, L. D. UHV High-Resolution Electron Microscopy and Chemical Analysis of Room-Temperature Au Deposition on Si(001)-2×1. *Phys. Rev. B* **1997**, *55*, 7910–7916.

- (63) Taleb-Ibrahimi, A.; Sebenne, C.A.; Bolmont, D.; Chen, P. Electronic Properties of Cleaved Si(111) Upon Room Temperature Deposition of Au. *Surf. Sci.* **1984**, *146*, 229–240.
- (64) Yeh, J. -J.; Hwang, J.; Bertness, K.; Friedman, D. J.; Cao, R.; Lindau, I. Growth of the Room Temperature Au/Si(111)-(7×7) Interface. *Phys. Rev. Lett.* **1993**, *70*, 3768–3771.
- (65) Hoshino, Y.; Kitsudo, Y.; Iwami, M.; Kido, Y. The Structure and Growth Process of Au/Si(111) Analyzed by High-Resolution Ion Scattering Coupled with Photoelectron Spectroscopy. *Surf. Sci.* **2008**, *602*, 2089–2095.
- (66) Hamers, R. J. Formation and Characterization of Organic Monolayers on Semiconductor Surfaces. *Annu. Rev. Anal. Chem. (Palo Alto, Calif.)* **2008**, *1*, 707–736.
- (67) Mirkin, C. A.; Taton, T. A. Semiconductors Meet Biology. *Nature* **2000**, *405*, 626–627.
- (68) Niemeyer, C. M.; Mirkin, C. A. *Nanobiotechnology: Concepts, Applications and Perspectives*; 1st ed.; Wiley, 2004; p. 491.
- (69) Tao, F. (Feng); Bernasek, S. *Functionalization of Semiconductor Surfaces*; Wiley, 2012; p. 454.
- (70) Cao, X.; Hamers, R. J. Molecular and Dissociative Bonding of Amines with the Si(111)-(7×7) Surface. *Surf. Sci.* **2003**, *523*, 241–251.
- (71) Yuan, Z. L.; Chen, X. F.; Wang, Z. H.; Yong, K. S.; Cao, Y.; Xu, G. Q. Dissociative Adsorption of Pyrrole on Si(111)-(7×7). *J. Chem. Phys.* **2003**, *119*, 10389.
- (72) Tao, F.; Yuan, Z. L.; Chen, X. F.; Qiao, M. H.; Wang, Z. H.; Dai, Y. J.; Huang, H. G.; Cao, Y.; Xu, G. Q. Multiple Configurations of N-Methylpyrrole Binding on Si(111)-7×7. *Phys. Rev. B* **2003**, *67*, 245406.
- (73) Bu, Y.; Shinn, D. W.; Lin, M. C. Adsorption and Thermal Decomposition of N₂H₄ and CH₃N₂H₃ on Si(111)7×7. *Surf. Sci.* **1992**, *276*, 184–199.
- (74) Tao, F.; Chen, X. F.; Wang, Z. H.; Xu, G. Q. Binding and Structure of Acetonitrile on Si(111)-7×7. *J. Phys. Chem. B* **2002**, *106*, 3890–3895.
- (75) Huang, J. Y.; Shao, Y. X.; Huang, H. G.; Cai, Y. H.; Ning, Y. S. Binding Mechanisms of Methacrylic Acid and Methyl Methacrylate on Si (111)-7×7 Effect of Substitution Groups. *J. Phys. Chem. B* **2005**, *109*, 19831–19838.
- (76) Bu, Y.; Lin, M. C. Adsorption and Thermal Decomposition of Acetaldehyde on Si(111)-7×7. *J. Phys. Chem. B* **1997**, *5647*, 1872–1877.

- (77) Carbone, M.; Comtet, G.; Dujardin, G.; Hellner, L.; Mayne, A. J. Different Role of Filled and Empty Surface States in a Polyfunctional Molecule Adsorption: Geranyl Acetone on Si(111)7×7. *J. Chem. Phys.* **2002**, *117*, 5012.
- (78) Carbone, M.; Piancastelli, M. N.; Casaletto, M. P.; Zanoni, R.; Besnard-Ramage, M. J.; Comtet, G.; Dujardin, G.; Hellner, L. Phenol Adsorption on Si(111)7×7 Studied by Synchrotron Radiation Photoemission and Photodesorption. *Surf. Interface Anal.* **1999**, *419*, 114–119.
- (79) Tao, F.; Wang, Z. H.; Xu, G. Q. Covalent Binding of Cyclohexene, 1,3-Cyclohexadiene and 1,4-Cyclohexadiene on Si(111)-7×7. *Surf. Sci.* **2003**, *530*, 203–215.
- (80) Tao, F.; Lai, Y. H.; Xu, G. Q. Si-C(N) σ Linkages and N-Si Dative Bonding at Pyridine/Si(111)-7×7. *Langmuir* **2004**, *20*, 366–368.
- (81) Yoshinobu, J.; Fukushi, D.; Uda, M.; Nomura, E.; Aono, M. Acetylene Adsorption on Si(111)(7×7): A Scanning-Tunneling-Microscopy Study. *Phys. Rev. B* **1992**, *46*, 9520–9524.
- (82) Piancastelli, M. N.; Motta, N.; Sgarlata, A.; Balzarotti, A. Topographic and Spectroscopic Analysis of Ethylene Adsorption on Si(111)7×7 by STM and STS. *Phys. Rev. B* **1993**, *48*, 17 892–896.
- (83) Shachal, D.; Manassen, Y.; Ter-Ovanesyan, E. Role of Chain Length on the Surface Chemistry of Dienes Studied by Scanning Tunneling Microscopy. *Phys. Rev.* **1997**, *55*, 9367–9370.
- (84) Baik, J.; Kim, M.; Park, C.; Kim, Y.; Ahn, J. R.; An, K.-S. Cycloaddition Reaction of 1,3-Butadiene with a Symmetric Si Adatom Pair on the Si(111)7×7 Surface. *J. Am. Chem. Soc.* **2006**, 8370–8371.
- (85) Kawasaki, T.; Sakai, D.; Kishimoto, H.; Akbar, A. A.; Ogawa, T.; Oshima, C. Adsorption and Desorption of Benzene on Si(111)-7×7 Studied by Scanning Tunneling Microscopy. *Surf. Interface Anal.* **2001**, *31*, 126–130.
- (86) Tomimoto, H.; Takehara, T.; Fukawa, K.; Sumii, R.; Sekitani, T.; Tanaka, K. Study of Benzene and Toluene on Si(111)7×7 Surface by Scanning Tunneling Microscopy. *Surf. Sci.* **2003**, *526*, 341–350.
- (87) Horn, S. A.; Patitsas, S. N. STM Study of Charge Transfer and the Role of Rest-Atoms in the Binding of Benzene to Si(111)7×7. *Surf. Sci.* **2008**, *602*, 630–637.

- (88) Yong, K. S.; Yang, S.; Zhang, Y. P.; Wu, P.; Xu, G. Q. Adsorption-Induced Desorption of Benzene on Si(111)-7×7 by Substrate-Mediated Electronic Interactions. *Langmuir* **2008**, 3289–3293.
- (89) Cao, Y.; Yong, K. S.; Wang, Z. Q.; Chin, W. S.; Lai, Y. H.; Deng, J. F.; Xu, G. Q. Dry Thienylation of the Silicon (111)-(7×7). *J. Am. Chem. Soc.* **2000**, 122, 1812–1813.
- (90) Cao, Y.; Yong, K. S.; Wang, Z. H.; Deng, J. F.; Lai, Y. H.; Xu, G. Q. Cycloaddition Chemistry of Thiophene on the Silicon (111)-7×7 Surface. *J. Chem. Phys.* **2001**, 115, 3287.
- (91) Chatterjee, A.; Zhang, L.; Leung, K. T. Surface [4+2] Cycloaddition Reaction of Thymine on Si(111)7×7 Observed by Scanning Tunneling Microscopy. *J. Phys. Chem. C* **2013**, 117, 14677–14683.
- (92) Guisinger, N. P.; Elder, S. P.; Yoder, N. L.; Hersam, M. C. Ultra-High Vacuum Scanning Tunnelling Microscopy Investigation of Free Radical Adsorption to the Si(111)-7×7 Surface. *Nanotechnology* **2007**, 18, 044011.
- (93) Yong, K. S.; Zhang, Y. P.; Yang, S.-W.; Xu, G. Q. Naphthalene Adsorption on Si(111)-7×7. *Surf. Sci.* **2008**, 602, 1921–1927.
- (94) Yong, K. S.; Zhang, Y. P.; Yang, S.; Wu, P.; Xu, G. Q. Studies of Chemisorbed Tetracene on Si(111)-7×7. *J. Phys. Chem. A* **2007**, 12266–12274.
- (95) Yong, K. S.; Zhang, Y. P.; Yang, S. W.; Wu, P.; Xu, G. Q. Chemisorption of Pentacene on Si (111)-7×7 Studied via Scanning Tunneling Microscopy and Density Functional Theory. *J. Phys. Chem. C* **2007**, 4285–4293.
- (96) Chatterjee, A.; Zhang, L.; Leung, K. T. Direct Imaging of Hydrogen Bond Formation in Dissociative Adsorption of Glycine on Si(111)7×7 by Scanning Tunneling Microscopy. *J. Phys. Chem. C* **2012**, 116, 10968–10975.
- (97) Zhang, L., Rahsepar, F. R., Farkhondeh, H., Leung, K. T. Adsorption Bonding Configuration of Alanine on Si(111)7×7 Determined by Scanning Tunneling Microscopy and X-Ray Photoelectron Spectroscopy. *to be Publ.*
- (98) Rahsepar, F. R.; Zhang, L.; Farkhondeh, H.; Leung, K. T. Biofunctionalization of Si(111)7×7 by “Renewable” L-Cysteine Transitional Layer-Chapter 4. *J. Am. Chem. Soc.* **2014**, 136, 16909–16918.
- (99) Chatterjee, A.; Zhang, L.; Leung, K. T. Bidentate Surface Structures of Glycylglycine on Si(111)7×7 by High- Resolution Scanning Tunneling Microscopy: Site-Specific

- Adsorption via N–H and O–H or Double N–H Dissociation. *Langmuir* **2012**, *28*, 12502–12508.
- (100) Chatterjee, A.; Zhang, L.; Leung, K. T. Self-Directed Growth of Aligned Adenine Molecular Chains on Si(111)7×7: Direct Imaging of Hydrogen-Bond Mediated Dimers and Clusters at Room Temperature by Scanning Tunneling Microscopy. *Langmuir* **2013**, *29*, 9369–9377.
- (101) Garah, M. E.; Makoudi, Y.; Duverger, E.; Palmino, F.; Rochefort, A.; Chérioux, F. Large-Scale Patterning of Zwitterionic Molecules on a Si(111)-7×7 Surface. *ACS Nano* **2011**, *5*, 424–428.
- (102) Florkin, M.; Stotz, E. H. *Comprehensive Biochemistry: Lipids, Amino Acids and Related Compounds, V.6*; Elsevier Science Ltd: Oxford, 1965.
- (103) Barlow, S. M.; Kitching, K. J.; Haq, S.; Richardson, N. V. A Study of Glycine Adsorption on A Cu{110} Surface Using Reflection Absorption Infrared Spectroscopy. *Surf. Sci.* **1998**, *401*, 322–335.
- (104) Lrfgren, P.; Krozer, A.; Lausmaa, J.; Kasemo, B. Glycine on Pt (111): A TDS and XPS Study. *Surf. Sci.* **1997**, *370*, 277–292.
- (105) Zhao, X.; Rodriguez, J. Photoemission Study of Glycine Adsorption on Cu/Au(111) Interfaces. *Surf. Sci.* **2006**, *600*, 2113–2121.
- (106) Iwai, H.; Egawa, C. Molecular Orientation and Intermolecular Interaction in Alanine on Cu(001). *Langmuir* **2010**, *26*, 2294–2300.
- (107) Haq, S.; Massey, A.; Moslemzadeh, N.; Robin, A.; Barlow, S. M.; Raval, R.; April, R. V.; Final, I.; June, F. Racemic Versus Enantiopure Alanine on Cu(110): An Experimental Study. *Langmuir* **2007**, *23*, 10694–10700.
- (108) Barlow, S. M.; Louafi, S.; Roux, D. L.; Williams, J.; Muryn, C.; Haq, S.; Raval, R. Supramolecular Assembly of Strongly Chemisorbed Size- and Shape-Defined Chiral Clusters: S- And R-Alanine on Cu(110). *Langmuir* **2004**, *20*, 7171–7176.
- (109) Barlow, S. M.; Louafi, S.; Le Roux, D.; Williams, J.; Muryn, C.; Haq, S.; Raval, R. Polymorphism in Supramolecular Chiral Structures of R- and S-Alanine on Cu(110). *Surf. Sci.* **2005**, *590*, 243–263.
- (110) Jones, G.; Jones, L. B.; Thibault-Starzyk, F.; Seddon, E. A.; Raval, R.; Jenkins, S. J.; Held, G. The Local Adsorption Geometry and Electronic Structure of Alanine on Cu{110}. *Surf. Sci.* **2006**, *600*, 1924–1935.

- (111) Madden, D. C.; Temprano, I.; Sacchi, M.; Blanco-Rey, M.; Jenkins, S. J.; Driver, S. M. Self-Organized Overlayers Formed by Alanine on Cu {311} Surfaces. *J. Phys. Chem. C* **2014**, *118*, 18589–18603.
- (112) Smerieri, M.; Vattuone, L.; Costa, D.; Tielens, F.; Savio, L. Self-Assembly of (S)-Glutamic Acid on Ag(100): A Combined LT-STM and Ab Initio Investigation. *Langmuir* **2010**, *26*, 7208–7215.
- (113) Smerieri, M.; Vattuone, L.; Kravchuk, T.; Costa, D.; Savio, L.; Dodecaneso, V. (S)-Glutamic Acid on Ag(100): Self-Assembly in the Nonzwitterionic Form. *Langmuir* **2011**, *27*, 2393–2404.
- (114) Tranca, I.; Smerieri, M.; Savio, L.; Vattuone, L.; Costa, D.; Tielens, F. Unraveling the Self-Assembly of the (S)-Glutamic Acid “ Flower ” Structure on Ag(100). *Langmuir* **2013**, *29*, 7876–7884.
- (115) Jones, T. E.; Baddeley, C. J. Molecular Ordering and Adsorbate Induced Faceting in the Ag {110}-(S)-Glutamic Acid System. *Langmuir* **2005**, *21*, 9468–9475.
- (116) Humblot, V.; Méthivier, C.; Pradier, C. Adsorption of L-Lysine on Cu(110): A RAIRS Study from UHV to the Liquid Phase. *Langmuir* **2006**, *22*, 3089–3096.
- (117) Humblot, V.; Méthivier, C.; Raval, R.; Pradier, C.-M. Amino Acid and Peptides on Cu(110) Surfaces: Chemical and Structural Analyses of L-Lysine. *Surf. Sci.* **2007**, *601*, 4189–4194.
- (118) Zhao, X.; Zhao, R. G.; Yang, W. S. Scanning Tunneling Microscopy Investigation of L-Lysine Adsorbed on Cu(001). *Langmuir* **2000**, *16*, 9812–9818.
- (119) Uvdal, K.; Bodo, P.; Liedberg, B. L-Cysteine Adsorbed on Gold and Copper: An X-Ray Photoelectron Spectroscopy Study. *J. Colloid Interface Sci.* **1992**, *149*, 162–173.
- (120) Fischer, S.; Papageorgiou, A. C.; Marschall, M.; Reichert, J.; Diller, K.; Klappenberger, F.; Allegretti, F.; Nefedov, A.; Woll, C.; Barth, J. V. L-Cysteine on Ag(111): A Combined STM and X-Ray Spectroscopy Study of Anchorage and Deprotonation. *J. Phys. Chem. C* **2012**, *116*, 20356–20362.
- (121) Kühnle, A.; Linderoth, T. R.; Hammer, B.; Besenbacher, F. Chiral Recognition in Dimerization of Adsorbed Cysteine Observed by Scanning Tunnelling Microscopy. *Nature* **2002**, *415*, 891–893.
- (122) Naitabdi, A.; Humblot, V. Chiral Self-Assemblies of Amino-Acid Molecules: D- And L-Methionine on Au(111) Surface. *Appl. Phys. Lett.* **2010**, *97*, 223112.

- (123) Pennec, Y.; Weber-bargioni, A.; Cvetko, D.; Schiffrin, A.; Riemann, A.; Auwa, W.; Cossaro, A.; Morgante, A.; Barth, J. V. Zwitterionic Self-Assembly of L-Methionine Nanogratings on the Ag(111) Surface. *Proc. Natl. Acad. Sci* **2007**, *104*, 5279–5284.
- (124) Schiffrin, A.; Reichert, J.; Pennec, Y.; Auwarter, W.; Weber-bargioni, A.; Marschall, M.; Dell'Angela, M.; Cvetko, D.; Bavdek, G.; Cossaro, A.; Morgante, A.; Barth, J. V. Self-Assembly of L-Methionine on Cu(111): Steering Chiral Organization by Substrate Reactivity and Thermal Activation. *J. Phys. Chem. C* **2009**, *113*, 12101–12108.
- (125) Humblot, V.; Tielens, F.; Luque, N. B.; Hampartsoumian, H.; Méthivier, C.; Pradier, C.-M. Characterization of Two-Dimensional Chiral Self-Assemblies L- and D-Methionine on Au(111). *Langmuir* **2014**, *30*, 203–212.
- (126) Méthivier, C.; Humblot, V.; Pradier, C.-M. L-Methionine Adsorption on Cu(110), Binding and Geometry of the Amino Acid as a Function of Coverage. *Surf. Sci.* **2015**, *632*, 88–92.
- (127) Wang, D.; Xu, Q.; Wan, L.; Bai, C.; Jin, G. Adsorption of Enantiomeric and Racemic Tyrosine on Cu(111): A Scanning Tunneling Microscopy Study. *Langmuir* **2003**, *19*, 1965–1969.
- (128) Reichert, J.; Schiffrin, A.; Auwarter, W.; Weber-bargioni, A.; Marschall, M.; Dell'Angela, M.; Cvetko, D.; Bavdek, G.; Cossaro, A.; Morgante, A.; Barth, J. V. L-Tyrosine on Ag(111): Universality of the Amino Acid 2D Zwitterionic Bonding Scheme? *ACS Nano* **2010**, *4*, 1218–1226.
- (129) Forster, M.; Dyer, M. S.; Persson, M.; Raval, R. Probing Conformers and Adsorption Footprints at the Single-Molecule Level in a Highly Organized Amino Acid Assembly of (S)-Proline on Cu(110). *J. Am. Chem. Soc.* **2009**, *131*, 10173–10181.
- (130) Simpson, G. J.; Grillo, F.; Greenwood, J.; Francis, S. M.; Schaub, R.; Lacovig, P.; Baddeley, C. J. Assembly of a Chiral Amino Acid on an Unreactive Surface: (S)-Proline on Au(111). *Langmuir* **2014**, *30*, 3495–3501.
- (131) Zhang, L.; Chatterjee, A.; Leung, K. T. Three-Stage Growth of Glycine and Glycylglycine Nanofilms on Si(111)7×7 and Their Thermal Evolution in Ultrahigh Vacuum Condition : From Chemisorbed Adstructures to Transitional Adlayer to Zwitterionic Films. *J. Phys. Chem. C* **2011**, *115*, 14155–14163.
- (132) Chatterjee, A.; Zhang, L.; Leung, K. T. Computational Surface Chemistry of Glycine on Si(111)7×7 and Si(100)2×1: Dissociative Adsorption through Adduct Formation. *Chem. Phys. Lett.* **2011**, *508*, 219–223.

- (133) Zhang, L.; Chatterjee, A.; Leung, K. T. Hydrogen-Bond-Mediated Biomolecular Trapping: Reversible Catch-and-Release Process of Common Biomolecules on a Glycine-Functionalized Si(111)7×7 Surface. *J. Phys. Chem. Lett.* **2010**, *1*, 3385–3390.
- (134) Zhou, X. J.; Li, Q.; Leung, K. T. Formation of C=C and Si-Cl Adstructures by Insertion Reactions of Cis-Dichloroethylene and Perchloroethylene on Si(100)2×1. *J. Phys. Chem. B* **2006**, *110*, 5602–5610.
- (135) Zhou, X. J.; Li, Q.; He, Z. H.; Yang, X.; Leung, K. T. Dissociative Adsorption and Thermal Desorption of Dibromoethylene on Si(100)2×1: Surface Mediated Dehalogenation and Recombinative Evolution of HBr. *Surf. Sci.* **2003**, *543*, L668–L674.
- (136) Ebrahimi, M.; Chong, J. M.; Leung, K. T. Selective Adsorption and Thermal Evolution of Bifunctional Carboxylic Acids: Competition of O-H Dissociation and Other Reaction Products in Acrylic Acid and Propanoic Acid on Si(100)2×1. *J. Phys. Chem. C* **2010**, *114*, 2947–2957.
- (137) Ebrahimi, M.; Leung, K. T. Selective Surface Chemistry of Allyl Alcohol and Allyl Aldehyde on Si(100)2×1: Competition of [2+2] C=C Cycloaddition with O–H Dissociation and with [2+ 2] CO Cycloaddition in Bifunctional Molecules. *Surf. Sci.* **2009**, *603*, 1203–1211.
- (138) Radi, A.; Ebrahimi, M.; Leung, K. T. Relative Reactivities of Amino and Ethenyl Groups in Allylamine on Si(100)2×1: Temperature-Dependent X-Ray Photoemission and Thermal Desorption Studies of a Common Linker Molecule. *Surf. Sci.* **2010**, *604*, 1073–1081.
- (139) Radi, A.; Leung, K. T. Competitive Bonding of Amino and Hydroxyl Groups in Ethanolamine on Si(100)2×1: Temperature-Dependent X-Ray Photoemission and Thermal Desorption Studies of Nanochemistry of a Double-Chelating Agent. *Mater. Express* **2011**, *1*, 144–153.
- (140) Ebrahimi, M.; Fernando Rios, J.; Leung, K. T. Dissociative Adsorption and Thermal Evolution of Acetic Acid on Si(100)2×1: Surface-Mediated Formation of Ketene and Acetaldehyde from Unidentate and Bidentate Acetate Adsorbates. *J. Phys. Chem. C* **2009**, *113*, 281–289.
- (141) Zhou, X. J.; Leung, K. T. Competition Between Associative and Dissociative Adsorption of 1,2-Dihalogenated Benzenes on Si(100)2×1: Formation of Dihalocyclohexadiene, Halophenyl and Phenylene Adstructures. *Surf. Sci.* **2006**, *600*, 3285–3296.
- (142) Li, Q.; Leung, K. T. Thermal Chemistry of Toluene and Benzene on Si(100)2×1 and Modified Surfaces. *Surf. Sci.* **2001**, *479*, 69–82.

- (143) He, Z.; Leung, K. T. Thermal and Ion-Induced Surface Reactions of 1,1-Difluoroethylene on Si(111)7×7 and Vitreous SiO₂. *J. Phys. Chem. B* **2005**, *109*, 14971–14978.
- (144) He, Z.; Li, Q.; Leung, K. T. Isomeric Effects on Room-Temperature Chemisorption and Thermal Evolution of Iso-, Cis- and Trans-Dichloroethylene on Si(111)7×7. *Surf. Sci.* **2006**, *600*, 514–526.
- (145) He, Z.; Li, Q.; Leung, K. T. Room-Temperature Chemisorption and Thermal Evolution of 1,1-Dichloroethylene and Monochloroethylene on Si (111)7×7: Formation of Vinylidene and Vinylene Adspecies. *J. Phys. Chem. B* **2005**, *109*, 14908–14916.
- (146) He, Z.; Leung, K. T. Room-Temperature Chemisorption and Thermal Evolution of Perchloroethylene and Trichloroethylene on Si(111)7×7: Formation of Chlorinated Vinylene and Vinylidene and Acetylde Adspecies, and Thermal Etching Reactions. *Surf. Sci.* **2005**, *583*, 179–190.
- (147) Venugopal, V.; Chatterjee, A.; Ebrahimi, M.; He, Z. H.; Leung, K. T. Adsorption and Thermal Decomposition of Acetic Acid on Si(111)7×7 Studied by Vibrational Electron Energy Loss Spectroscopy. *J. Chem. Phys.* **2010**, *132*, 174702.
- (148) Venugopal, V.; Ebrahimi, M.; He, Z. H.; Leung, K. T. Dissociative Adsorption and Thermal Evolution of Carbon Tetrachloride on Si(111)7×7. *Surf. Sci.* **2008**, *602*, 3000–3005.
- (149) Ataman, E.; Isvoranu, C.; Knudsen, J.; Schulte, K.; Andersen, J. N.; Schnadt, J. Modification of the Size of Supported Clusters by Coadsorption of an Organic Compound: Gold and L-Cysteine on Rutile TiO₂(110). *Langmuir* **2011**, *27*, 11466–11474.
- (150) Kühnle, A.; Linderoth, T. R.; Besenbacher, F. Self-Assembly of Monodispersed, Chiral Nanoclusters of Cysteine on the Au(110)-(1×2) Surface. *J. Am. Chem. Soc.* **2003**, *125*, 14680–14681.
- (151) Kühnle, A.; Linderoth, T. R.; Schunack, M.; Besenbacher, F. L-Cysteine Adsorption Structures on Au(111) Investigated by Scanning Tunneling Microscopy Under Ultrahigh Vacuum Conditions. *Langmuir* **2006**, 2156–2160.
- (152) Cavalleri, O.; Gonella, G.; Terreni, S.; Vignolo, M.; Floreano, L.; Morgante, A.; Canepa, M.; Rolandi, R. High Resolution X-Ray Photoelectron Spectroscopy of L-Cysteine Self-Assembled Films. *Phys. Chem. Chem. Phys.* **2004**, *6*, 4042–4046.
- (153) Gonella, G.; Terreni, S.; Cvetko, D.; Cossaro, A.; Mattera, L.; Cavalleri, O.; Rolandi, R.; Morgante, A.; Floreano, L.; Canepa, M. Ultrahigh Vacuum Deposition of L-Cysteine on Au(110) Studied by High-Resolution X-Ray Photoemission: From Early Stages of Adsorption to Molecular Organization. *J. Phys. Chem. B* **2005**, *109*, 18003–18009.

- (154) Cossaro, A.; Terreni, S.; Cavalleri, O.; Prato, M.; Cvetko, D.; Morgante, A.; Floreano, L.; Canepa, M. Electronic and Geometric Characterization of the L-Cysteine Paired-Row Phase on Au(110). *Langmuir* **2006**, *22*, 11193–11198.
- (155) Mateo-Martí, E.; Rogero, C.; Gonzalez, C.; Sobrado, J. M.; de Andrés, P. L.; Martín-Gago, J. A. Interplay Between Fast Diffusion and Molecular Interaction in the Formation of Self-Assembled Nanostructures of S-Cysteine on Au(111). *Langmuir* **2010**, *26*, 4113–4118.
- (156) Kühnle, A. Self-Assembly of Organic Molecules at Metal Surfaces. *Curr. Opin. Colloid Interface Sci.* **2009**, *14*, 157–168.
- (157) Xu, Q.; Wan, L.; Wang, C.; Bai, C.; Wang, Z.; Nozawa, T. New Structure of L-Cysteine Self-Assembled Monolayer on Au(111): Studies by In Situ Scanning Tunneling Microscopy. *Langmuir* **2001**, *17*, 6203–6206.
- (158) Einstein, A. Über Einen Die Erzeugung Und Verwandlung Des Lichtes Betreffenden Heuristischen Gesichtspunkt. *Ann. Phys.* **1905**, *17*, 132–148.
- (159) Nordling, C.; Sokolowski, E.; Siegbahn, K. Precision Method for Obtaining Absolute Values of Atomic Binding Energies. *Phys. Rev.* **1957**, *105*, 1676–1677.
- (160) Vickerman, J. C.; Gilmore, I. *Surface Analysis—The Principal Techniques*; 2nd ed.; John Wiley & Sons, Ltd: Chichester, UK, 2009; p. 686.
- (161) Binnig, G.; Rohrer, H.; Gerber, Ch.; Weibel, E. Tunneling through a Controllable Vacuum Gap. *Appl. Phys. Lett.* **1982**, *40*, 178.
- (162) Thomas, L. H. The Calculation of Atomic Fields. *Math. Proc. Cambridge Philos. Soc.* **1926**, *23*, 542.
- (163) Fermi, E. Eine Statistische Methode Zur Bestimmung Einiger Eigenschaften Des Atoms Und Ihre Anwendung Auf Die Theorie Des Periodischen Systems Der Elemente. *Zeitschrift Für Phys.* **1928**, *48*, 73–79.
- (164) Slater, J. C. A Simplification of the Hartree-Fock Method. *Phys. Rev.* **1951**, *81*, 385–390.
- (165) Hartree, D. R. The Wave Mechanics of an Atom with a Non-Coulomb Central Field. Part I. Theory and Methods. *Math. Proc. Cambridge Philos. Soc.* **1928**, *24*, 89–110.
- (166) Hartree, D. R. The Wave Mechanics of an Atom with a Non-Coulomb Central Field. Part II. Some Results and Discussion. *Math. Proc. Cambridge Philos. Soc.* **1928**, *24*, 111–132.

- (167) Fock, V. V. Näherungsmethode Zur Lösung Des Quantenmechanischen Mehrkörperproblems. *Zeitschrift für Phys.* **1930**, *61*, 126–148.
- (168) Fock, V. V. “Selfconsistent Field” Mit Austausch Für Natrium. *Zeitschrift für Phys.* **1930**, *62*, 795–805.
- (169) Hohenberg, P.; Kohn, W. Inhomogeneous Electron Gas. *Phys. Rev.* **1964**, *136*, B864–B871.
- (170) Kohn, W.; Sham, L. J. Self-Consistent Equations Including Exchange and Correlation Effects. *Phys. Rev.* **1965**, *140*, A1133–A1138.
- (171) Perdew, J. P.; Chevary, J. A.; Vosko, S. H.; Jackson, K. A.; Pederson, M. R.; Singh, D. J.; Fiolhais, C. Atoms, Molecules, Solids, and Surfaces: Applications of the Generalized Gradient Approximation for Exchange and Correlation. *Phys. Rev. B* **1992**, *46*, 6671–6687.
- (172) Perdew, J. P.; Burke, K.; Ernzerhof, M. Generalized Gradient Approximation Made Simple. *Phys. Rev. Lett.* **1996**, *77*, 3865–3868.
- (173) Wu, X.; Vargas, M. C.; Nayak, S.; Lotrich, V.; Scoles, G. Towards Extending the Applicability of Density Functional Theory to Weakly Bound Systems. *J. Chem. Phys.* **2001**, *115*, 8748.
- (174) Sholl, D.; Steckel, J. A. *Density Functional Theory: A Practical Introduction*; Wiley, 2009; p. 252.
- (175) Grimme, S. Accurate Description of van Der Waals Complexes by Density Functional Theory Including Empirical Corrections. *J. Comput. Chem.* **2004**, *25*, 1463–1473.
- (176) Grimme, S. Semiempirical GGA-Type Density Functional Constructed with a Long-Range Dispersion Correction. *J. Comput. Chem.* **2006**, *27*, 1787–1799.
- (177) Grimme, S.; Antony, J.; Ehrlich, S.; Krieg, H. A Consistent and Accurate Ab Initio Parametrization of Density Functional Dispersion Correction (DFT-D) for the 94 Elements H-Pu. *J. Chem. Phys.* **2010**, *132*, 154104.
- (178) Kresse, G.; Hafner, J. Ab Initio Molecular Dynamics for Liquid Metals. *Phys. Rev. B* **1993**, *47*, 558–561.
- (179) Kresse, G.; Hafner, J. Ab Initio Molecular-Dynamics Simulation of the Liquid-Metal—amorphous-Semiconductor Transition in Germanium. *Phys. Rev. B* **1994**, *49*, 14251–14269.

- (180) Kresse, G.; Furthmüller, J. Efficient Iterative Schemes for Ab Initio Total-Energy Calculations Using a Plane-Wave Basis Set. *Phys. Rev. B* **1996**, *54*, 11169–11186.
- (181) Kresse, G.; Furthmüller, J. Efficiency of Ab-Initio Total Energy Calculations for Metals and Semiconductors Using a Plane-Wave Basis Set. *Comput. Mater. Sci.* **1996**, *6*, 15–50.
- (182) Wang, Y.; Perdew, J. P. Correlation Hole of the Spin-Polarized Electron Gas, with Exact Small-Wave-Vector and High-Density Scaling. *Phys. Rev. B* **1991**, *44*, 13298–13307.
- (183) Blochl, P. E. Projector Augmented-Wave Method. *Phys. Rev. B* **1994**, *50*, 17953–17979.
- (184) Kresse, G.; Joubert, D. From Ultrasoft Pseudopotentials to the Projector Augmented-Wave Method. *Phys. Rev. B* **1999**, *59*, 1758–1775.
- (185) Braicovich, L.; Garner, C. M.; Skeath, P. R.; Su, C. Y.; Chye, P. W.; Lindau, I.; Spicer, E. Photoemission Studies of the Silicon-Gold Interface. *Phys. Rev. B* **1979**, *20*, 5131–5141.
- (186) Zhang, L.; Jeon, Y.; Shim, H.; Lee, G. Direct Observation of Hopping and Merging of Single Au Adatoms to Form Dimers on Si(111)-(7×7). *J. Vac. Sci. Technol. A* **2012**, *30*, 061406.
- (187) Rota, A.; Martinez-Gil, A.; Agnus, G.; Moyen, E.; Maroutian, T.; Bartenlian, B.; Mégy, R.; Hanbücken, M.; Beauvillain, P. Au Island Growth on a Si(111) Vicinal Surface. *Surf. Sci.* **2006**, *600*, 1207–1212.
- (188) Kirakosian, A.; Lin, J.-L.; Petrovykh, D. Y.; Crain, J. N.; Himpsel, F. J. Functionalization of Silicon Step Arrays I: Au Passivation of Stepped Si(111) Templates. *J. Appl. Phys.* **2001**, *90*, 3286–3290.
- (189) Kim, J. H.; Yang, G.; Yang, S.; Weiss, A. H. Study of the Growth and Stability of Ultra-Thin Films of Au Deposited on Si(100) and Si(111). *Surf. Sci.* **2001**, *475*, 37–46.
- (190) Molodtsov, S. L.; Laubschat, C.; Shikin, A. M.; Adamchuk, V. K. Effects of Adatom Concentration on Au/Si(111) and Si/Au Interface Formation. *Surf. Sci.* **1992**, *269/270*, 988–994.
- (191) Baskaran, A.; Smereka, P. Mechanisms of Stranski-Krastanov Growth. *J. Appl. Phys.* **2012**, *111*, 044321.
- (192) Iwami, M.; Terada, T.; Tochiyama, H.; Kubota, M.; Murata, Y. Alloyed Interface Formation in the Au-Si(111)2×1 System Studied by Photoemission Spectroscopy. *Surf. Sci.* **1988**, *194*, 115–125.

- (193) Abbati, I.; Braicovich, L.; Franciosi, A.; Lindau, I.; Skeath, P. R. Photoemission Investigation of the Temperature Effect on Si–Au Interfaces. *J. Vac. Sci. Technol.* **1980**, *17*, 930–935.
- (194) Narusawa, T.; Kinoshita, K.; Gibson, W. M.; Hiraki, A. Structure Study of Au–Si Interface by MeV Ion Scattering. *J. Vac. Sci. Technol.* **1981**, *18*, 872–875.
- (195) Brillson, L. J.; Katnani, A. D.; Kelly, M.; Margaritondo, G. Photoemission Studies of Atomic Redistribution at Gold–silicon and Aluminum–silicon Interfaces. *J. Vac. Sci. Technol. A* **1984**, *2*, 551–555.
- (196) Cros, A.; Salvan, F.; Commandre, M.; Derrien, J. Enhancement of the Room Temperature Oxidation of Silicon by Very Thin Predeposited Gold Layer. *Surf. Sci. Lett.* **1981**, *103*, L109–L114.
- (197) Zhao, L.; Siu, A. C.-L.; Petrus, J. A.; He, Z.; Leung, K. T. Interfacial Bonding of Gold Nanoparticles on a H-Terminated Si(100) Substrate Obtained by Electro- and Electroless Deposition. *J. Am. Chem. Soc.* **2007**, *129*, 5730–5734.
- (198) Hamers, R. J.; Coulter, S. K.; Ellison, M. D.; Hovis, J. S.; Padowitz, D. F.; Schwartz, M. P.; Greenlief, C. M.; Russell, J. N. Cycloaddition Chemistry of Organic Molecules with Semiconductor Surfaces. *Acc. Chem. Res.* **2000**, *33*, 617–624.
- (199) Leftwich, T.; Teplyakov, A. Chemical Manipulation of Multifunctional Hydrocarbons on Silicon Surfaces. *Surf. Sci. Rep.* **2008**, *63*, 1–71.
- (200) Filler, M. A.; Bent, S. F. The Surface as Molecular Reagent: Organic Chemistry at the Semiconductor Interface. *Prog. Surf. Sci.* **2003**, *73*, 1–56.
- (201) Mayne, A. J.; Riedel, D.; Comtet, G.; Dujardin, G. Atomic-Scale Studies of Hydrogenated Semiconductor Surfaces. *Prog. Surf. Sci.* **2006**, *81*, 1–51.
- (202) Buriak, J. M. Organometallic Chemistry on Silicon and Germanium Surfaces. *Chem. Rev.* **2002**, *102*, 1271–1308.
- (203) Wang, X.; Landis, E. C.; Franking, R.; Hamers, R. J. Surface Chemistry for Stable and Smart Molecular and Biomolecular Interfaces via Photochemical Grafting of Alkenes. *Acc. Chem. Res.* **2010**, *43*, 1205–1215.
- (204) Rahsepar, F. R.; Zhang, L.; Leung, K. T. Two-Dimensional Self-Assembled Gold Silicide Honeycomb Nanonetwork on Si(111)7×7-Chapter 3. *J. Phys. Chem. C* **2014**, *118*, 9051–9055.

- (205) Zhang, L.; Chatterjee, A.; Ebrahimi, M.; Leung, K. T. Hydrogen-Bond Mediated Transitional Adlayer of Glycine on Si(111)7×7 at Room Temperature. *J. Chem. Phys.* **2009**, *130*, 121103.
- (206) Ataman, E.; Isvoranu, C.; Knudsen, J.; Schulte, K.; Andersen, J. N.; Schnadt, J. Adsorption of L-Cysteine on Rutile TiO₂(110). *Surf. Sci.* **2011**, *605*, 179–186.
- (207) Huang, J. Y.; Ning, Y. S.; Yong, K. S.; Cai, Y. H.; Tang, H. H.; Shao, Y. X.; Alshahateet, S. F.; Sun, Y. M.; Xu, G. Q. Binding of Glycine and L-Cysteine on Si(111)-7×7. *Langmuir* **2007**, *23*, 6218–6226.
- (208) Gross, D.; Grodsky, G. On the Sublimation of Amino Acids and Peptides. *J. Am. Chem. Soc.* **1955**, *77*, 1678–1680.
- (209) NIST Chemistry Webbook. *Choice Reviews Online*, 1998, *35*, 35–2709–35–2709.
- (210) Fernández-Ramos, A.; Cabaleiro-Lago, E.; Hermida-Ramón, J. M.; Martínez-Núñez, E.; Peña-Gallego, A. DFT Conformational Study of Cysteine in Gas Phase and Aqueous Solution. *J. Mol. Struct. THEOCHEM* **2000**, *498*, 191–200.
- (211) Dobrowolski, J. C.; Rode, J. E.; Sadlej, J. Cysteine Conformations Revisited. *J. Mol. Struct. THEOCHEM* **2007**, *810*, 129–134.
- (212) He, J.; Patitsas, S. N.; Preston, K. F.; Wolkow, R. A.; Wayner, D. D. M. Covalent Bonding of Thiophenes to Si(111) by a Halogenation/thienylation Route. *Chem. Phys. Lett.* **1998**, *286*, 508–514.
- (213) Huang, H. G.; Huang, J. Y.; Ning, Y. S.; Xu, G. Q. Selective Bonding of Pyrazine to Silicon(100)-2×1 Surfaces: The Role of Nitrogen Atoms. *J. Chem. Phys.* **2004**, *121*, 4820–4825.
- (214) Cao, X.; Coulter, S. K.; Ellison, M. D.; Liu, H.; Liu, J.; Hamers, R. J. Bonding of Nitrogen-Containing Organic Molecules to the Silicon(001) Surface The Role of Aromaticity. *J. Phys. Chem. B* **2001**, *105*, 3759–3768.
- (215) Kugler, Th.; Thibaut, U.; Abraham, M.; Folkers, G.; Gopel, W. Chemically Modified Semiconductor 1,4-Phenylenediamine on Si(100) Surfaces: *Surf. Sci.* **1992**, *260*, 64–74.
- (216) Pauling, L. *The Nature of the Chemical Bond and the Structure of Molecules and Crystals*; Ithaca, N. Y., Ed.; 3rd ed.; 1960; Vol. 148.
- (217) Clark, D. T.; Peeling, J.; Colling, L. A Experimental and Theoretical Investigation of the Core Level Spectra of a Series of Amino Acids, Dipeptides and Polypeptides. *Biochim. Biophys. Acta* **1976**, *453*, 533–545.

- (218) Kerr, J. A. *CRC Handbook of Chemistry and Physics*; Lide, D. R., Ed.; 95th ed.; CRC Press: Boca Raton, Florida, USA,.
- (219) Qiao, M. H.; Cao, Y.; Tao, F.; Liu, Q.; Deng, J. F.; Xu, G. Q. Electronic and Vibrational Properties of Thiophene on Si(100). *J. Phys. Chem. B* **2000**, *104*, 11211–11219.
- (220) Stohr, J.; Gland, J. L.; Kollin, E. B.; Koestner, R. J.; Johnson, A. L.; Muetterties, L.; Sette, F. Desulfurization and Structural Transformation of Thiophene on the Pt(111) Surface. *Phys. Rev. Lett.* **1984**, *53*, 2161–2164.
- (221) Razado, I.; Zhang, H.; Uhrberg, R.; Hansson, G. STM Study of Site Selective Hydrogen Adsorption on Si(111)7×7. *Phys. Rev. B* **2005**, *71*, 235411–235416.
- (222) Zang, K.; Guo, Q.; Fu, H.; Yu, Y.; Qin, Z.; Cao, G. The Initial Stage of the Dissociative Adsorption and the Surface Electronic State Evolution of NH₃ on Si(111)-(7×7). *J. Phys. Condens. Matter* **2010**, *22*, 085002.
- (223) Jeffrey, G. A. *An Introduction to Hydrogen Bonding*; Oxford University Press: New York, 1997; Vol. 6, p. 320.
- (224) Rahsepar, F. R.; Leung, K. T. *Novel Self-Organized L-Methionine Y-Shaped Trimer Supported on Si(111)7x7-Chapter 5*.
- (225) Casalongue, H. S.; Kaya, S.; Viswanathan, V.; Miller, D. J.; Friebel, D.; Hansen, H. A.; Nørskov, J. K.; Nilsson, A.; Ogasawara, H. Direct Observation of the Oxygenated Species During Oxygen Reduction on a Platinum Fuel Cell Cathode. *Nat. Commun.* **2013**, *4*, 1–6.
- (226) Chen, Q.; Richardson, N. V. Enantiomeric Interactions Between Nucleic Acid Bases and Amino Acids on Solid Surfaces. *Nat. Mater.* **2003**, *2*, 324–328.
- (227) Barth, J. V.; Weckesser, J.; Cai, C.; Günter, P.; Bürgi, L.; Jeandupeux, O.; Kern, K. Building Supramolecular Nanostructures at Surfaces by Hydrogen Bonding. *Angew. Chem. Int. Ed.* **2000**, *39*, 1230–1234.
- (228) Csaszar, A. G. Conformers of Gaseous Glycine. *J. Am. Chem. Soc.* **1992**, 9568–9575.
- (229) Gronert, S.; O’Hair, R. A. J. Ab Initio Studies of Amino Acid Conformations. 1. The Conformers of Alanine, Serine, and Cysteine. *J. Am. Chem. Soc.* **1995**, *117*, 2071–2081.
- (230) Csaszar, A. G. Conformers of Gaseous α -Alanine. *J. Am. Chem. Soc.* **1996**, *100*, 3541–3551.
- (231) Wilke, J. J.; Lind, M. C.; Iii, H. F. S.; Csaszar, A. G.; Allen, W. D. Conformers of Gaseous Cysteine. *J. Chem. Theory Comput.* **2009**, *5*, 1511–1523.

- (232) Maul, R.; Ortmann, F.; Preuss, M.; Hannewald, K.; Bechstedt, F. DFT Studies Using Supercells and Projector-Augmented Waves for Structure, Energetics, and Dynamics of Glycine, Alanine, and Cysteine. *J. Comput. Chem.* **2007**, *28*, 1817–1833.
- (233) Rahsepar, F. R.; Leung, K. T. “Universal” Three-Stage Growth of α -Amino Acids on Si (111)7 \times 7 Surface-Mediated by Hydrogen Bonding-Chapter 5.
- (234) MedeA® and Materials Design® <http://www.materialsdesign.com/software>.
- (235) Vallee, A.; Humblot, V.; Pradier, C. Peptide Interactions with Metal and Oxide Surfaces. *Acc. Chem. Res.* **2010**, *43*, 1297–1306.
- (236) Chi, Q.; Zhang, J.; Nielsen, J. U.; Friis, E. P.; Chorkendorff, I.; Canters, G. W.; Andersen, J. E. T.; Ulstrup, J. Molecular Monolayers and Interfacial Electron Transfer of Pseudomonas Aeruginosa Azurin on Au(111). *J. Am. Chem. Soc.* **2000**, *122*, 4047–4055.
- (237) Gerster, D.; Reichert, J.; Bi, H.; Barth, J. V.; Kaniber, S. M.; Holleitner, A. W.; Visoly-Fisher, I.; Sergani, S.; Carmeli, I. Photocurrent of a Single Photosynthetic Protein. *Nat. Nanotechnol.* **2012**, *7*, 673–676.
- (238) Santos, E.; Avalle, L. B.; Scurtu, R.; Jones, H. L-Cysteine Films on Ag(111) Investigated by Electrochemical and Nonlinear Optical Methods. *Chem. Phys.* **2007**, *342*, 236–244.
- (239) Thomsen, L.; Wharmby, M. T.; Riley, D. P.; Held, G.; Gladys, M. J. The Adsorption and Stability of Sulfur Containing Amino Acids on Cu{531}. *Surf. Sci.* **2009**, *603*, 1253–1261.
- (240) Faj, J. L. C.; Gomes, J. R. B.; Nata, M.; Cordeiro, D. S. DFT Study of the Adsorption of D-(L-) Cysteine on Flat and Chiral Stepped Gold Surfaces. *Langmuir* **2013**, *29*, 8856–8864.
- (241) Felice, R. Di; Selloni, A. Adsorption Modes of Cysteine on Au(111): Thiolate, Amino-Thiolate, Disulfide. *J. Chem. Phys.* **2004**, *120*, 4906–4914.
- (242) Felice, R. Di; Selloni, A.; Molinari, E. DFT Study of Cysteine Adsorption on Au(111). *J. Am. Chem. Soc.* **2003**, *107*, 1151–1156.
- (243) Schreiber, F. Structure and Growth of Self-Assembling Monolayers. *Prog. Surf. Sci.* **2000**, *65*, 151–256.
- (244) Yang, G.; Hu, H.; Zhou, Y.; Hu, Y.; Huang, H.; Nie, F.; Shi, W. Synthesis of One-Molecule-Thick Single-Crystalline Nanosheets of Energetic Material for High-Sensitive Force Sensor. *Sci. Rep.* **2012**, *2*, 698.